DIESEL LOW TEMPERATURE COMBUSTION: AN EXPERIMENTAL STUDY

by

Asish Kumar Sarangi

B.E., Utkal University, Orissa, India 2001

M.Sc. by Research, Indian Institute of Technology Madras, India 2007

A Doctoral Thesis

Submitted in partial fulfilment of the requirements

for the award of

Doctor of Philosophy of Loughborough University

July 2012

LOUGHBOROUGH UNIVERSITY

Loughborough University

CERTIFICATE OF ORIGINALITY

This is to certify that I am responsible for the work submitted in this thesis, that the original work is my own except as specified in acknowledgments or in footnotes, and that neither the thesis nor the original work contained therein has been submitted to this or any other institution for a degree.

……. (Signed)

……. (Date)

ABSTRACT

Diesel engine emissions of oxides of nitrogen and particulate matter can be reduced simultaneously through the use of high levels of exhaust gas recirculation (EGR) to achieve low temperature combustion (LTC). Although the potential benefits of diesel LTC are clear, the main challenges to its practical implementation are the requirement of EGR levels that can exceed 60%, high fuel consumption, and high unburned hydrocarbon and carbon monoxide emissions. These limit the application of LTC to medium loads. In order to implement the LTC strategy in a passenger vehicle engine, a transition to conventional diesel operation is required to satisfy the expected high load demands on the engine. The investigation presented in this thesis was therefore aimed at improving the viability of the high-EGR LTC strategy for steady-state and transient operation.

An experimental investigation was carried out on a single cylinder high-speed direct injection diesel engine. This thesis presents research on engine in-cylinder performance and engine-out gaseous and particulate emissions at operating conditions (i.e. EGR rate, intake pressure, fuel quantity, injection pressure) likely to be encountered by an engine during transient and steady-state operation. At selected operating points, further investigation in terms of in-cylinder spray and combustion visualization, flame temperature and soot concentration measurements provided deeper insight into the combustion and emissions phenomena.

Increased intake pressure at single injection high-EGR LTC operation was investigated as a strategy to reduce the emissions of partial combustion by-products and to improve fuel economy. The higher intake pressure, although effective in reducing partial combustion by-products emissions and improving fuel economy, increased the EGR requirement to achieve LTC. A split fuel injection strategy with advanced injection timing on the other hand was effective in reducing the EGR requirement for LTC from 62% with single injection to 52% with split injections at 120 kPa (absolute) intake pressure. Unburned hydrocarbon emissions and fuel economy were particularly sensitive to intake oxygen mass fraction, and injection and dwell timings with the split injection strategy. In-cylinder soot formation and oxidation mechanisms with the split injection strategy were found to be significantly different from the single injection high-EGR LTC case.

Transient simulation of an engine during combustion mode transition identified engine operating parameters on a cycle-by-cycle basis. Steady-state investigation of these test conditions provided significant insight into the combustion conditions and their effect on emissions and performance. The results from this thesis demonstrated the importance of optimizing both the air handling system performance and the fuel injection system during engine transients. The increased emissions and impaired performance due to slow response of the EGR and turbocharger systems during transitions to and from LTC modes can in part be mitigated through split injections optimized for the specific transient point. This provides a clear direction for engine developers to pursue in optimizing engine calibration when running with LTC-conventional diesel dual-mode strategies.

ACKNOWLEDGEMENTS

While thinking back with gratitude on the wonderful time I spent at Loughborough University, I realize that the work described in this thesis could not have been completed without the support of the exemplary supervisors and colleagues with whom I was fortunate to work. My foremost acknowledgement goes to my supervisors Professor Colin Garner, Dr. Martin Davy and Dr. Gordon McTaggart-Cowan for their unending support, patience and advice during my PhD study. The development of both my technical proficiency and my abilities as an independent researcher is a direct result of their guidance and tutelage. They always provided encouragement and absolute freedom which made the PhD fun for me. My special recognition goes to the technical support and ceaseless efforts of Adrian Broster, Steve Horner, Steve Taylor and Graham Smith on the experimental setup. It was a great fun working with you; many thanks. For the financial support of the project and my studentship, I acknowledge Loughborough University and the UK EPSRC.

I want to acknowledge Shenghui Cong and Antonis Michailidis for the friendly research environment they have created. Their teamwork, collaboration and enthusiasm towards research have cheered me up whenever I have had difficulties during my research. Special thanks also go to Edward Winward for his help with the LABVIEW program used for image acquisition. His willingness to share his engine testing experiences is greatly appreciated. I also would like to thank the graduate student, Jugraj Atwal for his valuable contributions to the experimental setup. I would like to thank Alan Baker for his valuable advice on WAVE modelling. I would like to acknowledge my friends Vikrant and Kanik who always provided me with an ear to listen, and never failed to encourage me when I encountered a pitfall along the way. I had many fruitful discussions with them. Fikri, Josh, Saroj and Tarani are acknowledged for their contributions during my PhD. Stephen Johnson and Suji Sogbesan are specially acknowledged for their help in proof-reading the thesis.

The suggestions and advice of Professor Graham Hargrave and Dr. Graham Wigley during the development of the optical facility are gratefully acknowledged. I would like to acknowledge Professor Hua Zhao for giving permission to use the tungsten lamp calibration test facility at Brunel University. I would also like to thank Dr. Reza Mohammad at Brunel University for his help during the calibration of the two-colour pyrometer. Special acknowledgement goes to Dr. Emad Wahab and Andy Scarisbrick from Ford Motor Company and Dr. Mark Peckham from Cambustion Ltd for their valuable suggestions on the research. A special word of thank goes to Professor Pramod Mehta at IIT Madras for his encouragement and advice before and during the PhD study.

Finally, I want to thank my family, and especially my parents Sisir and Minati Sarangi, for their endless love and support during my educational pursuits. This thesis is dedicated to them. To my brother, Papun, you took most of the family responsibility and gave me unconditional support during my study; you deserve a big thank you. My grandmother, Kamal, uncles, Sagar and Sebananda, aunt Dipti, are gratefully acknowledged for their support and love all along.

TABLE OF CONTENTS

ACRONYMS, NOMENCLATURE AND SYMBOLS

AC = Alternating current

AGTDC = After gas exchange top dead centre

AR = Anti-reflective

ARTEMIS = Assessment and Reliability of Transport Emission Models and Inventory Systems

ATAC = Active thermo-atmosphere combustion

ATDC = After top dead centre

BGTDC = Before gas exchange top dead centre

BMEP = Brake mean effective pressure [Pa]

BSFC = Brake specific fuel consumption [g/kWh]

BTDC = Before top dead centre

^{o}CA = Crank angle degree

CA5 = Crank angle corresponding to 5% of cumulative energy release [^{o}CA ATDC]

CA50 = Combustion mid-point corresponding to 50% of cumulative energy release [^{o}CA ATDC]

CA90 = Crank angle corresponding to 90% of cumulative energy release [^{o}CA ATDC]

CA95 = Crank angle corresponding to 95% of cumulative energy release [^{o}CA ATDC]

CAD = Crank angle degree

CADC = Common ARTEMIS driving cycle

CCD = Charge coupled device

CDM = Crank degree marker

C_2H_2 = Acetylene

CH_2O = Formaldehyde

CI = Compression ignition

CLD = Chemiluminescence detector

CMD = Count median diameter [nm]

CO = Carbon monoxide

CO_2 = Carbon dioxide

COV = Coefficient of variation [%]

CWL = Centre wavelength [nm]

DC = Direct current

DI = Direct injection

DMS = Differential mobility spectrometer

DOC = Diesel oxidation catalyst

DOE = Design of experiments

DOHC = Double overhead camshaft

DPF = Diesel particulate filter

E_0 = Activation energy [J.mole^{-1}]

EBP = Exhaust back pressure [Pa]

ECE 15 = Urban drive cycle (ECE: Economic Commission for Europe)

ECU = Electronic control unit

EGR = Exhaust gas recirculation [%]

EI = Emission index [g/kg of fuel]

EMS = Engine management system

EPA = Environmental protection agency

ESC = European Stationary Cycle

ETC = European Transient Cycle

EU = European Union

EUDC = Extra-urban drive cycle

FOV = Field of view [degree]

FSN = Filter smoke number

FTP = Federal test procedure

FWHM = Full width at half maximum [nm]

GIMEP = Gross indicated mean effective pressure [Pa]

GISFC = Gross indicated specific fuel consumption [g/kWh]

H = Hydrogen atom

H_2 = Hydrogen molecule

HC = Hydrocarbons

HCCI = Homogeneous charge compression ignition

HCN = Hydrocyanic acid

HDD = Heavy-duty diesel

HFID = Hydrogen flame ionization detector

H_2O = Water

H_2O_2 = Hydrogen peroxide

HSDI = High-speed direct injection

I_b = Monochromatic black body radiance [W/m^2/μm]

ICCD = Intensified charge coupled device

IMEP = Indicated mean effective pressure [Pa]

IR = Infra-red

ISFC = Indicated specific fuel consumption [g/kWh]

k = Rate constant [cm^3.mole^{-1}. s^{-1}]

KL = Indicator of soot concentration (or soot loading)

L = Optical path length [m]

LDD = Light-duty diesel

LIVC = Late intake valve closure

LNC = Lean NO_X catalyst

LNT = Lean NO_X trap

LTC = Low temperature combustion

MBT = Maximum advance for best indicated torque

MK = Modulated kinetics

N = Engine speed [r/s]

N_2 = Nitrogen molecule

NA = Numerical aperture

NDIR = Non-dispersive infrared

NEDC = New European drive cycle

NH_3 = Ammonia

NIR = Near infra-red

NMHC = Non-methane hydrocarbon

NO = Nitric oxide

N_2O = Nitrous oxide

NO_2 = Nitrogen dioxide

NO_X = Oxides of nitrogen (include NO, NO_2)

NTC = Negative temperature coefficient

NVH = Noise, vibration and harshness

O = Oxygen atom

O_2 = Oxygen molecule

O_3 = Ozone

OBD = On-board diagnostic

OH = Hydroxyl radical

p = Cylinder pressure [Pa]

PAH = Polycyclic aromatic hydrocarbons

PCI = Premixed compression ignition

PCCI = Premixed charge compression ignition

PID = Proportional integral and derivative

P_{inj} = Injection pressure [Pa]

PLC = Programmable logic control

PLIF = Planar laser induced fluorescence

PLII = Planar laser induced incandescence

PM = Particulate matter

PMD = Paramagnetic detector

PMT = Photo multiplier tube

PN = Particle number

PW = Injection pulse width [mg]

Q_n = Apparent net energy release [J]

R_0 = Universal gas constant [$J.mole^{-1}.K^{-1}$]

RGF = Residual gas fraction [%]

rpm = Revolution per minute [r/min]

SCR = Selective catalytic reduction

SNR = Signal-to-noise ratio

SO_2 = Sulphur dioxide

SOC = Start of combustion [^oCA ATDC]

SOF = Soluble organic fraction

SOI = Start of injection [^oCA ATDC]

SOI1 = 1^{st} start of injection timing [^oCA ATDC]

SOI2 = 2^{nd} start of injection timing [^oCA ATDC]

T = True temperature [K]

T_a = Apparent temperature [K]

TDC = Top dead centre

THC = Total unburned hydrocarbon (C_1)

TTL = Transistor-transistor-logic

UNIBUS = Uniform bulky combustion system (Toyota)

USEPA = United States environmental protection agency

UV = Ultra-violet

V = Cylinder volume [m^3]

V_d = Engine swept volume [m^3]

VCO = Valve covered orifice

VGT = Variable geometry turbocharger

VNT = Variable nozzle turbine

VVT = Variable valve timing

WHSC = Worldwide harmonised steady state driving cycle

WHTC = Worldwide harmonised transient driving cycle

Y_{O2} = Intake oxygen mass fraction [%]

Greek symbols

γ = Specific heat ratio

ε = Emissivity

η_c = Combustion efficiency

θ = Crank angle [^oCA]

λ = Wavelength [nm]

ϕ = Equivalence ratio

$\frac{dp}{d\theta}$ = Rate of pressure rise [Pa/^oCA]

LIST OF FIGURES

LIST OF TABLES

CO-AUTHORSHIP STATEMENT

The work presented in this thesis was conceived, conducted and disseminated by the doctoral candidate. The co-authors of the manuscripts that comprise part of this thesis made contributions only as is commensurate with a thesis committee or as experts in a specific area as it pertains to the work. The co-authors provided direction and support. The co-authors reviewed each manuscript prior to submission for publication and offered critical evaluations; however, the candidate was responsible for the writing and the final content of these manuscripts.

Chapter 1
INTRODUCTION TO THESIS

1.1 Introduction

Concerns regarding rapidly depleting petroleum resources and increasing levels of greenhouse gases are driving the demand for fuel efficient engines, and hence, there is increasing interest in diesel engines. Diesels are currently the most fuel efficient engines due to their higher compression ratio, their higher specific heat ratio (due to overall lean mixtures), and their near zero throttling and pumping losses relative to conventional gasoline engines. Their high efficiency and high torque make diesels particularly desirable for heavy-duty commercial vehicles and off-road applications. The demand for diesel engines is also increasing in light-duty passenger vehicles in response to their fuel economy and recent improvement in driveability due to advances in turbocharging. Fuel pricing and taxation are also driving their demands for light-duty passenger vehicles. More than 50% of all the newly registered passenger cars in Europe are now diesel [ACEA, 2011]. The engine-out emissions of unburned hydrocarbon and carbon monoxide (CO) in conventional diesel engines are much less compared to typical gasoline engines due to an overall lean air-fuel ratio. However, diesel engines have higher emissions of oxides of nitrogen (NO_X) and particulate matter (PM) compared to gasoline engines and these emissions increase further during a transient operation. Diesel low temperature combustion (LTC) is a promising technique, wherein both NO_X and PM are simultaneously reduced to very low levels. The major disadvantages of LTC are increases in unburned hydrocarbon and CO emissions, reduced fuel economy and a limited maximum load compared to conventional diesel combustion. The limited load for diesel LTC operation results in the need to transition between LTC and conventional diesel during typical driving. The overall aim of this research was to investigate ways to manage these transitions, avoiding high emissions and perceptible changes in performance.

The objective of the research presented in this thesis was to improve the understanding of the combustion and emission phenomena associated with diesel LTC operation and the phenomena associated with the transition between LTC and conventional diesel. This understanding aids the development of novel techniques for emission reduction, while maintaining the diesel engine's advantageous performance and efficiency. The ultimate aim of this work was to improve the viability of the high-EGR LTC strategy.

1.2 Air Pollution and Health Impacts

Air pollution has long been recognized as a public nuisance. Air pollutants of concern include solid aerosol particles (PM) and gaseous pollutants such as NO_X, sulphur dioxide (SO_2), CO and ozone (O_3). All of these have their own health impacts, but PM has been shown to be the most harmful [Dockery *et al.*, 1993]. Particles are classified according to their size by their aerodynamic

diameters: nano particles (aerodynamic diameter <50 nm), ultra-fine particles (aerodynamic diameter <100 nm) and fine particles (aerodynamic diameter <2.5 μm, designated as PM2.5). Diesel engines tend to generate these fine, ultra-fine and nano particles [Kittelson, 1998]. Fine particles are mainly carbonaceous soot agglomerates formed directly by combustion; ultra-fine and nanoparticles (typically hydrocarbon or sulphate) are formed by nucleation during dilution and cooling of the exhaust gases [Kittelson, 1998].

With increasing numbers of diesel engine vehicles, there have been growing fears of the health risks associated with diesel particulates and also their effects on the environment. Numerous epidemiological studies have shown that PM significantly increases premature mortality through cardiovascular or pulmonary endpoints [Dockery *et al.*, 1993; Ayala *et al.*, 2011]. PM's adverse health effects are attributed to deposition on sensitive lung tissues, causing irritation and immune system reactions [EPA, 2002]. Primary health risks are due to the smaller particles penetrating and remaining deep in the human lung tissue. These particles can cause inflammatory response and pulmonary toxicity [EPA, 2002]. Smaller particles are also likely to pass into the bloodstream; thereby directly affecting the cardiovascular system [Sawyer, 2009]. Diesel PM also includes a significant quantity of adsorbed volatile organics and other potentially toxic or 'carcinogenic' species [EPA, 2000]. Other less serious, but certainly more widespread, health risks are associated with the aggravation of respiratory problems and problems with eye, nose and throat irritation. Environmental risks are numerous, such as soiling of buildings and poor visibility especially in cities [EPA, 2004]. The California Air Resources Board (CARB) has defined diesel PM as an 'air toxic', and estimated that in 2003, diesel PM was responsible for approximately 70% of the cancer cases attributed to all air toxics [CARB, 2003].

Of the gaseous air pollutants, the most significant related to a diesel engine is NO_X. The primary environmental impacts of NO_X are generally considered to be the formation of ground level ozone and photochemical smog [EPA, 2004]. Smog contains unburned hydrocarbon, peroxyacetyl nitrate ($C_2H_3NO_5$), NO_X, O_3 and nitric acid [Stone, 1999]. The constituent of the photochemical smog can cause eye irritation, cough, asthma and reduced pulmonary function [EPA, 2004]. The mechanism of the formation of ozone depends on the presence of nitrogen dioxide (NO_2), hydrocarbons and ultra-violet (UV) light from sunlight and therefore, is strongly dependent on the local geographic and meteorological conditions [Charmley, 2004]. Note that unlike ozone close to the ground, ozone in the atmosphere at a height of 20-40 km is important in absorbing the harmful UV radiation [Stone, 1999].

NO_X and SO_2 are also important precursors for the secondary formation of nitrate and sulphate aerosols respectively and in the formation of respective acids (nitric acid and sulphuric acid), which lead to acid rain [EPA, 2004]. Acid rain contributes to damage of trees at high elevations and in extreme cases may cause lakes and streams to become so acidic that they cannot support aquatic life. In addition, acid deposition accelerates the decay of building materials and

paints [EPA, 2004]. SO_2 is water soluble and deposits in the upper airways producing bronchial irritation; it also reduces lung function and aggravates asthma [Sawyer, 2009]. SO_2 emissions from diesel engines have reduced significantly due to low fuel sulphur concentration.

Unlike many gases, CO is odourless, colourless, tasteless and non-irritating, but it is fatal at high enough doses. At lower concentrations, it has been linked to increased risk for people with heart disease, reduced visual perception, cognitive functions and aerobic capacity, and possible fatal effects. Carbon monoxide enters the blood stream through the lungs and forms carboxy-haemoglobin, a compound that inhibits blood's capacity to carry oxygen to organs and tissues [EPA, 2004].

Noise has also been identified as a pollutant due to its adverse health effects on vehicle occupants and pedestrians [European Commission, 2004]. Noise levels from motor vehicles have been limited to 80 dB or less depending on the type of vehicle [European Commission, 2004]. Diesel engines have higher combustion noise compared to equivalent gasoline engines. In addition to fulfilling the current legislation requirement, noise and vibration influence comfort and hence play an essential role in the customers' purchasing decision.

Methane and carbon dioxide (CO_2) are the two most significant greenhouse gases whose ambient atmospheric concentrations have been significantly increasing over the past decades [EPA, 2012]. It is reported that internal combustion engines used in transportation produce about 23% of the UK's CO_2 emissions [Taylor, 2008]. For a given fuel, CO_2 emissions are directly related to an engine's fuel conversion efficiency. However, it should be noted that the CO_2 benefits of diesel are reduced by the fact that per unit energy it releases more CO_2 compared to gasoline as diesel has higher carbon to hydrogen ratio (0.59:1 for diesel compared to 0.53:1 for gasoline [Heywood, 1988]). Therefore, burning one mole of gasoline will release more chemical energy per mole CO_2 than burning one mole of diesel. Although high fuel efficiency of diesel engines relative to most other motive power sources minimize greenhouse gas emissions, these emission levels are still a matter of concern. Any improvement in engine efficiency will lead to a reduction in CO_2 emissions. CO_2 is now regulated for European light-duty vehicles on a fleet average basis, and is also a factor for vehicle taxation [ACEA, 2012]. In general, steps that improve engine efficiency tend to increase engine-out pollutant emissions. As a result, reducing engine-out CO_2 and other harmful emissions together poses a significant challenge.

1.3 Emission Legislation

Emission legislation is implemented to help minimize the adverse health and environmental impacts of air pollutants from different power sources. Vehicles in particular are being required to meet emissions legislation that is becoming progressively more stringent. For example, the Euro 6 emission legislation (applicable for the countries in the European Union) reduces NO_X emissions from the existing Euro 5 limit of 0.18 g/km to 0.08 g/km, while the PM limit is maintained constant

at 0.005 g/km for light-duty diesel (LDD) vehicles. These are reductions of 84% (NO_X) and 90% (PM) compared to 2000 model year vehicles [European Commission, 2008; DieselNet, 2009]. In addition, a particle number (PN) for all categories of LDD vehicles has been set at 6×10^{11} particles/km [European commission, 2008]. The proposal also aims at defining a maximum limit for the NO_2 component of NO_X emissions at a later time. Passenger cars (Category 'M' vehicles for the carriage of passengers and comprising no more than eight seats in addition to the driver's seat) and light commercial vehicles (Category 'N_1' with three different classes of vehicles for the carriage of goods and having a maximum mass not exceeding 3500 kg) are included in LDD vehicles categories for the European emission legislations [DieselNet, 2009].

Table 1.1 summarizes the emission limit requirements for passenger vehicles (Category 'M') and light-duty commercial vehicles (Category 'N_1, Class I' with reference mass less than 1305 kg) in the European Union (EU). Note that Category 'N_1, Class I' is subjected to the most stringent emission legislation amongst the different classes of N_1 category vehicles. Table 1.2 highlights the development of EU emissions legislation for heavy-duty diesel (HDD) engines for automotive applications in the last decade. The stringent regulations for controlling hydrocarbon (HC) and CO emissions are also evident from the tables, although the main focus for diesel engines has been to reduce PM and NO_X.

Table 1.1: EU Emission Legislations for Diesel Passenger Cars (Category 'M') and Light Commercial Vehicles (Category 'N_1, Class I') [European Commission, 2008; DieselNet, 2009]

Implementation Year	HC+ NO_X (g/km)	CO (g/km)	NO_X (g/km)	PM (g/km)	PN (#number/km)
2000 (Euro 3)	0.56	0.64	0.50	0.05	-
2005 (Euro 4)	0.30	0.50	0.25	0.025	-
2009 (Euro 5)	0.23	0.50	0.18	0.005	6×10^{11} *
2014 (Euro 6)	0.17	0.50	0.08	0.005	6×10^{11}

* Introduced in Euro 5b from September 2011

Table 1.2: EU Emission Legislations for HDD Engines [European Commission, 2008, 2011]

Implementation Year	HC (g/kWh)		CO (g/kWh)		NO_X (g/kWh)		PM (g/kWh)		PN (#number/kWh)	
	ESC	ETC	ESC	ETC	ESC	ETC	ESC	ETC	WHSC	WHTC
2000 (Euro III)	0.66	0.78	2.1	5.45	5.0	5.0	0.1	0.16	-	-
2005 (Euro IV)	0.46	0.55	1.5	4.0	3.5	3.5	0.02	0.03	-	-
2008 (Euro V)	0.46	0.55	1.5	4.0	2.0	2.0	0.02	0.03	-	-
2013 (Euro VI)†	0.13	0.16‡	1.5	4.0	0.4	0.46	0.01	0.01	8×10^{11}	6×10^{11}

† The test cycles for Euro VI legislations are WHSC (Worldwide Harmonised Steady-State Driving Cycle) and WHTC (Worldwide Harmonised Transient Driving Cycle); other European legislations (Euro III to Euro V) are ESC (European Stationary Cycle) and ETC (European Transient Cycle)

‡ THC (total hydrocarbons consisting of methane and non-methane hydrocarbon) for diesel engines in Euro VI

The latest EU legislation limits the fleet average CO_2 emissions to 130 g/km for passenger cars from 2012 onwards and aims at setting a target of 95 g/km as average emissions for the new car fleet [European Commission, 2009]. Starting from the Euro 3 stage, light-duty vehicles are equipped with an on-board diagnostics (OBD) system for emission control, where the driver is notified in case of a malfunction or deterioration of the emission system that would cause the emissions to exceed mandatory thresholds [DieselNet, 2009].

In the US, the entire light duty vehicles fleet sold by each manufacturer has to meet average NO_X and PM limits of 0.07 g/mi (0.04 g/km) and 0.01 g/mi (0.006 g/km) respectively as per Tier 2, Bin 5 emissions legislation of the United States Environmental Protection Agency (USEPA), fully implemented from the Model Year 2009 [USEPA, 2007]. From 2009 onwards, in Japan, passenger cars have to meet the NO_X and PM limits of 0.08 g/km and 0.005 g/km respectively [DieselNet, 2009]. Despite an initial delay, several Asian countries (e.g. India and China) have implemented the Euro 4 legislation for their LDD vehicles [DieselNet, 2009]. Table 1.3 compares the current emission legislations in the EU, USA, Japan and India for the LDD vehicles. Note that the applicability and emission test cycles differ in the EU, USA, Japan and India; hence, the emission limits are not directly comparable.

Table 1.3: Comparisons of Emission Legislations for LDD Vehicles, g/km [European Commission, 2008; USEPA, 2007; DieselNet, 2009]

	EU	**USA**	**Japan**	**India**
Test Cycle	NEDC	FTP 75	JC08	NEDC*
NO_X	0.08	0.04	0.08	0.25
PM	0.005	0.006	0.005	0.025
HC + NO_X	0.17	0.05†	0.024†	0.30
CO	0.50	2.62	0.63	0.50

NEDC: New European Driving Cycle; FTP: Federal Test Procedure.

* The test cycle has been the NEDC, but the maximum speed is limited to 90 km/h.

†HC represents non-methane hydrocarbon (NMHC) only. USEPA and Japanese legislations do not specify THC + NO_X emission limits, instead they represent NMHC limits.

1.4 Emission Reduction Strategies

To meet the emissions requirements, manufacturers have focussed on improved air handling, more advanced injection and exhaust after-treatment. Currently, variable geometry turbochargers (VGT) and variable nozzle turbines (VNT) are used not only to increase the power density and fuel economy of the engines but also to control the engine combustion processes. A variable boost system allows flexible control and optimization of the boost pressure for different engine operating conditions. In addition, these systems have also been proved to reduce emissions and improve engine transient response [Arnold, 2004]. The VGT/VNT system also maintains a desired exhaust

back pressure for exhaust gas recirculation (EGR) [Arnold, 2004]. Advanced combustion systems with increased injection pressure, EGR, improved piston-bowl geometries, improved in-cylinder flows, advanced turbocharger technology and availability of ultra-low sulphur diesel fuel have resulted in substantial reductions in engine-out emissions from diesel engines [Charlton, 2005; Johnson, 2006; Taylor, 2008; Dec, 2009]. Despite these efforts, it appears unlikely that mixing-controlled diesel combustion can meet the future emission legislations without expensive after-treatment systems [Dec, 2009]. Although various existing exhaust after-treatment systems are capable of meeting the current emission legislation and are continuously being developed to meet the future legislations, they impose additional complexity for the powertrain [Johnson, 2011] and increase their cost. The various existing exhaust after-treatment systems include: selective catalytic reduction (SCR) and lean NO_X trap (LNT) for NO_X reduction; diesel particulate filter (DPF) for PM reduction; and diesel oxidation catalyst (DOC) for THC, CO and PM reduction. In certain cases, changes in the engine hardware and the introduction of the exhaust after-treatment systems may also impair the overall fuel economy [Johnson, 2006]. Note that SCR enables improved fuel economy by more advanced fuel injection timing; however, the system complexity and cost is increased.

In-cylinder combustion control strategies are alternatives to reduce engine-out emissions. High pressure common rail fuel injection systems with multiple injections per cycle enable reductions in PM. Retarded fuel injection timing can reduce NO_X emissions at the expense of fuel economy. Presently, the most widely used in-cylinder technique to control NO_X is EGR, wherein a part of the exhaust gases are recirculated into the intake, thus lowering the intake oxygen concentration and combustion temperature [Ladommatos *et al*., 2000]. However, EGR levels are currently limited in diesel engines due to the trade-off between NO_X and exhaust PM emissions [Zheng *et al*., 2004]. During low and medium load operation, EGR rates up to 25% may be applied, whereas at high load, EGR rate is either very low or nil [Zheng *et al*., 2004]. It is reported that the implementation of both the EGR and the after-treatment techniques in tandem seem to be more effective and affordable at reducing emissions while optimizing efficiency for diesel engines [Johnson, 2011].

Higher EGR rates can further reduce NO_X. However, the EGR rates currently used are limited because of combustion instability, increased PM emissions and even power losses [Zheng *et al*., 2004]. High emissions of PM and CO during transient operation is another hindrance to the use of high EGR level, since these emissions increase significantly with a slight variation of the optimum EGR rate [Helmantel, 2008]. The transient response of the EGR system is a further barrier. Especially with EGR, the fuel flow rate may exceed the amount of available oxygen in the cylinder during transient operation, thereby increasing soot, hydrocarbon and CO emissions [Chen, 2000]. To address the combined needs of meeting stringent emission legislation, achieving improved fuel economy and maintaining a reasonable price, attention has been directed towards alternative forms of diesel engine combustion which rely on the principle of dilute premixed or partially premixed

combustion [Dec, 2009]. These techniques rely on improved premixing, low in-cylinder oxygen concentration and low combustion temperature for the simultaneous reduction of soot and NO_X, and hence, they are commonly referred to as 'Low Temperature Combustion' (LTC) [Sasaki *et al*., 2000; Kimura *et al*., 2001; Kimura *et al*., 2002; Yun and Reitz, 2007; Lachaux *et al*., 2008]. The various LTC strategies include: Homogeneous Charge Compression Ignition (HCCI), Active Thermo-Atmosphere Combustion (ATAC), Modulated Kinetics (MK), Premixed Charge Compression Ignition (PCCI), Toyota Uniform Bulky Combustion System (UNIBUS), High-EGR LTC, and many more, although implementation and application strategies differ for different LTC modes. These strategies will be discussed in more detail in Chapter 2.

1.5 Objectives of this Research

The overall aim of this research is to investigate ways to manage transitions between high-EGR LTC and conventional diesel combustion, avoiding high emissions and perceptible changes in performance and to improve the viability of the high-EGR LTC strategy. The research is intended to improve the understanding of the combustion and pollutant formation processes in a diesel engine operating with high levels of EGR in an LTC mode. A specific interest in this work is to improve the viability of the high-EGR LTC strategy both during steady-state and transient operation. This research project is primarily experimental, conducted using a single cylinder diesel engine. Deeper insights into these phenomena have been achieved through in-cylinder optical diagnostics. The specific objectives of the present research work are as follows:

1. To understand and minimize the source of PM emissions that often occur in the narrow operating window, where both low NO_X and good combustion efficiency are achieved;
2. To investigate the effects of boost pressure on total unburned hydrocarbon (THC) and CO emissions and fuel economy with high-EGR LTC operation and to correlate these emissions with in-cylinder spray and combustion visualization and measured flame temperature;
3. To investigate the effects of multiple injections on LTC emission and combustion phenomena at reduced EGR levels and to correlate them with the in-cylinder optical assessment; and
4. To identify the reasons for the high emissions of NO_X, PM, THC and CO during transition from LTC to conventional diesel combustion or *vice-versa* and to investigate different methodologies to reduce these emissions.

Meeting these objectives should provide a better understanding of the combustion and emission phenomena during high-EGR LTC operation. This will make it possible to identify improved LTC operating modes to optimize the combustion process, with the goal of maximizing thermal efficiency while minimizing emissions to make this strategy viable.

1.6 Thesis Outline

The thesis structure is as follows:

Up to this point in Chapter 1, the general background, motivation and objectives of this research project are discussed together with a summary of emission legislations for automotive applications. In the subsequent sections in this chapter, the contributions of this research to the body of knowledge along with a list of publications are provided.

Chapter 2 gives the background information of combustion and emission formation processes in conventional diesel operation. The current emission control strategies (both in-cylinder and exhaust after-treatment) in conventional diesel combustion are discussed briefly. Different low temperature combustion strategies are described in detail. A brief description is given regarding the effects of intake pressure and multiple fuel injections in high-EGR LTC operation. Emission and combustion processes during a transient operation both in conventional diesel and high-EGR LTC operation are also discussed. Gaps in the literature are identified.

In Chapter 3, the experimental apparatus, measurement techniques and experimental parameters are described. The details of the engine modification for optical access are also given along with the design, implementation and calibration of a two-colour pyrometry system.

Chapter 4 reports the effects of boost pressure on the combustion and emission characteristics during high-EGR LTC operation. The effects of fuel injection timing and fuel injection pressure on combustion stability and emissions are reported. The potential to extend the LTC load boundary with high boost pressure is also evaluated. Finally, the chapter presents the effects of variable intake and injection pressures on particle number and size distribution, both in conventional diesel and high-EGR LTC operation. Chapter 5 presents the optical assessment of high-EGR LTC and conventional diesel combustion with variable boost pressure to support the hypotheses laid out in Chapter 4 relating to the combustion and emission processes.

Chapter 6 presents the evaluation of the effect of a split fuel injection strategy on LTC emission and combustion at reduced EGR levels, and compares this strategy with a single injection high-EGR LTC strategy. The results are supported by in-cylinder spray and flame visualization and flame temperature measurement.

Chapter 7 presents the details of the modelling of a multi-cylinder engine which is used to predict the operating conditions during a combustion mode transition. Specific points from this transition are then investigated under steady-state conditions. The effects of various fuel injection parameters on reducing emissions and increasing thermal efficiency during the combustion mode transition are also reported here. Finally, a summary of the main conclusions from this thesis and suggestions for future work are provided in Chapter 8.

1.7 Contributions to the Body of Knowledge

The major contributions of this research work to the body of knowledge in the field of diesel LTC are listed below:

1. Higher intake pressure was characterized by higher flame temperature, increased soot luminosity and advanced combustion phasing which resulted in the delayed onset of bulk quenching. This phenomenon reduced THC, CO and smoke emissions. With higher intake pressure, higher EGR levels were required to reduce smoke emissions and the peak smoke emission was shifted towards lower intake oxygen mass fractions. (Chapters 4 and 5)
2. Combustion stability was dependent on intake charge dilution, engine speed, fuel injection timing, fuel injection pressure, and combustion phasing. (Chapter 4)
3. Increased intake pressure reduced PN emission both in LTC and conventional diesel operation. PN emissions were higher with LTC compared to conventional diesel combustion. Count median diameters of the emitted particles were smaller in high-EGR LTC operation compared to low-EGR conventional diesel operation and were independent of injection and intake pressures. (Chapter 4)
4. A split fuel injection strategy achieved smoke emissions at reduced EGR levels similar to the single injection high-EGR LTC strategy with insignificant effect on NO_X emissions. Optical assessment showed that higher intake oxygen mass fraction and higher intake pressure enhanced soot oxidation more than they increased soot formation. (Chapters 5 and 6)
5. Modelling of the combustion mode transitions (from LTC to conventional diesel operation and *vice-versa*) was used to identify the operating conditions at individual cycles during a transient. It was found that smoke emissions during a combustion mode transition are largely controlled by the EGR system response. Therefore, reducing the number of cycles that encounter the intermediate levels of EGR will be required to control the smoke emissions during a combustion mode transition. (Chapter 7)
6. Split fuel injection strategy with optimized fuel injection timing, fuel split ratio and injection pressure with a marginally increased intake pressure was effective in meeting the drive cycle load requirement with acceptable smoke, THC, CO and NO_X emissions in the intermediate cycles during a combustion mode transition. (Chapter 7)
7. Combustion mode transition needs to be coupled with a similar combustion phasing transition strategy (from a near-TDC combustion phasing for high combustion efficiency in high-EGR LTC operation to a retarded combustion phasing for low NO_X emission in conventional diesel operation) to achieve the desired engine performance and emissions. (Chapter 7)

1.8 Publications from this Research

This research work has led to the following publications:

1. A. K. Sarangi, C. P. Garner, G. P. McTaggart-Cowan, M. H. Davy, E. Wahab and M. S. Peckham, 2012, “Managing the Transition between Low Temperature Combustion and Conventional Diesel Combustion during a Load Change”, ASME Internal Combustion Engine Division Fall Technical Conference, Vancouver, Canada. Accepted.
2. A. K. Sarangi, C. P. Garner, G. P. McTaggart-Cowan, M. H. Davy, E. Wahab and M. Peckham, 2012, “The Effects of Split Injections on High EGR Low Temperature Diesel Engine Combustion”, International Journal of Engine Research. Accepted.
3. A. K. Sarangi, C. P. Garner, G. P. McTaggart-Cowan, M. H. Davy, E. Wahab and M. Peckham, 2012, “Effects of Engine Operating Parameters on Diesel Low Temperature Combustion with Split Fuel Injection”, IMechE, Part D, Journal of Automobile Engineering. In Press.
4. A. K. Sarangi, G. P. McTaggart-Cowan and C.P. Garner, 2010, “The Effects of Intake Pressure on High EGR Low Temperature Diesel Engine Combustion”, SAE Paper No. 2010-01-2145.
5. A. K. Sarangi, C. P. Garner, G. P. McTaggart-Cowan, M. H. Davy, E. Wahab and M. Peckham, “Extending the Use of Two-colour Pyrometry into Low-Temperature, Low-Sooting Diesel Engine Combustion Regimes”, under review for publication in The Journal of Combustion Science and Technology.

Chapter 2
BACKGROUND INFORMATION

2.1 Introduction

In the past, numerous investigations have been carried out to advance the understanding of diesel engine combustion and emissions processes. With this improved understanding, diesel emissions have been reduced substantially over the last decade with a minimal loss in engine efficiency. This chapter gives an overview of conventional diesel engine combustion and describes the different pollutant formation mechanisms. Exhaust after-treatment and in-cylinder techniques that have been investigated or implemented over the years for the simultaneous reduction of NO_X and PM from diesel engines to meet the current emission standards are also reviewed. Various diesel low temperature combustion strategies, either in their advanced stages of research or implementation are reviewed, highlighting their merits and hurdles for practical implementation. Transient emissions, which contribute a significant proportion of the total engine-out emissions both in conventional and low temperature combustion diesel engines, are reviewed to identify the sources and factors affecting engine-out emissions. This chapter will also identify the gaps in the literature related to high-EGR diesel combustion both during steady-state and transient operation.

2.2 Conventional Diesel Engine Combustion

Diesel engine combustion is an unsteady, heterogeneous process which depends primarily on fuel properties, combustion chamber design, engine operating conditions and the fuel injection system. In a diesel engine, the ignition and combustion processes are primarily controlled by the timing and rate of fuel injection. Ignition and combustion processes are also influenced by temperature, pressure and turbulence of the compressed charge (air, EGR and residuals) in the cylinder. Fuel injection generally begins a few crank angle degrees before TDC; the exact point is controlled to optimize, for example, the rate of pressure rise, NO_X emissions and brake specific fuel consumption (BSFC). In general, an early start and short injection duration increase both maximum pressure and thermal efficiency, since combustion approaches constant volume, rather than constant pressure conditions. Thus modern diesel engines operate close to the ideal Otto cycle, although combustion is initiated by auto-ignition. Historically, a diesel combustion event was thought to consist of the following four phases: ignition delay, premixed or rapid combustion, diffusion or mixing controlled combustion and late combustion [Heywood, 1988].

Over the past decade, diesel combustion has advanced significantly especially with high pressure common rail fuel injection systems. With the advances in optical diagnostics techniques in the last two decades, the understanding of diesel combustion has also greatly improved. A model for the DI diesel combustion based on laser sheet imaging as conceptualized by Dec [1997] is depicted in Fig. 2.1. This model explains the above four phases of combustion events better than the previous

understanding provided by Heywood [1988]. It should be noted that Dec's work had significant complexities in the experimental methodology and hence, the model is not universally accepted[*]. The various phases are explained in the following paragraphs with a summary of traditional and advanced understandings of conventional diesel combustion.

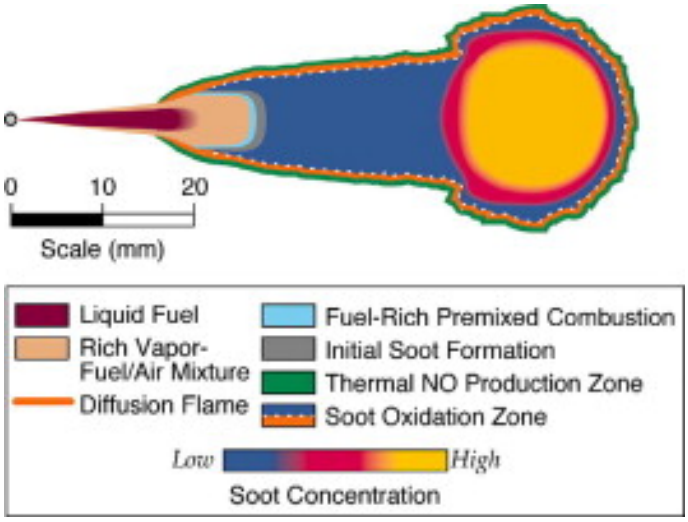

Fig. 2.1: Conceptual schematic of conventional diesel combustion [Dec, 1997]. Reprinted with Permission from SAE Paper No. 970873 © 1997 SAE International.

The fuel is injected as a number of high velocity jets through small orifices by the fuel injection system into the engine cylinder towards the end of the compression stroke. During injection, the fuel atomizes into small droplets (entraining air) while penetrating into the combustion chamber. As it heats up, it vaporizes and mixes with the high temperature and high pressure cylinder gases. The vapour phase continues to penetrate across the chamber and a head vortex is developed with the leading portion of the jet containing a fuel vapour-air mixture with equivalence ratio ranging from 2 to 4 [Dec, 1997]. In small DI engines, depending on the injector location, injection pressure and injection timing, part of the spray may impinge on the combustion chamber walls; this either increases emissions or helps to vaporize the fuel and break up the jet [Obert, 1970; Stone, 1999]. The spray-wall interaction at the impacted surface is quite complex and difficult to systematize [Moreira *et al*., 2010].

[*] The main concerns are the low signal to noise ratio of photon count on NO_X reading. Therefore, it is possible that the NO_X elsewhere could not be measured except at the edge of the flame. Dec's model is also based on two-dimensional imaging data taken primarily at one typical operating condition with idealized fuels. In contrast, combustion is a three dimensional phenomenon, which cannot be explained thoroughly with planar visualization obtained through a section of the fuel jet. In addition, different parameters such as gas temperature and density at TDC, injection pressure and fuel properties affect both temporal and spatial distributions of various combustion generated radicals, atoms and molecules within the reacting fuel jet.

Spontaneous ignition of a portion of already mixed fuel and air occurs rapidly in a few crank angle degrees after a short ignition delay phase. During the first part of the premixed phase following auto-ignition, the fuel breaks down and large quantities of polycyclic aromatic hydrocarbons (PAH) form almost uniformly across the entire cross-section of the leading portion of the jet. PAH is reported to be formed during combustion, since fuel pyrolysis is a strong function of temperature [Stone, 1999]. The formation of the PAH coincides with the rapid rise in the combustion rate indicating that a premixed burn spike consists of the combustion of this fuel rich mixture. Soot particles start forming throughout the cross-section of the downstream region of the jet from fuel-rich premixed combustion [Dec, 1997].

A diffusion flame starts forming at the jet periphery between the products of the fuel-rich premixed burn and unconsumed fuel and surrounding air, without any indication of a corresponding increase in soot concentration at the jet periphery with the formation of the diffusion flame [Dec, 1997]. This is in contrast to the earlier understanding of soot formation in diesel combustion [Heywood, 1988; Dec, 1997]. The last part of the premixed phase is a combination of jet growth and penetration along with a thin diffusion phase reaction zone at the jet periphery, which implies that all of the fuel first undergoes fuel-rich premixed combustion and later diffusion flame combustion, which is nearly stoichiometric. Dec's model suggests that diffusion flame (mixing-controlled) combustion occurs as a flame between the products of the fuel rich premixed combustion and air rather than being a more classical pure fuel-air diffusion flame.

In the late combustion phase, energy release still continues in the expansion stroke, although at a lower rate, primarily from soot oxidation and fuel-rich combustion products burning as they mix with the surrounding air. In addition, mixing of the air with the burning and already burned gases continues throughout the combustion and expansion processes, unless the flame is quenched by thermal boundary layers or rapid mixing with air [Heywood, 1988]. As temperature drops during the expansion stroke, reaction rates slow down relative to mixing rates and the reaction rates are insufficient to burn the remaining soot and stable hydrocarbons [Heywood, 1988].

2.3 Conventional Diesel Engine Emissions

Conventional diesel engines produce pollutants such as soot, NO_X and THC, in addition to traces of CO. Pollutant formation processes are strongly dependent on fuel distribution and mixing with air. The following subsections describe the fundamentals of the chemical reaction mechanisms of these pollutants. A brief description regarding combustion generated noise is also included.

2.3.1 Soot Formation and Oxidation Mechanisms in Diesel Engines

Diesel particulates consist of combustion generated carbonaceous materials (soot) on which some organic compounds get absorbed. Most of the PM (black carbon) results from fuel (due to incomplete fuel-air mixing), while some are from the lubricating oil. Particulate is often separated

into a soluble and an insoluble or dry fraction. The fraction of the total mass of particulate, which is soot, is often estimated by finding the insoluble portion of the particulate. The fraction of soot in particulates from diesel exhaust varies, but is typically higher than 50% [Kittelson, 1998]. Other particulate matter constituents are partially burned or unburned fuel and lubricating oil, wear metals and sulphate derived from lubricating oil or fuel [Kittelson, 1998].

Soot is a solid substance consisting of roughly eight parts of carbon and one part of hydrogen. Newly formed particles have the highest hydrogen content with a carbon to hydrogen ratio as low as one, but the hydrogen fraction decreases as the soot matures [Tree and Svensson, 2007]. The process of transition of liquid or vapour phase hydrocarbons into solid soot particles and possibly back to gas-phase products involves six commonly identified processes: (1) pyrolysis, (2) nucleation, (3) surface growth, (4) coalescence, (5) agglomeration and (6) oxidation. The sequence of the soot formation process is illustrated schematically in Fig. 2.2. A detailed review of soot formation and oxidation mechanisms with particular reference to compression ignition engines has been reported by Tree and Svensson [2007] and is mostly referred here.

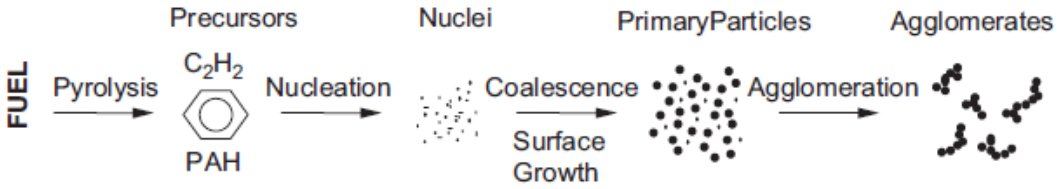

Fig. 2.2: Soot formation process from gas phase hydrocarbon to solid agglomerated particles [Tree and Svensson, 2007]

During pyrolysis, the decomposition and atomic rearrangement of a fuel molecule into smaller hydrocarbon molecules occurs primarily in a region with both a shortage of oxygen and relatively high temperatures. Fuel pyrolysis reactions are generally endothermic forming unsaturated hydrocarbons, polyacetylenes, PAH and acetylenes which are precursors to soot formation and a function of temperature and fuel concentration. Soot precursor formation is a competition between the rate of fuel pyrolysis and the rate of fuel and precursor oxidation. Although both pyrolysis and oxidation rates increase with temperature, the oxidation rate increases faster [Tree and Svensson, 2007]. The local equivalence ratio (ϕ) vs. local flame temperature (T) map shown in Fig. 2.3 demonstrates the soot formation region. From Fig. 2.3 it can be seen that soot is formed at high equivalence ratios and at intermediate temperatures.

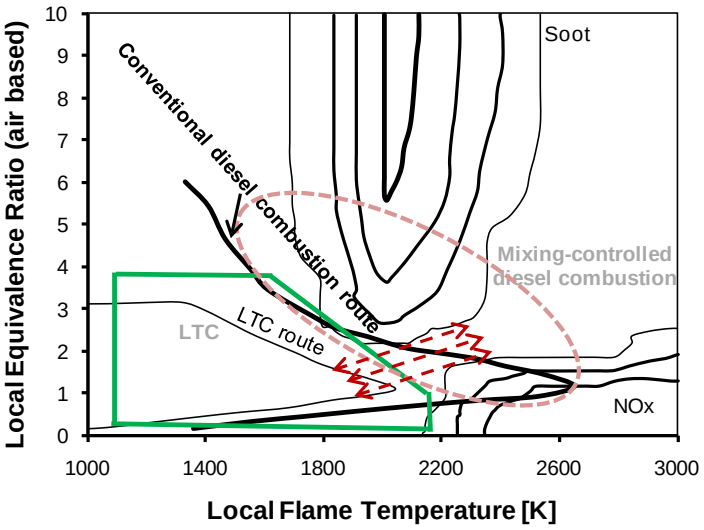

Fig. 2.3: LTC and conventional diesel combustion on the ϕ–T map. 'Mixing-controlled conventional diesel combustion' and the 'expected LTC operation' regions are highlighted in the figure. NO_X and soot islands in the ϕ–T map: Adapted from SAE Paper No. 2006-01-3386.

In the nucleation mode, particles are formed (particle inception temperatures vary from 1300-1600 K) from gas phase reactants. The smallest identifiable solid particles in luminous flames have diameters in the range of 1.5-2 nm, and are generally referred to as nuclei [Tree and Svensson, 2007]. The nuclei mode typically consists of particles smaller than 100 nm diameter containing 1-20% of the particle mass, but more than 90% of the total number of particles [Kittelson, 1998; Myung and Park, 2012]. Most of the particulate mass is found in the accumulation mode, with particle diameters between 0.1 and 1 μm. The coarse mode, with particle sizes larger than 1 μm, represents 5-20% of the particle mass, but the particle number in this mode is low [Myung and Park, 2012]. Although the nuclei mode particles do not contribute significantly to the total soot mass, they provide sites for surface growth. During surface growth, condensation of hydrocarbon species on the hot reactive surfaces of the soot particles lead to an increase in soot mass, while the number of particles remain constant. The majority of the soot mass is added during surface growth and thus, the residence time of the surface growth process has a large influence on the total soot mass.

Coalescence and agglomeration are both processes by which particles combine. During the coalescence process, particles collide and coalesce, thereby decreasing the number of particles, while holding the mass of the two soot particles constant. During coalescence, two roughly spherically shaped particles combine to form a single spherically shaped particle. Agglomeration occurs when individual or primary particles stick together to form large groups of primary particles. The primary particles maintain their shape. Primary soot particle size varies depending on operating condition, injector type and injector conditions, but mostly, primary particle size ranges from 20-70 nm. After combustion ends, during the expansion and exhaust strokes, particles agglomerate further and are

seen to be chain-like and typically range in aerodynamic diameters from 100 nm to 2 μm [Tree and Svensson, 2007].

Oxidation processes convert hydrocarbons to CO, CO_2 and H_2O at any point in the process, but mostly when the temperature is higher than 1300 K. Smith [1981] suggested that soot's graphite like structure is responsible for its high resistance to oxidation. Hydroxyl (OH) radicals are reported to dominate soot oxidation under fuel-rich and stoichiometric conditions, whereas both OH and oxygen molecule (O_2) contribute to soot oxidation under lean conditions [Tree and Svensson, 2007].

For conventional mixing-controlled diesel combustion, initial soot formation takes place just downstream of the fuel-rich premixed flame in the products of fuel-rich combustion as illustrated in Fig. 2.1. Soot formation and particle growth continue as the soot moves down the jet to the head vortex and outward towards the diffusion flame. Since the diffusion flame is the only source of high OH radicals and oxygen concentrations, it has been proposed that soot oxidation occurs at the diffusion flame alone [Dec, 1997]. PM changes significantly in the post combustion expansion and exhaust processes. The stable hydrocarbons remaining unoxidized after the end of combustion have a tendency to be absorbed onto the soot particles and become a part of particulate soluble fraction. Condensation of the hydrocarbon species in the exhaust gases also forms new particles. Condensation and absorption occurs in the exhaust system and in the dilution tunnel which simulates what happens in the atmosphere. It is suggested that, if the combustion process ends early, the exhaust concentration of soot can be made relatively low, allowing the high cylinder temperature to oxidize the soot (assuming there is enough oxygen), even though large amounts of soot are formed in a conventional diesel combustion [Tree and Svensson, 2007]. However, it should be easier to eliminate or minimize soot formation rather than trying to optimize soot oxidation to reduce PM emissions.

Effects of engine design and operating parameters on soot formation and oxidation

Temperature has the highest effect on the soot formation and oxidation processes. It is reported that soot inception begins at around 1400 K, while rapid oxidation ceases below 1300 K [Glassman, 1989]. As temperature is increased, the rate of oxidation increases more rapidly than the rate of formation as long as sufficient oxygen is available. In premixed flames, soot formation goes up as temperature is increased. Generally, increased oxygen concentration through premixing tends to reduce soot formation; however, this is not always the case since oxygen is closely associated with temperature, which has an exponential effect on soot formation and oxidation [Tree and Svensson, 2007]. It does not require a stoichiometric amount of oxygen to completely eliminate soot. As long as the carbon becomes partially oxidized to CO, it does not contribute significantly to soot formation reactions [Tree and Svensson, 2007].

The various design and operating parameters affecting soot formation and oxidation in diesel engine combustion include: combustion chamber shape, fuel injection pressure, fuel injection

timing, number of injections, engine transients and intake temperature and pressure. The most critical aspects of combustion chamber shape and geometry relative to particulates depends on swirl and liquid fuel impingement. Air entrainment into the jet is dominated by the jet velocity and the cone angle of the spray and is not greatly affected by swirl [Tree and Svensson, 2007]. However, swirl increases turbulence and mixing, and thus increasing the rate of combustion late in the injection process and after the end of injection. This allows the soot to oxidize more rapidly while the gas temperature remains high early in the expansion stroke [Benajes *et al*., 2004; Tree and Svensson, 2007].

Advanced fuel injection timing results in low particulate emissions and high NO_X, whereas retarded fuel injection timing produces more particulate and less NO_X, which leads to the well-known NO_X-PM trade-off for diesel engines. Advanced fuel injection timing also increases the soot formation if a greater fraction of the fuel is burned at higher temperature; however, due to an early end of injection, the in-cylinder temperature is higher facilitating soot oxidation. The case of increasing intake temperature is similar to the advanced fuel injection timing strategy. It is reported that an increase in ambient temperature decreases the flame lift-off length. The flame lift-off length is defined as the most upstream location of combustion of the spray during fuel injection and is estimated as the axial distance between the injector orifice/nozzle and the location where the intensity of OH chemiluminescence is approximately 50% of that just downstream of the initial rapid rise in OH chemiluminescence [Siebers and Higgins, 2001]. Decreased flame lift-off length causes the peak soot level in a fuel jet to increase and move upstream. However, due to an even greater increase in the rate of oxidation of soot with increasing temperature, soot burns out more rapidly [Pickett and Siebers, 2004].

2.3.2 NO_X Formation and Reduction Mechanisms in Diesel Engines

While nitric oxide (NO) and nitrogen dioxide (NO_2) are usually grouped together as NO_X; NO is the predominant oxide of nitrogen produced inside the engine cylinder by the combustion of near-stoichiometric fuel-air mixtures. The thermal, prompt and N_2O routes are mainly responsible for the formation of NO_X in diesel engines.

(a) Thermal NO

Oxidation of atmospheric nitrogen by the thermal mechanism is a major source of NO_X emissions. The principal reactions governing the formation of NO from atmospheric nitrogen are given by the extended Zeldovich mechanism [Lavoie *et al*., 1970] and are represented through the following reactions:

$$O + N_2 \xrightarrow{k_1} NO + N \text{ , temperature range 2000-5000 K} \qquad (2.1)$$

$$N + O_2 \xrightarrow{k_2} NO + O \text{ , temperature range 300-3000 K} \quad (2.2)$$

and $$N + OH \xrightarrow{k_3} NO + H \text{ , temperature range 300-2500 K} \quad (2.3)$$

where k_1, k_2 and k_3 are the rate constants. The rate constant (k) is expressed with the modified Arrhenius law [Glarborg *et al*., 1986] as

$$k = AT^{\beta}\, \mathrm{e}^{(-E_0/R_0T)} \quad (2.4)$$

where E_0 is the activation energy (activation energy corresponds to an energy barrier which has to be overcome during the reaction), A is the pre-exponential factor, R_0 is the universal gas constant, T is the reaction temperature, and β is a dimensionless number. The unit of the rate constant, k is $cm^3.mole^{-1}.s^{-1}$. The forward rate constants (k_{1f})for the extended Zeldovich mechanism are given by [Warnatz *et al*., 2000]:

$$k_{1f} = 1.8 \times 10^{14}.e^{(\frac{-318000}{R_0T})} \quad (2.5)$$

$$k_{2f} = 9 \times 10^{9}.e^{(\frac{-27000}{R_0T})} \quad (2.6)$$

$$k_{3f} = 2.8 \times 10^{13} \quad (2.7)$$

The reverse rate constants (k_{1r}) for Equations (2.1-2.4) are given by [Bowman, 1975]:

$$k_{1r} = 1.6 \times 10^{13} \quad (2.8)$$

$$k_{2r} = 1.5 \times 10^{9}.T.e^{(\frac{-162123}{R_0T})} \quad (2.9)$$

$$k_{3r} = 2.0 \times 10^{14}.e^{(\frac{-196626}{R_0T})} \quad (2.10)$$

Note that out of the above three expressions, Reactions 2.1-2.3, Reaction (2.1) is very slow and is the rate limiting step of the thermal NO formation as it (k_{1f}) has a very high activation energy due to the strong triple bond in the N_2 molecule, which needs high temperatures (only way to form atomic nitrogen), thus sufficiently fast only at high temperatures [Warnatz *et al*., 2000].

The NO formation rate shows a strong correlation to temperature and oxygen concentrations [Warnatz *et al*., 2000]:

$$\frac{d[NO]}{dt} = 2.k_{1f}[O][N_2] \quad (2.11)$$

where [ ] denotes concentration of the molecule or atom. Thus, it can be seen that NO formation can be minimized by decreasing [N_2], [O], or k_{1f} (i.e. by decreasing the temperature). Therefore, temperature and oxygen concentration are the primary factors influencing the thermal NO formation. Note that oxygen atoms form by the chain reactions (e.g. $H + O_2 = OH + O$; $O + H_2 = OH + H$;

and $OH + H_2 = H_2O + H$), or possibly from the dissociation of O_2, and these oxygen atoms attack nitrogen molecules to start the initial reaction represented by Equation (2.1) [Glassman, 1996; Warnatz *et al*., 2000].

(b) Prompt NO formation

NO formation rates in combustion of hydrocarbon fuels can exceed those by the thermal mechanism discussed above, especially for fuel-rich conditions. This rapidly formed NO in the fuel-rich condition is termed 'prompt NO' or 'Fenimore NO' [Warnatz *et al*., 2000] and is confined to the regions near the flame zone. It is formed by a reaction sequence that is initiated by the rapid reaction of hydrocarbon radicals (basically CH) with molecular nitrogen leading to the formation of hydrocyanic acid (HCN) that subsequently reacts to form NO [Glassman, 1996]:

$$CH + N_2 \rightarrow HCN + N \quad (2.12)$$

$$HCN + O \rightarrow NCO + H \quad (2.13)$$

$$NCO + H \rightarrow NH + CO \quad (2.14)$$

$$NH + (H, OH) \rightarrow N + (H_2, H_2O) \quad (2.15)$$

$$N + OH \rightarrow NO + H \quad (2.16)$$

$$N + O_2 \rightarrow NO + O \quad (2.17)$$

Because C_2H_2 as a CH radical precursor is accumulated under fuel-rich conditions, prompt NO is favoured in rich flames. The activation energy of the reaction:

$$CH + N_2 \rightarrow HCN + N \quad (2.18)$$

is only about 75 kJ.mole^{-1}, compared to 318 kJ.mole^{-1} for the formation of thermal NO; therefore, in contrast to thermal NO, prompt NO is produced at relatively low temperatures (about 1000 K) [Warnatz *et al*., 2000] and may be particularly relevant for low temperature combustion.

(c) NO generated from nitrous oxide (N_2O)

NO generated from N_2O is analogous to the thermal mechanism, in which an oxygen atom attacks a nitrogen molecule in the presence of a third molecule (M), thus forming an N_2O molecule as given below:

$$N_2 + O + M \rightarrow N_2O + M \quad (2.19)$$

The N_2O molecule may subsequently react with an oxygen atom to form an NO molecule [Warnatz *et al*., 2000]:

$$N_2O + O \rightarrow NO + NO; \qquad E_0 = 97 \text{ kJ.mole}^{-1} \quad (2.20)$$

Reaction (2.19) is a three-body reaction (promoted at high pressures), which is more sensitive to pressures than the other two NO formation mechanisms. Note that a three-body reaction involves reactions of two species (e.g. A and B) to yield one single product species (AB). This reaction requires a third body M to stabilize the excited product AB^* by collision. The third body M is an inert molecule (generally N_2) that can remove the excess energy from AB^* and eventually dissipate it as heat. Reaction (2.19), typical for three body reactions, has a low activation energy so that low temperatures do not penalize this reaction as much as they do the Zeldovich-NO reaction [Warnatz *et al*., 2000]. This reaction has often been overlooked since it is an insignificant contributor of the total NO. For lean conditions (local ϕ <0.8) where the formation of CH is suppressed, prompt NO will be reduced. Furthermore, low temperatures will suppress the thermal NO mechanism. However, the N_2O route may become the major source of NO formation in the lean premixed low temperature combustion regimes due to its lower activation energy [Miller and Bowman, 1989].

(d) Decomposition of NO

All of the NO molecules produced during the combustion process are not necessarily emitted, since some of them get decomposed later. One proposed mechanism for the decomposition of NO is the HCN recycle route, where HCCO radicals react with NO molecules to form HCN and CO_2 [Nishioka *et al*., 1996]. The HCN recycle route does not come into play in the premixed flame due to the low concentration of HCCO, whereas it may be a significant NO decomposition mechanism in diffusion flames. Some of the burned gases containing NO may pass through this reaction zone again, and may get decomposed and removed. Other routes proposed for the decomposition of NO are the reverse of thermal, prompt and nitrous oxide mechanisms [Miller and Bowman, 1989; Easley and Mellor, 1999] and in a diesel engine, the importance of NO decomposition is found to increase with engine load [Easley and Mellor, 1999]. How much of the species formed during the decomposition mechanism recombine again to form NO is not clear.

(e) Formation of NO_2

NO formed in the flame zone can be converted rapidly to NO_2 via the reactions:

$$NO + HO_2 \rightarrow NO_2 + OH \qquad (2.21)$$

Subsequently, this NO_2 is converted back to NO, unless the NO_2 formed in the flame is quenched by mixing with cooler fluid [Heywood, 1988] via:

$$NO_2 + O \rightarrow NO + O_2 \qquad (2.22)$$

Typically, the ratio of NO_2 to NO_X for diesel engine varies approximately from 5% to 30% [Heywood, 1988]. However, for modern diesel engines, this ratio might in some circumstances be outside this range.

(f) NO_X formation in diesel engines

During conventional diesel combustion, the initial premixed combustion just after auto-ignition and the hypothesized standing premixed flame are not conducive to NO production either by the thermal or prompt mechanisms as little oxygen is present and the adiabatic flame temperature (1600 K) is far below those required for thermal NO production. Also, little prompt NO is produced at equivalence ratio above 1.8 [Dec, 1997]. However, HCN production might still occur in this rich combustion, and if it does, it is likely that the HCN would later be released as NO in the diffusion flame [Dec, 1997]. On the lean side of the diffusion flame (at the jet periphery), higher flame temperatures (since combustion is nearly stoichiometric) and presence of oxygen are nearly ideal for thermal NO production (refer to Fig. 2.1). However, it is important to realize that the NO production zone shown in Fig. 2.1 may not be the location where most of the NO is produced during typical diesel combustion. Thermal NO production is a relatively slow process and this could delay the onset of significant NO production until after the time period of initial premixed energy release spike. Since thermal NO production is a relatively slow process, the bulk of the NO production might occur during the latter part of the mixing controlled combustion or in the hot gas regions remaining even after the end of combustion. Although peak temperatures may be lower in these regions than they are the mixing-controlled flame, there is considerably more time for the NO-production reactions [Dec, 1997]. At low temperatures (T <2000 K), NO formation is dominated by the prompt NO mechanism and as the temperature increases, the relative importance of the prompt NO formation decreases; for temperatures above 2500 K, NO formation is controlled mainly by the thermal mechanism [Miller and Bowman, 1989].

As fuel injection timing is retarded, NO formation occurs later at a reduced rate, since peak temperatures are lower. At high load, with higher peak pressures and temperatures, and larger regions of close to stoichiometric burned gases, NO levels increase. Thermal NO levels decrease less proportionally with respect to the decreased global equivalence ratio (ϕ <0.85), since much of the fuel still burns close to stoichiometric due to the non-uniform fuel distribution in diesel engines [Heywood, 1988].

2.3.3 Hydrocarbon Formation Mechanisms in Diesel Engines

Hydrocarbon is caused by either over-lean or over-rich fuel-air mixtures unable to auto-ignite or support a flame at the conditions inside the combustion chamber. Thus, hydrocarbons remain unconsumed due to incomplete mixing or quenching of the oxidation process. Engine idling and light load operation produces relatively more THC than at full load due to over-mixing. Over-mixing of the injected fuel during the ignition delay period can be a significant source of hydrocarbon emissions, if the ignition delay period exceeds its optimum value due to changes in engine operating conditions. Under transient conditions, as the engine goes through an acceleration process, over-fuelling causes locally over-rich conditions, although the overall equivalence ratio does remain lean.

Cycle-by-cycle variation in the combustion process becomes significant under adverse conditions such as low compression temperatures and pressures, and retarded injection timings resulting in misfiring and THC emissions. Fuel retained in the injector sac and spray holes may enter the combustion chamber late in the cycle when the pressure drops and becomes a source of THC emissions [Stone, 1999]. High strain of flame fronts (due to intense turbulence) leads to local flame extinction and this phenomenon is increasingly important for rich or lean mixtures, where temperatures are lower and thus reaction times may become longer than the mixing times [Warnatz *et al*., 2000]. Flame extinction at combustion chamber walls or cold piston due to heat transfer (cooling of the reaction zone) as well as the removal of the reactive intermediate radicals by surface reaction may also contribute to THC emissions [Warnatz *et al*., 2000].

2.3.4 Carbon Monoxide Formation Mechanisms in Diesel Engines

Carbon monoxide formation is one of the principal reaction paths in the hydrocarbon combustion mechanism and CO is one of the main intermediate species. In both overall stoichiometric and rich combustion conditions, CO results due to a lack of oxygen in the combustion chamber. However, in an overall lean system, sufficient oxygen is always present for the oxidation of CO to CO_2. Improper fuel-air mixing might lead to higher CO emissions in an overall lean system, if enough oxygen is not present in the reaction zone to oxidize the CO to CO_2.

The CO formed in the combustion process is oxidized to CO_2 at a slower rate via the reaction [Bowman, 1975]:

$$CO + OH \rightarrow CO_2 + H \tag{2.23}$$

The rate constant, $k_{CO,}$ for this reaction is a function of temperature [Warnatz *et al*., 2000]:

$$k_{CO} = 6 \times 10^6 . T^{1.5} e^{\left(\frac{3100}{R_0 T}\right)} \tag{2.24}$$

Hence, the oxidation of CO to CO_2 might cease, if the temperature of the reaction zone falls too far.

Oxidation of CO via the reaction:

$$CO + O_2 \rightarrow CO_2 + O \tag{2.25}$$

is very slow ($k = 2.5 \times 10^{12} e^{\left(-\frac{200000}{R_0 T}\right)}$) and should not be an important reaction in hydrocarbon flames, which generally have relatively large OH concentrations in the combustion gas [Bowman, 1975]. Note that Reaction (2.24) has a lower activation energy (-3.1 kJ.mole^{-1}) compared to 200 kJ.mole^{-1} for Reaction (2.25). For flame temperatures of 1500 K, the exponential term in the Arrhenius equation is essentially 1 and, thus, the rate coefficient is effectively temperature

independent. However, the strong temperature dependence of CO oxidation is probably due to the strong temperature dependence of OH concentration [Warnatz *et al*., 2000].

Since diesel engines operate globally on the lean side of stoichiometric with high flame temperatures, CO emissions are low and are generally considered unimportant. However, higher CO emission is a matter of concern in LTC regimes where equivalence ratio is higher and temperatures are lower. It is expected that the poor oxidation rate of CO in LTC and lean fuel-air ratio (resulting in a low flame temperature) may be due to a decreasing OH concentration and not a decreasing rate coefficient [Warnatz *et al*., 2000].

2.3.5 Combustion Noise in Diesel Engines

Combustion noise in diesel engines is generally caused by the initial rapid combustion of a premixed fuel-air mixture in the cylinder that causes a large pressure gradient. This large pressure gradient is a very strong excitation source that forces the in-cylinder charge to oscillate. Generally, the ignition delay influences the premixed combustion stage by affecting the availability of the flammable fuel-air mixture [Heywood, 1988]; longer ignition delays often result in a higher premixed combustion rate and higher combustion noise. Note that the maximum cylinder pressure rise rate is a constraint parameter for the smooth operation of the engine while avoiding engine damage.

2.4 Current Emissions Control Strategies

Various emission control strategies, including both in-cylinder and exhaust after-treatment methods are continuously being developed to meet the stringent emission regulations outlined in Sec. 1.3. This section reviews a selection of the most prevalent emission reduction techniques currently in use.

2.4.1 In-Cylinder Techniques

(a) Exhaust gas recirculation (EGR)

EGR is one of the most reliable systems to effectively reduce NO_X emissions and has been used in gasoline and diesel engines. In an EGR system, recirculation is usually achieved either by external EGR or by trapping the burned gases within the cylinder by not fully expelling them during the exhaust stroke (residuals). Recirculated exhaust gases consisting of primarily N_2, CO_2, water (H_2O) vapour and O_2 with some other pollutants when added to the intake air replaces the intake oxygen and reduces NO formation rate, the primary effect being the reduction of the burned gas temperature [Ladommatos *et al.,* 2000]. However, participation of CO_2 and H_2O vapour in the combustion process and an increase in the charge specific heat capacity may also contribute to NO_X reduction, but these are considered almost insignificant in the context of diesel engines [Ladommatos *et al.,* 2000]. Ladommatos *et al.* [2000] reported a reduction of flame temperature

from 2300 K to 2075 K, when oxygen concentration was reduced from 23% to 17.5% by mass. Typically, EGR is capable of reducing engine-out NO_X by 20-50% [Chatterjee *et al.*, 2008].

Reduction in oxygen flow rate to the engine and reduction in inlet charge due to thermal throttling also result in a very large reduction in exhaust NO_X at the expense of higher PM emissions [Ladommatos *et al.,* 2000]. Higher inlet charge temperature contributes to higher emissions of both NO_X and PM. The increase in NO_X has been attributed partly to the effects of the higher charge temperature on the reduced ignition delay (shortened ignition delay causes the bulk of the combustion process to move closer to TDC, resulting in an increased gas temperature and so a higher NO_X formation rate, but it has negligible effect on PM) and partly to the rise in post ignition combustion temperature.

An EGR rate of up to 25% may be used for NO_X reduction, without increasing PM emissions significantly, depending on load [Zheng *et al*., 2004]. At full load conditions, the equivalence ratio (based on air-fuel ratio) is significantly higher and the addition of EGR lowers the oxygen concentration even further leading to excessive soot and CO emissions [Heywood, 1988]. Note that oxygen concentration in the exhaust varies depending on fuel-oxygen equivalence ratio in the combustion chamber, with a little oxygen at high load. Note that the current heavy-duty diesel engines are going to lower EGR rates; instead SCR is being used for NO_X reduction (some Euro VI heavy-duty engines are non-EGR).

(b) Multiple injections

Recent advances in high pressure common rail fuel injection systems and multiple injection strategies (consisting of pilot, main and post injections with independently controlled fuel quantity and injection timing through electronic control) within a single cycle enable the reduction of PM. Generally, high pressure injection results in smaller spray droplets and shorter injection periods. The well atomized spray shortens the ignition delay, and reduces fuel consumption, smoke, THC and PM emissions [Park *et al*., 2004].

With the pilot injection, the temperature prior to the main injection increases, thereby reducing the ignition delay for the main injection event by reducing the fraction of fuel burned in the premixed phase of the main combustion event [Mancaruso *et al.,* 2008]. This, in turn, results in combustion noise reduction due to the reduced rate of pressure rise and peak pressure during the premixed burn. Pilot injection, however, results in an increase in particulates (most of the time) which can be attributed to the higher temperatures in the cylinder at the time of the main injection [Park *et al*., 2004], resulting in a decreased lift-off length and less air entrainment into the jet [Tree and Svensson, 2007]. Pilot injection can also suppress NO_X emissions and combustion noise with retarded main injection timings. Reitz [1998] reported that significant NO_X and particulate emissions reductions can be achieved together with improved fuel economy by using split injections combined with EGR. Note that the EGR levels in the work reported by Reitz was limited to low levels (<20%).

The benefits of multiple injections related to particulates come from a post injection (small amount of fuel of the order of 10% of the total fuel quantity per cycle being injected 10-40 ^{o}CA after the main injection event) providing higher temperatures late in the cycle when soot oxidation normally starts to quench, and therefore promotes soot oxidation through increased temperature, improved mixing and OH radical attack [Dec and Kelly-Zion, 2000]. During post injection, new soot is produced, with the post injection amount of soot lower than the main injection one [Mancaruso *et al.*, 2008] as observed in a high speed direct injection (DI) optical diesel engine. However, post injection timing needs to be optimized to reduce THC emissions and BSFC; retarded post injection seems to be more effective in reducing smoke, although the reason for this is not quite clear [Chen, 2000].

2.4.2 Exhaust After-Treatment Techniques

Although there are various techniques to reduce in-cylinder pollutant formation (at which the above are just a brief summary), these may fall short of meeting the upcoming stringent emission standards. Therefore, a number of exhaust after-treatment techniques are available to reduce the tail-pipe emissions. These include: selective catalytic reduction (SCR), lean NO_X trap (LNT), lean NO_X catalyst (LNC) for NO_X reduction; diesel particulate filter (DPF) for PM reduction; and diesel oxidation catalyst (DOC) for PM, THC and CO reduction. These after-treatment systems, however, have problems in operation under light load conditions because low exhaust temperature tends to slow the reaction rates of these catalysts [Johnson, 2011].

(a) NO_X after-treatment

SCR technology using ammonia (NH_3) derived from the rapid hydrolysis of on-board urea as the reductant has been demonstrated to be very effective at reducing NO_X for HDD engines. NH_3 reacts with both NO and NO_2 species in the presence of a catalyst such as zeolite or vanadia and effectively reduces them to nitrogen and water. However, the leakage and possible secondary emissions of ammonia may be a matter of concern in the SCR system as the Euro VI emission legislation limits NH_3 concentration to 10 ppm in diesel engine exhaust [European Commission, 2008]. Operation of the SCR catalyst is most effective above 300^{o}C exhaust temperatures and is greatly diminished at lower temperatures; however, this can be improved with a high proportion of NO_X being converted to NO_2 [Charlton, 2005]. Hydrogen promoted hydrocarbon-SCR systems with silver catalysts are also being investigated for NO_X reduction [Theinnoi *et al.*, 2008]. Although it looks promising, this system requires optimized hydrogen addition for different engine exhaust conditions to achieve high NO_X conversion efficiency (60-92%) [Theinnoi *et al.*, 2008; Johnson, 2009]. Note that urea based SCR is the de-facto standard for heavy-duty Euro VI and EPA 2010 diesel engines.

In a LNT system, when the engine operates with excess oxygen, NO_X is converted from NO to NO_2 in the presence of a catalyst. The NO_2 then reacts with the base metal oxide component of the catalyst surface to form stable nitrate compounds which are subsequently stored in the trap [Brogan *et al.*, 1998; Charlton, 2005]. In this process, when all the available base metal storage sites are occupied by nitrate, NO_X starts slipping through the catalyst leading to increased NO_X emissions. Then the exhaust is enrichened by controlling the air flow rate, EGR rate or fuel injection parameters, which causes the nitrates to become unstable and gets released into the exhaust as NO_2. Under these rich conditions, a three-way reaction is established, which allows NO_X to be reduced, provided an adequate supply of THC and CO is available. Note that the regeneration of LNT requires a rich mixture and hence has a fuel consumption penalty. When the engine runs either under excess fuel conditions or at elevated temperatures, the nitrate species decompose and the NO is reduced over the trap [Brogan *et al.*, 1998]. It is expected that LNT would be ideal to combine with LTC, if the exhaust temperature is high enough.

(b) THC, CO and PM after-treatment

A DOC is effective in reducing the amount of volatile component, non-methane hydrocarbons and CO emitted from diesel engines. A DOC consisting of a monolith honeycomb substrate coated with combinations of platinum, palladium and rhodium catalysts does not significantly reduce the total particle count as it reduces the PM mass by primarily oxidizing the soluble organic fraction (SOF) and hydrocarbons that are present in the PM, but not the soot. The DOC also eliminates volatiles that could nucleate in the exhaust stream and increase the particle numbers. As a side effect, a DOC also oxidizes sulphur dioxide (SO_2) to sulphur trioxide (SO_3) which is emitted from the exhaust as sulphuric acid apart from reducing the conversion efficiency of the exhaust after-treatment systems [Charlton, 2005]. Note that this is one of the reasons why sulphur is removed from diesel fuel. DOCs also burn the fuel to actively regenerate the filters and also form NO_2 for DPF regeneration [Johnson, 2009]; however, low temperature light-off (T50, the temperature of 50% conversion) is important in all the cases. It is reported that NO_2 is not generated until the CO and THC are removed first [Johnson, 2009]. The NO_2 generated by the DOC also enhances the SCR deNO_X reactions, particularly at low temperatures [Johnson, 2012]. Various low temperature premixed combustion strategies have high THC and CO emissions with reduced exhaust temperature and oxygen concentration. Therefore, these strategies present significant challenge to DOCs; however, new catalyst formulation for DOC systems are under development to cope with these challenges [Johnson, 2010].

A catalysed DPF is effective in reducing total PM, both in mass and particle count. These filters have a cellular structure where the exhaust gases flow through the pores of the cell walls where the soot particles are trapped. As the trap loads up, pressure drop across the filter increases. This increasing back pressure increases the pumping work for the engine and increases fuel

consumption. Therefore, periodically, the filter is regenerated to oxidize the soot and clean the filter. In active regeneration techniques, exhaust manifold fuel injection, post fuel injection and retarded fuel injection timings are used to increase the exhaust temperatures to oxidize the soot [Khair, 2003]. DPF temperatures of 500-600°C are generally required to oxidize the soot. Catalyst enabled regeneration typically uses a wash coat on the substrate to reduce the temperature at which rapid oxidation of the PM occurs. This allows regeneration at lower exhaust gas temperatures and uses less energy. However, these systems require expensive catalyst materials such as platinum [Khair, 2003].

In passive regeneration techniques, soot is oxidized by NO_2 that is generated by the DOC upstream of the DPF [Johnson, 2011]. It is reported that active regeneration costs about 2-3% fuel consumption, and passive regeneration techniques can reduce this penalty by about 20% [Johnson, 2011]. New techniques such as electric-discharge generated plasmas are under development to regenerate the DPF using low power without a catalyst, at all expected engine exhaust conditions without interacting with the diesel combustion processes [Williams *et al*., 2009].

In view of the above descriptions, a 4-way emission control system consisting of EGR, DOC, DPF and LNT/SCR working in tandem to reduce THC, CO, PM and NO_X simultaneously was proposed [Neely *et al.*, 2005]. The oxidation catalyst located upstream of the DPF oxidizes THC, CO and SOF as well as promotes NO_2 generation from NO. A catalysed DPF located after the oxidation catalyst traps PM to clean the EGR for a low pressure EGR system. The LNT/SCR in the downstream of DPF reduces NO_X, although the high regeneration temperatures (650^{o}C) required for DPF may seriously affect the durability of the LNT/SCR catalyst. It was estimated that CO_2 emissions increased by 1.7% over the baseline with a rich pulse control for the 4-way catalyst system [Neely *et al.*, 2005]. Note that current systems for HDD engines (i.e. EPA 2010 and Euro VI) use DOC-DPF-SCR with low EGR levels. SCR enables lower tailpipe NO_X emissions than could be achieved with in-cylinder control, while also achieving higher thermal efficiency because the engine calibration is no longer focussed on minimizing NO_X (fuel injection timing can be advanced for reduced BSFC and PM, while still meeting tailpipe NO_X legislation). Furthermore, lower EGR level, than currently being used, generates less engine-out PM. Therefore, the DPF is not loaded rapidly, leading to fewer fuel consuming active regeneration events.

2.5 Diesel Low Temperature Combustion

At present, due to the trade-off between NO_X and smoke emissions, EGR is limited to relatively low levels (0-25% depending on load) in spite of its potential for further reduction of NO_X emissions. As was discussed in Sec. 1.3, the use of very high EGR rates (>50%) have been investigated as a technique to achieve low temperature combustion with low NO_X and low PM simultaneously. A number of LTC strategies have been developed such as HCCI, PCCI, MK, UNIBUS and smoke-less fuel-rich combustion (high-EGR LTC). In all these systems, NO_X emission

is reduced by reducing the flame temperature with the use of high levels of EGR. Soot formation is suppressed by enhanced fuel-air mixing due to the increase in the ignition delay of the fuel. Ignition delay is increased either by using high levels of EGR or by different fuel injection strategies. Soot formation can also be suppressed by reducing the combustion temperature even with a rich fuel-air ratio [Sasaki *et al*., 2000; Akihama *et al*., 2001]. Note that the maximum rate of pressure rise and combustion noise decrease significantly with high rates of EGR in spite of the increased ignition delay due to the slow rate of combustion.

2.5.1 Basics of LTC

Reference is made to Fig. 2.3, which shows the distribution of the soot and NO formation regions as a function of local equivalence ratio (ϕ) and temperature (T) for different LTC strategies (such as PCCI, HCCI and high-EGR LTC) along with conventional diesel combustion. The contours in the figure represent the amount of soot and NO_X formation as a function of local equivalence ratio and local flame temperature. The ϕ–T map was plotted based on zero-dimensional calculations with detailed chemical kinetic analysis at a fixed reaction time with fixed fuel and oxidizer composition at a constant pressure [Kamimoto and Bae, 1988; Akihama *et al*., 2001]. Both conventional diesel operation and the expected LTC operation regions are highlighted in the figure. Note that these highlighted regions are for illustration only and they do not necessarily represent the actual local flame temperatures and equivalence ratios during combustion. Both LTC and conventional diesel combustion will tend to move through different areas in the ϕ–T map, depending on the phases of combustion as described earlier in Sec. 2.2 and elsewhere [Kook *et al*., 2005; Dec, 2009; Bittle *et al*., 2011]. Examples are shown in the figure both for conventional diesel combustion and the hypothesized LTC routes from the start of combustion up to the late cycle combustion.

It can be seen from Fig. 2.3 that NO formation is favoured at high temperatures (T >2200 K) and low equivalence ratios ($\phi \leq 2.5$). Soot is formed at medium to high temperatures (1700 K <T <2500 K) in very rich equivalence ratios (ϕ >2.5). During conventional diesel combustion, local equivalence ratios and temperatures pass through the soot and NO formation regions as shown in the ϕ–T map. Note that the combustion route shown for conventional diesel operation is for illustration only and would change significantly for different operating conditions. By lowering the combustion temperature with high levels of EGR, NO formation can be suppressed. If the temperature is further reduced to approximately 1700 K or below, combustion no longer occurs in the soot and NO formation regions independent of equivalence ratios, and the combustion process can be considered to be LTC [Ogawa *et al*., 2007]. Similarly, LTC can be achieved when the local flame temperature remains below 2200 K and improved air-fuel mixing keeps the local equivalence ratio below two. By using flexible fuel injection, air-exchange and EGR systems, the

local combustion temperature and equivalence ratio are shifted into different zones in the ϕ–T map so that soot and NO_X can be reduced simultaneously.

2.5.2 Homogeneous Charge Compression Ignition (HCCI)

Onishi *et al.* [1979] first described a new combustion process for internal combustion engines and termed it as ATAC (Active Thermo-Atmosphere Combustion), wherein combustion is initiated by the controlled auto-ignition of a premixed charge without knocking and they reported that stable combustion could be achieved with lean mixtures at part-throttle operation. With the ATAC system, fuel consumption and exhaust emissions of the engines were remarkably improved because of stabilized lean combustion that resulted in noise and vibration reduction. Since then, many researchers have investigated similar combustion concepts for gasoline and diesel engines under the general name Homogeneous Charge Compression Ignition (HCCI) combustion [e.g. Thring, 1989; Christensen *et al*., 1997; Stangmaier and Roberts, 1999; Lida and Igarashi, 2000]. HCCI is one of the most heavily researched advanced combustion strategies. It is outside of the scope of the current work; however, Yao *et al.* [2009] summarize the progress and trends in the HCCI engines in a review paper.

HCCI combustion is achieved when a mixture of air, fuel and recycled combustion products are compressed until it auto-ignites resulting in energy release reactions that initiate simultaneously at multiple sites within the combustion chamber. HCCI is generally limited to low load operating conditions with lean air-fuel ratios ($\phi < 0.3$) or for equivalence ratios up to stoichiometric with large amounts of EGR; the rate of pressure rise is typically the strongest restrictor [Dec, 2009]. Unlike diesel (mixing-controlled) combustion, HCCI is not limited by the mixing rate at the interface between the fuel jet and oxidizer, but is rather characterized by distributed low temperature reactions that occur relatively quickly at multiple sites. Attempts have been made to obtain diesel-fuelled HCCI operation with intake port fuel injection; however, significant intake charge heating (135-205^{o}C) is required to minimize the accumulation of liquid fuel in the intake system and to prevent soot and NO_X formation as a result of in-cylinder inhomogeneities [Dec, 2009]. HCCI engines suffer from higher THC and CO emissions than conventional diesel combustion because of low in-cylinder temperature due to lean mixtures and/or high levels of EGR which are necessary for satisfactory HCCI operation. High levels of THC and CO contribute to poor combustion efficiency (combustion efficiency is the fraction of the supplied fuel energy released during combustion) which results in higher fuel consumption compared to conventional diesel engines [Dec, 2009].

2.5.3 Other Forms of LTC (PCI, PCCI)

Premixed Compression Ignition (PCI) combustion as defined by Iwabuchi *et al*. [1999] of Mitsubishi Motors Corporation is another form of LTC, where fuel is injected early in the

compression stroke and a premixed lean mixture is formed over a long mixing period. In PCCI combustion, a large fraction of fuel is injected very early before TDC (-100 ^{o}CA ATDC) and a 2nd injection with a small amount of fuel is injected near TDC to ignite all the air-fuel mixture as well as to control combustion phasing [Kook and Bae, 2004; Lu *et al*., 2011]. In PCCI combustion, a luminous flame was only seen in the heterogeneous regions of the 2nd injection event, whereas the main combustion corresponding to the 1st injection event was mostly non-luminous [Kook and Bae, 2004; Kanda *et al*., 2005; Fang *et al*., 2008].

In order to achieve low smoke and NO_X levels at higher loads, combustion temperature needs to be reduced, while utilizing a higher oxygen content (on a mass basis) to suppress excessive CO and THC emissions. High load HCCI or PCCI operation may be obtained by high boost pressure and high levels of EGR [Christensen *et al*., 1997; Stanglmaier and Roberts, 1999; Kimura *et al.*, 1999; Iwabuchi *et al.*, 1999]. Chiara and Canova [2009] investigated a HCCI-DI strategy to enhance the load boundary, wherein at low load, external mixture formation was performed through a diesel fuel atomizer for HCCI operation and a DI diesel type of combustion was induced to increase the IMEP (indicated mean effective pressure). This strategy allowed a smooth transition from HCCI to conventional DI diesel mode at high load, while retaining HCCI combustion benefits on emissions and efficiency at part load [Chiara and Canova, 2009].

2.5.4 High-EGR LTC (Dilution-controlled, MK, UNIBUS)

In diesel LTC, high levels of EGR (up to ~60%) are used and fuel injection timing is advanced (20-30 ^{o}CA BTDC) or retarded (very close to TDC) compared to conventional diesel engines (so that the combustion phasing can be controlled regardless of the fuel's auto-ignition kinetics). In the high-EGR LTC regimes, images of natural combustion luminosity exhibited no soot luminosity until late in the premixed phase [Kook *et al.*, 2005; Musculus, 2006; Lachaux *et al*., 2008]. The overall soot luminosity decreased and became more uniform with increasing charge dilution (higher EGR).

The combustion temperature reducing effect of EGR reduces NO formation, resulting in a reduction to near zero levels at EGR rates above approximately 40%, which means that the combustion process occurs at temperatures not high enough to form thermal NO. The NO_X measured in the engine tailpipe at these EGR levels likely results from the prompt NO or the nitrous oxide routes [Desantes *et al*., 2012]. Soot emissions rise with EGR, up to an EGR rate around 50%, depending on the engine and operating conditions. For EGR >50%, soot emissions decrease as the flame temperature in the fuel-rich region is reduced to the point that soot formation is suppressed. At 60% EGR, both soot and NO_X emissions can approach near-zero levels depending on load [Cong, 2011]. However, THC and CO emissions increase sharply at 60% EGR [Cong, 2011], which can be attributed to the lower temperatures and low oxygen concentrations during combustion, both of

which adversely affect the oxidation of THC and CO. Therefore, it is critical to optimize the EGR system to balance the NO_X and PM reduction against CO and THC emission increases.

High-EGR advanced injection LTC, also known as dilution-controlled combustion, is different from high-temperature combustion which is dominated by fuel-air mixing, and also from HCCI combustion, which is controlled by fuel-air chemical kinetics. Compared to conventional diesel combustion, LTC forms a more uniform mixture before auto-ignition. However, compared to HCCI and PCCI combustion, high-EGR LTC (smoke-less rich combustion) employs high levels of EGR (>60%). In addition, fuel injection strategy controls the combustion phasing unlike fuel-air chemical kinetics in HCCI combustion. Strong in-cylinder turbulence and fuel-air mixing also play important roles in combustion and emissions [Lu *et al*., 2011]. Imaging measurement showed that in dilution-controlled combustion, the liquid fuel penetrated further into the combustion chamber before vaporizing compared to conventional diesel combustion. Rather than forming just downstream of the liquid fuel, and throughout the jet cross-section, soot was formed much further downstream, only at the head of the jet, in the head vortex [Musculus, 2006].

Idicheria and Pickett [2005] investigated the soot formation mechanism with high EGR levels in an optically accessible constant volume combustion vessel using laser extinction and planar laser induced incandescence (PLII) techniques and reported that peak soot volume fraction decreased and the width of the sooting region (in the diesel jet) increased with increasing EGR. A decrease in the ambient oxygen concentration increased the lift-off length, thereby allowing approximately the same amount of oxygen to be entrained into the jet prior to the reaction zone, as the rate of oxygen entrainment decreased [Idicheria and Pickett, 2005]. PLII images also showed that the distance between the lift-off length and the appearance of the first soot incandescence increased with increasing EGR levels suggesting a longer residence time for soot precursor formation. The total jet cross-section of the soot increased initially with increasing EGR and then gradually reduced to zero as the EGR rate was increased to an equivalent ambient oxygen concentration of 8%. This explains the typical NO_X-PM trade-off with EGR. When employing EGR, the trend in soot production is determined by a competition between increased residence time and decreased flame temperature with decreasing oxygen concentration [Idicheria and Pickett, 2005].

In the Nissan MK (simultaneous low temperature and premixed combustion) strategy, fuel is injected directly into the combustion chamber near or after TDC, but the ignition delay is extended through the use of large amounts of cooled EGR [Mase *et al.*, 1998; Kimura *et al.*, 1999; Kimura *et al.*, 2001; Kimura *et al.*, 2002] during low-load operation. Late in-cylinder injection of diesel appears to avoid most of the problems associated with fuel wall impingement [Lachaux *et al*., 2008] and provides some control of the combustion phasing, but the short ignition delay of diesel limits this approach to low engine loads. With advanced high pressure common rail fuel injection system, injection duration can be made shorter than the ignition delay, thus extending the MK operation to medium loads [Kimura *et al.*, 2002; Jacobs *et al.*, 2005].

Toyota's UNIBUS technique involves a combination of an early injection (~-50 ^{o}CA ATDC) and a late injection (~13 ^{o}CA ATDC) at high EGR levels (~60%) [Yanagihara, 2001]. In this system, a low compression ratio (12:1) was used presumably to avoid overly advanced combustion of the premixed fuel. The 2nd injection was used as a trigger for a portion of the energy release from the early injected fuel that significantly improved the combustion efficiency [Yao *et al*., 2009]. Singh *et al*. [2007] optically investigated an EGR-diluted, double injection strategy with the first injection early in the compression stroke, similar to the UNIBUS scheme, and reported that due to a long ignition delay for the first early injection, the fuel was significantly premixed with the relatively cool charge gases and therefore, the combustion was rapid. Hot second stage combustion with a short ignition delay was characterized by broadly distributed OH fluorescence throughout the jet, indicating leaner and more uniform mixtures than conventional diesel combustion. For this LTC strategy, soot formation occurred only in tiny pockets in the less well-mixed jet cross-section (formed downstream only in the fuel-rich head vortex) indicating that most of the jet regions were below the sooting limit which was in contrast to Dec's conceptual model for conventional diesel combustion where soot was formed upstream and throughout the jet cross-section [Singh *et al*., 2007]. Similar phenomena were also reported for single injection LTC conditions [Musculus, 2006; Bobba and Musculus, 2012]. For the double injection strategy, significant broadband fluorescence from the fuel and the combustion intermediates persisted near the injector late in the combustion phase suggesting that the mixture near the injector did not undergo complete combustion which would significantly affect THC emissions [Singh *et al*., 2007].

Diesel LTC is characterized by high CO and THC emissions, much like HCCI combustion. In diesel LTC, fuel injection ends well before the start of combustion. Although this improved mixing in the downstream region is central to the benefits of LTC, sometimes the increased mixing associated with the early end of injection causes the upstream region near the injector to become very lean and is unlikely to burn to completion. This appears to be a major source of THC emissions. Kim *et al.* [2008] reported that increased dilution slows down oxidation rates throughout the cylinder, but most noticeably within the squish volume, thereby significantly increasing THC emissions from this region. CO was generally observed near the cylinder centre line and broadly distributed within the squish volume. Engine performance in LTC regimes is reported to be sensitive to minor variations in the operating conditions [Henein *et al.*, 2008; Cong, 2011].

2.6 Low Temperature Cool Flame Reactions in LTC

The major steps involved in fuel preparation and combustion for LTC operation are 1) fuel atomization and vaporization; 2) fuel-air mixing; 3) low temperature cool flame reactions; 4) negative temperature coefficient (NTC); 5) auto-ignition; and 6) main high temperature combustion. The initial step in the preparation of the fuel involves atomization and vaporization. Droplet vaporization plays an important role in determining air-fuel mixing which has a significant impact

on fuel oxidation and combustion. The fuel preparation mechanism in LTC is similar to the conventional diesel operation discussed in Sec. 2.2. A typical auto-ignition process during LTC operation is known to undergo two distinct stages of energy release in which low and high temperature oxidation mechanisms govern the first and second stages of energy release reactions respectively. The details of the cool flame reaction and the high temperature oxidation mechanisms are discussed below.

Low temperature oxidation (consisting of both cool flame reactions and NTC) reactions are preceded by a 1st stage ignition delay period during which little reaction occurs. Low temperature oxidation is characterized as a process starting with the fuel + OH reaction, finally reproducing OH via the formation of alkylperoxy ($R\dot{O}_2$) and hydroalkylperoxy ($ROOH$) radicals. In a first step, hydrocarbon radicals ($\dot{R}$) react with oxygen and form alkylperoxy radicals. These can abstract hydrogen atoms forming alkylhydroperoxy compounds. After an external hydrogen atom abstraction, the hydroperoxy compound decomposes into an alkyloxy radical ($R\dot{O}$) and OH. Low temperature oxidation initially proceeds by increasing the amount of OH by repeating the fuel oxidation cycle. In the later stages of low temperature oxidation, the reactions of intermediate species with OH, which do not reproduce OH, compete with the fuel + OH reaction, and low temperature oxidation eventually terminates when OH consumption by these reactions exceeds its formation [Yamada *et al*., 2008]. Since the overall process is a branched radical chain reaction, the most influential steps are those that change the number of radicals, namely the initiation, branching and termination reactions. More details regarding the different stages of hydrocarbon low temperature oxidation reactions and chemical kinetics are given by Pilling [1997].

During the initial stage of low temperature oxidation reactions, a combustible mixture reacts accompanied by a small temperature increase. Some chemiluminescence occurs during the initial reaction stages, and it appears as if a flame propagates through the mixture. It is a faint blue luminosity, primarily due to the chemiluminescence of electronically excited formaldehyde. The reactions in the system are exothermic and the temperatures are known to increase only marginally (200 K)—hence the name cool flames [Glassman, 1996]. The small temperature rise is due to the heat produced by the breaking and reforming of the fuel chemical bonds [Naidja *et al*., 2003].

The NTC phenomenon follows the cool flame reaction. The NTC is a unique phenomenon in hydrocarbon oxidation, in which the overall reaction rate decreases with increasing temperature and it represents a barrier for auto-ignition to occur. The region of NTC is characterized by the fact that a temperature increase causes an increase of the ignition delay time, instead of the usual temperature dependence where delay time would decrease [Warnatz *et al*., 2000].

Auto-ignition in a compression ignition engine is a combustion phenomenon in which chemical kinetics plays the dominant role. Auto-ignition occurs at temperatures in the range of 800-900 K. The decomposition of H_2O_2 is quite slow at these temperatures, and other chain-

branching mechanisms govern the ignition process. The key is that H_2O_2 decomposes rapidly at temperatures between 900 and 1000 K; so this temperature can be considered as the critical value in systems in which the temperature approaches this value from lower temperatures. Temperatures varying from 1000 to 1200 K correspond to the intermediate temperature range, where HO_2 chemistry is important. Temperature rises, and the high temperature combustion chemistry takes over to complete the combustion and to provide a large part of the energy release. Following ignition, the primary fuel produces unsaturated hydrocarbons and hydrogen. A little of the hydrogen is concurrently oxidized to water. Subsequently, the unsaturated compounds are further oxidized to CO and hydrogen. Simultaneously, the hydrogen present and formed is oxidized to water. Finally, large amounts of CO formed are oxidized to CO_2 and most of the energy release from the overall reaction is obtained. It should be noted that the CO is not oxidized to CO_2 until most of the fuel is consumed owing to the rapidity with which OH reacts with the fuel compared to its reaction with CO [Glassman, 1996]. It is reported that, in essence, the low temperature chemistry prepares the mixture for ignition, the intermediate chemistry ignites it and the high-temperature chemistry burns it [Pilling, 1997].

In HCCI engines, low and intermediate temperature reaction sequences process the fuel-air mixture during its compression; the amount of low temperature cool flame energy release reaction varies, depending on the composition of the fuel. H_2O_2 forms at lower temperature and remains relatively inert, until increasing temperatures from compression and exothermic reactions reach a level where it decomposes rapidly producing large numbers of OH radicals that rapidly ignite the fuel [Westbrook, 2000]. Variation in any engine parameter that gets the reactive fuel-air mixture to the H_2O_2 decomposition temperature earlier advance the ignition (such as increased intake manifold temperature or ignition additives), while EGR retards the ignition [Westbrook, 2000]. The effects of different operating parameters (fuel quantity, injection pressure, EGR rate and intake temperature) on the phasing and magnitude of the cool flame and high temperature reactions in high-EGR LTC operation are reported by Cong *et al*. [2011b].

2.7 Effects of Intake Pressure on Diesel Low Temperature Combustion and Emissions

An increase in ambient gas density causes a nonlinear increase in soot levels in a fuel jet. This has been attributed to an increase in soot number density [Pickett and Siebers, 2004]. However, increased charge density improves air-fuel mixing throughout the combustion process resulting in higher soot oxidation rates [Colban *et al*., 2007]. Musculus [2006] reported that moderate changes in the boost pressure had no observable effects on the general characteristics of the in-cylinder processes in LTC operation.

Colban *et al*. [2007] investigated the effects of boost pressure on performance and emissions in a diesel engine in two low temperature combustion regimes: (i) high exhaust gas recirculation (EGR) levels with maximum brake torque injection timing and (ii) moderate EGR levels with

retarded injection timing. Colban *et al.* used simulated EGR in a light duty automotive engine at low and medium loads, and reported that increased intake pressure reduced THC and CO emissions, thereby improving combustion efficiency and hence, indicated specific fuel consumption (ISFC), particularly at higher loads. The authors also demonstrated that increased intake pressure reduced peak soot emissions and shifted the maximum soot emissions towards lower oxygen concentrations. Contrary to an expected rise in NO_X with higher oxygen concentration, NO_X emissions reduced in high-EGR LTC. The authors hypothesized that as the global equivalence ratio reduced with increased boost pressure, mixing with cooler excess air available with higher boost levels likely suppressed the relatively slow NO forming reactions. In the late injection LTC regime, at low load, change in boost pressure had little effect on NO_X emissions. At moderate load, increased boost pressure yielded slightly higher NO_X emissions. Late-injection LTC (similar to MK) generally had higher CO emissions than dilution-controlled LTC, whereas soot showed a reverse trend [Colban *et al.*, 2007].

2.8 Effects of Multiple Injections on Diesel Low Temperature Combustion and Emissions

High injection pressure with multiple injection events have been shown to reduce THC and PM emissions in conventional diesel combustion, as discussed in Sec. 2.4. Multiple injection strategy has also been investigated in high-EGR LTC operation to reduce the emissions of combustion by-products and soot. There are numerous publications reporting the potential benefits of two-stage injections under highly dilute LTC conditions; however, most of the investigations are limited to optimizing the fuel mass ratio between the two injection events and the injection dwell time to reduce emissions and improve fuel economy with either advanced or retarded injection timings [Koci *et al.*, 2009; Li *et al.*, 2010; Diez and Zhao, 2010; Kokjohn and Reitz, 2010; Lu *et al.*, 2011]. The effects of late-cycle mixing and turbulence enhancement by the post-injection strategy on combustion and engine-out emissions in the high-EGR LTC regimes were also investigated. It was reported that post injection could lead to further reductions in soot emissions without deteriorating the NO_X emissions due to negligible temperature changes caused by small post injection fuel quantity [Yun and Reitz, 2007; Bobba, *et al.*, 2010]. However, the dwell between main and post injections needs to be optimized to suppress increase in THC emissions. With longer dwell periods, the temperature in the cylinder during the expansion stroke may be too low to burn all the injected fuel completely [Yun and Reitz, 2007]. Post fuel injection was also investigated by Cong [2011] to reduce emissions through enhanced fuel-oxygen mixing in the later part of the combustion process. The results showed that the post injection had an insignificant effect on LTC emissions, probably due to the low local oxygen concentrations (after the high temperature reactions) and the low in-cylinder temperatures.

In the high-EGR diesel LTC regime, late split injections (two injection events very close to TDC) led to combustion that was almost independent of injection pressure (little influence on energy

release, emissions and efficiency) especially at low oxygen concentrations. It was reported that with optimized swirl ratio, EGR conditions, SOI timings, fraction of fuel per injection and piston bowl geometry (a stepped piston bowl rather than the conventional open or re-entrant piston bowl), significant improvements in exhaust emissions and fuel economy can be achieved with a small pressure rise rate [Benajes *et al*., 2008; Kashdan *et al*., 2009; Horibe *et al*., 2009; Anselmi *et al*., 2010; Dolak and Reitz, 2010; Kokjohn and Reitz, 2010]. Koci *et al*. [2009] showed that at certain injection timings and fuel-split fractions, multiple injections were effective in further reduction of THC and CO emissions from the single injection optimal emissions at LTC with 67% EGR (by mass). Soot emissions, however, increased. Multiple advanced fuel injection strategies (with up to 3 pulses per cycle) with high levels of EGR also showed improvements in combustion phasing and thermal efficiency in LTC [Asad *et al.*, 2008]. Li *et al.* [2010] investigated various fuels with different cetane numbers with high levels of EGR (60% by volume) with retarded close-spaced injection timings with a fuel split ratio of 20:80 along with various dwell timings. They showed that with optimized dwell timing and injection ratio, two-stage injection can reduce THC and CO emissions. With an optimized low pressure early cycle injection combined with high pressure near-TDC injection it was shown that near-zero NO_X and soot levels could be achieved while maintaining good control over the combustion phasing for a PCCI engine with trade-offs between soot, THC and CO emissions with respect to EGR levels, NO_X emissions and rate of pressure rise [Benajes *et al.*, 2009].

2.9 Transient Effects on Conventional and Low Temperature Diesel Combustion Regimes

Some technical hurdles such as extension of the operating map to higher loads, and control of combustion phasing over the load-speed range and through transients need to be resolved before LTC can be applied to practical transportation engines [Dec, 2009]. Since LTC is difficult to achieve at high load, mixed-mode combustion is emerging, wherein LTC is used at low and medium loads and traditional diesel combustion is used at higher loads. Also, it is important to ensure that during combustion mode transitions (transition from LTC to conventional diesel or *vice-versa*) the majority of the combustion processes progress through the low NO_X and PM regions; the preferred paths are shown by the dashed arrows in Fig. 2.3.

Engines rarely experience steady-state conditions when considering actual in-vehicle operation. Transient behaviour includes frequent and sudden changes in engine speed, load or both. The transients are so fast that fuel, air and EGR cannot be well controlled and significant excursions from optimal in-cylinder conditions occur due to different response times of the fuel injection, turbocharger and EGR systems; it is widely reported that for turbocharged diesels, the air handling system has the maximum delay due to ‘turbo-lag’ at the beginning of a transient event [Chan *et al*., 1999; Benajes *et al*., 2002; Rakopoulos *et al*., 2010; Hagena *et al*., 2011]. These deviations of in-cylinder composition from optimal conditions have a great impact on emissions. Pelkan and Debal

[2006] reported that the emissions levels measured in the New European Driving Cycle (NEDC) are lower than the emissions produced in real traffic, with the transient emissions contributing a substantial share to the net emissions. Particulate emissions increase rapidly, primarily because the fuel flow rate can exceed the availability of oxygen in the cylinder and the low charge air density allows increased liquid fuel penetration causing liquid fuel impingement on the cylinder surfaces resulting in either an entire cylinder full of a fuel-rich mixture or rich pockets of poorly mixed product gases producing soot [Chan *et al*., 1999]. Chan *et al.* also predicted that during acceleration (constant torque, variable speed), NO emissions increased to a peak level at the initial stage of the engine transient, exceeding the values of their corresponding steady-states with the peak values occurring at high load acceleration. The engine transient of most concern to particulate emission is a rapid change from idle or low load to high load and high speed in case of acceleration in conventional diesel operation [Rakopoulos *et al*., 2010]. Non-uniform distributions of EGR between cylinders and EGR delay in low-pressure EGR systems can cause high NO_X emissions during a transient [Peckham *et al*., 2011]. Engine cold-starting contributes to high smoke emissions, combustion instability and combustion noise [Rakopoulos *et al*., 2010]. Cold-start also results in high NO_X, CO and THC emissions as it takes some time for the after-treatment system to start working. Kang and Farrell [2005] reported about the transient (constant speed variable torque and constant torque variable speed) effect of EGR rate and injection timing on THC and NO_X emissions in a diesel engine. Their results showed that peak NO_X emissions occurred during transient operation at low EGR levels, but there were no evident step load change effects on NO_X when higher EGR levels were used. However, THC emission sensitivity to transients increased drastically when EGR rate was increased.

Mode transition between high-EGR LTC and conventional diesel operation or *vice-versa* are not widely reported with only a few studies available in literature [Burton *et al*., 2009; Tanabe *et al*., 2010; Cong, 2011; Kim *et al*., 2011]. Burton *et al.* [2009] investigated a mode shift between high-EGR LTC with advanced injection timing (i.e. PCCI) and conventional diesel combustion with moderate EGR levels and retarded injection timings and showed that a step change from PCCI to conventional diesel combustion resulted in high THC emissions. Similarly, the step load change from conventional diesel to PCCI mode resulted in a NO_X spike and high rate of pressure rise. The initial and final loads in this investigation were 250 kPa and 500 kPa net IMEP respectively and this study did not consider any load ramp-up duration. Kim *et al.* [2011] investigated combustion mode shift between conventional diesel and high-EGR LTC with a gradual load ramp-up in a naturally aspirated engine and showed that IMEP fluctuation occurred during the early stage of mode transition from LTC to conventional diesel operation because of air flow overshoot, resulting in advanced combustion phasing and rapid energy release rates. However, in the cited work [Kim *et al*., 2011], the important aspects of a multi-cylinder turbocharged engine on the transient were not

considered. None of these studies discussed above considered the real time transients that are likely to be encountered in an in-service engine while following a legislated driving cycle.

Tanabe *et al.* [2010] developed and investigated a control system which controlled the fuel injection and air management systems using CA50, intake oxygen concentration and excess air ratio for a smooth combustion mode transition between premixed compression ignition (PCI) combustion and conventional diesel operation without increased exhaust emissions during a Japanese transient test cycle (JE05) with a gradual load ramp-up period (10 s). However, this gradual load ramp-up period is not realistic for LDD applications. In the cited work [Tanabe *et al.*, 2010], by smoothly varying the CA50 location corresponding to the change in intake oxygen concentration, the NO_X spike was minimized during mode transition from conventional diesel to PCI combustion. Similarly, the spike in smoke emissions during mode transition from PCI to conventional diesel combustion was reduced by preventing excessively retarded CA50 by controlling the fuel injection and air management systems. This study, although useful for investigating different control strategies for minimizing smoke and NO_X spikes during combustion mode transitions, however, did not report other combustion by-product (THC and CO) emissions. NO_X emissions in Tanabe *et al.*'s study were particularly high (1 g/kWh) even in the PCI mode of combustion as high intake oxygen concentration limit (13%) was chosen for the PCI combustion. A more detailed literature review regarding the effects of transients on LTC and conventional diesel combustion is provided in Chapter 7.

2.10 Gaps in the Literature

From the literature review, it is found that there has been increased interest amongst researchers on the practical implementation of diesel LTC in transportation. In high-EGR LTC, high EGR rates cause cyclic variability, unstable combustion and high THC and CO emissions. Various explanations are provided in the literature to justify the observed trends of emissions and performance in the low temperature combustion regimes; however, the fundamental physics of combustion remains mostly unexplained without in-cylinder optical diagnostics. Diesel LTC is also limited to low to medium loads and poses serious emission problems during transitions from LTC to conventional diesel combustion and *vice-versa*. There is currently little published literature dealing with this transitional behaviour. There is also limited information studying the effects of intake pressure on diesel low temperature combustion and emissions, and the trends of emissions with different boost pressure remain unexplained. Various multiple injection strategies in high-EGR diesel LTC have been studied with the aim of optimizing the injection timings and fuel split ratios between the injection events to reduce emissions; however, these investigations have not evaluated the corresponding potential of this strategy to reduce the EGR requirements for LTC. Additional research is also required to obtain good combustion efficiency while maintaining low NO_X and soot emissions over a wider operating range.

Chapter 3
EXPERIMENTAL METHODOLOGY

3.1 Introduction

This chapter describes the components of the research engine test facility. This consists of a single cylinder research engine, fuelling system, air exchange system and an engine test bed along with various associated instrumentation. Engine modifications for optical access and the development of a two-colour pyrometry system for flame temperature measurement are described in this chapter. Measurement techniques and experimental parameters are also discussed here.

A fundamental tool for undertaking combustion research and development in internal combustion engines is the single cylinder engine because it allows segregation of the performance within an individual cylinder compared to an average performance of a multi-cylinder engine configuration. This eliminates the often complex inter-cylinder interactions. In addition, in a turbocharged multi-cylinder engine, the availability of boost pressure and EGR rate are fixed at a given operating condition which severely restricts the exploration of engine conditions for advanced combustion regimes. With independent control of boost pressure, intake temperature, exhaust back pressure and EGR rate, the operational flexibility of a single cylinder engine is also enhanced.

3.2 Experimental Apparatus

The research facility used in this work was based on a fully instrumented AVL 5402 single cylinder diesel research engine which had a combustion system typical of an automotive two-litre four-cylinder light-duty high-speed direct injection (HSDI) diesel engine. The engine test bed consisted of a dynamometer and a coolant and oil conditioning unit. The air exchange system consisted of a boost system and an EGR system to vary intake pressure and EGR levels respectively. The instrumented engine and the EGR system existed prior to the commencement of this research. They were developed by an earlier Loughborough researcher Shenghui Cong and were reported in detail in his PhD thesis [Cong, 2011]. Therefore, only a brief description will be provided regarding the existing facility (engine instrumentation and EGR system). However, the new research facilities (i.e. the boost system, the optically accessed engine and the two-colour pyrometer) that were developed as part of this present research work will be described in more detail in the following subsections.

3.2.1 Single Cylinder Research Engine and Fuelling System

The AVL 5402 single cylinder HSDI diesel engine had a combustion system in the form of a re-entrant ω shaped piston bowl as shown in Fig. 3.1 incorporating a central fuel injector. The engine had a 4-valve (two inlet valves and two exhausts valves) double overhead camshaft (DOHC) valve-train arrangement. This engine was equipped with a 1st order mass balancing system for

compensating the oscillating forces to keep vibrations low. The specifications of the engine are given in Table 3.1.

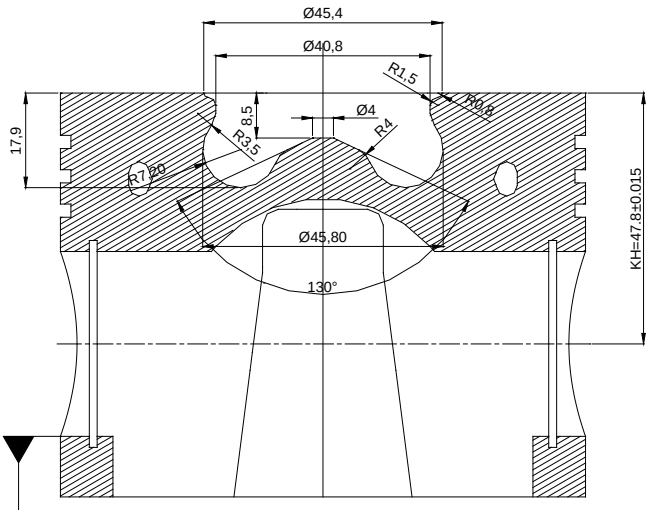

Fig. 3.1: Piston bowl geometry for the AVL 5402 single cylinder research engine

Table 3.1: Specifications of Single Cylinder Research Engine

Engine	AVL 5402 Single Cylinder Engine
Bore/Stroke/Connecting rod length	85/90/148 mm
Swept volume	0.51 Litre
Compression ratio	17.1:1
Rated speed/Maximum speed	4200 rpm/4500 rpm
Maximum power (Supercharged)	16 kW
Nominal swirl ratio	1.78
Combustion chamber geometry	Re-entrant Bowl
Intake port	Tangential and Swirl
Fuel injection system	Bosch Common Rail CP3
Engine management system	AVL-RPEMS™ and ETK7 (Bosch)
Intake valve open	8 ^{o}CA BGTDC
Intake valve close	226 ^{o}CA AGTDC
Exhaust valve open	128 ^{o}CA ATDC
Exhaust valve close	18 ^{o}CA AGTDC
Maximum cylinder pressure	17 MPa

The engine was fitted with a Bosch common rail CP3 fuel injection system consisting of a production type high pressure common rail fuel pump and a five-hole valve covered orifice (VCO)

fuel injector. The maximum needle lift of the injector was 0.2 mm with a steady fuel flow rate of 375 ml/30 s. The specification of the fuelling system is given in Table 3.2.

Table 3.2: Specification of Fuelling System

Injector type	CP3 VCO
Injections	Bosch Common Rail
Nozzle type	DSLA 142P
Maximum injection pressure	135 MPa
Number of holes/Hole diameter	5/0.18 mm
Spray included angle	142^{o}
Needle lift	0.2 mm
Fuel flow rate @ 0.2 mm lift	375 ml/30 s
Minimum dwell between injections	200 μs

A fuel conditioning unit maintained a constant temperature fuel supply to the injector. The AVL-RPEMS™ (rapid prototyping engine management system, capable of flexible control of injection timing, injection quantity, number of fuel injections per cycle and fuel pressure) was adapted to run the research engine. An open loop fuel injection control strategy designed by AVL was loaded in the ETAS system to allow independent control of fuel injection parameters. This control system consisted of an electronic control unit (ECU), a communication interface (ETAS ETK 7.1 Emulator probe) and an INCA programme (a commercial tool for automotive calibration). The injection parameters for each injection event could be modified and logged independently through the INCA software, which was used to communicate with the ETAS system. This control system enabled up to four injections (two pilot injections, single main and one post injection) per cycle. The start of injection (SOI) timing could be varied from -120 ^{o}CA to 60 ^{o}CA ATDC (angle increment of 0.125 ^{o}CA) with a minimum injection dwell period of 200 μs in case of multiple injections. The injection events could be setup using either a characteristic map (map based mode) or user defined parameters (manual mode). For the work reported here, all the test results were obtained using the manual mode. For the manual mode operation, the fuel injection timing, injection pressure and fuel quantity were specified individually.

An automotive grade sulphur-free diesel (sulphur content <10 mg.kg^{-1}) fuel that meets the current British Standard BS EN 590 and complies with the current requirements of the UK "Motor Fuel (Composition and Content) Regulations" was used in this work. It should be noted that 5% bio-diesel by volume was blended with this fuel. Some salient characteristics of this fuel (both Winter and Summer Grades) are summarized in Table 3.3 as outlined by the Marketing Specifications of Total UK Ltd [Total UK Ltd, 2008].

Table 3.3: Specification of Diesel Fuel [Total UK Ltd, 2008]

Density @ 15^{o}C	840 kg.m^{-3}
Polycyclic aromatic hydrocarbons (PAH)	9% by mass
Sulphur contents	8 mg.kg^{-1}
Flash point	65^{o}C
Cetane number	52
Kinematic viscosity @ 40^{o}C	2.9 mm^{2}.s^{-1}

3.2.2 Engine Test Bed

An AVL single cylinder engine compact test bed (AVL 570-SCTB) housed a steady state AC (alternating current) dynamometer and a cooling unit consisting of a water circulation pump, a heat exchanger and a flow sensor. The AC dynamometer consisted of an asynchronous motor (38 kW) with rated torque and speed up to 120 Nm and 7000 rpm respectively. The motor in combination with an AMK digital drive unit provided constant torque levels during engine motoring, while absorbing varying torque levels for a desired engine speed during engine firing. With a stand-alone EMCON 400 system, the engine speed and torque could be controlled independently. The engine speed could be controlled within ±0.5 rpm for the desired speed, whereas the torque readings from the EMCON were marginally unstable especially at low load operating conditions (typically <12 Nm torque). Heat generated in the dynamometer was rejected to a high pressure externally conditioned recirculation water-coolant circuit. An air-water heat exchanger dissipated heat from the enclosure, thus protecting the temperature sensitive components in the test bed. The temperature of the external recirculation water-coolant circuit was maintained below 30^{o}C at all operating and ambient conditions.

A close loop controlled, close circuited lubricating oil and coolant conditioning unit (AVL 577) was integrated in the compact test bed. It was equipped with an independent heat exchanger and a heater to vary temperatures between 40^{o}C and 120^{o}C for the lubricating oil circuit (maximum pressure 500 kPa) and 50 to 110^{o}C for the coolant circuit (maximum pressure 140 kPa). Coolant used for this engine was a 75/25 blend of demineralised water and ethylene glycol. The temperatures of the oil and coolant were manually pre-set on the unit's control panel and were maintained in the range of ±2^{o}C for the set temperatures. Over-temperature protection was provided for both the oil and coolant temperatures. The oil pressure was sensed by a pressure gauge; loss of oil pressure caused the engine to shut down automatically. The engine inlet temperatures for the coolant circuit and lubricating oil circuit were maintained at 80^{o}C and 90^{o}C respectively in this work.

3.2.3 Air Exchange System (Boost and EGR Systems)

A custom-built air exchange system consisting of boost and EGR systems, as illustrated schematically in Fig. 3.2, provided wide possible ranges of intake pressure and EGR, along with the provision to control the exhaust back pressure (EBP). This was controlled independently from the engine allowing investigation of wider ranges of intake pressures and EGR fractions, thus removing the sensitivity of the air exchange system to changes in engine operating conditions. The air exchange system was capable of providing either fresh air (without EGR) or diluted air (with EGR) with variable intake pressures ranging from atmospheric up to 210 kPa (absolute). Two insulated 25 litre surge tanks (one upstream of the intake manifold and the other downstream of the exhaust manifold) capable of withstanding temperatures and pressures up to 620^{o}C and 500 kPa (gauge) respectively reduced acoustic pulsations in the intake and the exhaust systems. The exhaust surge tank also acted as a reservoir that stored the exhaust gases from the previous cycles for subsequent use in the EGR loop. Additionally, the intake surge tank ensured thorough mixing of fresh air with EGR. The boost system had a provision to switch between naturally aspirated and boosted mode as required.

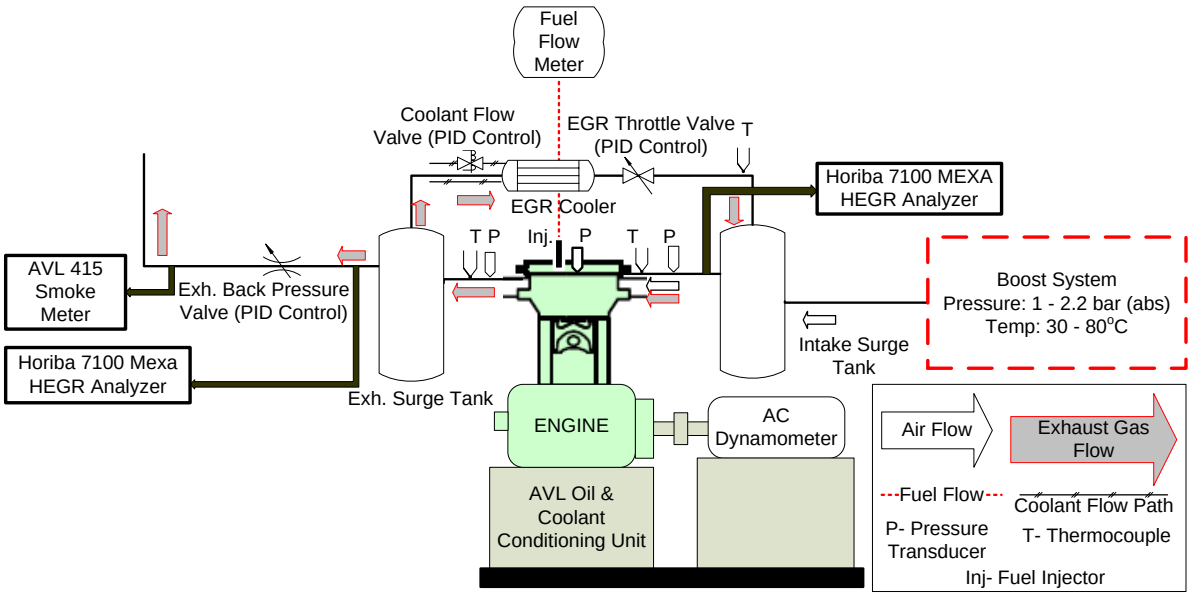

Fig. 3.2: Schematic of the experimental set-up

(a) Boost system

As part of this work, a new boost system was designed and fabricated. Details of the boost system are shown schematically in Fig. 3.3 and are described in the following paragraphs. Note that Fig. 3.3 shows the details of the boost system which is shown in dotted lines in Fig. 3.2.

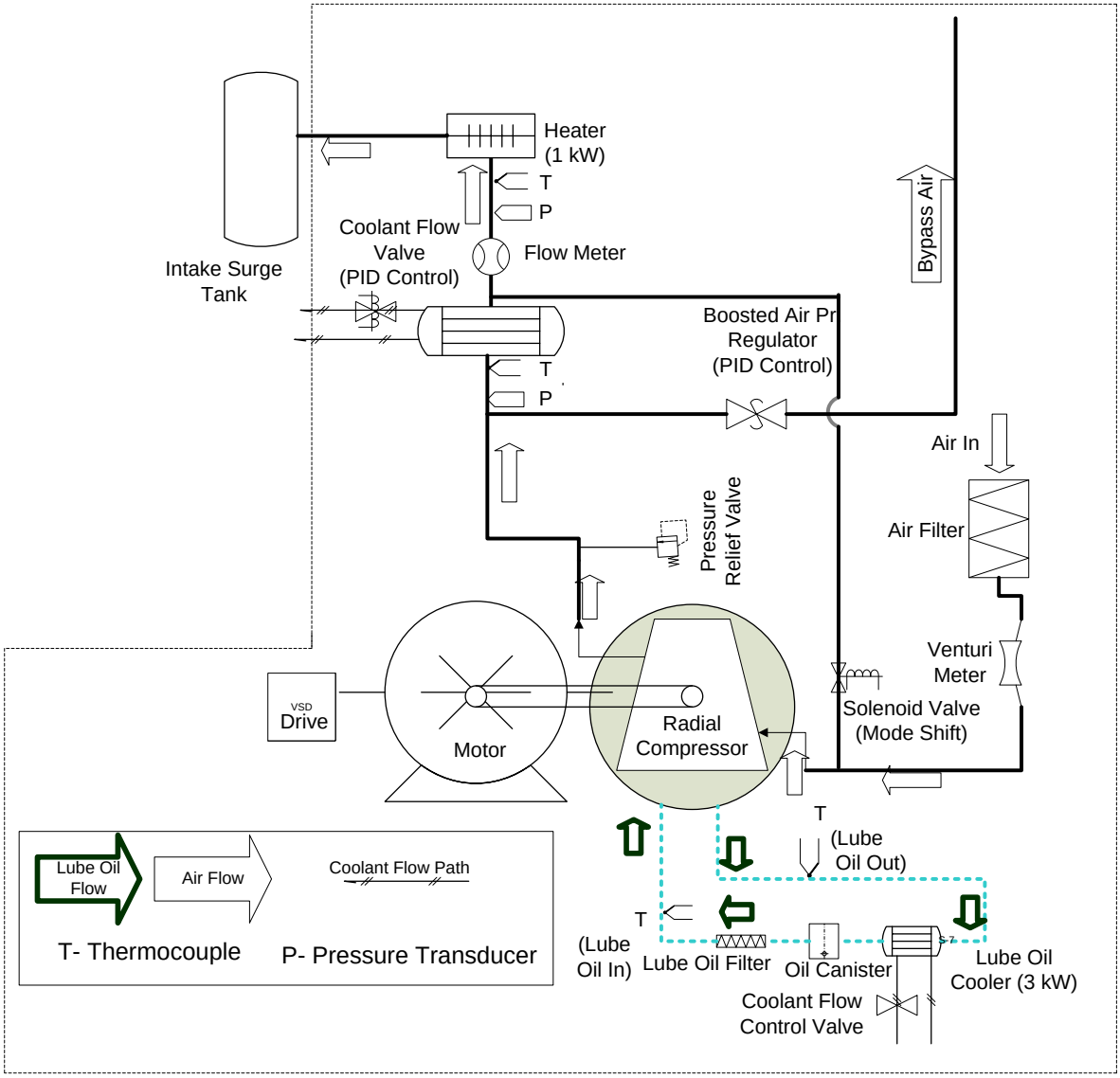

Fig. 3.3: Schematic of the boost system

Fresh air was supplied to the engine by the boost system which essentially consisted of a Rotrex C15-16 centrifugal supercharger, driven by an ABB asynchronous AC motor with a Eurotherm variable frequency drive. The maximum mass flow rate of the compressor was 0.11 kg/s with a maximum pressure ratio of 2.48:1. The peak impeller speed was 201500 rpm with an input shaft speed of 15900 rpm. In the present design, the maximum mass flow rate of the compressor was limited to 0.05 kg/s with a maximum pressure ratio of 2.2:1. A boost pressure regulator maintained the desired flow rate into the engine, bypassing excess air to the atmosphere, thus, acting as a surge control mechanism for the supercharger. A PID (proportional-integral-derivative) controlled Burkert solenoid valve controlled coolant flow rate to the air-water heat exchanger (12 kW), thereby, maintaining the desired fresh charge air temperature. A PID controlled Farnam FT-200 charge air heater (1 kW) installed upstream of the intake surge tank was used to heat up the fresh charge air up to 80^{o}C when no EGR was used. The actuators for the boost pressure regulator and the coolant valve

were electronically controlled through a Moeller CP8-ME easy 800 series programmable logic control (PLC) unit coupled with an interface module and an MFD-TA17 I/O module. Closed loop PID controllers were developed to control these parameters. The controller logic was developed using the Moeller EASY-SOFT V6.22 Pro software. The pressure at the outlet of the supercharger was sent to the PLC as a feedback signal or as a PID control algorithm; from this, the controller generated an analogue output to command the valve position via a pneumatic actuator. The charge air cooler temperature was controlled based on temperature measurement downstream of the charge air cooler; another PID algorithm was used to generate the coolant flow valve position command, which was then sent to the proportional valve in the control circuit.

(b) EGR system

The EGR system shown in Fig. 3.2 had the provision to control the EBP, EGR rate and the EGR temperature. An electronically actuated PID controlled butterfly valve in the exhaust line maintained the desired back pressure to closely simulate the EBP experienced by a turbocharged engine with various exhaust after-treatment systems [Cong *et al*., 2009b]. A fraction of the exhaust gases from the exhaust surge tank were fed to the intake surge tank through a PID controlled EGR throttle valve. The EGR rate was controlled by adjusting the EBP valve and the EGR valve positions simultaneously. Another PID controlled valve controlled the coolant flow rate through the EGR cooler to achieve the desired EGR temperature. Either the EGR cooler or the charge air heater or both maintained the desired charge air temperature at the engine's intake manifold. Another Moeller CP8-ME easy 800 series PLC with an interface module and a MFD-TA17 I/O module was developed and used to control the EBP and EGR valve positions and intake manifold temperature [Cong, 2011]. All controllers were tuned to achieve the desired control accuracies. EBP and intake pressure were controlled with an error of ±1 kPa; the EGR rate control accuracy was ±0.5%.

3.3 Measurement Techniques

The research engine facility was fully instrumented with provision to measure air temperature and pressure, air and fuel flow rates as well as in-cylinder pressure-time histories. A brief description to the most important pieces of instrumentation used in this work is given here; further details of the instruments including Make/Model, range and accuracy are given in Appendix A1.

3.3.1 Instrumentation and Data Acquisition System

The mass flow rate of air was measured with an EPI 8712MPNH thermal mass flow meter installed upstream of the charge air heater. This thermal mass flow meter had two reference grade resistance temperature detectors (RTDs). A forced null Wheatstone bridge heated one RTD, while the 2nd RTD measured the temperature of the flowing gases and was used as a reference. By maintaining a constant temperature difference between the RTDs, the flow meter could measure the

amount of heat dissipated by the flowing gases. As heat was dissipated, more power was used to maintain constant temperature, the power being directly proportional to the gas mass flow rate. Gravimetric fuel consumption was determined with an AVL733 dynamic fuel meter. The mass of fuel in a small reservoir was monitored over time to provide a measure of absolute fuel mass consumption.

The inlet and exhaust gas temperatures upstream of the intake and exhaust surge tanks and temperatures in various locations of the auxiliary systems were measured with standard K-type thermocouples. Intake manifold air temperature was measured with an Omega RTD (PT100) probe. An RTD probe instead of the standard K-type thermocouple was used for the measurement of intake manifold temperature as it is a critical parameter for combustion. Inlet and exhaust pressures were measured with PXM219-006GI Omega pressure transducers upstream and downstream of the intake and exhaust surge tanks respectively.

The crank angle was measured at 0.5 ^{o}CA intervals by an AVL 365C optical crank angle encoder mounted directly on the engine crank shaft. It generated an index pulse and 720 square waves (once every 0.5 ^{o}CA) for every crankshaft revolution. Note that this crankshaft encoder could generate 3600 square waves (once every 0.1 ^{o}CA) for every crankshaft revolution. This angle encoder was indexed to the engine TDC. Note that the TDC location was determined by determining the crank angle corresponding to the peak cylinder pressure during motoring. However, the thermodynamic offset due to heat transfer losses was not considered. The effect of thermodynamic offset due to heat transfer losses is expected to be less than 0.5 ^{o}CA.

The intake manifold pressure was measured at a high frequency of 0.5 ^{o}CA interval with a Kistler 4045A5 0-500 kPa piezo-resistive absolute pressure transducer. The signal from the transducer was amplified and converted to a measurable voltage by a Kistler 4618A2 piezo-resistive amplifier. In-cylinder pressure was also measured at a high frequency of 0.5 ^{o}CA interval with a flush mounted water-cooled AVL QC34C quartz piezo-capacitive pressure transducer. The signal from this transducer was amplified and converted into a measurable voltage by a Kistler 5007 charge amplifier which filtered the signals at a frequency of 200 kHz. Pressure in the fuel rail was measured with an AVL SL31D-2000 strain gauge pressure transducer at 0.5 ^{o}CA interval. An AVL 3009A04 amplifier was used to amplify the signals at a frequency of 100 kHz.

An injector drive current transducer developed in-house measured the commanded current input signal to the injector, thereby indicating the injector opening and closing points. An instrumented injector was also available, but was not used in this work. A comparison between the needle lift signal and the commanded drive current signal showed that there was a 1.5 ^{o}CA delay for the actual needle lift compared to the commanded injector drive current.

All the above data were acquired through an existing NI cDAQ 9172 and a USB6125 system. Two data acquisition routines were written in LabVIEW™ version 8.5: one for the high speed data acquisition of 200 consecutive cycles and the other for low-speed data acquisition at a frequency of

1 Hz [Cong, 2011]. NI cDAQ 9172 consisted of 7 modules: one each of NI 9215, NI 9205, NI 9217, NI 9203, NI 9401 and two NI 9211. The NI 9215 module was used for high speed data acquisition of cylinder pressure, intake manifold pressure, fuel rail pressure and injector drive current at 0.5 ^{o}CA interval. The index pulse and the 0.5 ^{o}CA resolution square pulses were imported to the digital I/O module (NI 9401) as trigger and clock for the high speed data acquisition. Two NI 9211 modules were dedicated for thermocouples, while the NI 9205 module (±10 V analogue input) acquired fuel flow rate, exhaust pressure and supercharger inlet air flow rate. The NI 9217 module acquired intake temperature; the NI 9203 module (±20 mA analogue input) acquired inlet pressure and air flow rate all at a frequency of 1 Hz. Data from emission analysers (Horiba Mexa 7100HEGR and AVL 415) were also acquired through the NI 9203 module.

3.3.2 Emission Measurements

Exhaust samples for emission measurements were drawn downstream of the surge tank, as shown in Fig. 3.2. Although sampling downstream of the surge tank would result in some 'ageing' of the exhaust gas species, it avoided sample biasing caused by pressure pulsations and inhomogeneity in the exhaust gas stream if sampled immediately downstream of the exhaust port [Cong, 2011]. Emissions measurements were carried out to determine the gaseous emissions of CO, CO_2, THC, NO_X and O_2 concentrations in the exhaust with a Horiba Mexa 7100HEGR emission analyser with undiluted raw exhaust gases. This analyser also measured CO_2 concentration in the intake to determine the EGR level. For determining the EGR level, samples were drawn downstream of the intake surge tank so that the mixture was homogeneous. A Horiba Mexa 485L exhaust gas analyzer (CO: 0-100000 ppm) was used for some operating conditions where the CO emissions exceeded the measurement limit of the Horiba Mexa 7100HEGR analyzer (CO: 0-5000 ppm). The Horiba Mexa 485L is a portable instrument generally used for determining vehicle tailpipe emissions and its accuracy is much lower than the Horiba Mexa 7100HEGR. Raw exhaust gases were fed to a sampling smoke meter (AVL 415) to determine the smoke emissions. Raw exhaust gases were diluted and fed to a Cambustion DMS500 (Model 34) fast particulate spectrometer to determine the particle size distribution for the PM. The emission analysers were calibrated regularly before conducting the experiments. The detailed specifications of the emission analysers are given in Appendix A1. A brief description regarding their principles of operation is given in the following paragraphs.

(a) Horiba Mexa 7100 HEGR analyser

Concentrations of CO, CO_2, THC, NO_X and O_2 in the exhaust were measured with a Horiba Mexa 7100HEGR emission analyser. Intake CO_2 concentration was also measured with this analyser to determine the EGR level. Exhaust samples were drawn through a heated sample line (temperature set to 191^{o}C), 4 mm internal diameter and 6 m length PTFE tube so that NO_2 was not absorbed by

water in the sample. Also, the heated line prevented unburned gases or high boiling point hydrocarbons in the fuel from adhering to the sample pipes. This unit consisted of an internal oil catcher, filter and a heat exchanger to remove oil mist, dust and water from the sample downstream of the hydrogen flame ionization detector (HFID). The dehumidified samples were then fed through the respective gas analysers to determine their concentrations in terms of ppm 'dry' and hence, were converted to 'wet' basis which accounted for the water vapour in the exhaust stream.

Concentrations of CO and CO_2 were measured by an NDIR (non-dispersive infrared) detector. In this method, the sample gases were pumped into a chamber through which infrared light passed. Since water vapour's infra-red absorption overlaps with the absorption bands of CO_2 and CO, the exhaust gas sample needs to be cooled to remove the condensate and then dried before it enters the NDIR instrument. The wavelength of the infrared light is specifically selected depending on the gas component to be detected. The component in the exhaust sample absorbed infra-red light, thereby reducing the light intensity. This intensity was then compared against a reference infrared light source and the resulting difference was expressed as concentration of the specific gas component [Horiba Manual, 2001].

For measuring the concentration of NO_X (consisting of both NO and NO_2), the sample gases were routed through a converter, where NO_X was dissociated into NO when passed through a heated stainless steel tube. NO reacts with ozone to produce nitrogen dioxide in an activated state (NO_2^*) which emits photons as it reverts to its normal state [Horiba Manual, 2001]. The chemiluminescent detection (CLD) method for the detection of NO uses a photomultiplier tube to count the number of photons emitted which are proportional to the concentration of NO. The ozone for this reaction is generated by an electrical discharge in oxygen at low pressure.

The measurement of total hydrocarbon (THC) in the sample gases was accomplished by the HFID, where the sample gases were passed through a hydrogen flame. The hydrocarbons in the sample gases when burned in a hydrogen flame within an electric field produced an ionization current proportional to the total number of carbon atoms present. A collector electrode surrounding the flame measured this change in ionization current. The amount of hydrocarbon in a sample was expressed as ppm-C_1. This is based on the theory that the response of a propane molecule (C_3H_8) is three times that of a molecule with single carbon atom, for example, methane (CH_4) [Horiba Manual, 2001].

A paramagnetic detector (PMD) takes advantage of the magnetic properties of O_2 to measure its concentration in the exhaust sample. The sample gases passed through a nitrogen stream past an alternating magnetic field. The pressure between the two detector plates varied depending on O_2 concentration [Horiba Manual, 2001].

(b) *AVL 415 Smoke meter*

Samples of raw exhaust gases were extracted with a probe through an unheated, non-insulated silicone sampling line downstream of the exhaust back pressure valve and sucked through a filter paper in the AVL 415 variable sampling smoke meter. The blackening of the filter paper, primarily depending on the soot concentration in the exhaust gases, was measured with a reflectometer. The filter blackening when compared to a non-black filter paper gives an indication of soot content in the exhaust gases and is indicated as filter smoke number (FSN) [AVL Smoke meter Manual, 2005]. The FSN is closely related to the elemental carbon, or soot, as long as the emitted particulates contain more than 15% carbon [Hagena *et al.*, 2006]. To obtain soot emissions on a mass per volume basis ($mg.m^{-3}$), the following correlation is recommended [AVL Smoke meter Manual, 2005]:

$$\text{Soot Concentration} = \frac{1}{0.405}.4.95.FSN.e^{0.38.FSN} \qquad (3.1)$$

The smoke meter cannot account for the soluble organic fraction (SOF) in the exhaust species. With high EGR levels (as used in this work), it is expected that a significant amount of SOF would contribute to the total PM mass and hence, the above correlation may no longer be valid. Therefore, none of the smoke measurement data have been corrected to find out PM mass concentration in this work.

(c) Cambustion DMS500 differential mobility spectrometer

The Cambustion differential mobility spectrometer used in this work could determine the number/size spectrum for aerosol particles between 5 and 1000 nm. Exhaust gas was sampled downstream of the exhaust surge tank after the EBP valve and was diluted by compressed air as recommended by the manufacturer.

The fundamental operating principle of the DMS has been described in detail by Reavell *et al.* [2002]. In brief, sample gases are drawn through a conductive rubber sample tube to a classifier column operating at sub-atmospheric pressure via a corona discharge charger. The corona charger uses a single fine tungsten wire as the ion source. The corona discharge produces a large number of positive ions, which collide and charge the incoming particles. A cyclone separator prevents larger particles (>1000 nm) from entering and clogging the instrument. Two simultaneous dilution stages are provided to achieve a total dilution ratio (ratio of total diluted flow to the raw exhaust sample flow) in the range of 1:1 to 2000:1. The charge particles flow within a particle free sheath flow which is a uniform, cylindrical laminar column of air designed to carry the charged particles in a predictable manner. A high voltage central electrode repels and deflects the charged particles towards the electrometer rings. The classifier separates the charged particles according to their electrical mobility (ratio of electrical charge to aerodynamic drag), so that particles with a higher electrical mobility (higher electrical charge and lower aerodynamic drag and hence, lower particle

size/diameter) are deflected more, and gets deposited on an electrometer ring closer to the sample inlet. Electrometers with an amplifier measure the small currents of the order of fA (10^{-15} A) caused by the group of particles getting deposited on the metal rings, which forms the basis of particle detection. The quantity of classified particles in each size range is deduced from the charge flow to a set of electrometers [Reavell *et al*., 2000].

For raw diesel exhaust gas sampling, it is recommended to set the primary and secondary dilution ratio to 4:1 and 100:1-250:1 respectively [DMS500 User Manual, 2010] to achieve a total dilution ratio of approximately 400:1-1000:1. For sampling the particles, the 1st stage dilution ratio was fixed at 4:1, while the 2nd stage dilution ratio was varied (100:1-250:1) to maintain a good signal to noise ratio as recommended by the instrument manufacturer to minimize the cleaning requirement [DMS500 User Manual, 2010]. The 'dilution correction enabled' feature of the instrument was activated so that any minor variations in the total dilution ratios while sampling could be corrected in the DMS software without any further post-processing [DMS500 User Manual, 2010].

The mobility diameter measured by the DMS is a function of both the size and shape of the particle. Due to the condensation/absorption of large amounts of THC and water, the particle structure may collapse and the whole agglomerates may be covered with volatile condensed materials. Thus, the larger particles would almost be spherical despite the collapsed agglomerate core. Hence, the mobility size distribution can be integrated to provide particle volume.

The effective density (ρ_e) is a function of the fractal dimension (d_{fm}) of the agglomerates as given by Park *et al.* [2003]:

$$\rho_e \propto D_b^{d_{fm}^{-3}} \tag{3.2}$$

where D_b is the mobility equivalent diameter. The fractal dimension may have values from 1 to 3; 3 being for spherical particles, resulting in a constant, size independent value of effective density. However, the fractal dimension of agglomerates is less than 3 and therefore, the effective density decreases as particle size increases. The looser the agglomerate structure, the smaller is the fractal dimension. For simple chain agglomerates, the fractal dimension is 1. Primary particle density varies between 1100 kg.m^{-3} and 1200 kg.m^{-3}, for particle size approximately 50 nm [Virtanen *et al*., 2002]. The effective density decreases with increase in the mobility diameter. Due to the above uncertainties, the volume concentrations of the particles measured in this work were not converted to mass concentration.

3.4 Experimental Parameters

Generally, load (torque or mean effective pressure (MEP)) and speed define an engine's operating condition. Torque is a measure of a particular engine's ability to do work and it depends on the engine size. On the other hand, MEP is a more useful relative engine performance measure

which is obtained by dividing the work done per cycle by the engine's displacement volume. Overall equivalence ratio (calculated on the basis of actual fuel-air or fuel-oxygen ratio), intake pressure and temperature, EGR rate, exhaust back pressure, fuel injection timing and injection pressure at a given operating condition influence the performance and emission characteristics of an engine.

The brake work per cycle is given by:

$$\text{Brake work per cycle, } W_b = 2P/N \tag{3.3}$$

where P is the brake power developed by the engine and absorbed by the dynamometer and N is the engine speed (r/s). The brake mean effective pressure (BMEP) is given by:

$$\text{BMEP} = P/(N.V_d/2) \tag{3.4}$$

where V_d is the engine swept volume.

Brake work per cycle obtained at the engine's crank shaft is the work transfer from the combustion gases at the engine's piston minus a portion of it being used to overcome the friction of the bearings, piston and other mechanical components of the engine and to drive the engine accessories (together called frictional work). In the case of a single cylinder engine, high internal frictional work makes brake work substantially lower than an equivalent multi-cylinder engine at a similar operating condition. As a result, BMEP becomes a poor indicator of a single cylinder engine's load and hence, a more independent measure of load is required. To provide a more reliable representation of the engine's load, the net cyclic work done on the engine's piston (indicated work) derived from the engine's in-cylinder pressure traces is used, since it excludes frictional work. The relevant normalized parameter independent of engine size used to define the engine's load is the indicated mean effective pressure (IMEP). The definitions and methods of estimation of some important in-cylinder performance and combustion parameters, deduced from in-cylinder pressure-crank angle data, are described in the following paragraphs.

3.4.1 In-cylinder Conditions

As described earlier, the in-cylinder pressure traces were measured with a piezo-capacitive pressure transducer. Since a piezo-capacitive pressure transducer measures only the change in pressure (relative pressure), these signals need to be corrected to get absolute pressure by referencing them to the intake manifold pressure at BDC, before the start of the compression stroke. In this work, the relative pressures recorded from the in-cylinder pressure transducer were referenced to the intake manifold pressure at 26 ^{o}CA before the intake valve closure (intake valve closed at 20 ^{o}CA after BDC). To reduce the influence of measurement noise, the average pressure over 20 ^{o}CA (from BDC to 20 ^{o}CA after BDC—40 samples) from the intake manifold pressure and in-cylinder pressure measurements were recorded. The in-cylinder pressure was then adjusted to be

the same as the intake manifold pressure over this period ('pegging' of the pressure signal) [Cong, 2011].

Integrating the in-cylinder pressure trace over the compression and expansion strokes and normalizing the results with the engine swept volume gives the gross indicated mean effective pressure (GIMEP) as defined in Heywood [1988]:

$$\text{GIMEP} = \oint_{Comp,Exp} \frac{p.dV}{V_d} \tag{3.5}$$

where p is the in-cylinder pressure at a given crank angle and dV is the change in cylinder volume at the same crank angle. Subtracting the pumping work per cycle (work transfer between the piston and cylinder gases during the intake and exhaust strokes) gives the net indicated work per cycle. However, the net IMEP does not strongly relate to the engine combustion behaviour. Therefore, to provide the most representative comparisons when investigating the combustion characteristics, all IMEP in this work will be based on gross indicated basis, unless otherwise stated specifically.

The maximum rate of pressure rise (dp/dθ), a derivative of pressure traces at each crank angle, indicated acceleration of combustion process and knocking. This parameter is used as a control variable which indicates how early the fuel injection event may be allowed. 1 MPa/ ^{o}CA is generally recognized as a limiting value to avoid engine damage [Schaberg *et al*., 1990].

The mass-averaged bulk gas temperature was computed using the ideal gas law with the measured in-cylinder pressure, the known cylinder volume and the measured mass of air and the recirculated exhaust gases. The molecular mass was calculated from the molecular mass of the constituent recirculated exhaust gases and the fresh air.

The instantaneous apparent net energy release, Q_n, is defined as the difference between the energy released due to combustion of fuel and energy loss due to heat transfer and crevice flows. Q_n, obtained from the average of the recorded in-cylinder pressure-time traces, can be calculated using:

$$\frac{dQ_n}{d\theta} = \frac{\gamma}{\gamma - 1} p \frac{dV}{d\theta} + \frac{1}{\gamma - 1} V \frac{dp}{d\theta} \tag{3.6}$$

where θ is the crank angle and γ is the specific heat ratio (γ = 1.33, assumed constant in this work). The value of γ depends on charge composition and temperature, and does not vary over the compression and power strokes; however, it is generally between 1.26 and 1.35 and frequently assumed to be constant [Heywood, 1988]. In this work, the energy release rate (in units of kJ/^{o}CA) was normalized by the displacement volume of the cylinder (m^3), resulting in the units of kJ/m^3/^{o}CA. This ensured that the energy release rate results were independent of engine size. Note that both the GIMEP and energy release rate were estimated from average cylinder pressure measurements of 200 cycles. Two arguments can be made for averaging many consecutive cycles of pressure data, rather

than trying to obtain meaningful information from a single cycle measurement [Lancaster *et al*., 1975]:

i. the first argument is statistical: the average of a number of cycles of data is a more reliable estimator of the pressure at any crank angle than any individual cycle measurement and the variance of this average diminishes with the number of cycles used to compute it; and
ii. the second argument for averaging concerns comparison of combustion parameters (calculated from the average pressure data) to performance and emission measurements made concurrently in the test cell as the engine itself is an averaging device which responds to mean values of air and fuel flows by generating a mean indicated power.

A time (^{o}CA) marching integration of net energy release rate resulted in the estimation of cumulative energy release. Integrating the net energy release up to a certain crank angle and normalizing it by the cumulative energy release provided the fraction of energy release up to that point. Typical points of interest in this work included the phasing of the 5%, 50%, 90% and 95% values of the cumulative energy release (designated CA5, CA50, CA90 and CA95, respectively). The start of combustion (SOC) was identified as being the start of the main energy release and did not include the 'cool-flame' or 'pilot fuel' pre-combustion reactions. The crank angle at which the instantaneous energy release rate became positive was identified as the SOC [Stone, 1999]. It should be noted that this is not the true SOC, but is a repeatable representative measure. Ignition delay for the single injection case was the time interval (in ^{o}CA) between the commanded start of fuel injection timing (main) and SOC. Premixing time for the split injection cases was defined as the difference in time (in ^{o}CA) between the start of injection for the first injected fuel mass (SOI1) and the SOC. The combustion duration was defined as the time interval between CA5 and CA95. In this work, CA50 was used as the variable to represent the combustion phasing. Note that CA50 is generally a reliable and distinct representation of combustion timing and is independent of the ignition delay variability. Hence, it is used as an effective parameter for online engine tuning [Klimstra, 1985].

The coefficient of variation (COV) of GIMEP is a useful indicator of cyclic variability in gross indicated work per cycle; the COV of GIMEP is calculated as a ratio of standard deviation to the mean of the GIMEP.

3.4.2 EGR Fraction

In this work, recirculated exhaust gas fraction (by volume or mole) was controlled by changing the EGR valve and the exhaust back pressure valve positions as described earlier in Sec. 3.2.3. It was calculated by measuring the intake, exhaust and ambient CO_2 concentrations as:

$$\%\text{EGR} = \frac{[CO_2]_{int} - [CO_2]_{amb}}{[CO_2]_{exh} - [CO_2]_{amb}} \times 100 \quad (3.7)$$

where the subscripts int, exh and amb refer to intake, exhaust and ambient respectively. Ambient CO_2 concentration is fixed at 0.038% by volume. Consideration of the trapped residual gases from the previous cycle would contribute to an increase in the effective EGR fraction. This in turn would increase the charge temperature, thus influencing the combustion and emission characteristics of a diesel engine operating under conventional diesel and LTC modes to a varying degree as reported by Cong *et al.* [2009a]. Exhaust back pressure affects the residual gas fraction (RGF) and a maximum RGF up to 10% was observed in this AVL single cylinder research engine with a large positive pressure differential (200 kPa) between the exhaust and intake measured through a skip-firing technique [Cong *et al.*, 2009a]. In this work, the calculation of EGR fraction did not include RGF as a relatively small pressure differential (<20 kPa) was maintained between the intake and the exhaust; therefore, the RGF would have only a small contribution.

3.4.3 Fuel-Oxygen Ratio

In a diesel engine, load is varied by changing the amount of fuel injected per cycle. Hence, an insight into overall mixture stoichiometry is essential, although the overall fuel-air ratio is always lean in a conventional diesel engine. Due to the overall lean operation of diesel engines, exhaust gases contain varying amounts of oxygen depending on load and equivalence ratio. When the intake air is diluted with recirculated exhaust gases, intake oxygen concentration varies and hence the actual fuel-oxygen ratio. This is not included in the definition represented by fuel-air equivalence ratio. Therefore, an equivalence ratio based on in-cylinder mass of oxygen ($\emptyset_{O2}$), rather than air provides a better representation of overall fuel-oxygen ratio and is calculated as:

$$\emptyset_{O2} = \frac{[m_f/m_{O2}]_{actual}}{[m_f/m_{O2}]_{stoichiometric}} \quad (3.8)$$

where *m* indicates mass per cycle; the subscripts '*f*' denote fuel and other subscripts have their usual meanings. Similarly, for a diesel engine where the exhaust gas contains significant quantities of oxygen; the EGR fraction does not give a valid representation of the level of dilution of the intake charge. In this case, intake oxygen mass fraction (Y_{O2}) is more representative of the intake charge dilution than is the EGR rate. Y_{O2} is defined as [McTaggart-Cowan *et al.*, 2004]:

$$Y_{O2} = \frac{Y_{O2[a]}\dot{m}_a + Y_{O2[exh]}\dot{m}_{EGR}}{\dot{m}_a + \dot{m}_{EGR}} \quad (3.9)$$

$$m_{charge} = (\dot{m}_a + \dot{m}_{EGR})\, 2/N \quad (3.10)$$

$$m_{O2} = Y_{O2} m_{charge} \quad (3.11)$$

where $Y_{O2[a]}$ is the oxygen mass fraction in fresh air (fixed at 23%); $Y_{O2[exh]}$ is oxygen mass fraction in the exhaust; $\dot{m}_a$ is fresh air mass flow rate; $\dot{m}_{EGR}$ is EGR mass flow rate; m_{charge} is the net charge mass per cycle (combined mass of fresh air and exhaust gases inducted into the cylinder neglecting residuals); m_{O2} is the oxygen charge mass per cycle.

3.4.4 Thermal Efficiency

Gross indicated specific fuel consumption (GISFC) is a measure of fuel conversion efficiency which neglects both frictional and pumping losses. It can be calculated as:

$$\text{GISFC} = \frac{\dot{m}_f}{P_{gross}} \times 3600 \tag{3.12}$$

$$P_{gross} = \text{GIMEP}.V_d.N/2 \tag{3.13}$$

where $\dot{m}_f$ is the mass flow rate of fuel and P_{gross} is the gross indicated power.

Combustion efficiency (η_c) is defined as the fraction of the fuel energy which is released in the combustion process and is calculated as [Heywood, 1988]:

$$\eta_c = 1 - \frac{\sum_i x_i Q_{iL}}{[\dot{m}_f/(\dot{m}_f+\dot{m}_a)]Q_{fL}} \tag{3.14}$$

where x_i are the mass fractions of CO, THC, hydrogen (H_2) and particulates. Q_{iL} and Q_{fL} are the lower heating values of these species and fuel respectively. The lower heating values of CO, THC (assumed to be the same as the fuel) and fuel are 10.1 MJ/kg, 42.5 MJ/kg and 42.5 MJ/kg respectively [Heywood, 1988]. The subscripts '*f*' and '*a*' denote fuel and air respectively. Note that in this work, the mass fractions of H_2 and particulates were not taken into account for the estimation of combustion efficiency because H_2 was not measured and PM was negligible.

3.4.5 Emissions

Levels of emissions of NO_X, CO and THC were measured either in ppm or by percentage volume. These values need to be expressed either in terms of mass based specific emissions (g/kWh) or emission index (g/kg of fuel). In this work, these gaseous emissions are reported by their emission index (*EI*), for example:

$$EI_{NO_x} = \frac{\dot{m}_{NO_x}}{\dot{m}_f} \tag{3.15}$$

where EI_{NO_X} (g of NO_X/kg of fuel) is the emission index of NO_X and $\dot{m}_{NO_X}$ is the mass flow rate of NO_X (g/h, normalized against total exhaust flow rate). Mass flow rates of NO_X, CO and THC are given by:

$$\dot{m}_{NO_X} = \frac{\dot{m}_{exh}}{MW_{exh}} . 1000. \frac{NO_X}{10^6} . MW_{NO_X} \tag{3.16}$$

$$\dot{m}_{CO} = \frac{\dot{m}_{exh}}{MW_{exh}} . 1000. \frac{CO}{10^6} . MW_{CO} \tag{3.17}$$

$$\dot{m}_{THC} = \frac{\dot{m}_{exh}}{MW_{exh}} . 1000. \frac{THC}{10^6} . MW_{THC} \tag{3.18}$$

$$\dot{m}_{exh} = \left(\dot{m}_a + \dot{m}_f\right) \tag{3.19}$$

where MW_{exh} is the molecular mass of exhaust calculated as the mole fraction average of the component molecular masses; MW_{NO_X}, MW_{CO} and MW_{THC} are the molecular masses of NO_2, CO, and CH_4 respectively. Note that the molecular mass of NO_2 was taken for normalizing NO_X emissions as per the emission legislation guidelines [Stone, 1999] and the molecular mass of CH_4 was taken for normalizing THC emissions as the output from the emission analyzer was in terms of 'ppm—C_1' [Horiba Manual, 2001]. PM emission was not normalized due to the uncertainties of the various mass conversion correlations at high EGR levels as discussed earlier in Sec. 3.3.2.

3.5 Uncertainties of Experimental Parameters

A level of uncertainty in the results exists with any experimental work, irrespective of the sophistication of the instruments used for measurement. Experimental errors mainly fall into two categories, namely systematic and random errors. Systematic errors are repeatable in nature and so it would be easy to account for them. By regular calibration of instruments, these errors can be minimized. However, random errors are stochastic in nature and it is not possible to account for them during measurement and hence, a statistical estimate of the uncertainty is mandatory.

To quantify the magnitude of uncertainties in the measurements, random error estimation is made based on the Gaussian distribution method with a confidence limit of 95% (±1.96 times the standard deviation) [Holman, 2001]. In this work, in some cases, where sufficient repeated data were available at the same operating condition, Gaussian distribution with a 95% confidence limit was used to estimate the uncertainties. In other cases, where it was cumbersome to obtain repeated data, the uncertainties of the output parameters were estimated based on the reported uncertainties of the measuring instruments (fixed errors). The detailed procedure for uncertainty analysis is given in Appendix A3 and the maximum uncertainty values for some parameters are presented in Table 3.4. For all the reported uncertainty values, the contributing sources have also been identified.

Table 3.4: Estimated Uncertainties for Key Parameters

Parameters	Uncertainty (%)	Contributing Sources
GISFC (g/kWh)	2.8	Gross power, fuel flow rate
Smoke (FSN)	3.5	Smoke meter
EI_{CO} (g/kg of fuel)	3.5	CO analyser, air flow rate, fuel flow rate
EI_{NOx} (g/kg of fuel)	9.1	NO_X analyser, air flow rate, fuel flow rate
EI_{THC} (g/kg of fuel)	9.1	THC analyser, air flow rate, fuel flow rate

3.6 Optically Accessed Engine

The optically accessed engine used in this work was essentially the same single cylinder AVL engine as described in Sec. 3.2.1 with a modified cylinder head and piston to allow insertion of a borescope. This enabled optical observation of a portion of the combustion chamber with minimum intrusion into the combustion chamber and therefore, had minimal effect on the engine's performance. Although more complete access is possible with other techniques, these tend to result in comprehensive mechanical modifications to the engine which can cause interference with the spray and combustion processes; a small diameter borescope based imaging system can provide optical access with minimal engine modifications [Werlberger and Cartellieri, 1987; Winklhofer, 2001; Alam *et al*., 2006]. In the borescopic in-cylinder visualization system, a borescope can be fitted into the engine through a hole of pressure transducer size.

Optical access into the combustion chamber was made possible through optical windows in the cylinder head and a borescope. All the design features and mechanical strength (peak cylinder pressure and peak cylinder temperature) of the original engine were retained in the optical engine with only minor mechanical modifications (except one exhaust valve). These details are described in the following paragraphs.

3.6.1 Modifications to the Engine for Optical Access

The new cylinder head was machined to adopt two outer hollow steel insert sleeves, inside which either, an inner pressure sleeve or, a light guide could be installed and secured with locking nuts. Two AVL fused silica optical windows (BO2737 and BO2738) with 0^o and 30^o direction of views respectively were used in this research. For in-cylinder visualization, one of the optical windows was attached to the end of an installation tube which was threaded to the end of the inner sleeve into which a standard borescope was fitted to ensure that the cylinder was pressure tight. A similar optical light guide arrangement was provided to allow light access. This is shown schematically in Fig. 3.4. Window fouling due to soot contamination decreases the amount of light transmitted and limits the test duration in a firing engine condition [Bakenhus and Reitz, 1999; Pastor *et al*., 2000]. These transfer units and the optical windows, however, could be easily removed from the cylinder head by removing the locking nuts from the end of the outer insert sleeves, without

the need to dismantle the cylinder head or the overhead cam shaft. The modified cylinder head and the piston are shown in Fig. 3.5. Note that fused silica is transparent in the spectral range of 300-3800 nm [Stirling and Ho, 1961].

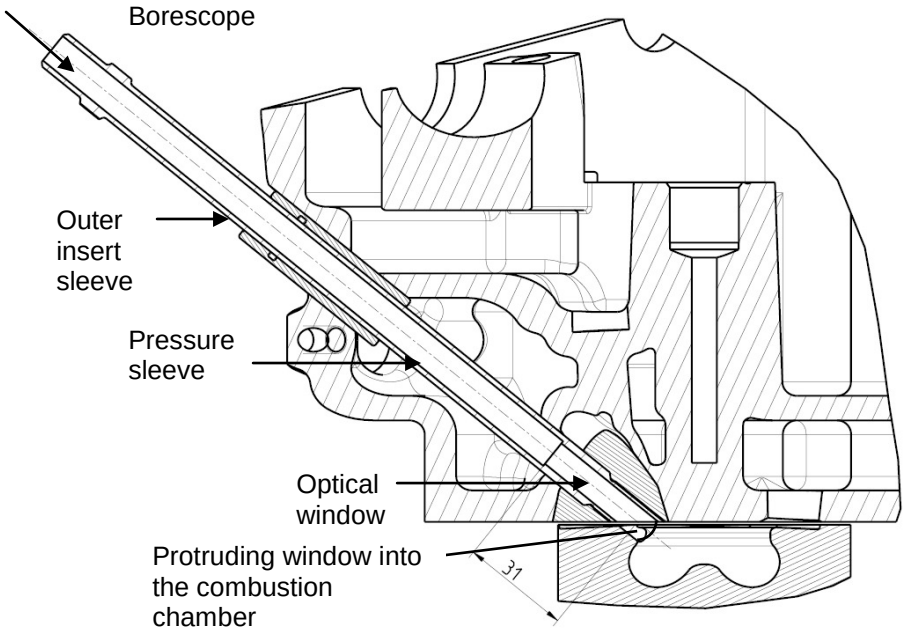

Fig. 3.4: Schematic of the modified cylinder head and piston for optical access [AVL Report, 2009]

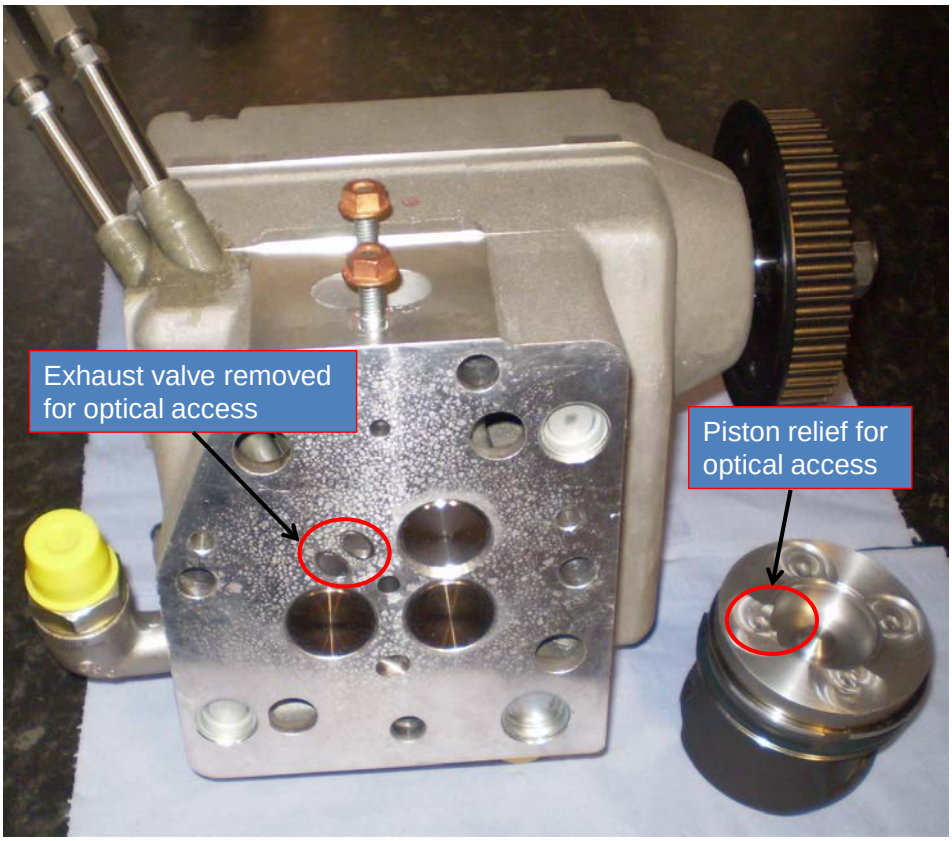

Fig. 3.5: Modified cylinder head and piston for optical access

To enable borescopic access to the combustion chamber, one of the original two exhaust valves was removed and deactivated. The optical window and the light guide tip protruded slightly into the combustion chamber and so the piston lip was machined to provide relief for the borescope and light guide. The protruding optical window, however, did not alter the combustion chamber shape thereby preventing interference with any in-cylinder fluid dynamic or combustion phenomena. Dummy plugs were installed in the outer sleeves when the borescope and light guide were not in use, so that the optical engine was the same as the original engine minus one exhaust valve.

3.6.2 Effects of Removing One Exhaust Valve

It is expected that the removal of one of the exhaust valves may have some effect on engine performance due to the increased exhaust back pressure (due to decreased valve flow area). Therefore, a validation test was conducted at a fixed operating condition to establish the performance of the modified engine with one exhaust valve. The *p-V* diagram of the two engines plotted in a log-log scale is shown in Fig. 3.6 at a constant operating condition corresponding to 2500 rpm engine speed and 16 mg/cycle fuel quantity at 180 kPa intake pressure. No EGR was used in this test and CA50 was maintained constant (10 ^{o}CA ATDC) for both the cases.

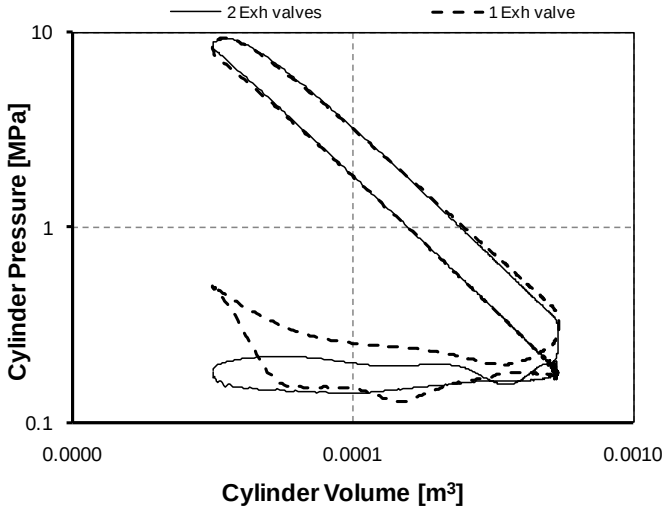

Fig. 3.6: Comparison of in-cylinder performance of the two engines at a fixed operating condition plotted on a log-log scale [2500 rpm engine speed, 16 mg/cycle fuel quantity, 180 kPa intake pressure, 80^{o}C intake temperature and 0% EGR]

From Fig. 3.6, it can be seen that there is a negligible difference between the area under the curve during the compression and expansion strokes (gross indicated work done per cycle); therefore, GIMEP would not be affected in the two engines. However, it is interesting to note that the exhaust back pressure at the beginning of the intake stroke was higher with one exhaust valve engine. The area under the curve during the gas exchange process (pumping work per cycle) with

one exhaust valve was significantly higher than the engine with two exhaust valves as shown in the figure. As mentioned earlier in this chapter, as GIMEP was considered as the indicator of in-cylinder performance of the engine in this work, it is not affected by the increased exhaust back pressure and pumping work.

Higher exhaust back pressure had been shown to affect RGF [Senecal *et al.* 1996; Cong *et al.*, 2009a] because of the back flow of the burned gases from the exhaust port to the cylinder and from the cylinder to the intake during the valve overlap period. During the early stage of the valve overlap period, the cylinder pressure is generally higher than both the intake and exhaust pressures. Hence, there is a backflow from the cylinder to the intake manifold, as well as from the cylinder to the exhaust. When the intake valves open, cylinder pressure drops until it is lower than the exhaust pressure whereupon backflow from the exhaust to the cylinder occurs until the exhaust valve closes. The combustion products that flow back to the intake manifold are re-inducted, later in the intake stroke, and contribute to an increase in RGF. The trapped gas in the cylinder due to the dead volume at TDC also affects RGF. For a given engine geometry (swept volume, valve seat diameters and valve lifts) and valve timings (valve overlap period), RGF is affected by the intake and exhaust pressure, burned gas density and engine speed.

A one-dimensional Ricardo WAVE model for this engine was built and validated to determine the RGF with different engine back pressures at different operating conditions [Cong *et al.*, 2009a; Cong, 2011]. This model was used in this work for both the engines (with one and two exhaust valves) to predict the RGF at different intake pressures. The simulation was conducted at a fixed engine speed of 2500 rpm and a fuel quantity of 16 mg/cycle without any EGR. The exhaust pressure was maintained 20 kPa above the intake. The predicted RGF for both these engines from this simulation are listed in Table 3. 5. It can be seen that the RGF increased by only ~1% for the engine with one exhaust valve and this contribution was considered insignificant to the in-cylinder performance and combustion of the engine.

Table 3.5: Predicted RGF Values at Different Intake Pressures

Intake pressure (kPa)	**Intake temperature (K)**	**Predicted RGF (%) with 1 exhaust valve**	**Predicted RGF (%) with 2 exhaust valves**
120	358	4.34	4.05
150	354	4.34	3.61
180	353	4.37	3.32
200	352	4.18	3.32

3.6.3 Optical Instrumentation for Spray and Flame Imaging

Borescope, light source and camera were the core components for in-cylinder visualization in this work. A Karl-Storz rigid borescope (3.8 mm outer diameter with a working length of 300 mm with Hopkins rod lenses) was used to visualize the spray and combustion events. A Prosilica

GC1380 monochrome CCD camera with a 2 Mega-Pixels (1600×1200) Pentax Machine-Vision lens (focal length of 25 mm and an F number of 1.4) was connected directly to the borescope via a quick snap connector with a C mount. Note that 'F number' is a measure of the light gathering ability of a lens and is determined by dividing the focal length of the lens by its clear aperture or diameter. A PerkinElmer CX1200 stroboscope (xenon flash lamp) through a Karl-Storz 81599V fibre-optic light guide and a light guide tip illuminated the combustion chamber for imaging the spray. A Gigabit Ethernet interface cable communicated between the camera and the PC. The salient features of the borescope, camera and stroboscope are listed in Table 3.6. The details are described briefly in the following paragraphs.

Table 3.6: Specifications of Components for Optical Instrumentation and Imaging

Borescope	Camera	Stroboscope
Make/Model: Karl-Storz/ 84583A and 84583B; Material: Anti-reflection (AR) coated borosilicate (BK7) glass; Field of view (FOV): 67^o; Direction of view: 0^o and 30^o; Depth of field: 1 mm to infinity	Make/Model: Prosilica/GC1380; Imaging device: 2/3" Sony ICX285AL; Cell size: 6.45 × 6.45 μm; Material: AR coated BK7 glass; Maximum resolution: 1360 × 1024 pixels; Camera speed at maximum resolution: 20 frames per second (fps); Shutter speed: 10 μs-60 s; Gain control: 0-33 dB; Maximum quantum efficiency: 70%	Make/Model: PerkinElmer/ CX1200; Maximum flash rate: 45 Hz; Flash duration: 8-10 μs

(a) Borescope

In this work, two Karl-Storz rigid borescopes with the specifications outlined in Table 4.6 were used to view different regions in the combustion chamber. These borescopes were equipped with cooling channels which were supplied with filtered compressed air to prevent overheating of the internal optics (limited to 150^oC). The working principle and construction of the borescope are described in Appendix A3. The lenses of these borescopes are made of BK7 glass. Note that BK7 glass is transparent in the 300-2700 nm region [Stirling and Ho, 1961].

In order to find out the effective spectrum of the borescope (84583A with 0^o direction of view), its spectral transmittance was obtained with an Avantes Avaspec USB2000 Spectrophotometer. The results are shown in Fig. 3.7. Note that the photon counts at each wavelength were normalized by the maximum photon counts for the reference light source (a cold white light source optimized in the visible range). The other borescope with 30^o direction of view

was assumed to behave similarly. Note that the laboratory experimental result presented in Fig. 3.7 was not intended to be an evaluation of the borescope as such but to have some idea regarding its potential for the present optical assessment requirements.

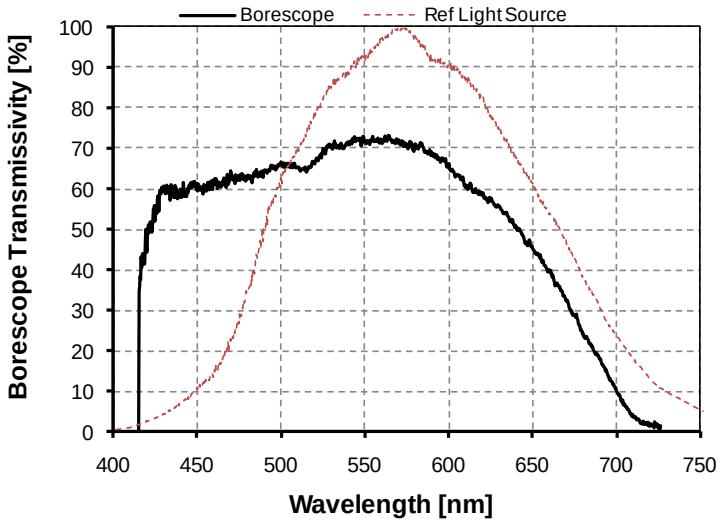

Fig. 3.7: Spectral transmissivity of the borescope

As can be seen from the figure, the transmissivity of the borescope is in the range of 50-70% between 420 to 650 nm and decreases rapidly for wavelengths shorter than 420 nm and longer than 700 nm. The sharp decrease of transmissivity of the borescope below 420 nm was due to the limited spectral range of the reference light source used in this validation as shown in the figure. The decrease in transmissivity above 650 nm was due to the properties of the AR coating materials used in the borescope. Large numbers of AR-coated surfaces in the borescope rapidly reduced its transmissivity outside the visible spectrum. This may significantly limit the detection of auto-ignition phenomenon using hydroxyl (OH) and formaldehyde (CH_2O) as tracers which have their maximum intensity of radiation at 310 nm and 398 nm respectively [Kamimoto and Kosaka, 2000].

(b) Camera

The Prosilica GC1380 digital monochrome, 1.4 Mega-pixels camera used in this work had a maximum frame rate of 20 frames per second (fps) with an option to increase the frame rate to 37 fps with binning techniques, where adjacent pixels were combined (640×480 pixels resolution). The camera had a peak quantum efficiency (ratio of number of electron-hole pairs generated per number of photons hitting the surface of a photo detector) of 70%. The high quantum efficiency was considered to be suitable for detecting low light level in the low temperature combustion regimes, which are hypothesized to be more premixed and hence, less luminous. The lenses in the camera were also made of BK7 glass with a spectral range of 400-1000 nm. A good signal to noise ratio (66 dB) with a 12 bit analog to digital (A/D) conversion rate provided higher sensitivity for the camera

with lower noise. However, due to the lower speed of the camera, only one image could be captured per cycle. To have crank angle resolved images, images were captured from subsequent cycles with a certain crank angle increment. Therefore, cycle-by-cycle variation in the engine plays an important role in the sequence of images obtained.

(c) Light source

A PerkinElmer CX1200 stroboscope was used to illuminate the combustion chamber for imaging the non-luminous spray injection events. The xenon flash lamp in the strobe produced intense pulses of radiant energy covering the UV, visible and near infra-red (NIR) spectrums. The strobe had a radiometric light output of 145 mJ with a variable input energy per flash (1-2.2 J). The illumination angle of the light guide tips used in this work were variable (0^o and 30^o) and were selected depending on the angle of view of the borescope used.

3.6.4 Image Acquisition

The camera was externally triggered with a 0-5 V TTL (transistor-transistor-logic) pulse from the NI USB6210 data acquisition system based on the input engine crank angle encoder signals (both TDC and CDM (crank degree marker)). The strobe was triggered and synchronized by the camera. The arrangement for the borescope, strobe, camera and the details of the triggering and image acquisition are shown schematically in Fig. 3.8. All the triggering routines were written in LabVIEW version 8.5. Norpix software was used to control the shutter speed, region of interest, gain, exposure time, frame rates of the camera and to adjust the flash duration of the strobe and the delay between the camera and the strobe.

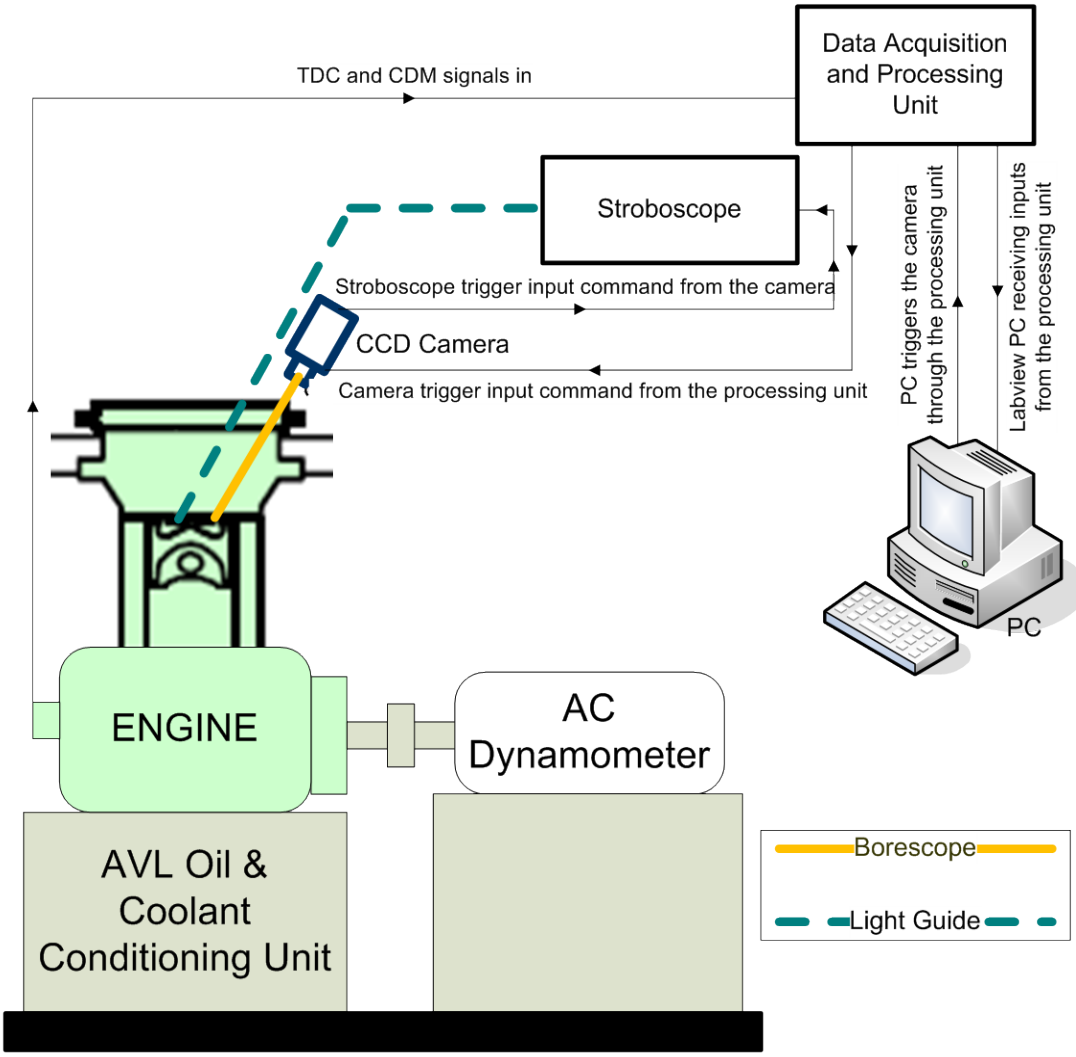

Fig. 3.8: Schematic of the camera, strobe, borescope and image acquisition

3.7 Two-Colour Optical Pyrometry

Two-colour pyrometry is a radiation thermometry technique. It is thus well suited for combustion studies in conventional diesel combustion systems, as the flame radiation emission during most of the energy release period is dominated by soot incandescence. This method makes it possible to obtain a qualitative description of the soot distribution within the flame, with the added value of the temperature information; and hence, is used widely by the diesel engine community [Arcoumanis *et al*., 1995; Shiozaki *et al*., 1996; Vattulainen *et al*., 2000; Han *et al*., 2008 and several others] due to its simplicity, low cost and ease of application. Since the temperature difference between the soot particles and the surrounding gases is negligible (<1 K) for diesel flame conditions, the measured soot temperature provides a very close estimate of the true flame temperature [Matsui *et al*., 1979]. It is to be noted that the ambient gas and the soot particles attain equilibrium in about 10^{-50} to 10^{-6} s within the cylinder [Zhao and Ladommatos, 1998]. Two-colour pyrometry has been implemented to measure maximum flame temperature in a diesel engine up to 2700 K [Vattulainen

et al., 2000]. Since temperatures below 1800 K are of little interest in studies of conventional diesel flames, the typical two-colour systems are optimized for a temperature range of 1800-2800 K.

Despite the widespread use of two-colour pyrometry techniques, the measurement of flame temperature in low temperature diesel combustion engines is not widely reported in the literature. Only a few studies are known to the author [Singh *et al*., 2005; Musculus *et al*., 2008; Diez and Zhao, 2010], with reported temperatures down up to 1650 K using two-colour pyrometry. Bobba *et al.* [2010] measured the flame temperature in a low temperature combustion regime in a heavy-duty diesel engine at low intake oxygen concentrations (12.7%, corresponding to 55% EGR levels) and reported a minimum quantifiable temperature limit at 1500 K. Note that the reported smoke emissions in the work of Bobba *et al.* were still relatively high (FSN >2). Recent research has shown that the use of higher levels of EGR (>60% by volume) in high-EGR LTC strategies effectively eliminates in-cylinder soot formation leading to smoke emissions comparable to conventional diesel operation (FSN <1) with ultra-low NO_X emissions [Cong, 2011]. Therefore, a two-colour pyrometry system was designed and implemented in this work to measure flame temperature in low-temperature and low soot combustion regimes.

3.7.1 Description of Two-Colour Pyrometry

In the two-colour method, the radiation emitted by a cloud of incandescent soot particles is split into two beams and the instantaneous signals are measured at two different wavelengths. Soot temperature and soot loading (*KL* factor) are then estimated from the measured radiation intensities. The two-colour method measures the flame temperature and soot concentration in a small control volume and therefore, is essentially a line-of-sight measurement. In diesel engine combustion study, the two-dimensional temperature and soot distribution can also be obtained using an imaging device (camera) as a detector in the two-colour system. The theory and implementation aspects of the two-colour method have been reported by several authors [Zhao and Ladommatos, 1998; Vattulainen *et al*., 2000; Payri *et al*., 2007] and are only discussed here briefly.

From Planck's radiation law, the monochromatic black body radiance (a function of temperature, T and wavelength, λ) may be expressed as

$$I_b(\lambda, T) = \frac{c_1 \lambda^{-5}}{(e^{c_2/\lambda T} - 1)} \tag{3.20}$$

where c_1 and c_2 are constants; $c_1 = 1.1910439 \times 10^{-16}$ W.m^2. sr^{-1} and $c_2 = 1.4388 \times 10^{-2}$ m.K.

The monochromatic emissivity (ε) is defined as

$$\varepsilon(\lambda) = \frac{I_g(\lambda,T)}{I_b(\lambda,T)} \tag{3.21}$$

where $I_g(\lambda, T)$ and $I_b(\lambda, T)$ are the monochromatic radiance of an actual surface and a black body respectively at the same temperature.

The monochromatic emissivity (ε) is estimated for soot particles using the empirical correlation of Hottel and Broughton [1932], and expressed as

$$\varepsilon(\lambda, f_v, L) = 1 - e^{(-k_{soot}L/\lambda^{\alpha})} \tag{3.22}$$

where k_{soot} is the soot absorption coefficient, a variable proportional to the soot volume fraction (f_v). α depends on the physical and optical properties of the soot in the flame. It is reported that the morphology, particle numbers, particle diameters and hydrogen to carbon ratio of soot would influence the spectral emissivity [Stasio and Massoli, 1994; Kamimoto and Murayama, 2011]. However, it is unknown how soot composition at different engine operating conditions would alter the value of α. Therefore, a constant value of α was used in this work. The optical path length (L) is the longest distance from which radiation reaches the optical sensor and is proportional to the flame thickness. Due to the exponential relationship between emissivity and optical path length, a linear relationship is not always possible between the optical and geometrical length and hence, the emissivity within the optical path is usually expressed in terms of the product $KL = k_{soot}L$ [Payri *et al*., 2007].

The explicit dependence of radiance on temperature, soot and wavelength can be expressed as

$$I_{soot}(\lambda, T, KL) = \left[1 - e^{(-KL/\lambda^{\alpha})}\right] \left[\frac{c_1 \lambda^{-5}}{(e^{c_2/\lambda T} - 1)}\right] \tag{3.23}$$

There are two unknowns in Equation (3.23): T and KL. However, both of these should be insensitive to the wavelength being measured. As a result, by measuring at two distinct wavelengths, the above equation can be solved for either T or KL.

In the two-colour method, an apparent temperature T_a, (also known as brightness temperature) is introduced, defined as the temperature of a black body that will emit the same radiation intensity as a non-black body at temperature T and expressed as:

$$I_b(\lambda, T_a) = I_g(\lambda, T) \tag{3.24}$$

Substituting Equation (3.23) into Equation (3.21), the monochromatic emissivity can be written as:

$$\varepsilon(\lambda) = \frac{I_b(\lambda, T_a)}{I_b(\lambda, T)} \tag{3.25}$$

$$\varepsilon(\lambda) = \frac{(e^{c_2/\lambda T} - 1)}{(e^{c_2/\lambda T_a} - 1)} \tag{3.26}$$

Equating Equations (3.22) and (3.26), the monochromatic emissivity of soot can be expressed as:

$$\varepsilon(\lambda) = \frac{\left(e^{c_2/\lambda T} - 1\right)}{\left(e^{c_2/\lambda T_a} - 1\right)} = 1 - e^{(-KL/\lambda^{\alpha})} \tag{3.27}$$

Taking logarithms of both the sides of Equation (3.27) and rearranging the expression, *KL* can be derived as:

$$KL = -\lambda^{\alpha} \ln\left[1 - \left(\frac{e^{c_2/\lambda T} - 1}{e^{c_2/\lambda T_a} - 1}\right)\right] \tag{3.28}$$

For the flame temperature *T*, *KL* can be eliminated by rewriting Equation (3.28) for two specific wavelengths, λ_1 and λ_2 as:

$$\left[1 - \left(\frac{e^{(c_2/\lambda_1 T)} - 1}{e^{(c_2/\lambda_1 T_{a1})} - 1}\right)\right]^{\lambda_1^{\alpha 1}} = \left[1 - \left(\frac{e^{(c_2/\lambda_2 T)} - 1}{e^{(c_2/\lambda_2 T_{a2})} - 1}\right)\right]^{\lambda_2^{\alpha 2}} \tag{3.29}$$

Equation (3.29) can then be solved for *T* when the two apparent temperatures, T_{a1} and T_{a2} are known for the two wavelengths λ_1 and λ_2. These two apparent temperatures are determined by calibrating the two-colour pyrometer at selected wavelengths using a black body light source at known temperatures.

3.7.2 Selection of Wavelengths

Different combinations of wavelengths varying from 400-1200 nm have been used for measuring flame temperatures in diesel engines using two-colour pyrometry. Fig. 3.9 shows the emissive power of soot, estimated at four different temperatures for a constant *KL* factor (*KL*=1). The selected temperature range (1250-2000 K) covers the expected flame temperature from LTC to conventional diesel combustion regimes. In order to select two suitable wavelengths for the two-colour pyrometry, the emissive power of soot was estimated using Equation (3.23) and plotted on a logarithmic scale from the visible to NIR spectrum as a function of flame temperature as shown in Fig. 3.9. It can be seen from the figure that the soot emissive power reduces significantly in the visible spectrum for lower soot temperatures, and the peak intensity shifts towards NIR spectrum. In low-soot LTC regimes, it is expected that both the flame temperature and *KL* factor will be low, suggesting that wavelength pairs for two-colour pyrometry in LTC applications should be selected in the NIR spectrum. However, there are other factors that influence the final choice of a wavelength pairing.

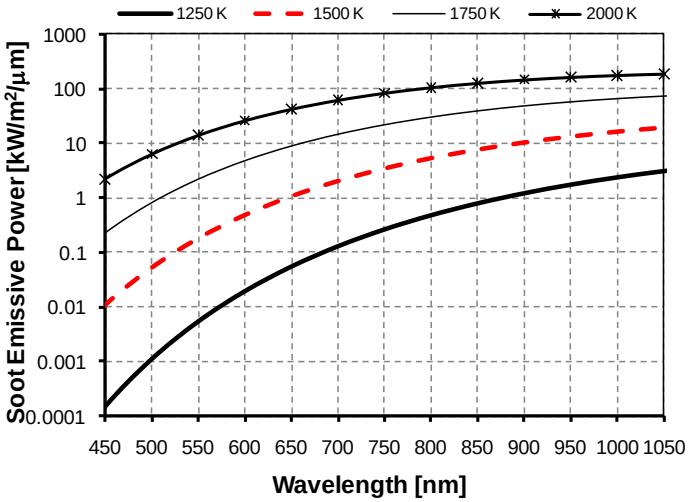

Fig. 3.9: Spectral emissive power of soot at different temperatures for a fixed soot loading (*KL*=1)

The wavelength pairs of two-colour pyrometers applied in conventional diesel combustion studies are typically selected such that either both wavelengths are in the visible spectrum or one is from the visible spectrum and the other from the infra-red. However, the results presented in Fig. 3.7 show the transmissivity of the borescope to be less than 10% above 700 nm. Thus, the potential gain in signal strength that would accrue from the higher emissive power and emissivity of soot in the NIR region of the spectrum is negated by the poor transmittance of the device above 700 nm—effectively limiting the choice of wavelengths in this application to the visible spectrum only.

There are some established advantages to using a wavelength pair from the visible spectrum for studies of conventional diesel combustion; the sensitivity of the measuring system to the changes in flame temperature (the rate of change of spectral radiance with respect to temperature) is greater in the visible spectrum compared to the infra-red spectrum for temperatures above ~2000 K [Matsui *et al*., 1979; Yan and Borman, 1988; Zhao and Ladommatos, 1998]. However, this arrangement does lead to a narrow temperature measurement range due to low signal levels in the visible spectrum at temperatures below 2000 K. While these considerations again suggest that signal collection in the infra-red region of the spectrum would be advantageous for low temperature applications, the theoretical benefits are again compromised by practical considerations. Selecting two wavelengths in the visible spectrum reduces the sensitivity of the calculations for both temperature and *KL* factor to the value of α in Equation (3.23) such that a fixed value (1.39) can be selected for most fuels [Hottel and Broughton, 1932; Zhao and Ladommatos, 1998]. This is not the case when infra-red wavelengths are used [Stasio and Massoli, 1994; Zhao and Ladommatos, 1998]. Finally, with respect to the selection of visible wavelength pairs for combustion applications, care must be taken to avoid wavelengths where significant chemiluminescence occurs. Accordingly, the spectral emissions of the CH radical (390 and 431.5 nm), the C_2 radical (473.7 and 516.5 nm), the C_3 radical (405 nm) and the NH_2 radical (543.6, 571.3, 604.2, 630.2, and 665.2 nm) along with the emissions

of formaldehyde, CH_2O, at 395.2 nm, and broadband between 422 and 440 nm must be considered [Gaydon, 1974].

With the above considerations in mind, two possible wavelength pairs were examined for use in the present work—550/650 nm and 550/700 nm. The error between the true (T) and measured temperatures (T_m) due to different emissivities at the measuring wavelengths may be derived from Equation (3.20) as

$$\frac{1}{T} - \frac{1}{T_m} = \frac{\lambda_1 \lambda_2}{C_2(\lambda_2 - \lambda_1)} \ln \frac{\varepsilon_1}{\varepsilon_2} \tag{3.30}$$

The calculated error due to the variations of ε_1 and ε_2 is minimized when the two wavelengths are far apart. The relationship between the ratio (R) of the two narrow bands of emitted radiation may be derived from Equation (3.20) as

$$R = \frac{\varepsilon_1}{\varepsilon_2} \frac{{\lambda_2}^5}{{\lambda_1}^5} e^{-\frac{C_2}{T}\left(\frac{1}{\lambda_1} - \frac{1}{\lambda_2}\right)} \tag{3.31}$$

It is desirable that the instrument gives as large as possible a change in ratio for a small change in temperature. Differentiation of Equation (3.31) gives

$$\frac{dR}{dT} = \frac{C_2}{T^2} \frac{\varepsilon_1}{\varepsilon_2} \frac{{\lambda_2}^4}{{\lambda_1}^6} (\lambda_2 - \lambda_1) e^{-\frac{C_2}{T}\left(\frac{1}{\lambda_1} - \frac{1}{\lambda_2}\right)} \tag{3.32}$$

Analysis showed that the sensitivity of the pyrometer was higher with the 550/700 nm wavelength pair, without significantly affecting the accuracy compared to the 550/650 nm wavelength pair (the difference in temperature between the two wavelength pairs was less than 15 K for the whole temperature range). Hence, the wavelength pair of 550/700 nm was selected for the two-colour pyrometry system developed in this work. Also, with a larger separation between the two wavelengths, the response of the two-colour pyrometry system improved.

3.7.3 Two-Colour Pyrometry Components

As described previously, a borescope device was used to capture flame radiation. The transmitted radiation from the borescope was then split into two beams using a dichroic mirror. The transmitted and the reflected light beams were passed through 700 nm and 550 nm interference filters respectively. Subsequently, the two signals were detected by identical amplified photomultiplier tube (PMT) modules. The specifications of these optical components are given in Table 3.7. More details about these components are given in the following paragraphs.

Table 3.7: Two-Colour Pyrometry Components

Components	Make/Model	Specifications
Optical window	AVL/BO2737	Material: Fused silica good up to 18 MPa pressure and combustion temperature
Borescope	Karl-Storz/84583A	Field of view (FOV): 67^o; Direction of view: 0^o
Dichroic mirror block	Hamamatsu/A10034-04	Effective beam diameter: 8 mm
Dichroic mirror	Hamamatsu/DM660	Reflectance >95% between 460 and 625 nm; Transmittance >90% above 625 nm
Interchangeable filter block	Hamamatsu/A10033-90	Effective beam diameter: 8 mm
Interference filters	Thorlabs/FB05550-10-SP and FB05700-10-SP	Centre wavelength (CWL): 550/700 nm; Full width at half maximum (FWHM): 10 nm; Minimum transmissivity: >50%
Amplified photomultiplier tube module	Hamamatsu/H5784-20	Spectral response range: 300-900 nm; Peak sensitivity wavelength: 630 nm; Effective beam diameter: 8 mm; Cathode radiant sensitivity at 630 nm: 78 mA/W; Anode radiant sensitivity at 0.8 V control voltage: 39 V/nW; Maximum settling time (change of control voltage from 1 V to 0.5 V): 2 s; Current to voltage conversion factor: 1 V/μA; Frequency bandwidth: 0-20 kHz.

(a) Dichroic mirror

The dichroic mirror block consists of a built-in Hamamatsu DM660 dichroic mirror that reflects or transmits light depending on wavelength. This dichroic mirror has more than 95% reflectance and less than 5% transmittance between 460 and 625 nm; whereas above 625 nm, the transmittance is more than 90%. UV light shorter than 380 nm is absorbed by the coating materials deposited on the dichroic mirror, thereby, decreasing the reflectance and transmittance significantly. It is often used for the control of heat within an optical system, where it is referred as a hot or a cold mirror.

(b) Interference filter

An interference filter is an optical filter manufactured from a number of vacuum deposited dielectric layers resulting in a narrow-band filter typically of 5 to 50 nm full width at half maximum (FWHM, is a convenient and standard way of characterizing a well-behaved Gaussian photometric distribution and measured at half the height of the peak). Two sets of custom built Thorlab interference filters (black anodized aluminium outer housing to minimize light reflection from the

edges; 12.7 mm diameter and 5 mm thickness) with centre wavelengths of 550 and 700 nm were used in the two-colour pyrometer. The Hamamatsu A10033-90 interchangeable filter block housed the filter.

(c) Photomultiplier tube (PMT)

A photomultiplier tube is a vacuum tube consisting of an input window, a photocathode, focusing electrodes, an electron multiplier and an anode usually sealed into an evacuated glass tube. Photons entering a PMT through the input window excite the electrons in the photocathode so that photoelectrons are emitted into the vacuum due to the external photoelectric effect. Electron movement in a PMT is influenced by the electric field, which is dominated by the electrode configuration, arrangement and the voltage applied to the electrode. These photoelectrons are then accelerated and focused by the focusing electrode onto the first dynode, where they are multiplied by means of secondary electron emission. This secondary emission is repeated at each of the successive dynodes. The secondary electrons emitted from the last dynode are finally collected by an anode. The anode of a PMT is an electrode that collects secondary electrons multiplied in the cascade process through multi-stage dynodes and outputs the electron current to an external circuit [Hamamatsu Photomultiplier Tubes Hand Book, 2006].

The short wavelength limit (300 nm) of the PMT is determined by the PMT window material (wavelength at which the incident light is abruptly absorbed by the window material), while the long wavelength limit (900 nm) depends on the photocathode material (wavelength at which photocathode sensitivity falls to 0.1% of the maximum sensitivity). These wavelength limits also depend on the amount of incident light, dark current and signal-to-noise (SNR) ratio of the measurement system [Hamamatsu Photomultiplier Tubes Hand Book, 2006]. PMT modules used in this work comprised of a metal package photomultiplier tube, a low power consumption high-voltage power supply and a low noise amplifier. The electrical current from the PMT was converted to voltage by the amplifier for easy signal processing. The PMT module used in this work was highly resistant to noise since the amplifier was installed near the anode output pin of the PMT.

One significant advantage of using PMTs in this application is that the anode radiant sensitivity (gain) of a PMT is adjustable by varying the control voltage without increasing the noise [Hamamatsu Photomultiplier Tubes Hand Book, 2006]. Anode radiant sensitivity at a fixed PMT gain setting is defined as the photoelectric voltage generated by the anode divided by the incident radiant flux at a given wavelength. Current amplifications in the range of 2×10^2 to 2×10^6 can be achieved depending on the control voltage, thereby significantly enhancing the sensitivity of the PMT [Photosensor Modules, 2007]. This allows a sensible voltage output to be obtained from the PMT at low flame temperatures without significantly reducing the SNR of the system. Similarly, for high temperature measurement, the PMT gain can be reduced independently for each PMT to avoid saturation at higher wavelength without having to use neutral density filters.

3.7.4 Calibration of Two-Colour Pyrometer

The two-colour pyrometer was calibrated with a pre-calibrated tungsten strip lamp to determine the apparent temperatures, Ta_1 and Ta_2 at λ_1 and λ_2 so that the voltage output from the PMT (radiation intensity) could be correlated with the apparent temperature. Tungsten strip lamps have been found to be repeatable, accurate and suitable as secondary standard sources in photoelectric pyrometry [Barber, 1946; Jones, 1963; Matsui *et al*., 1979]. Although in principle, a lamp can be calibrated at any desired wavelength, most of the lamp calibration facilities are for wavelengths in the vicinity of 650 nm, with the possibility of calibration at 900 nm [Cezairliyan and Righini, 1996]. The tungsten strip lamp used in this work was pre-calibrated at 660 nm between 700 and 1700^{o}C. The temperature of the tungsten lamp was varied by changing the current setting of a high-capacity and highly stable DC power supply. Maximum current fluctuation of the DC power supply during calibration was ±0.04 A which corresponds to a variation of only ±2 K in the apparent temperature at 660 nm.

Since the spectral emissivity of tungsten is wavelength dependent, the apparent temperature of the tungsten lamp was corrected for the chosen wavelength by first determining the true temperature of the tungsten strip from a known apparent temperature at 660 nm and then calculating the apparent temperature of the tungsten strip at 550 and 700 nm for a range of temperatures, as described below.

The true temperature was determined from the apparent temperature and emissivity by means of Wien's law of radiation (Wien's approximation), i.e.

$$\frac{1}{T} = \frac{1}{T_a} + \frac{\lambda}{C_2}\log_e \varepsilon \tag{3.33}$$

The spectral emissivity of tungsten as a function of true temperature (wavelength varying between 450 and 800 nm and temperature between 1600 and 2400 K) was calculated using the empirical correlations proposed by Larrabee [1959] for the emissivity of tungsten (ε_W) in an iterative calculation method outlined by Lu and Yan [2006].

$$\varepsilon_W = 0.4655 + 0.01558\lambda + 0.2675\times10^{-4}T - 0.7305\times10^{-4}\lambda T \tag{3.34}$$

valid between 450 and 680 nm; and

$$\varepsilon_W = 0.6552 - 0.2633\lambda - 0.7333\times10^{-4}T + 0.7417\times10^{-4}\lambda T \tag{3.35}$$

valid between 680 and 800 nm.

The two-colour pyrometer was calibrated at 550 and 700 nm to determine the apparent temperatures, Ta_1 and Ta_2 respectively at different gain settings (corresponding to control voltages of 0.25-0.8 V) of the PMT. The calibration of the two-colour pyrometer at three gain settings (0.3 V, 0.4 V and 0.7 V control voltages) of the PMT is shown in Fig. 3.10. A logarithmic trend line was

fitted to the data points as monochromatic emissive power is an exponential function of temperature. Equations of the trend lines and the index of correlations (R^2-values >0.98) are also given in the figures. Note that the pyrometer could not be calibrated below 1250 K because of high current fluctuation of the power supply for the tungsten lamp. This limitation dictated the lower limit of temperature measurement for the two-colour pyrometer system under consideration here.

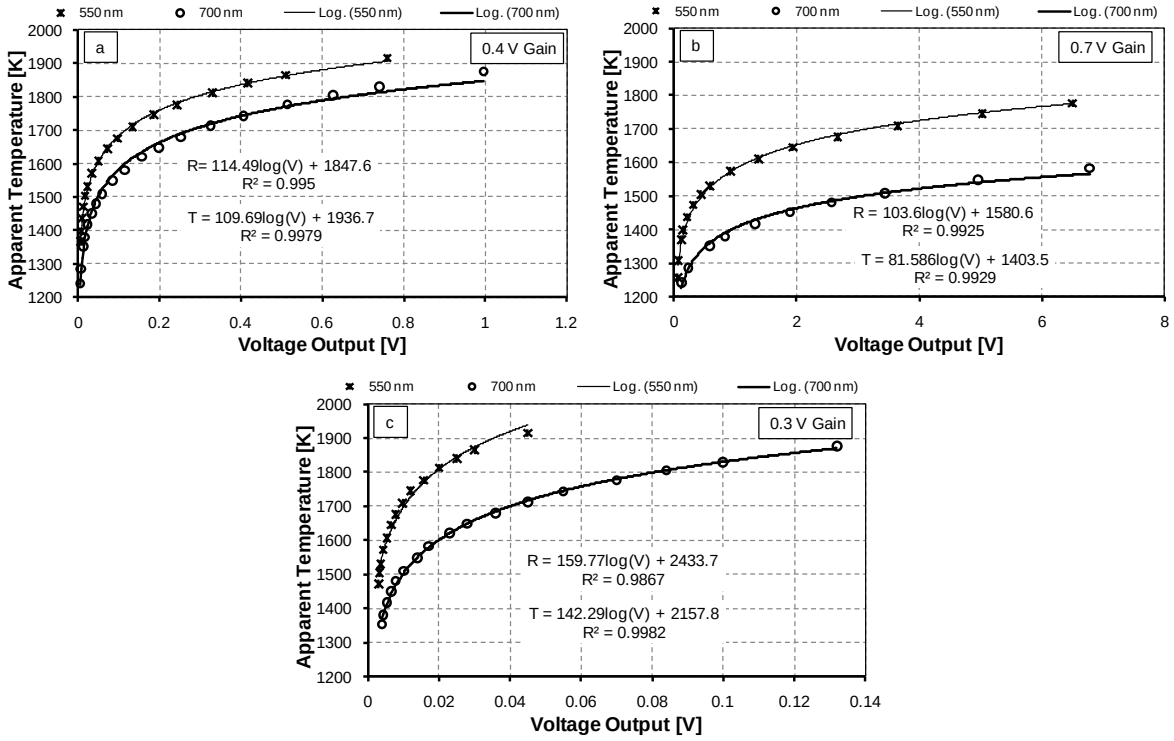

Fig. 3.10: Calibration of the two-colour pyrometer at 550 nm and 700 nm wavelengths
T: Transmitted apparent temperature; R: Reflected apparent temperature; V: PMT voltage output.

Note that during data acquisition, the gain settings of the two PMTs were varied independently depending on the maximum flame temperatures to be measured. For conventional diesel non-EGR cases, low PMT gain setting was used so that the logarithmic curve fitted equation represented a better fit for high apparent temperatures (for example, calibration at 0.4 V gain setting shown in Fig. 3.10a). At lower PMT gains (<0.4 V), the outputs from the PMT corresponding to low apparent temperatures of the calibrated tungsten strip were noisy and hence those points were not used to fit the trend line (see Fig. 3.10c at 0.3 V gain). Similarly, for measuring low peak flame temperature cases (high EGR), high PMT gain settings were used. At high PMT gain, the outputs from the PMT were saturated at high apparent temperatures of the tungsten strip and hence, trend lines could only be fitted at low apparent temperatures (refer to Fig. 3.10b). Therefore, the errors in the curve fitted equations were minimized by calibrating the two-colour pyrometer system at different PMT gain settings. This made it possible to implement the two-colour pyrometry system to measure a wide range of flame temperatures.

3.7.5 Uncertainty Analysis

Although two-colour pyrometry is a simple and widely used technique to measure flame temperature, there are some associated errors due to the principle of measurement and various assumptions. The most important limitation of this method is due to the assumption of homogeneous temperature and soot loading (*KL* factor) in the line-of-sight. However, this is not the case for the turbulent mixing-controlled diesel combustion where flame temperature and *KL* factor vary significantly in the control volume and therefore tend to make the flame temperature measurement by the two-colour method skewed towards the high temperature in the reaction zone [Matsui *et al*., 1979; Svensson *et al*., 2005; Payri *et al*., 2007; Musculus *et al*., 2008].

Yan and Borman [1988] reported that the effect of a non-uniform soot loading (*KL* factor) on the flame temperature measured by the two-colour method is less severe than that of the uneven temperature on the *KL* factor. This is supported by the work of Payri *et al.* [2007] who modelled the propagation of radiation inside the flame as an emission and absorption process occurring before the measurement device, and showed that for low temperature and/or low *KL* values, deviations for the two-colour derived *KL* factor were of the order of 10-20%, whereas temperature values were not so strongly affected (maximum of 5% error).

Matsui *et al.* [1979] reported that errors can also be caused, either when the flame does not fill the entire field of view of the sensor, or due to wall effects, including reflection and radiation from the wall itself. However, these errors are difficult to quantify and can be ignored compared to the radiation from the flame if visible wavelengths are used. Optical window fouling due to soot contamination also causes error in the measurement which is again difficult to quantify [Matsui *et al*., 1980].

In principle, the two-colour method measures radiation at a particular wavelength. Accordingly, the use of narrow bandwidth interference filters introduces a further fixed source of error into the measurements. This error, however, is small. Stasio and Massoli [1994] estimated that the uncertainty in temperature and soot concentration measurements for an interference filter with a 10 nm FWHM (as in the present work) is less than 6 K and 2% respectively for visible wavelengths.

3.7.6 Implementation of Two-Colour Pyrometry on the Engine

The orientation of the two-colour pyrometry in the engine generated a field of view (FOV) as shown in Fig. 3.11 that was centred between two of the diesel spray plumes from the injector. In the context of the present work, it should be noted that no significant difference for the flame temperature and *KL* factor are reported when the FOV of the optical probe is targeted, either on one spray, or between two sprays [Yan and Borman, 1988]. The wide FOV of the borescope used in this work also ensured that soot luminosity can be captured late during the combustion process and in the less luminous LTC regimes. Fig. 3.11 details the two-colour pyrometer setup and the borescope's FOV within the combustion chamber.

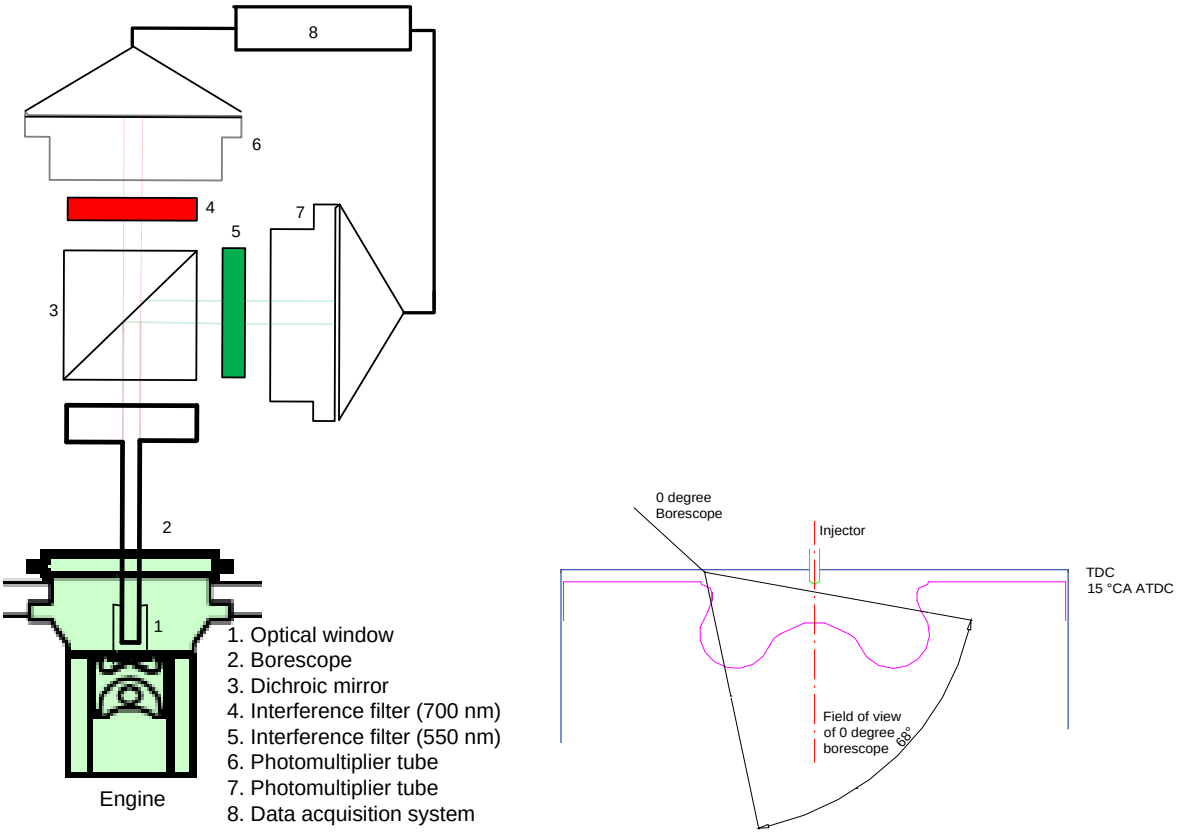

Fig. 3.11: Schematic of two-colour pyrometry (left hand figure) and the control volume covered by the FOV of the borescope at 15 ^{o}CA ATDC (right hand figure)

Radiation signals from the optical pyrometer were acquired at every 0.5 ^{o}CA interval by the NI high-speed data acquisition system and the LabVIEW program described earlier. Because Equation (3.23) is highly nonlinear, this equation was solved iteratively with the procedure outlined by Zhao and Ladommatos [1999] to obtain the true flame temperature. In this approach, the apparent temperature was estimated at the first wavelength, T_{a1}, for an assumed T and measured T_{a2}. An iteration process was carried out until the calculated T_{a1} was within 0.5^{o}C of the measured T_{a1}. Equation (3.23) was rearranged based on the assumption that the variation of T_{a1} with T at a given T_{a2} is approximately linear for a short temperature range:

$$\frac{1}{T_{a1}} = \frac{\lambda_1}{C_2}\ln\left[1+\left(\frac{e^{(C_2/\lambda_1 T)}-1}{A}\right)\right] \tag{3.36}$$

where

$$A = 1-\left[1-\left(\frac{e^{(C_2/\lambda_2 T)}-1}{e^{(C_2/\lambda_2 T_{a2})}-1}\right)\right]^{\lambda_2^{\alpha 2}/\lambda_1^{\alpha 1}} \tag{3.37}$$

3.7.7 Operating Conditions to Validate the Two-Colour Pyrometer

In order to verify the range and lower limit of the flame temperature measured by the two-colour pyrometer, an EGR sweep was carried out under low-load conditions. For this, the EGR level was varied from 4 to 64% by volume at a constant fuelling quantity of 8 mg/cycle, an engine speed of 1500 rpm and with an unboosted intake (pressure 100 kPa, absolute). Note that in the course of this EGR sweep, the engine transitioned from conventional diesel operation to a high-EGR low-sooting LTC mode. In all cases, SOI timing of the fuel injection was advanced depending on the EGR level to improve combustion efficiency while keeping the rate of pressure rise below 1 MPa/^{o}CA. The full range of operating conditions examined is specified in Table 3.8. Smoke emissions at different conditions are also listed in Table 3.8. Note that the exhaust back pressure was maintained at least 10 kPa above the intake pressure in all the cases to drive the required amount of EGR. Intake air temperature was maintained at 45±5^{o}C.

Table 3.8: Test Points (Constant Engine Speed, 1500 rpm)

Case	Injected fuel mass (mg/cycle)	Injection mode	Injection pressure (MPa)	SOI timing (ATDC)	EGR (% vol.)	Intake pressure (kPa)	Smoke emission (FSN)
A	8	Single	65	-3	4	100	0.32
B	8	Single	65	-3	28	100	0.34
C	8	Single	65	-3	38	100	0.27
D	8	Single	65	-15	54	100	0.24
E	8	Single	65	-21	57	100	0.03
F	8	Single	65	-24	61	100	0.04

Cases A-C: Conventional Diesel / Low Load; Cases D-F: High-EGR LTC / Low Load

The crank-angle resolved radiation signal at the 550 nm wavelength for conventional diesel combustion (Case C) and high-EGR LTC (Case E) are shown in Figs. 3.12a and 3.12b, respectively. Cyclic variation in the sample data is represented by the standard deviation of the radiation signals. Standard deviations greater than mean radiation values shown during the initial premixed energy release phase and during the late burn out phase of combustion indicate significant cyclic variations in the radiation signal at these times. It is interesting to note that neither the ignition and early-stage combustion of the conventional diesel mode, nor the cool-flame reactions in the high-EGR low temperature mode are evident in the PMT signal. The start of the radiation signal coincides with the start of the high-temperature energy release rate (i.e., SOC) in both cases, although phasing of the two peaks differ. This characteristic of the results is due to the low PMT gain setting used in the conventional diesel experiments and the fact that the wavelength of the cool-flame chemiluminescence in LTC is in the ultra-violet region of the spectrum (<440 nm) and therefore is not visible to the pyrometer system.

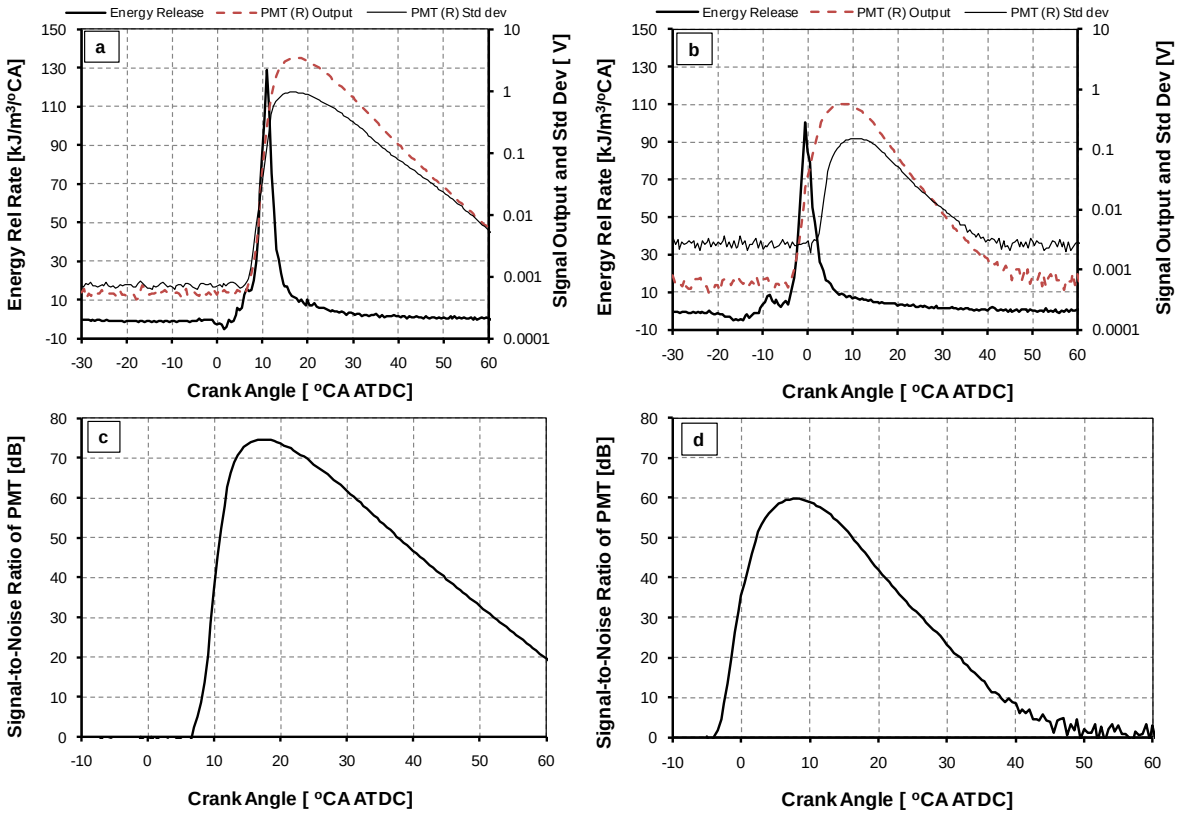

Fig. 3.12: a. Energy release rate, radiation signal and standard deviation of conventional diesel combustion (Case C); b. Energy release rate, radiation signal and standard deviation of high-EGR LTC (Case E); c. SNR of PMT at 550 nm in Case C; d. SNR of PMT at 550 nm in Case E

Dark current noise and ripple noise (<1 mV) in the PMT was determined without fuel injection for all the cases. SNR was determined as a ratio of the measured signal with fuel injection to the noise from an equivalent case without fuel injection. Figs. 3.12c and 3.12d show the SNR corresponding to the two cases shown in Figs. 3.12a and 3.12b respectively. SNR in conventional diesel combustion (Case C) remained very high (>20 dB) up to 60 ^{o}CA ATDC indicating significant soot luminosity, whereas SNR decreased rapidly for the high-EGR LTC case (Case E) at the corresponding crank angle, indicating low levels of soot luminosity. As was highlighted by Rothamer and Ghandhi [2002], there is no fixed SNR criterion to determine the reliability of an optical measurement; therefore, individual experimental setups and applications require individual assessment in this regard. Based upon the results shown in Fig. 3.12 and similar results for other engine operating conditions, the criteria of both a SNR >20 dB and a mean radiation signal greater than the standard deviation of the sample as an indicator of trustworthy data for the estimation of the flame temperature and soot loading was adopted for all the results reported in this work.

The voltage outputs corresponding to the radiation intensity at two wavelengths at each crank angle for 200 cycles were ensemble averaged to estimate the flame temperature and *KL* factor. It was verified that there was no significant difference in the measured flame temperature when the

temperature at each cycle was averaged compared to the ensemble average of 200 cycles' data. One such case (Case C) is shown in Fig. 3.13. Note that flame temperatures were same for the two averaging methods up to 57 ^{o}CA ATDC (see the curves corresponding to 'Avg 200 cycles' and 'Each cycle avg' in the legend), whereas after this crank angle, flame temperature with individual cycles' average were higher (and noisier) than the temperature determined by the average radiation signals; however, these temperatures at later crank angles are of little interest in this work. Therefore, to reduce computational time, flame temperature and *KL* factor were determined from ensemble average data of 200 cycles, which is consistent with the previous study by Yan and Borman [1988].

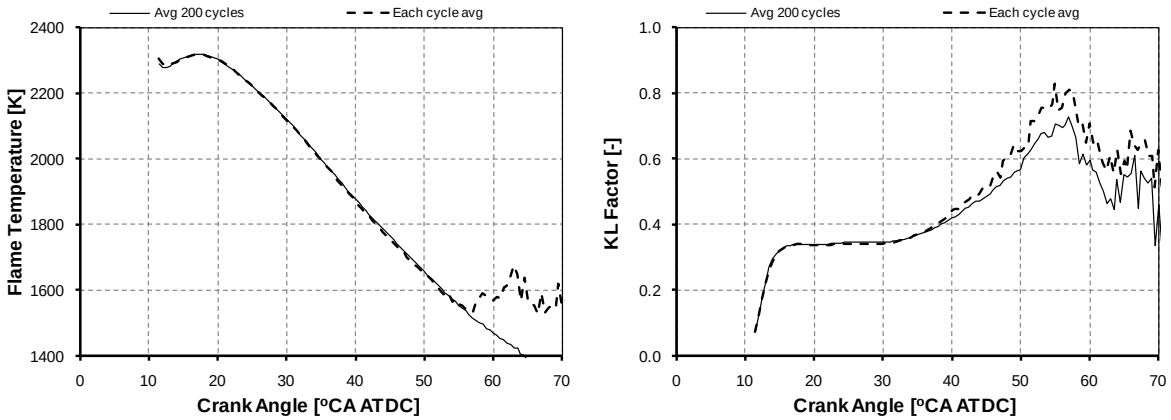

Fig. 3.13: Flame temperature and *KL* factor for Case C for two different averaging approaches (i.e. average from individual cycles and calculated from average signals)

It is reported in the literature that window fouling may reduce the transmissivity of the optical window during data acquisition, which may influence the measured flame temperature and the *KL* factor. However, for the two-colour pyrometry results reported in the thesis, it was not possible to measure the transmissivity of the optical window before and after the flame temperature measurement. For the temperature and soot loading measurements reported here, only the data without visible window fouling have been presented and hence, the uncertainty due to soot contamination is minimized. In order to verify the effects of window fouling during data acquisition (even without visible window fouling) on the two-colour pyrometry results, the first and last 50 cycles data from the acquired 200 cycles were processed (average of individual cycles) and shown in Fig. 3.14 for a high-EGR LTC case (Case E). The maximum difference in peak flame temperature and peak *KL* factor were found to be 30 K and 0.3 respectively between the averages of the 1st 50 cycles and last 50 cycles. Note that the flame temperature obtained from the average of the last 50 individual cycles' data was lower than the data obtained from the 1st 50 cycles, whereas the *KL* factor showed a reverse trend. This trend agrees with the analysis of Mastsui *et al.* [1980]; however, the authors had concluded that a certain difference in the transmissivity of the optical window

(measured at 550 nm) due to window fouling could not explain the cause of the difference in the flame temperature and *KL* factor results. Therefore, in this work, the effect of window fouling on the two-colour results has not been considered.

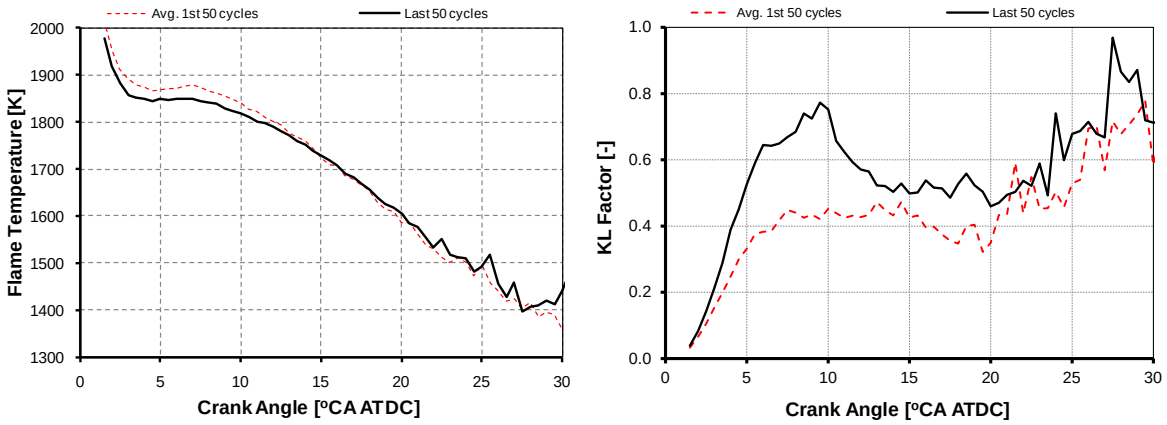

Fig. 3.14: Effects of optical window fouling on flame temperature and *KL* factor during high-EGR LTC operation (Case E) (i.e. average from 1st and last 50 cycles' data)

With the criteria outlined above (SNR, standard deviation of measured signal and averaging procedure), the apparent temperatures were processed to determine the flame temperatures and *KL* factors for the EGR sweep covered by Cases A-F in Table 3.8. The results are shown in Fig. 3.15. Peak flame temperature (Fig. 3.15a) is shown to decrease monotonically with increasing charge dilution (higher EGR). Note that Cases A-C essentially represent conventional diesel combustion with constant SOI timing, while Cases D-F represent a transition to high-EGR LTC with advanced SOI timing. In conventional diesel combustion cases (A-C), the results presented in Fig. 3.15a show that the peak flame temperature occurs later in the cycle as the level of intake charge dilution is increased. The prolonged tail of the flame temperature late in the expansion stroke with increasing intake charge dilution in conventional diesel combustion indicates combustion extending later in the cycle. With advanced SOI timing (Cases D-F), the position of the peak flame temperature is advanced. As expected, LTC is characterized by lower peak flame temperature, rapid temperature drop and shorter high-temperature residence time compared to conventional diesel combustion.

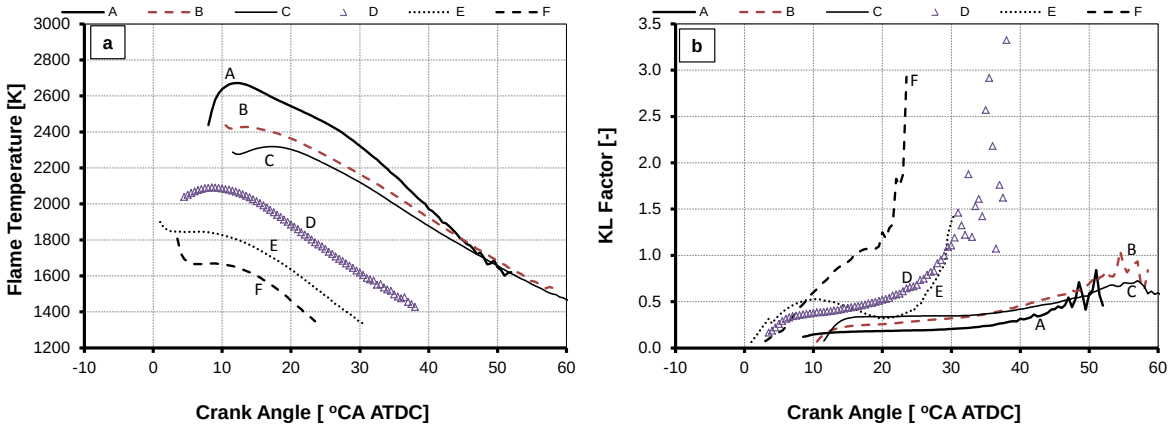

Fig. 3.15: a. Flame temperature; b. *KL* factor for an EGR sweep (4-61% by volume) for the 8 mg/cycle fuelling quantity (Case A: 4% EGR to Case F: 61% EGR)

The *KL* factors determined from the flame temperatures and the apparent temperatures for the EGR sweep (4%–61%) is shown in Fig. 3.15b. It can be seen that the *KL* factor calculated for the three conventional diesel cases (Cases A-C) show similar behaviour. In each of these cases, the *KL* factor is approximately constant through the bulk of the combustion event to approximately CA90 (~35 °CA ATDC). After 35 °CA ATDC, the *KL* factors for the conventional diesel cases show a steady increase until the calculation is terminated according to the aforementioned criteria. The calculated *KL* factors for the high-EGR LTC regimes (Cases D-F) exhibit quite different behaviour. In these cases, the calculated values of *KL* factor increase rapidly to levels far in excess of those calculated for the conventional diesel cases. Given the low soot measurements recorded under these operating conditions (FSN <0.05), the behaviour of the calculated *KL* factor in high-EGR LTC is clearly unrealistic.

The trend of increasing *KL* factor in the high-EGR LTC cases (Cases D-F) is attributable to a combination of low soot concentration and/or the combustion only occupying a small part of the borescope's FOV. When FOV of the borescope is essentially empty of soot luminosity, as is expected to be the case for low-load, low-sooting high-EGR LTC strategy and perhaps at the end of a conventional diesel combustion event at low-load, the average *KL* factor tends towards that of a black body.

The uncertainty in the measured flame temperatures and calculated *KL* factors due to random errors (corresponding to a 95% confidence interval) for Case C (conventional diesel combustion) and Case E (high-EGR LTC) are shown in Fig. 3.16. Close to the peak temperature region, the uncertainty in the flame temperature measurements is ~0.5%, whereas it is ~3% in the late combustion phase for both conventional diesel and high-EGR LTC conditions because of the larger standard deviations (refer to Figs. 3.12a and 3.12b). The uncertainty in the *KL* factor for the conventional diesel case is ~3% in the low *KL* factor region rising to ~20% in the late combustion phase (refer to Fig. 3.16a), values that are consistent with the uncertainty values for the *KL* factor

reported by Payri *et al.* [2007] in conventional diesel combustion. Note that due to the unrealistic trends of the calculated *KL* factor for low-load high-EGR LTC operation, the uncertainty in the *KL* factor results for this operating condition is not discussed.

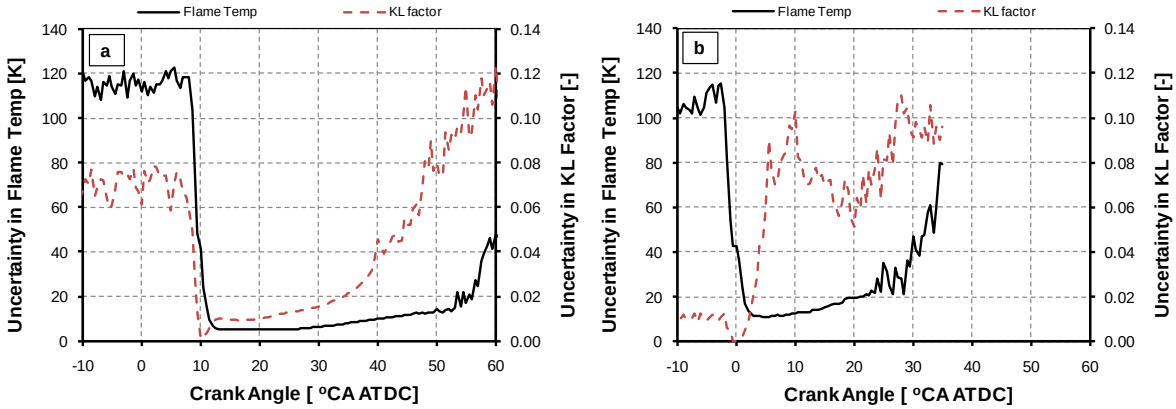

Fig. 3.16: Uncertainty (95% confidence interval) in flame temperature and *KL* factor; (a) Conventional diesel combustion (Case C); (b) High-EGR LTC (Case E)

To validate the measured flame temperatures and to assess the effect of EGR on flame temperature, stoichiometric adiabatic flame temperatures were determined from the bulk gas temperature for conventional diesel combustion (Case A) and high-EGR LTC (Case E) cases and are shown in Fig. 3.17. The methodology used to determine the adiabatic flame temperature is described later in Sec. 5.6 in Chapter 5. In-cylinder pressure and mass averaged bulk gas temperature just after CA50 were taken as the ambient condition to determine the adiabatic flame temperature.

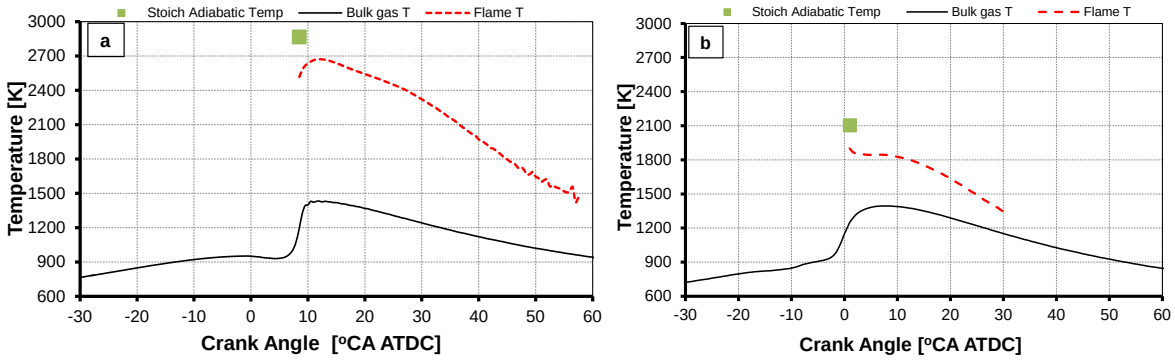

Fig. 3.17: Measured flame temperature and calculated bulk gas and stoichiometric adiabatic flame temperatures; (a) Conventional diesel combustion (Case A); (b) High-EGR LTC (Case E)

From Fig. 3.17 it is observed that the peak flame temperature measured by the two-colour pyrometer is lower by 200-300 K than the stoichiometric adiabatic flame temperature which agrees with previous studies [Yan and Borman, 1988; Musculus, 2005; Singh *et al.*, 2005]. Note that the stoichiometric adiabatic flame temperature is shown by a filled square in the figures. This validates

the flame temperature measured by the two-colour pyrometer in the present work. It should be noted that in conventional diesel combustion (Fig. 3.17a), the difference between the bulk gas temperature and the measured flame temperature is significant, whereas this difference is marginal in high-EGR LTC (Fig. 3.17b). This is attributed to the high local flame temperature in conventional diesel, whereas the flame temperature is more uniform in high-EGR LTC operation.

The measured peak flame temperatures for the various cases investigated in this section were plotted against the measured NO_X emissions as shown in Fig. 3.18a. The trend clearly follows an exponential relationship. The results also show that NO_X emissions are essentially independent of flame temperature below 2100 K which suggests that thermal NO_X produced via the Zeldovich mechanism is limited to 2100 K. This is consistent with the data reported by Plee *et al*. [1982] for a diesel engine and this value is within 5% of the limiting temperature data based on fundamental studies reported earlier [Bowman, 1975]. Therefore, with further reduction in flame temperature, there may not be any significant effect on NO_X emissions, which highlights the limitation of EGR to reduce NO_X production further. However, NO_X produced (<10 ppm) by the 'prompt NO route' and the 'N_2O route' may still be relevant in high-EGR LTC cases [Desantes *et al*., 2012]. To fit an Arrhenius type of correlation between the engine-out NO_X emissions and the measured peak flame temperatures, the flame temperatures above 2100 K were plotted in a logarithmic scale as shown in Fig. 3.18b. A trend line (linear) fitted between these two parameters shows a good correlation with an index of correlation (R^2) close to 1. The slope of the trend line is -38454 K which is within 5% of (E_0/R_0) of the Arrhenius correlation (-38000 K) for thermal NO_X production via the Zeldovich mechanism [Bowman, 1975] and -36700 K obtained by Plee *et al.* [1982] for a diesel engine at different operating conditions. This also validates the two-colour pyrometer developed in this work.

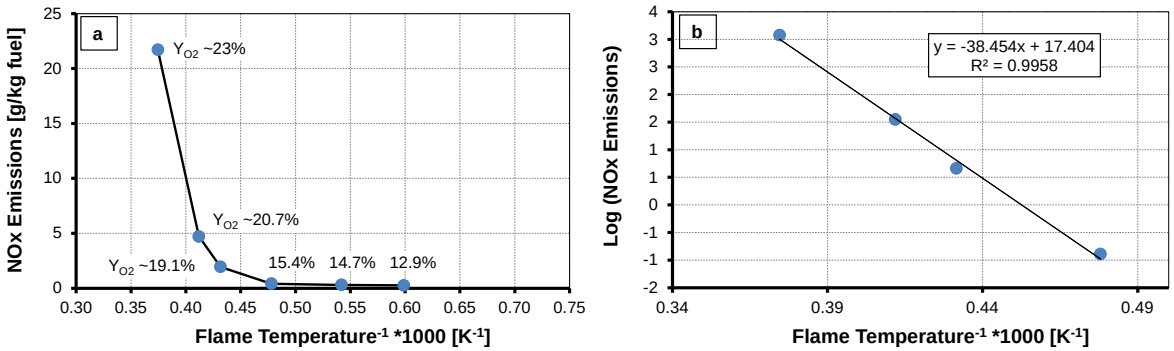

Fig. 3.18: NO_X emissions and peak flame temperatures for different cases

3.8 Identification of Operating Conditions

The selected specific test conditions are different in various chapters. However, the basis of selection of operating conditions in this study is based on engine behaviour while following a New European Driving Cycle (NEDC) driving cycle. The operating conditions selected in this work correspond to low to intermediate speeds and intermediate loads frequently encountered during the

NEDC driving cycle. The operating conditions are, engine speeds: 1500 rpm and 2500 rpm; fuelling quantity: 16 mg/cycle and 21 mg/cycle. These fuelling quantities relate to 600 and 900 kPa IMEP, respectively, for conventional diesel combustion. However, in cases where the efficiency changes significantly, the IMEP also changes. To maximize comparability, the fuelling quantity, rather than IMEP, was held constant in this work.

In Chapter 4, two operating conditions corresponding to 1500 rpm and 2500 rpm engine speeds and 16 mg/cycle fuelling quantity are investigated with a wide range of intake pressures both in conventional diesel and low temperature combustion regimes. An operating condition corresponding to 2500 rpm engine speed and 21 mg/cycle fuelling quantity is also investigated in this chapter. A limited number of operating points corresponding to 1500 rpm engine speed and 16 mg/cycle fuelling quantity are investigated optically in conventional diesel and high-EGR LTC regimes in Chapter 5. The effects of split injections on LTC (Chapter 6) are investigated at reduced EGR levels at 1500 rpm engine speed, and 15.6 mg/cycle fuelling condition. Different pseudo-transient operating conditions at 1500 rpm and 1600 rpm engine speeds are investigated in Chapter 7. Note that due to the advanced fuel injection timing and variable intake oxygen mass fraction (EGR levels) used in this work, engine loads (GIMEP) were variable for a given fuelling quantity. Therefore, fuelling quantity and engine speed are used to define the engine operating condition.

Chapter 4

DIESEL LOW TEMPERATURE COMBUSTION WITH VARIABLE INTAKE PRESSURE

4.1 Introduction

High-EGR LTC can be realized in a conventional production diesel engine without any significant modification to the combustion chamber design and fuel injection system. This ensures dual-mode operation (both LTC and conventional diesel) of the engine so that the high load conventional diesel combustion operation is not sacrificed. In a previous work, high-EGR low temperature combustion was realized on the AVL single cylinder research engine (as described in Chapter 3) at four different operating conditions in the naturally aspirated mode: engine load corresponding to 8 and 16 mg/cycle fuelling quantities and engine speeds of 1500 rpm and 2500 rpm [Cong, 2011]. For the 8 mg/cycle fuelling case, it was shown that the overall combustion was still lean in the LTC mode and with advanced combustion phasing (because of advanced SOI), the thermal efficiency of LTC could be made higher than conventional diesel combustion [Cong, 2011]. However, for the 16 mg/cycle fuelling cases, the engine was operated with an overall near-stoichiometric fuel-oxygen ratio (and ~60% EGR) to suppress smoke emissions and thus, despite the more advanced combustion phasing, the emissions of partial combustion by-products increased significantly which reduced the thermal efficiency [Cong, 2011]. Post fuel injection was investigated to reduce these emissions through enhanced fuel-oxygen mixing in the later part of the combustion process, but post injection had an insignificant effect on LTC emissions due to the low oxygen concentration and low in-cylinder temperature after the main reactions [Cong, 2011]. This chapter reports the effects of boost pressure on combustion and emission phenomena with variable levels of EGR from conventional diesel combustion to low temperature diesel combustion regimes. The effects of variable injection timings and injection pressures on key combustion parameters (GISFC, CA50) and emissions in the LTC regime are also investigated at a constant intake pressure. The potential to extend the LTC load boundary with high boost pressure is also presented in this chapter.

4.2 Experimental Methodology

Two operating conditions corresponding to 16 mg/cycle fuelling quantity at 2500 rpm and 1500 rpm engine speeds were investigated at different intake pressures. A higher fuelling quantity of 21 mg/cycle at 2500 rpm engine speed was investigated at a fixed intake pressure (200 kPa) and an EGR sweep was carried out to cover conventional diesel to high-EGR LTC operation. The effects of variable intake pressure were investigated for the EGR sweep from conventional diesel combustion (0% EGR by volume) to high-EGR LTC (~65% EGR by volume). It is acknowledged that diverting a substantial fraction of the exhaust gases away from the turbocharger would reduce the turbocharger's ability to meet the targeted boost pressure due to low exhaust gas flow rates and low

exhaust enthalpy (due to low exhaust temperature). This will be discussed in more detail in Chapter 7. Fuel injection pressure was held constant throughout the EGR sweep for a fixed operating condition. With increasing intake dilution, combustion phasing (CA50) retarded significantly for a fixed SOI timing; hence, the SOI timing was advanced to avoid retarded combustion phasing and misfire at high-EGR LTC conditions.

Two fuel injection timing strategies were used in the work reported in this chapter. In the first, the timing of the start of fuel injection was adjusted to maintain a constant combustion phasing (based on the CA50) at 10±0.5 ^{o}CA ATDC. The second strategy involved adjusting the start of fuel injection timing for the 'maximum advance for best indicated torque' (MBT start of injection timing), where fuel injection timing was advanced such that maximum torque was achieved. This latter strategy was limited by the need to avoid excessive rates of pressure rise; for this work, the injection timing advance was restricted to limit the pressure rise rates ≤1 MPa/^{o}CA. The intake temperature varied between 70^{o}C and 110^{o}C, and increased at higher EGR levels, as would be encountered in real EGR applications. This effect was more pronounced at 2500 rpm because of higher exhaust gas temperature compared to 1500 rpm. The exhaust back pressure was maintained 15-20 kPa above the intake pressure to drive the required amount of EGR. The operating conditions corresponding to 16 mg/cycle and 21 mg/cycle fuelling quantities at two different engine speeds are listed in Table 4.1.

Table 4.1: Engine Operating Conditions with MBT Start of Injection Timings

Engine Speed (rpm)	2500	1500	2500
Fuel Quantity (mg/cycle)	16.2±0.4	16.2±0.5	21±0.3
Start of Injection (SOI)	MBT (see Fig. 4.2a)	MBT (see Fig. 5.2b)	MBT (see Fig. 4.23b)
Intake Pressure (abs) (kPa)	120, 150 and 180	100, 120 and 150	200 kPa
Intake Temperature	See Fig. 4.3a	See Fig. 4.3b	See Fig. 4.24
Fuel injection pressure (MPa)	60	90	100
EGR levels (% by vol.)	0 to 65	0 to 64	0 to 64
Exhaust back pressure	20 kPa above intake	15 kPa above intake	20 kPa above intake

4.3 Effects of Boost Pressure in LTC [§]

The results corresponding to 16 mg/cycle fuelling quantity are subdivided into three sub-sections to provide a more focused investigation of the effects of variable intake pressures on emission and combustion processes:

[§] Part of the work reported in this section was presented at the SAE Powertrains, Fuels and Lubricants Meeting, October 2010, San Diego, USA. A. K. Sarangi, G. P. McTaggart-Cowan, and C. P. Garner, "The effects of intake pressure on high EGR low temperature diesel engine combustion", SAE Paper No. 2010-01-2145. All texts and figures reprinted with permission from SAE © 2010 SAE International.

I. Effects of boost pressures with injection timing set for MBT (16 mg/cycle, 2500 rpm and 1500 rpm);

II. Effects of injection timing strategy at a constant intake pressure (16 mg/cycle, 2500 rpm); and

III. Effects of injection pressure at a constant intake pressure for MBT timing (16 mg/cycle, 2500 rpm).

4.3.1 Effects of Boost Pressure with MBT Injection Timing

The upper limit of the intake pressures for the two operating conditions corresponding to 16 mg/cycle fuelling quantity, listed in Table 4.1, were selected from the boost pressure characteristics of a multi-cylinder 2 liter engine in the steady-state while following an NEDC driving cycle. Note that a single main injection per cycle was used throughout the EGR sweep for the 2500 rpm case, whereas a small quantity of fuel (pilot injection*) was used along with the main fuel injection for the 1500 rpm case for EGR levels less than 40% to restrict the rate of pressure rise. The EGR rates and oxygen based equivalence ratios with respect to intake oxygen mass fractions are plotted in Fig. 4.1 for different intake pressures.

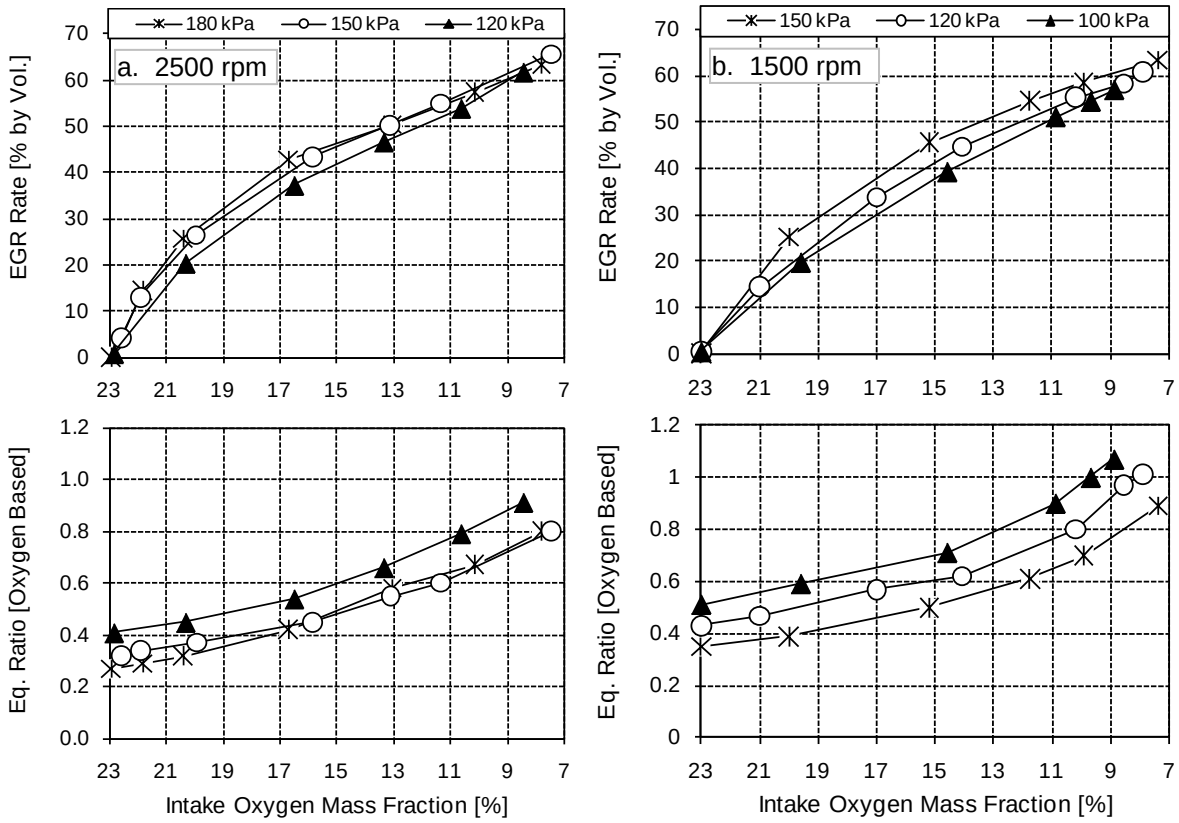

Fig. 4.1: Variations of EGR rate and equivalence ratio (oxygen based) with intake oxygen mass fraction for MBT injection strategy at variable intake pressures

* Pilot injection had no benefit except restricting the rate of pressure rise and in fact tended to be detrimental to emissions.

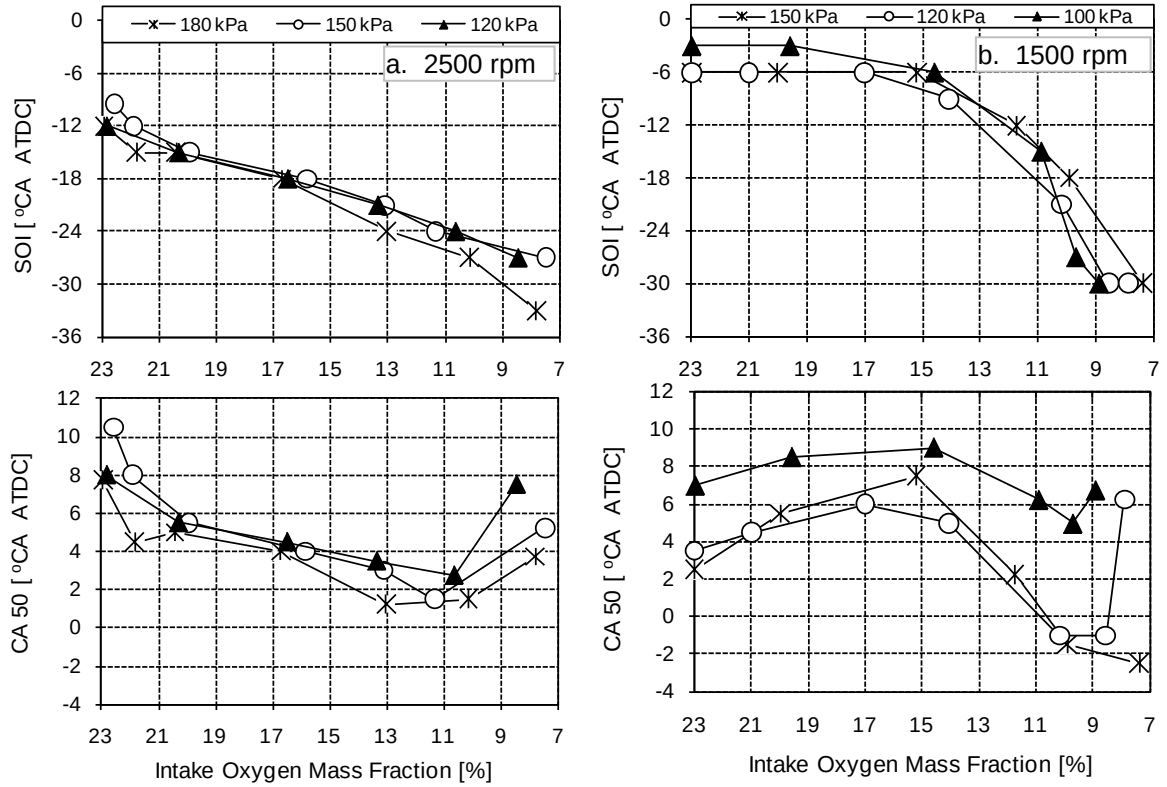

Fig. 4.2: Variations of start of injection (SOI) and CA50 with intake oxygen mass fraction for MBT injection strategy at variable intake pressures

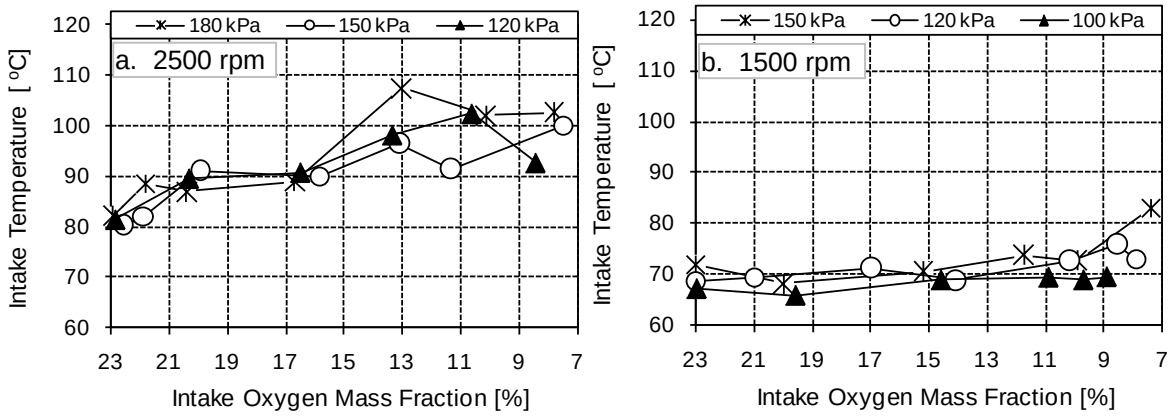

Fig. 4.3: Variations of intake manifold temperature with intake oxygen mass fraction for MBT injection strategy at variable intake pressures

Since increasing the EGR rate resulted in a reduction in $dp/d\theta$, higher EGR levels permitted earlier fuel injection timings. The fuel injection timing and the resultant combustion phasing (CA50) are shown in Fig. 4.2. Increasing EGR levels resulted in higher exhaust gas flow rates through the EGR cooler, resulting in an increase in the intake temperature as shown in Fig. 4.3, where it can be seen that individual test conditions showed significant variations around the general increase in intake temperature.

Engine speed impacts in-cylinder conditions by changing the available time for the air exchange and fuel injection processes. For the work reported in this chapter, the decrease in engine speed was also accompanied by advanced fuel injection timing, higher injection pressure and pilot injection. These factors along with changes in piston speed would result in significant differences in the in-cylinder fluid motion, which are expected to influence the combustion and emission processes. The results shown in Fig. 4.4 suggest that engine speed had some impact on the rate of reduction of NO_X at low to moderate EGR levels (high Y_{O2}); the rate of reduction being higher at the lower engine speed of 1500 rpm. This is a result of the more advanced fuel injection timings permitted because of lower injection pressure and lower rate of pressure rise at higher engine speed. NO_X emissions were much higher at lower speed without intake charge dilution. It may be recalled that a pilot injection was used at 1500 rpm up to 40% EGR to limit the rate of pressure rise. The advanced fuel injection timing significantly increased NO_X emission (refer to Fig. 4.4) at low EGR levels due to advanced CA50. Note that higher intake pressure permitted advanced fuel injection timing due to the lower rate of pressure rise. The results presented in Fig. 4.4 showed that near-zero NO_X emissions could be achieved irrespective of boost pressure for intake oxygen mass fractions below 13% and 14% for 2500 rpm and 1500 rpm engine speeds respectively due to the well-known NO_X reduction effects of EGR by reducing the flame temperatures [Ladommatos *et al*., 2000].

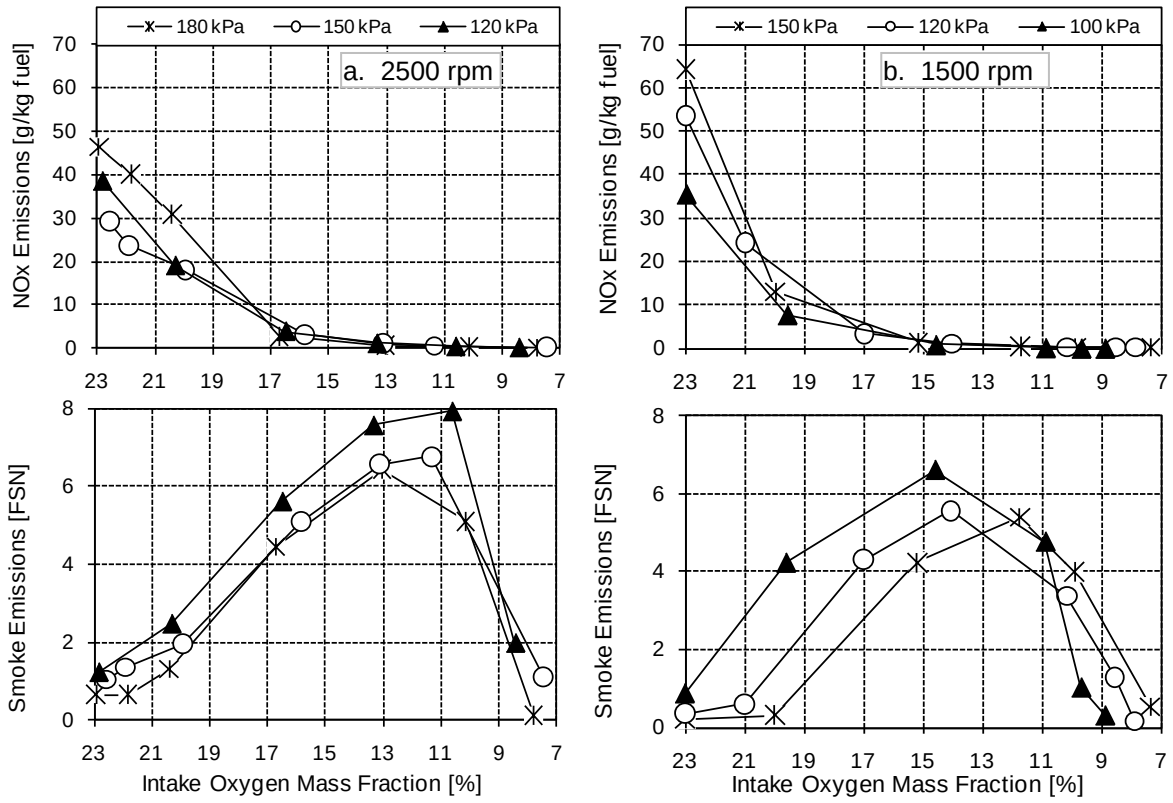

Fig. 4.4: Variations of NO_X and smoke emissions with intake oxygen mass fraction for MBT injection strategy at variable intake pressures

Smoke emissions reached their peak values at oxygen mass fractions in the range of 11-13% for 2500 rpm and 11-15% for 1500 rpm irrespective of intake pressure due to the well-known smoke-NO_X trade-off with EGR. This increase in smoke emissions is due to the competing effects of soot formation and subsequent oxidation at the intermediate EGR levels. Because of the stronger temperature dependence of soot oxidation than soot formation, decreases in flame temperature and oxygen concentration caused significant reductions in soot oxidation resulting in more tailpipe smoke emissions [Tree and Svensson, 2007]. Below about 11% intake oxygen mass fraction, smoke emissions decreased rapidly, reaching levels similar to the non-EGR case, for Y_{O2} <9% irrespective of engine speeds. The results presented here also show that simultaneous low smoke and low NO_X combustion is possible even with near-stoichiometric and rich overall fuel-air ratios. Higher intake pressures resulted in slightly lower FSN under conventional diesel combustion which suggests that the lack of oxygen for oxidation is the key cause of higher smoke emissions with increasing EGR levels. The marginal reduction in FSN when normalized* against the exhaust mass flow rates would be offset by the increase in air flow rates at higher intake pressures, suggesting that the change in PM mass is likely to be small. This is shown in Fig. A4.1 in Appendix A4, assuming that the correlation for converting FSN into PM mass was valid at all intake charge dilution levels.

Smoke emissions at 2500 rpm were consistently higher compared to 1500 rpm throughout the EGR sweep, the main reason being the shorter ignition delay (will be discussed later in this section) on absolute time basis at higher engine speed. It can also be partly attributed to the lower injection pressure (60 MPa) at 2500 rpm compared to 90 MPa at 1500 rpm. There was a rapid reduction in smoke emissions from the peak smoke value with increased intake charge dilution going into the LTC regime at higher speed. It is hypothesized that higher piston speed at 2500 rpm would enhance the in-cylinder fluid motion and improve the fuel-oxygen premixing for a fixed ignition delay and injection pressure. This enhanced in-cylinder motion at higher engine speed might result in a locally leaner (less rich) oxygen-fuel charge at the SOC compared to lower speed. Therefore, the reduced ignition delay (on absolute timescale) and the lower fuel injection pressure at higher engine speed would be compensated by the enhanced in-cylinder motion to produce similar smoke emissions at higher intake charge dilution.

* PM mass [g/kg of fuel] = Soot concentration [mg/m^3] × exhaust mass/kg of fuel [kg/kg of fuel] × 10^{-3} × T_{ref} [K] × R [$kJ.kg^{-1}.K^{-1}$] × $1/p_{ref}$ [kPa^{-1}], where T_{ref} and p_{ref} are the reference temperature (298 K) and reference pressure (100 kPa), respectively [AVL Smoke meter Manual, 2005]. R is the gas constant of air (0.287 $kJ.kg^{-1}.K^{-1}$). Soot concentration (mg/m^3) is given by Equation (3.1) in Chapter 3.

The variations in THC and CO emissions and GISFC with intake oxygen mass fractions are shown in Fig. 4.5. THC emissions increased at high EGR levels, consistent with previous results [Colban *et al*., 2007; Musculus *et al*., 2007; Cong *et al*., 2010; Cong, 2011]. High hydrocarbon emissions at low intake oxygen mass fractions (Y_{O2} <13%: equivalent to EGR levels >45%) were attributed to either over-rich or over-lean mixtures [Colban *et al*., 2007; Mendez *et al*., 2009]. It has been suggested that THC may come from over-lean mixtures because of the longer ignition delay at lower oxygen mass fractions [Colban *et al*., 2007; Musculus *et al*., 2007]. However, the results presented here, where higher intake pressures reduced THC emissions at the same intake oxygen mass fraction, suggest that the THC originated from a locally fuel-rich mixture later in the combustion process. This can be explained by an increased probability of the unburned or partially oxidized fuel finding oxygen molecules at higher intake pressures due to higher oxygen volume concentrations (moles of oxygen per unit volume).

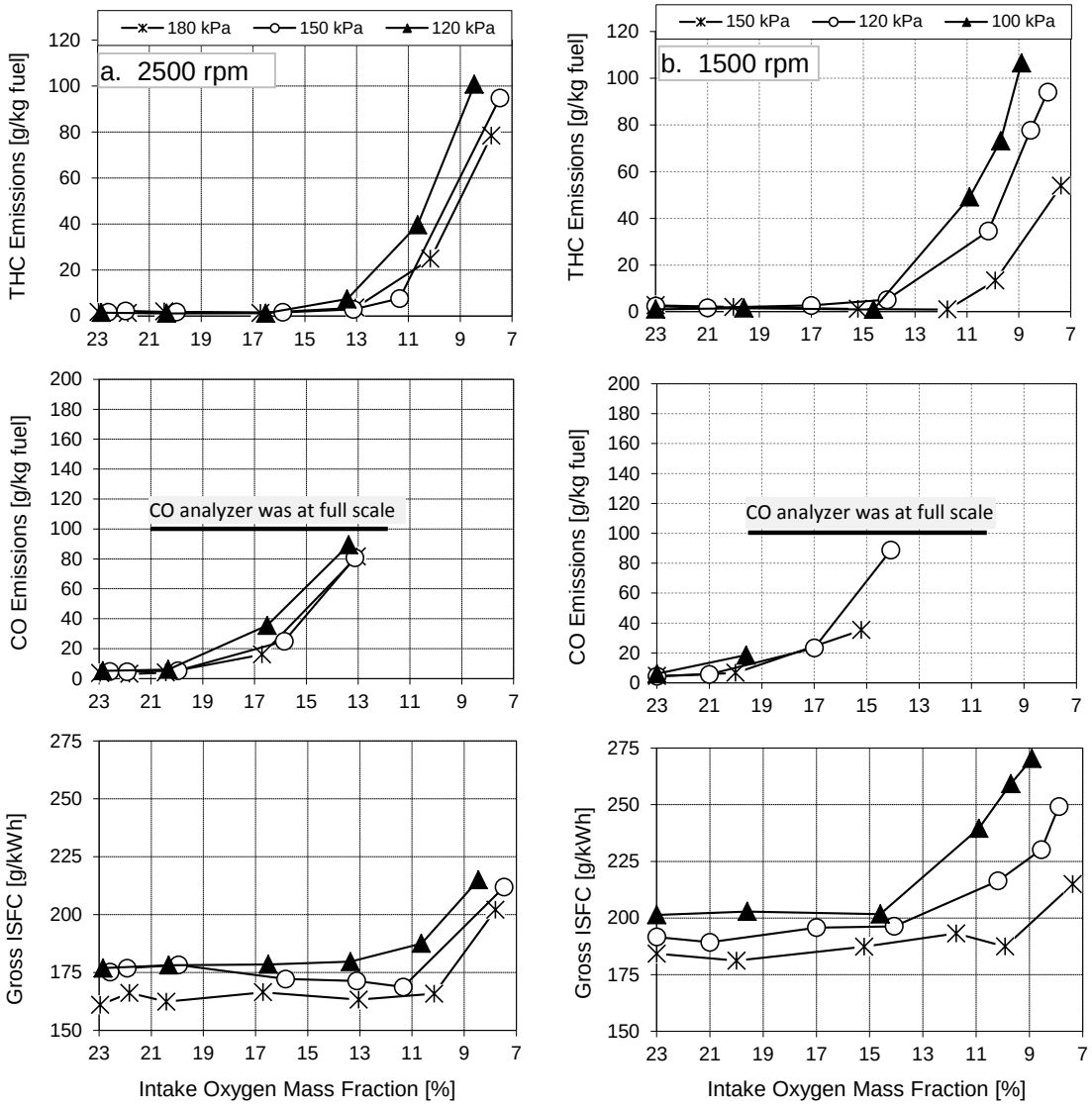

Fig. 4.5: Variations of THC, CO emissions and Gross ISFC with intake oxygen mass fraction for MBT injection strategy at variable intake pressures

For the high EGR parts of the work presented here, CO levels were beyond the measurement range of the instrument and hence were not available. CO emissions were high with increased intake charge dilution, although CO emissions increased more rapidly than THC emissions. CO emissions decreased with higher intake pressure at the intermediate EGR levels consistent with the trend observed for the THC emissions. Higher CO emissions with increased intake charge dilution are envisaged to be originating either from the locally rich or stoichiometric fuel-oxygen mixture which would get exacerbated due to the reduced flame temperature and low in-cylinder oxygen concentration in the high-EGR LTC operation.

Gross ISFC at 2500 rpm was consistently 4-7% lower compared to 1500 rpm throughout the EGR sweep at a given intake pressure. This is generally attributed to the lower heat transfer losses at higher engine speed. However, at 1500 rpm, GISFC increased considerably at the lowest intake oxygen mass fraction (Y_{O2} ~8-9%) at 100 kPa and 120 kPa intake pressures because of the increased intake charge dilution (indicated by the increased global oxygen based equivalence ratios shown in Fig. 4.1b) and retarded combustion phasing (refer to Fig. 4.2b). The trend of GISFC with variable intake pressure over the EGR sweep, shown in Fig. 4.5, can also be explained with the help of the GIMEP results shown in Fig. 4.6 (recalling that fuel quantity was fixed). The latter figure shows that higher intake pressure resulted in an increase in GIMEP at the same intake oxygen mass fraction, consistent with the IMEP trends observed in conventional diesel combustion with higher boost pressure reported in the literature [Tanin *et al*., 1999].

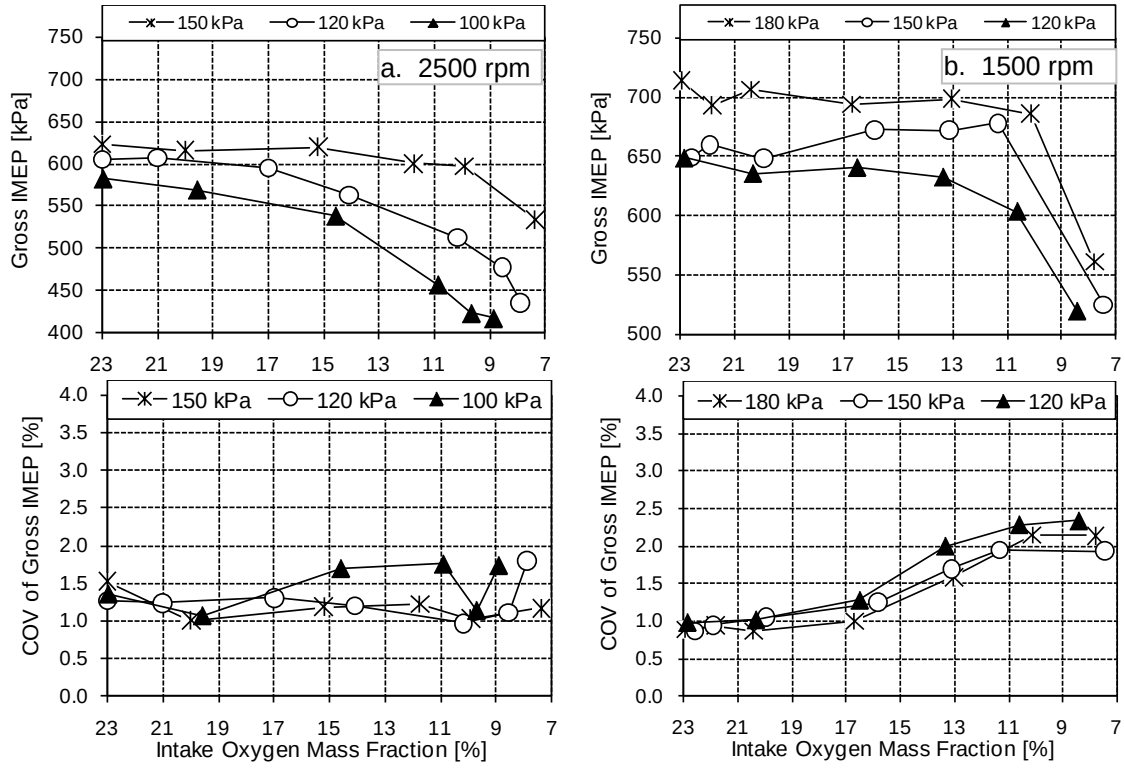

Fig. 4.6: Gross IMEP and COV of GIMEP with intake oxygen mass fraction for MBT injection strategy at variable intake pressures

The increase in GIMEP at higher intake pressure can in part be attributed to lower heat transfer and advanced combustion phasing. Lower heat transfer is expected at higher intake pressure, because with a greater charge mass with increased intake pressure, the bulk average temperature of the in-cylinder gases will in general be lower for a given amount of fuel chemical energy released, which would reduce heat transfer losses for a fixed cylinder wall temperature. Higher intake pressure resulted in combustion phasing closer to TDC at high EGR levels resulting in more work being extracted in the expansion stroke, thus improving the thermal efficiency [Tanin *et al*., 1999]. This increase in efficiency with more advanced combustion phasing has been shown by other researchers to be an important engine control parameter [Klimstra *et al*., 1985; Kook *et al*., 2006]. Pumping work was not greatly affected since the differential between the intake and exhaust pressures was kept the same for all boost pressures, and it is this differential which primarily dictates the pumping work.

The magnitude and variability of the GIMEP were sensitive to charge dilution as shown in Fig. 4.6. Intake oxygen mass fractions below 11% led to reductions in the GIMEP for all intake pressures at higher speed. At lower speed, GIMEP reduced consistently with increased levels of intake charge dilution at lower intake pressures (100 and 120 kPa). However, at 150 kPa intake pressure and 1500 rpm engine speed, GIMEP was constant (~600 kPa) up to Y_{O2} ~10% and reduced to 550 kPa at Y_{O2} ~7%. Since the fuel flow rate was essentially constant, the reduction in GIMEP increased GISFC as shown in Fig. 4.5.

The coefficient of variation (COV) of GIMEP, an indication of cyclic variability in the combustion, remained almost constant at low EGR levels, but increased at higher EGR levels, the effect being more pronounced at higher engine speed. Even at high EGR levels at 2500 rpm, the COV of GIMEP was relatively low (<2.5%) as shown in Fig. 4.6a. Misfiring cycles were not observed even at the highest EGR levels. Combustion variability represented by the standard deviations of combustion phasings (CA5 and CA50), and the COV of peak energy release rate and peak cylinder pressure with the highest level of intake charge dilution at various intake pressures are listed in Table A4.1 in Appendix A4. These parameters were found to vary marginally at both speeds. In general, higher intake pressure reduced the variability in combustion phasing and the COV of peak pressure and energy release rate. Interestingly, for intake oxygen mass fractions below 11%, the COV of GIMEP remained almost constant and insensitive to boost pressure with the MBT injection timing strategy for 2500 rpm. For the 1500 rpm case, higher combustion variability was seen in the naturally aspirated mode (100 kPa) at higher intake charge dilution level; however, they were still lower than the 2500 rpm case at the corresponding intake charge dilution level. At 150 kPa intake pressure at 1500 rpm, there was no degradation in the combustion stability even at the highest intake charge dilution level as evident by similar COV of GIMEP throughout the EGR sweep. This suggests that the combustion at 1500 rpm was less susceptible to instability at higher charge dilutions with increased boost pressure compared to higher speed. Higher variability at higher speed

with LTC means that at higher engine speeds, there is less time for the reactions to occur and hence a greater probability of earlier bulk quenching, higher THC and CO emissions. The increased combustion variability may explain the higher THC emissions at higher engine speed consistent with an earlier investigation which showed that THC emissions correlate well with the COV of GIMEP in high-EGR LTC operation [Cong *et al*., 2010].

The MBT injection timing strategy, combined with the high levels of EGR required to achieve LTC had a significant impact on the ignition delay and combustion duration as shown in Fig. 4.7. A reduction in intake oxygen mass fraction increased the ignition delay, thereby facilitating better fuel-oxygen premixing prior to the start of combustion. In general, higher intake pressure reduced ignition delay, but the magnitude of the difference was substantially less than that of higher charge dilution. As explained earlier, the ignition delay in high-EGR LTC was approximately the same (on a ^{o}CA basis) irrespective of engine speeds; as such, 1500 rpm had higher ignition delay on an absolute time basis.

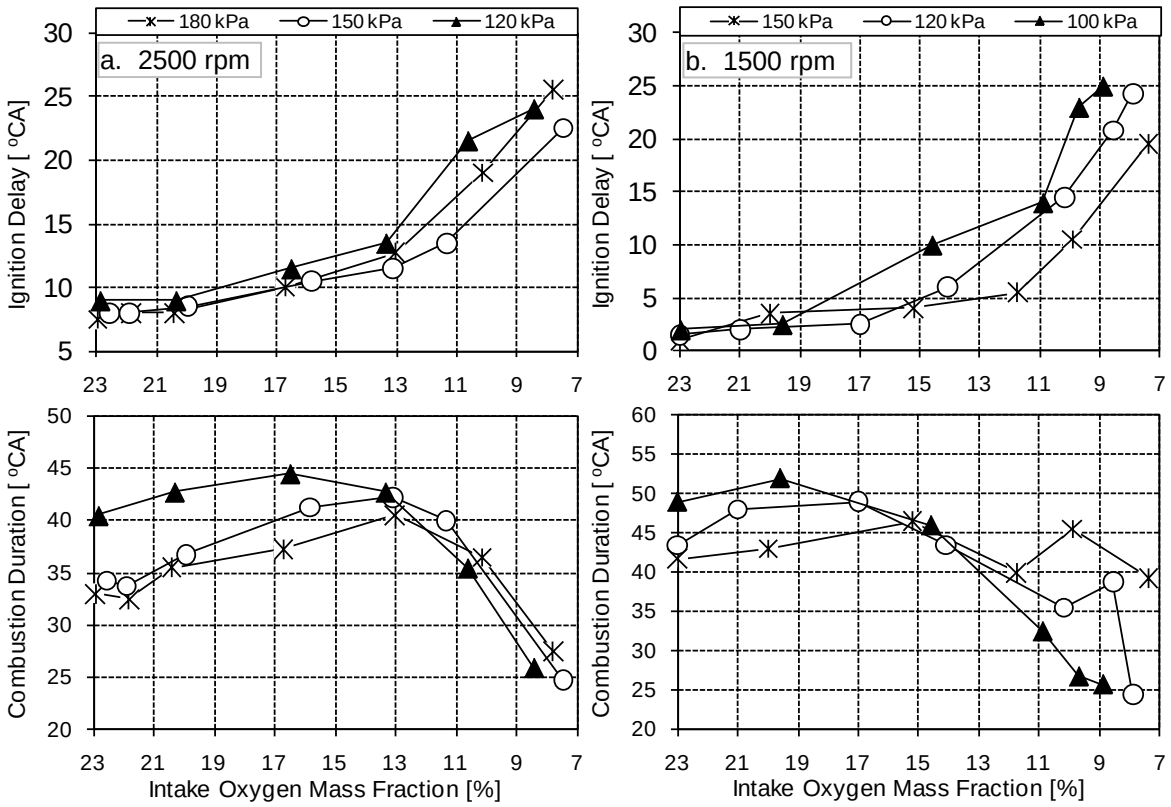

Fig. 4.7: Variations of ignition delay and combustion duration with intake oxygen mass fraction for MBT injection strategy at variable intake pressure

Combustion duration (CA95-CA5) shown in Fig. 4.7 was shorter both in terms of ^{o}CA and absolute time basis at higher engine speed at all intake charge dilution levels. Longer combustion durations at 1500 rpm and low EGR levels (i.e. higher intake oxygen mass fraction) could be

attributed to very advanced CA5 due to the pilot injection (~8% of the total fuelling quantity was in the pilot injection). Note that the pilot injection was used at 1500 rpm only for EGR levels below 40%. Higher engine speed of 2500 rpm also increased in-cylinder turbulence and swirl velocity and enhance fuel-air mixing, thus, leading to shorter combustion durations on a time basis. With increased intake pressure and low EGR, combustion duration was reduced for both the speeds at higher intake oxygen mass fraction. On the other hand, at higher charge dilution (Y_{O2} <11%), higher intake pressures appeared to increase the combustion duration. This is thought to be a result of better late-phase combustion, with the onset of bulk quenching delayed by both the greater availability of oxygen molecules at higher intake pressure and the higher in-cylinder temperatures due to the advanced CA50, shown in Fig. 4.2.

Bulk quenching is characterized by incomplete fuel oxidation in the regions of the combustion chamber where local temperature, local equivalence ratio and oxygen concentration are insufficient to sustain fast and complete oxidation of the fuel. This principally occurs during the expansion stroke, and typically the main limiting factor is excessively low local temperature [Benajes *et al*., 2010]. At high-EGR levels (i.e. lower intake oxygen mass fractions) the longer combustion duration shown in Fig. 4.7 at higher intake pressure indicated more complete oxidation of the fuel. This is supported by the lower THC and CO emissions with higher intake pressure at high-EGR LTC and the intermediate EGR operating conditions.

The general combustion results presented in Fig. 4.7 are supported by the energy release plots shown in Fig. 4.8 for both speeds at the highest intake charge dilution levels. The cool flame reactions, typical of LTC, occurred before TDC and depended on the injection timing. The timing and phasing of the 'cool flame' reactions may also have significantly influenced the phasing and magnitude of the main combustion [Cong *et al*., 2011b]; however, these low-temperature reactions varied discernibly with intake pressure.

The shape of the energy release plot suggests that the combustion is primarily premixed, with no clear indication of a mixing-controlled combustion phase independent of engine speeds. Peak energy release rate with increased intake pressure occurred earlier in the expansion stroke for both the speeds attributed to the advanced injection timing and reduced ignition delay for the main combustion. This also supports the earlier supposition that increasing intake pressure has delayed the onset of bulk quenching and is allowing more complete oxidation of the fuel. However, these effects are highly sensitive to the injection timing selected, and hence may have been confounded by the use of the ‘MBT’ timing strategy.

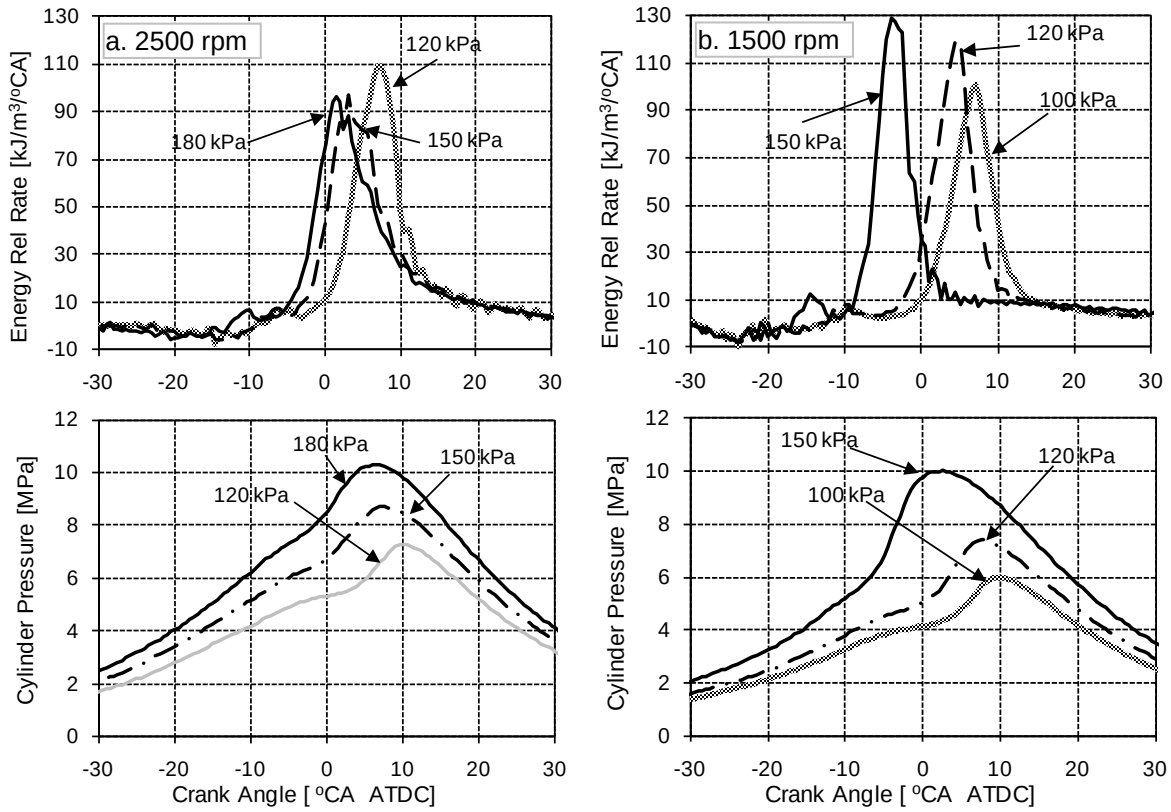

Fig. 4.8: Energy release rate and in-cylinder pressure for MBT injection strategy at three intake pressures [a: 2500 rpm— 64% EGR (Y_{O2} ~7.8%) at 180 kPa; 65% EGR (Y_{O2} ~7.5%) at 150 kPa; and 63% EGR (Y_{O2} ~8.5%) at 120 kPa. b: 1500 rpm— 63% EGR (Y_{O2} ~7.4%) at 150 kPa; 61% EGR (Y_{O2} ~7.9%) at 120 kPa; and 57% EGR (Y_{O2} ~8.9%) at 100 kPa]

It is interesting to note that the energy release rate with reduced intake pressure at 2500 rpm occurred later in the expansion stroke and had a larger magnitude compared to the other two boost pressure cases (150 kPa and 180 kPa) as shown in Fig. 4.8a. This is consistent with the earlier findings reported by Benajes *et al.* [2010], who attributed this effect to a longer ignition delay at lower in-cylinder gas density. However, contrary to the cited work [Benajes *et al.*, 2010], the ignition delays between SOI and the start of the low temperature combustion reactions are essentially constant for all three intake pressures, taking into account the differences in the SOI timings (120 kPa and 150 kPa at -27 ^{o}CA ATDC, 180 kPa at -33 ^{o}CA ATDC). However, the delay between the start of LTC reactions and high-temperature energy release does vary, being significantly shorter at 150 kPa compared to 120 kPa and 180 kPa. However, the peak energy release rate was higher at the lower intake pressure. Again, note that the higher magnitude of the peak energy release rate at 120 kPa intake pressure did not necessarily result in higher GIMEP at 2500 rpm (refer to Fig. 4.6a) due to the retarded CA50 (refer to Fig. 4.2a). The trend of energy release rates seen at higher engine speed was not seen at lower speed where the peak of the energy release rate increased with higher intake pressure despite having a lower ignition delay.

4.3.2 Comparison of Injection Timing Strategy at Constant Intake Pressure and Engine Speed

In the previous subsection, it was found that the combustion phasing strategy had a large impact on combustion stability and the onset of bulk quenching which influences the emissions of combustion by-products. Particularly, higher combustion instability and higher emissions of combustion by-products were more pronounced at higher speed. Hence, in this section, two fuel injection timing strategies (corresponding to MBT injection timing and constant CA50) are compared at a constant intake pressure (180 kPa) at higher engine speed (2500 rpm). The start of injection timings and the corresponding CA50 and combustion duration are shown in Fig. 4.9 over a range of intake oxygen mass fractions at a constant intake pressure (180 kPa) for both the injection timing strategies. The EGR levels and the corresponding oxygen based equivalence ratios are shown in Fig. 4.10.

Interestingly, the oxygen based equivalence ratio was richer with MBT injection timing, although EGR levels were lower than the constant CA50 strategy. This was a result of less oxygen in the exhaust gas, which suggests higher oxygen utilization with the MBT injection timing strategy. The reduction of the oxygen content in the recirculated exhaust gases resulted in a lower intake oxygen mass fraction with the MBT strategy for a given EGR fraction. At higher EGR levels, the exhaust oxygen concentration (not shown) was 2% with the MBT timing strategy compared to 3.6% with the constant CA50 injection timing at the same intake oxygen mass fraction. This is due to improved combustion efficiency resulting in better oxygen utilization with MBT timing.

The combustion duration shown in Fig. 4.9 showed no significant difference between the injection timing strategies except at the lowest intake oxygen mass fractions (i.e. the highest EGR levels), where the combustion duration was actually increased with MBT timing. This is most likely a result of the earlier combustion resulting in more of the fuel burning before bulk quenching occurred. This agrees with the discussion in the previous subsection, that a longer duration of the combustion event under highly-dilute conditions was indicative of a more complete combustion and a delay in the onset of bulk quenching (relative to the start of combustion).

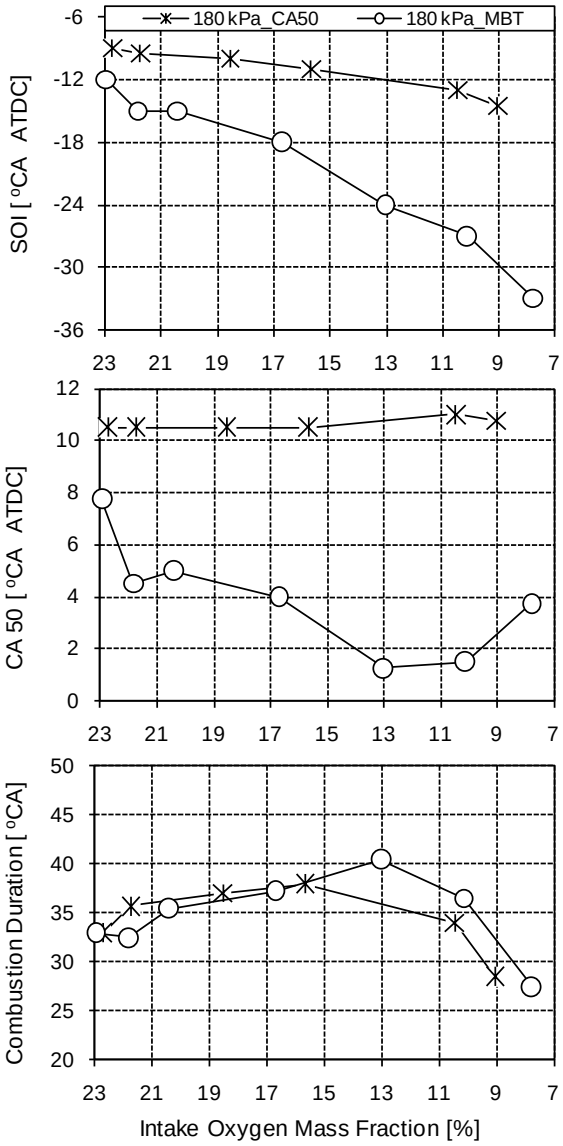

Fig. 4.9: Variations of the start of injection, CA50 and combustion duration at variable injection timings at 2500 rpm and 180 kPa intake pressure

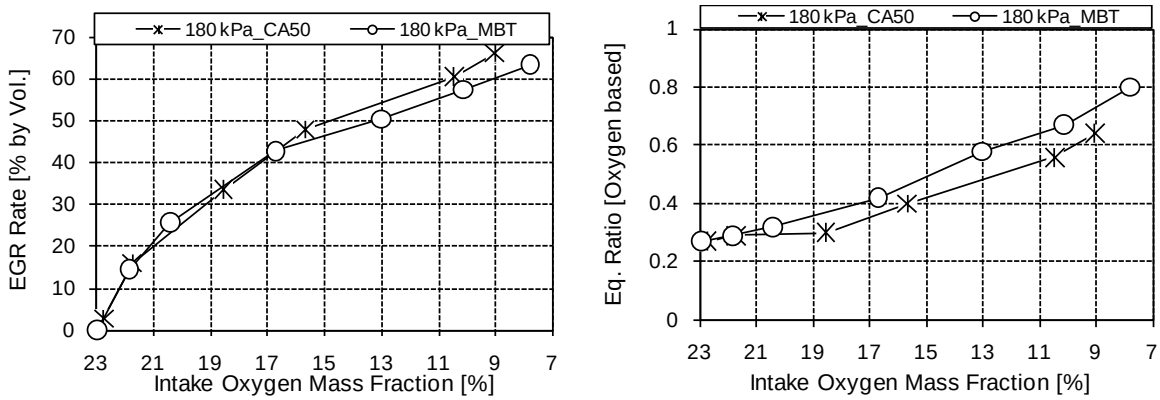

Fig. 4.10: Variations of EGR rate and equivalence ratio (oxygen based) at variable injection timings at 2500 rpm

The injection timing strategy also significantly influenced emissions. The advanced injection timing of the MBT strategy resulted in higher NO_X emissions with lower smoke as compared to constant CA50 injection timing for intake oxygen mass fractions between 23% and 17%, as shown in Fig. 4.11. At lower intake oxygen mass fractions, NO_X emissions became insensitive to injection timings; smoke emissions increased marginally at the intermediate intake oxygen mass fractions ($13\% < Y_{O2} < 10\%$) with advanced injection timings.

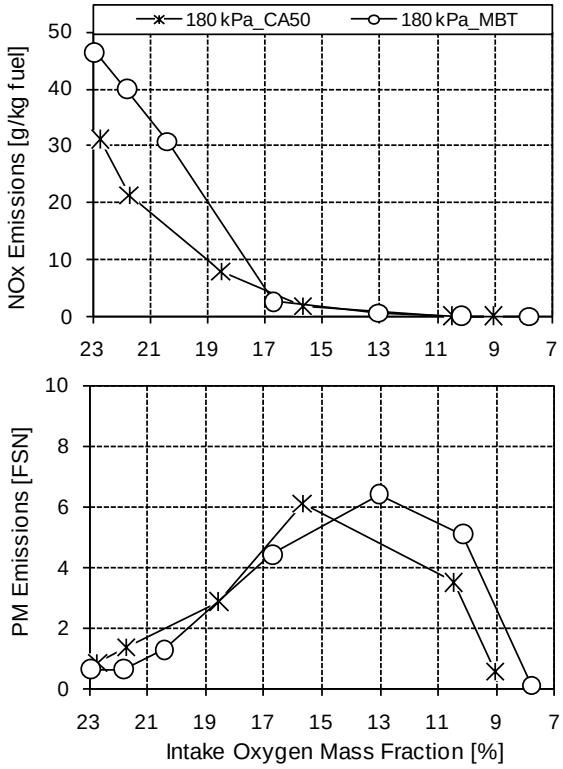

Fig. 4.11: Variations of NO_X and smoke emissions with intake oxygen mass fraction at variable injection timings at 2500 rpm

The ignition delay was longer with the MBT injection timings, especially at higher EGR levels. However, this did not necessarily increase THC emissions, suggesting that over-leaning of the early injected fuel was not a significant contributor to these emissions. This trend is shown in Fig. 4.12. In both the cases, bulk quenching, slower reaction rates and lower in-cylinder temperatures seemed to have a larger influence on THC emissions. THC emissions and GISFC deteriorated under more dilute charge conditions (higher EGR levels), the magnitudes of emissions and fuel consumption being lower with MBT injection timing.

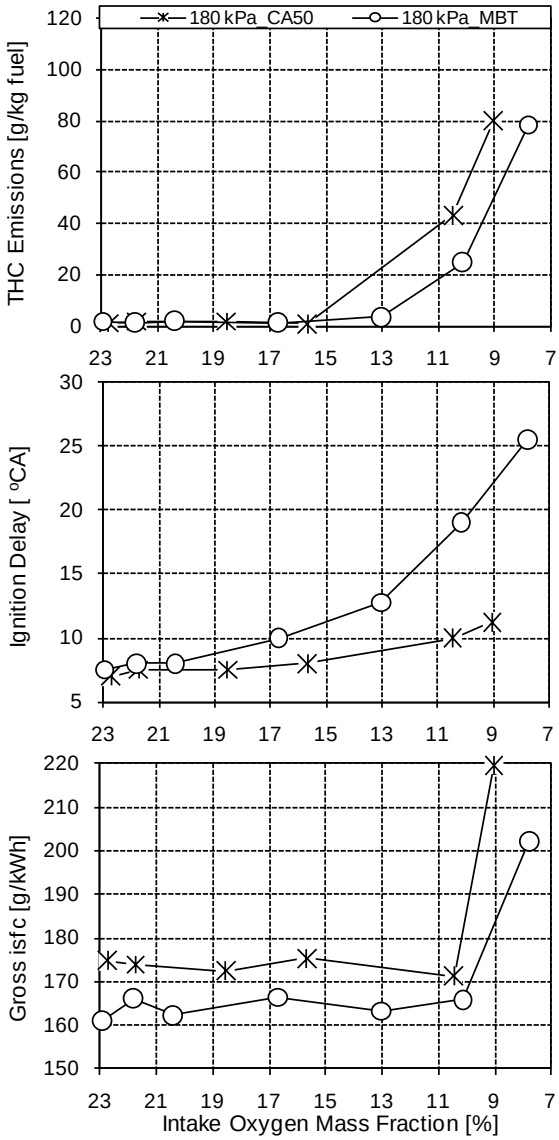

Fig. 4.12: Variations of THC emissions, ignition delay and GISFC at variable injection timings at 2500 rpm

The variability in the combustion event (demonstrated by the COV of GIMEP) increased with increased intake charge dilution under all the boost pressure conditions studied with constant CA50, as shown in Fig. 4.13a. This is opposite to the MBT case, where the more advanced timing 'stabilized' the combustion at lower intake oxygen mass fraction (higher EGR levels), as was shown earlier in Fig. 4.6. The increased instability at low intake oxygen mass fraction with constant (retarded) combustion phasing compared to advanced combustion phasing may be attributed to retarded injection timings that would lead to reduced combustion duration, poor fuel-oxygen mixing (due to shorter ignition delay with constant CA50 strategy shown in Fig. 4.12), lower in-cylinder temperature and bulk quenching that is in part offset through the use of MBT timing. This effect also allowed higher EGR levels to be used with MBT timing than with constant CA50 timings before combustion instability became unreasonably high.

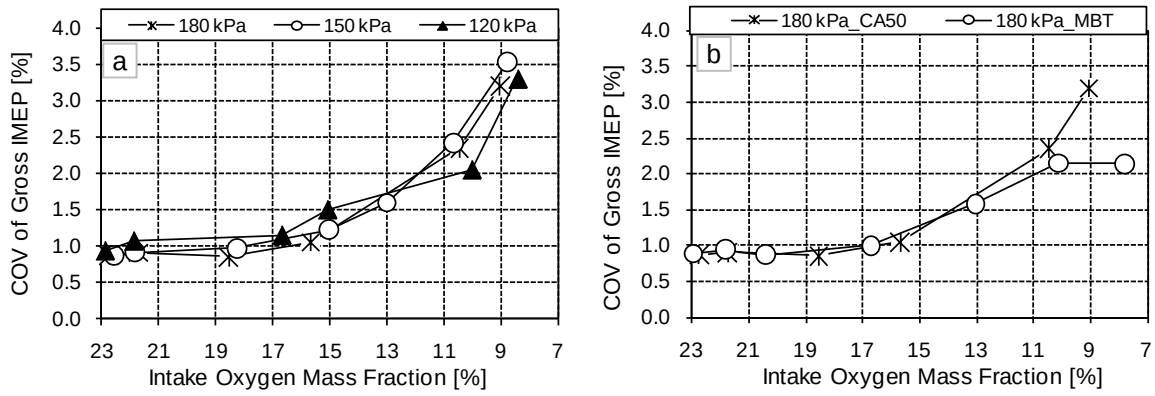

Fig. 4.13: Cyclic variations of GIMEP at 2500 rpm [a: with constant combustion phasing (CA50 ~10 ^{o}CA ATDC) injection timings at variable intake pressures; b: with constant intake pressure (180 kPa) at variable injection timings]

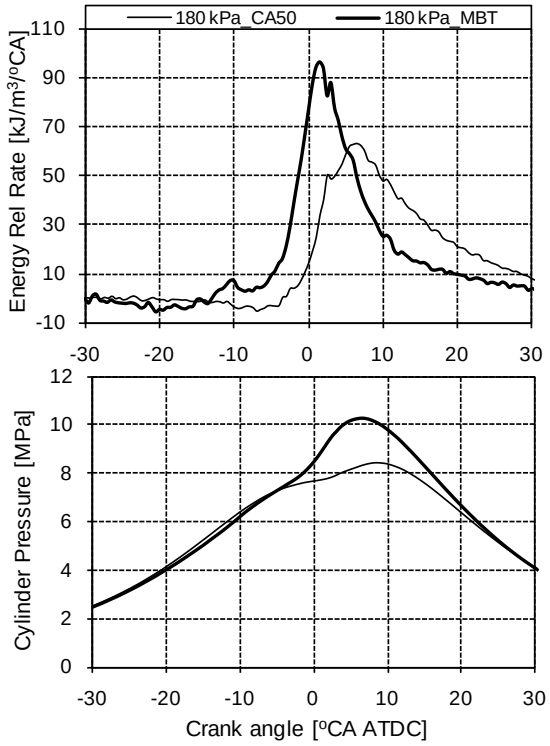

Fig. 4.14: Energy release rate and in-cylinder pressure at variable injection timings at 2500 rpm; 66% EGR (Y_{O2} = 9%) at constant CA50 strategy, intake temperature 96^{o}C; 63.5% EGR (Y_{O2} = 7.8%) at MBT injection strategy, intake temperature 103^{o}C

The energy release rates shown in Fig. 4.14 support the results seen in Fig. 4.13. Combustion with MBT injection timing occurred earlier and had a higher energy release rate. Note that MBT injection strategy had a lower intake oxygen mass fraction compared to the constant CA50 strategy indicating improved combustion efficiency resulting in better oxygen utilization with the MBT strategy. The earlier and more intense combustion resulted in a greater peak pressure for the MBT

case, resulting in higher output power for the same total fuel consumption. Similarly, the earlier combustion phasing in the MBT injection timing strategy delayed the onset of bulk quenching, thereby improving the combustion stability. Interestingly, the distinct cool flame reaction observed in the MBT case was not seen with the constant combustion phasing strategy.

4.3.3 Variable Fuel Injection Pressures with MBT Injection Timings

The injection timing evaluated in the previous subsection has been shown to have significant influences on high-EGR LTC and conventional diesel combustion processes. The effects of injection pressure have the potential to be sensitive to boost pressure as higher intake pressure will lead to higher in-cylinder charge density during the injection event, influencing spray penetration and fuel-oxygen mixing. To evaluate this effect further, a comparison was made between two injection pressures (60 MPa and 90 MPa) at a constant intake pressure (150 kPa) with MBT (advanced) injection timings at the higher engine speed of 2500 rpm. The injection pressure influenced the combustion event, with longer injection duration at lower injection pressure. Hence, the start of injection was advanced for the 60 MPa injection pressure as shown in Fig. 4.15. The magnitudes of the differences between the two injection pressures appear to become smaller with increasing intake charge dilution (higher EGR levels or lower intake oxygen mass fractions). The corresponding EGR levels and oxygen based equivalence ratios are shown in Fig. 4.16. Interestingly, the oxygen based equivalence ratio was richer with higher fuel injection pressure, although EGR levels were lower. Note that higher injection pressure at higher intake charge dilution level resulted in lower oxygen concentration in the exhaust gases (refer to Fig. 4.16) due to better oxygen utilization. This suggests higher oxygen utilization with higher injection pressure, similar to the effects with more advanced injection timing discussed in the previous section.

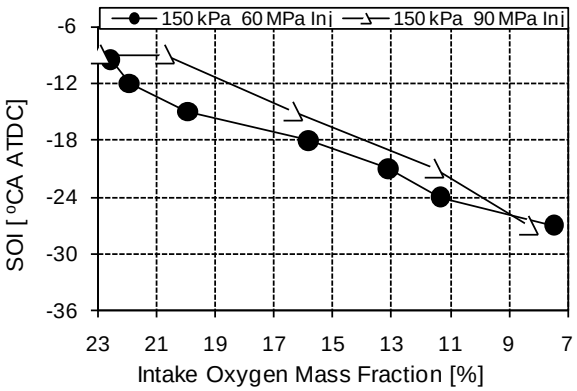

Fig. 4.15: Variations of SOI timings with intake oxygen mass fraction at variable injection pressures at 2500 rpm and 150 kPa intake pressure

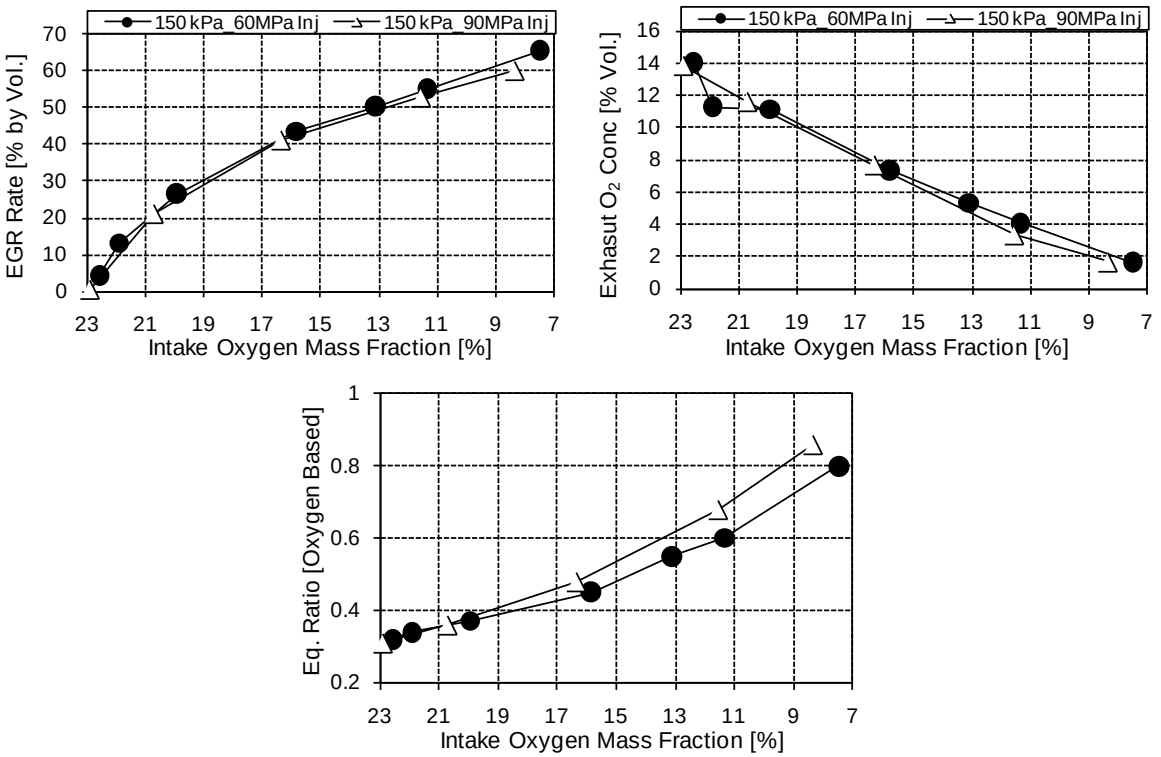

Fig. 4.16: Variation of EGR level, exhaust oxygen concentration and oxygen based equivalence ratio with intake oxygen mass fraction at variable injection pressures at 2500 rpm

Higher injection pressures reduced smoke emissions irrespective of intake oxygen mass fraction, although the peak smoke emissions corresponded to the same intake oxygen mass fraction. These results are shown in Fig. 4.17. There were no discernable influences on NO_X emissions (not shown), which were extremely low at ~10 ppm.

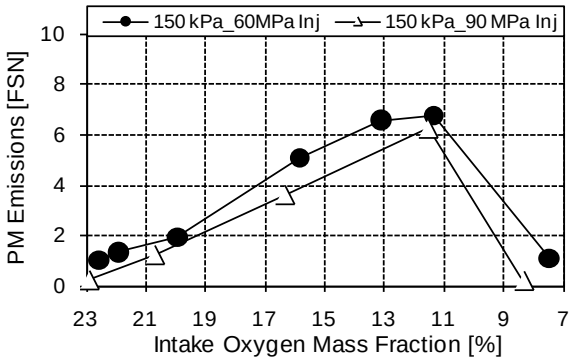

Fig. 4.17: Variations of smoke emissions with intake oxygen mass fraction at variable injection pressures at 2500 rpm

Higher fuel injection pressure did lead to lower GISFC, as shown in Fig. 4.18. This may have resulted from improved fuel atomization and/or better fuel-oxygen mixing (as shown by the lower exhaust oxygen concentration in Fig. 4.16). It should be noted that as this is the GISFC, it explicitly

excludes any increase in fuel pump work required to achieve the higher fuel rail pressure. Injection pressure showed no significant effects on THC emissions or combustion stability (as represented by the COV of the GIMEP); these results are not shown here.

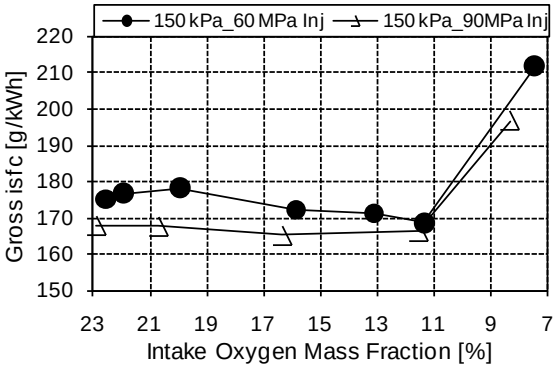

Fig. 4.18: GISFC with intake oxygen mass fraction at variable injection pressures at 2500 rpm

4.4 Effects of Variable Intake and Injection Pressures on Particle Number and Size Distributions

The number and size distributions of the emitted particles are important especially in high-EGR LTC operation, where SOF contributes to a significant proportion of the total PM mass [Ogawa *et al*., 2007]. The number spectral densities of the particulates were determined at a fixed operating condition (2500 rpm and 16 mg/cycle fuelling quantity) at variable intake pressures (120 and 180 kPa) and variable injection pressures (60 and 90 MPa) as shown in Figs. 4.19-4.21 both in conventional diesel combustion (EGR levels varying between 0% and 20% by volume) and high-EGR LTC (EGR levels varying between 55% and 65% by volume depending on the intake pressure). Note that PN measurement was not conducted at the intermediate EGR levels (between 20 and 55%) due to very high smoke emissions. PN measurement was carried out with a Cambustion DMS500 fast particulate spectrometer. Both the number and volume spectral densities of the particulate are shown in the figures to assess the relative contributions of the exhaust particles towards PN and PM mass respectively. The conversion from particle number to volume distribution is explained in Sec. 3.3.2 in Chapter 3.

It can be seen from the figures that both the particle number concentration and size increased with the introduction of EGR in conventional diesel combustion. Conventional diesel combustion was dominated by the particles in the ‘accumulation mode’ (30 nm to 200 nm) and no distinct ‘nucleation-mode’ particles (<30 nm diameter) were seen at lower injection pressure (60 MPa) independent of the intake pressures (refer to Figs. 4.19 and 4.20). Similarly, at higher injection pressure (90 MPa), in the conventional diesel combustion without EGR, no bimodal or Gaussian distribution was seen at 180 kPa intake pressure (refer to Fig. 4.21). However, distinct ‘nucleation mode’ particles with particle size ~10 nm were seen. Similar unimodal distribution with ~10 nm particles in the ‘nucleation mode’ were also seen at 120 kPa intake pressure at 90 MPa injection

pressure (not shown here). These results are consistent with earlier publications, where high injection pressure shifted the number and size distributions towards more nuclei mode particles and fewer accumulation mode particles [Pagan, 1999; Leidenberger *et al*., 2012]. For conventional diesel combustion, the nucleation mode particles are thought to be primarily condensed liquid droplets, comprising of sulphuric acid (sulphuric acid originating from sulphur in the lubricating oil rather than from the diesel, which was extremely low at 8 mg.kg^{-1}), water and volatile hydrocarbons that have nucleated in the exhaust stream [Khalek *et al*., 2000].

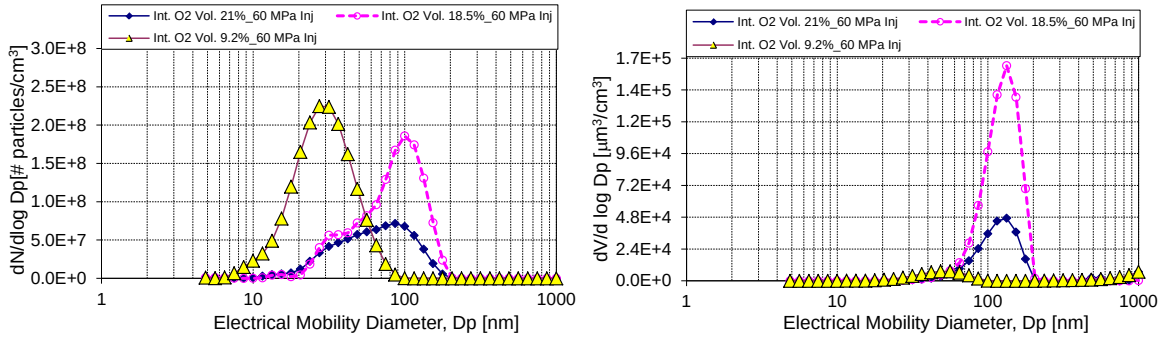

Fig. 5.19: Particulate size distributions with EGR sweep at 60 MPa injection pressure and 120 kPa intake pressure at 16 mg/cycle fuelling quantity and 2500 rpm speed

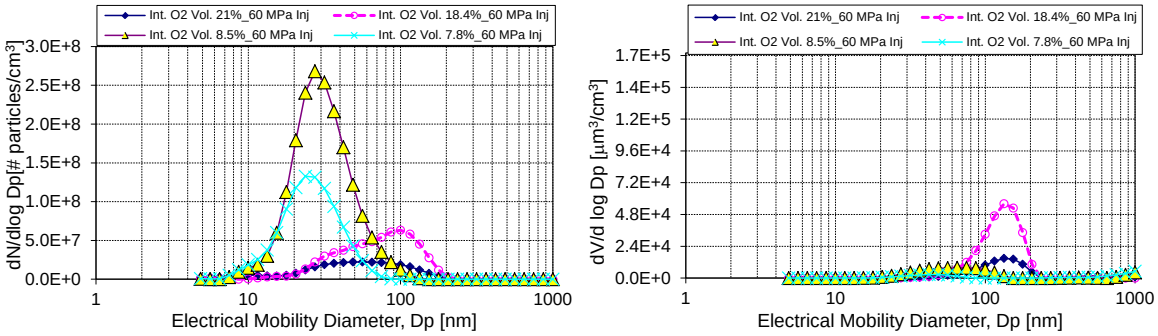

Fig. 4.20: Particulate size distributions with EGR sweep at 60 MPa injection pressure and 180 kPa intake pressure at 16 mg/cycle fuelling quantity and 2500 rpm speed

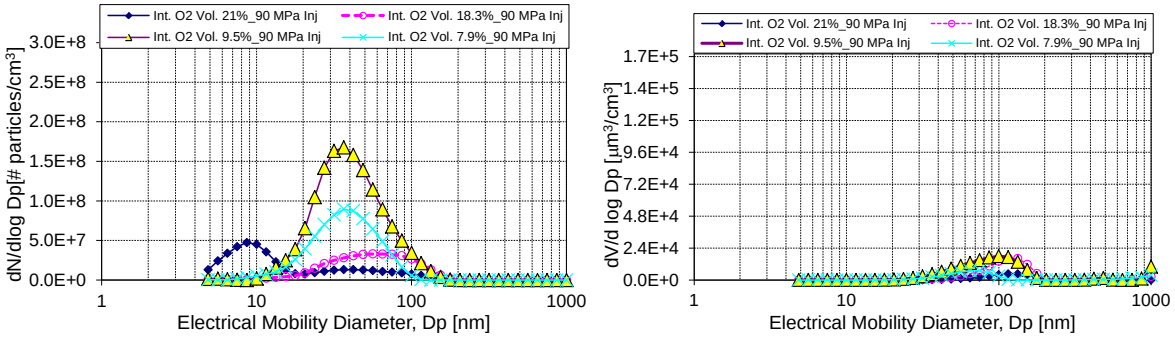

Fig. 4.21: Particulate size distributions with EGR sweep at 90 MPa injection pressure and 180 kPa intake pressure at 16 mg/cycle fuelling quantity and 2500 rpm speed. [N: number; V: volume].

Conventional diesel combustion with low levels of EGR was characterized by an increase in particle number and volume concentration, thus, contributing to the overall increase in the PM mass. No nucleation mode particles were seen with the introduction of low levels of EGR even with increased injection pressure (90 MPa) at higher intake pressure (refer to Fig. 4.21) and the log-normal distribution changed from nucleation mode to accumulation mode. This indicates that various particles in the exhaust stream (both engine-out particles and particles that have nucleated in the exhaust stream) would make greater contribution to the total PM mass. It is interesting to note that the volume fraction of the particles shown in Figs. 4.19 and 4.20 qualitatively correlate well with the measured smoke emissions (in terms of FSN; see Fig. 4.4a).

With very high intake dilution (high-EGR LTC), there was a steep increase in the PN and the spectrum was characterized by the nucleation mode particles with diameters ~30 nm with no significant increase in the particle volume concentration which correlates well with the lower smoke emissions in high-EGR LTC operation. It is likely that the PM composition changes from the black carbon dominated mode in conventional diesel combustion to the SOF mode in high-EGR LTC operation which was supported qualitatively by the change of the filter paper colour to more grey/yellow than black. The higher PN in high-EGR LTC operation may be because of the nucleation of the SOF. The particle volume, shown in Figs. 4.19-4.21, seem to indicate an increase in particle size in high-EGR LTC conditions compared to baseline conventional diesel cases. This may be due to oil droplets, although it is unclear.

The particle number concentrations were normalized* on per kg of fuel basis compensating for the reduced volume flow of the exhaust gases due to increased EGR level. The particle numbers normalized for the exhaust flow rate at various intake charge dilution levels at various intake and injection pressures are shown in Fig. 4.22. Note that in the figure below, the intake charge dilution levels are presented in terms of the intake oxygen volume fractions rather than the intake oxygen mass fractions. It can be seen from the figure that at a given intake and injection pressure, particle numbers were the lowest without EGR which increased at low EGR levels. However, the PN concentration increased significantly with high-EGR LTC operation, and decreased marginally with further intake charge dilution. The particle number concentrations in high-EGR LTC operation were at least 2 to 3 times more than no EGR cases.

---

* Particle numbers [# particles/kg of fuel] = Particle numbers [# particles/cm^3] × exhaust mass/kg of fuel [kg /kg of fuel] × 10^6 × T_{ref} [K] × R [$kJ.kg^{-1}.K^{-1}$] × $1/p_{ref}$ [kPa^{-1}]

where T_{ref} and p_{ref} are the reference temperature (273 K) and reference pressure (100 kPa) respectively [DMS User Manual, 2010]. R is the gas constant of air (0.287 $kJ.kg^{-1}.K^{-1}$).

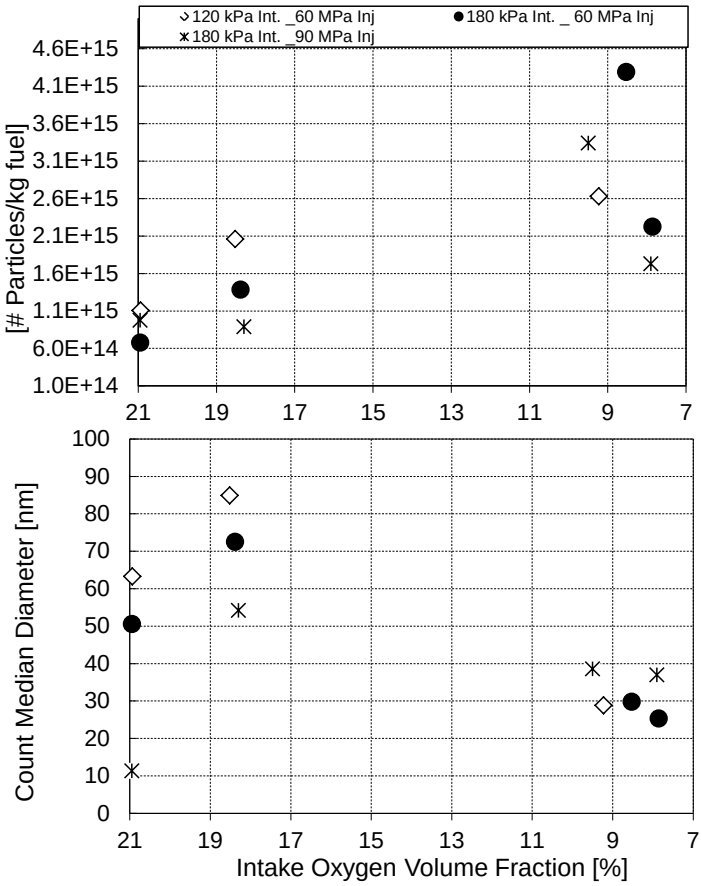

Fig. 4.22: Normalized particulate numbers and particulate size at various intake and injection pressures at different intake charge dilution at 16 mg/cycle fuelling quantity and 2500 rpm speed

The cumulative spectrum was used to calculate the count median diameter (CMD) of the particles, which corresponds to 50% of the total number of particles in the defined size range. CMD varied between 25 and 40 nm for high-EGR LTC operation with different operating parameters and were seen to be relatively insensitive to the intake and injection pressures. Conventional diesel combustion (no and low EGR levels) was characterized by particle CMD varying from 10 to 85 nm; CMD decreased with increasing intake and injection pressures. In summary, these results indicate that engine operation in the LTC mode would result in a significant increase in PN and reduction in size, which needs to be considered for the upcoming emissions regulations. The use of a DOC might substantially remove the SOF that may nucleate to form new particles in the exhaust stream. However, low exhaust temperature and low oxygen concentration in the exhaust may reduce the conversion efficiency of the DOC significantly as the light-off temperature of DOC increases with decreasing oxygen and increasing THC and CO levels [Johnson, 2010]. Note that exhaust temperature in high-EGR LTC operation was ~50^{o}C lower than conventional diesel operation. For example, at 16 mg/cycle fuel quantity, 2500 rpm (150 kPa intake pressure, 90 MPa injection pressure and ~90^{o}C intake temperature), exhaust temperature in conventional diesel combustion (with 21% EGR) was 297^{o}C compared to 241^{o}C in high-EGR LTC operation (60% EGR). It is

reported that DOCs are being developed to use with premixed combustion engine strategies that function better at low exhaust temperatures, low oxygen levels and at high THC and CO levels [Johnson, 2010].

4.5 Load Enhancement with MBT Injection

Enhancing the LTC load boundary of an engine through modification of the combustion chamber design and fuel injection system or by alteration of the compression ratio (either geometric compression ratio or effective compression ratio by late intake valve closing) is a topic of extensive research by several researchers [Murata *et al*., 2007; He *et al*., 2008; Dec, 2009; Li *et al*., 2009; Kuhnert *et al*., 2010]. However, for a given engine configuration, higher load in high-EGR LTC operation can be achieved by increasing the boost pressure [Colban *et al*., 2007; Asad and Zheng, 2009]. As discussed in Sec. 4.3.1, the effectiveness of EGR to reduce NO_X emission was evident as NO_X emissions decreased monotonically with increasing EGR. At high EGR levels, NO_X was unaffected by increased boost pressure. The increase in intake pressure increased the moles of oxygen per unit volume in the cylinder and reduced the oxygen based equivalence ratio. At very high EGR levels, increased boost pressure reduced smoke and combustion by-products emissions. Therefore, with the increase in boost pressure, the in-cylinder mass of oxygen could be increased for a given EGR level and the additional oxygen mass would then make it possible to increase the fuelling quantity that could increase LTC load without increasing the smoke and combustion by-product emissions significantly.

With the addition of the highly flexible boost system to the research facility (as described in Chapter 3), it was envisaged to increase the LTC load limit at higher speed. Higher speed was selected, as the boost pressure in a turbocharged diesel engine is expected to be higher at higher speed as the turbocharger would operate in a more efficient zone (and there is a possibility that the turbocharger will not be hitting the surge limit) to achieve the high boost pressure required to enhance the LTC load limit. The boost pressure used for achieving high load LTC operation is consistent with the achievable boost pressure at high load and high speed operating condition as would normally be encountered while following the NEDC driving cycle. Constant fuelling quantity (~21 mg/cycle) at an intake pressure of 200 kPa without EGR was used throughout the EGR sweep. The EGR rate was variable between 0 and 64% by volume at a constant engine speed of 2500 rpm. The corresponding overall oxygen based equivalence ratio inferred from carbon balance results [Heywood, 1988] with the EGR sweep is shown in Fig. 4.23a, which increased from an overall very lean mixture at no EGR case to close to stoichiometric at the highest intake charge dilution. Note that the EGR sweep at a lower load (corresponding to 16 mg/cycle fuelling quantity) at 180 kPa intake pressure is also included in the figures to compare the combustion and emission characteristics at two different loads. The SOI timings for the EGR sweep are shown in Fig. 4.23b. The intake temperature was variable between 80^{o}C and 110^{o}C and did generally increase with high

EGR levels, similar to the case with 16 mg/cycle fuelling quantity at 2500 rpm at 180 kPa intake pressure shown in Fig. 4.24. The operating conditions are specified in Table 4.1.

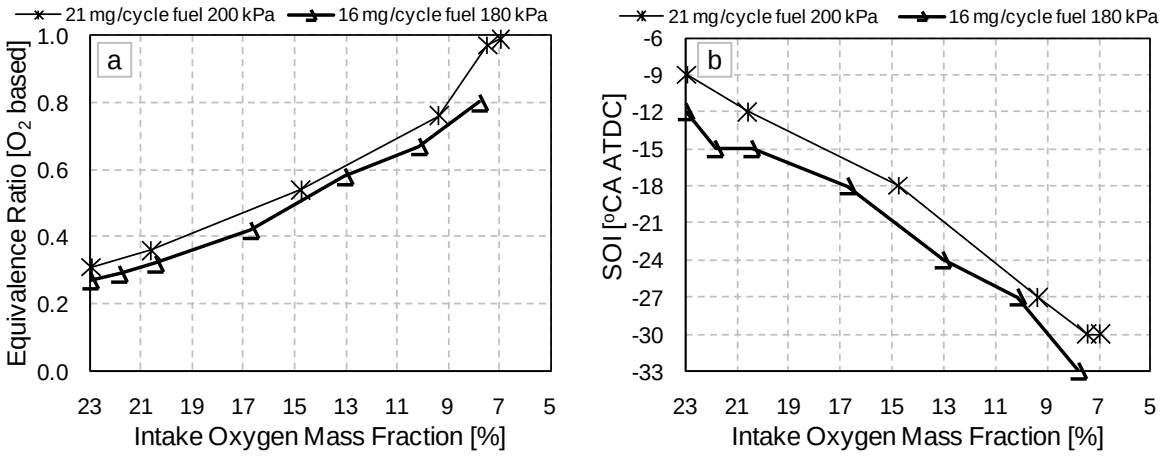

Fig. 4.23: a. Variations of oxygen based equivalence ratio; b. variations of SOI timings with 21 mg/cycle (200 kPa intake pressure) and 16 mg/cycle (180 kPa intake pressure) fuelling quantities at 2500 rpm engine speed

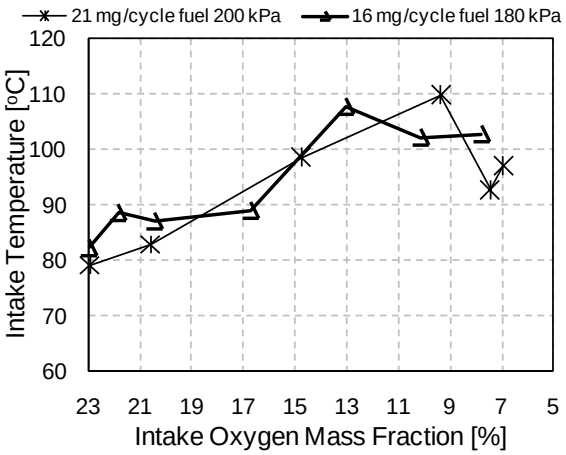

Fig. 4.24: Variations of intake temperatures with 21 mg/cycle (200 kPa intake pressure) and 16 mg/cycle (180 kPa intake pressure) fuelling quantities at 2500 rpm engine speed

In conventional diesel combustion (without EGR), the increase in fuelling quantity, intake and fuel injection pressures contributed to increased NO_X emissions compared to the low load case, as shown in Fig. 4.25. It can be seen from the figure that for both the operating conditions (21 mg/cycle and 16 mg/cycle fuelling quantities), near-zero NO_X emissions were achieved for intake oxygen mass fractions less than 13%. Smoke emissions were lower at lower EGR levels and increased at higher intake charge dilutions due to the well-known smoke-NO_X trade-off and reached a peak value of ~8 FSN at Y_{O2} ~9% (where near-zero NO_X was achieved). Smoke emissions reduced considerably with increased charge dilution in the LTC regime due to both improved fuel-air mixing

(due to increased ignition delay shown in Fig. 4.26) and lower flame temperature. Smoke emissions at the higher fuelling quantity were consistently lower in conventional diesel combustion despite a shorter ignition delay because of higher fuel injection pressure. However, smoke emissions with higher fuelling quantity in high-EGR LTC operation were higher than the low fuelling case despite a longer ignition delay, advanced CA50 (refer to Fig. 4.26) and lower intake oxygen mass fraction probably due to higher oxygen based equivalence ratio, as shown in Fig. 4.23.

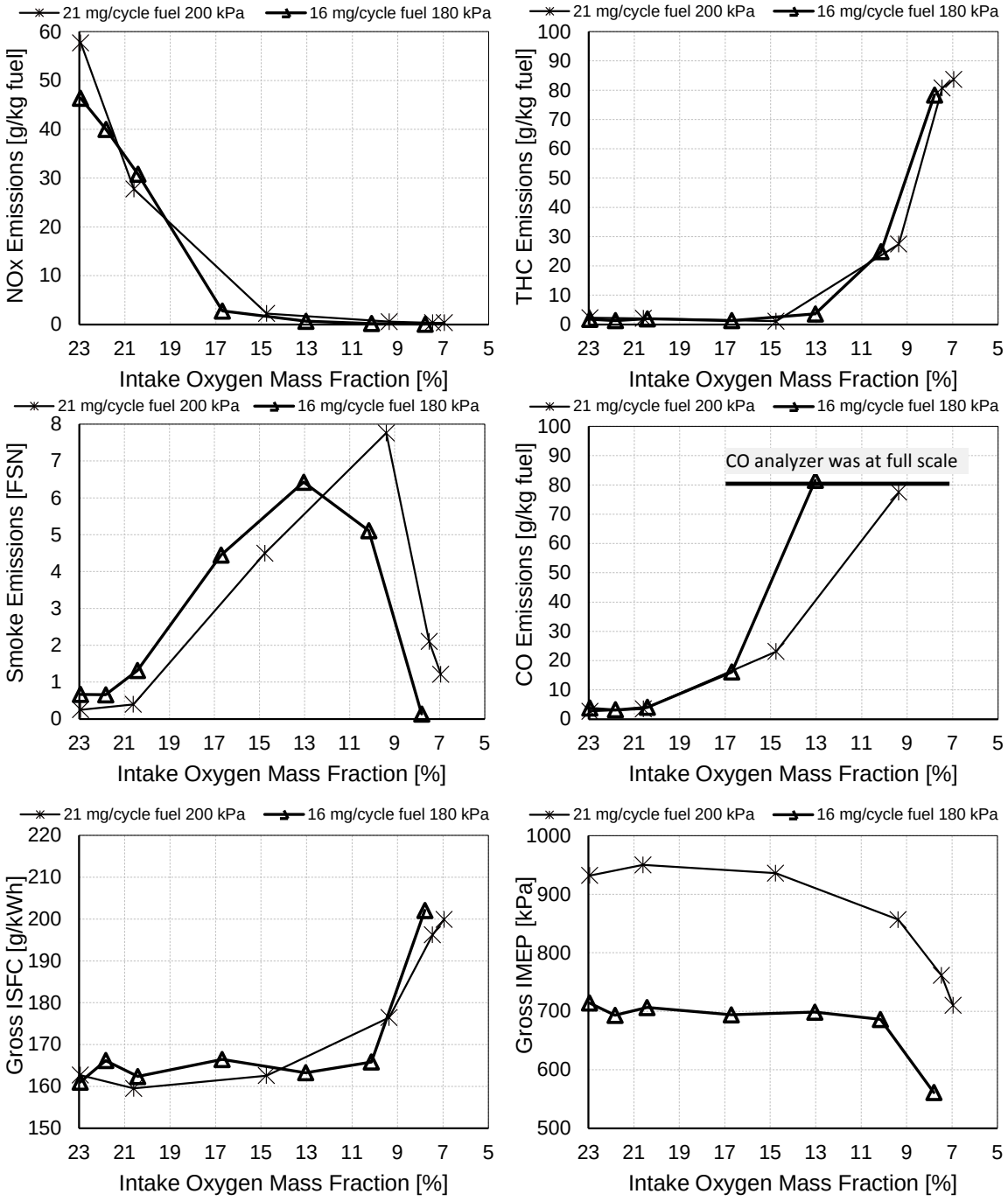

Fig. 4.25: Variations of NO_X, smoke, THC, CO emissions, GISFC and GIMEP with 21 mg/cycle (200 kPa intake pressure) and 16 mg/cycle (180 kPa intake pressure) fuelling quantities at 2500 rpm engine speed

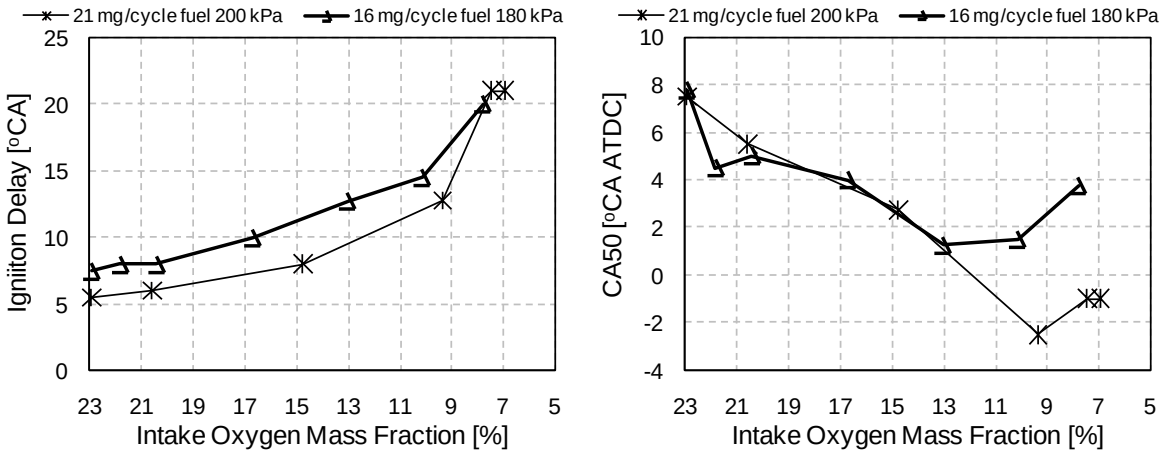

Fig. 4.26: Variations of ignition delay and combustion phasing (CA50) with 21 mg/cycle (200 kPa intake pressure) and 16 mg/cycle (180 kPa intake pressure) fuelling quantities at 2500 rpm engine speed

THC emissions over the range of intake oxygen mass fractions (shown in Fig. 4.25) increased considerably for Y_{O2} <13% for both the fuelling quantities. CO emissions also showed a similar trend although they could be measured only up to Y_{O2} ~9% for the higher fuelling case. The less rapid rise of CO emissions at higher fuelling quantity can be attributed to higher flame temperature at higher fuelling quantity compared to the lower fuelling case shown in the figure. It was discussed in Sec. 2.3.4 in Chapter 2 that CO oxidation depends on OH and O_2 concentration, the oxidation via OH being faster than via O_2. OH concentration is a strong function of temperature. Because of low flame temperature and low high-temperature reaction time, OH concentration in LTC is expected to be lower; therefore, CO oxidation is reduced. It has been reported that hydrocarbons also inhibit the oxidation of CO as the oxidation of CO to CO_2 comes late in the reaction scheme. Conversion of CO to CO_2 is retarded until all the original fuel and intermediate hydrocarbon fragments have been consumed [Glassman, 1996]. This phenomenon may also explain the trend of an early increase in CO emission compared to THC emission during an EGR sweep.

Now returning to the gross ISFC data shown in Fig. 4.25, it is observed that GISFC in the high load operating condition at 200 kPa intake pressure was similar to the low load case at 180 kPa intake pressure at all intake charge dilution levels. GISFC closely followed the trend of THC emissions which suggests that the reduction of combustion efficiency reduced GIMEP and therefore, increased the GISFC. Note that combustion efficiency could not be calculated as CO measurement was not possible at higher charge dilution levels.

Combustion stability was degraded with increased intake charge dilution at the higher load operating condition similar to the low load case (see Fig. 4.27). However, the COV of GIMEP at higher load was lower than the lower fuelling case at low intake oxygen mass fraction. It is hypothesized that advanced combustion phasing may favour the delayed onset of bulk quenching in

high-EGR LTC operation at higher load, thereby reducing the combustion variability as indicated by the COV of GIMEP. It is also expected that higher injection pressure (100 MPa) at higher fuelling quantity may influence the combustion stability compared to the lower injection pressure (60 MPa) at lower fuelling quantity case. Injection pressure was shown to influence the COV of GIMEP in the high-EGR LTC strategy [Cong *et al*., 2010; Cong *et al*., 2011b].

The net energy release rates shown in Fig. 4.28 at Y_{O2} ~7.5% for the two fuelling quantity cases shows that the combustion process was more intense at higher load. It is interesting to note that in spite of the intense premixed phase of combustion at higher fuelling quantity, the net energy release was also characterized by mixing-controlled combustion late in the combustion process as shown by the highlighted region. Note that the highlighted region shows an energy release rate similar to mixing-controlled conventional diesel combustion. For both the fuelling quantity cases, the initial phase of the net energy release rate was characterized by the pre-combustion cool-flame reactions typical of high-EGR LTC.

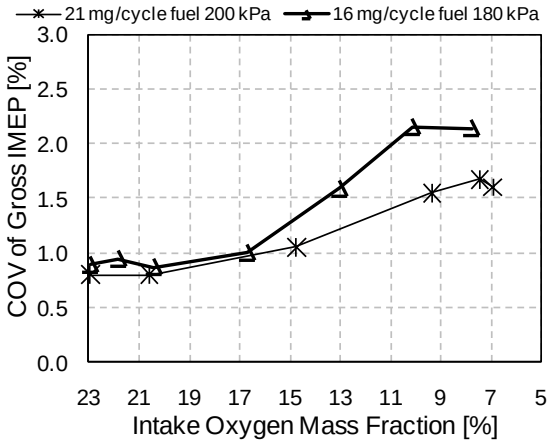

Fig. 4.27: Cyclic variations of GIMEP with 21 mg/cycle (200 kPa intake pressure) and 16 mg/cycle (180 kPa intake pressure) fuelling quantities at 2500 rpm engine speed

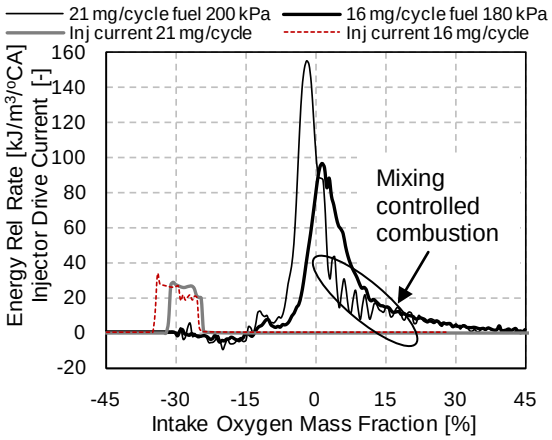

Fig. 4.28: Energy release rate and injector drive current signals at 7.5% Y_{O2} at two different fuelling quantities at 2500 rpm engine speed: [21 mg/cycle, 64% EGR, 100 MPa P_{inj}, SOI -30 ^{o}CA ATDC; 16 mg/cycle, 63.5% EGR, 60 MPa P_{inj}, SOI -33 ^{o}CA ATDC]

4.6 Conclusions

The work presented in this chapter investigated the effects of variable intake pressures and variable EGR levels under both conventional and low temperature diesel combustion regimes at two different speeds. The effects of variable fuel injection timing and injection pressures were also investigated at a constant speed and constant intake pressure. Particle number concentrations and size distributions were measured at several combinations of intake and injection pressures at various levels of intake charge dilution. Increased intake pressure enhanced the LTC load limit although smoke emission in LTC was higher compared to low load. It was found that:

1. Under LTC, unburned hydrocarbon and CO emissions and gross ISFC were reduced with higher intake pressures. Near-zero smoke and NO_X emissions were achieved at the same intake oxygen mass fraction (<9%) independent of engine speed for a fixed intake pressure.
2. Advancing the combustion phasing at high EGR levels through earlier injection (MBT) timing reduced THC emissions and GISFC at a given intake pressure compared to standard combustion phasing. Higher intake pressures with more advanced injection timing led to earlier combustion phasing (CA50) and lower GISFC compared to a constant combustion phasing strategy for the EGR sweep. With the MBT injection strategy, increasing the intake pressure reduced smoke emissions and shifted the peak smoke emissions towards lower intake oxygen mass fractions.
3. Combustion stability was relatively insensitive to boost pressure. While constant CA50 combustion phasing led to increasing levels of variability, MBT combustion phasing resulted in stabilized combustion at low intake oxygen mass fractions. Higher combustion variability was seen at higher speed; however, at lower engine speed, combustion stability remained almost the same independent of the intake charge dilution levels at higher intake pressure.
4. Higher injection pressure resulted in lower smoke and unburned hydrocarbon emissions, and improved GISFC, without influencing NO_X emissions in the high-EGR LTC regime.
5. Total particle numbers in high-EGR LTC operation increased compared to conventional diesel combustion (with no and low EGR level) independent of intake and injection pressures. High injection pressure reduced the count median diameter of the particles in conventional diesel combustion without EGR, whereas low EGR levels in conventional diesel combustion pushed the particles further into the accumulation mode. Higher intake pressure reduced the particle numbers both in LTC and conventional diesel combustion. Count median diameters were independent of injection and intake pressures in high-EGR LTC operation.
6. Higher intake pressure and intake charge dilution was required to achieve LTC at higher load. Smoke emissions were higher at higher load, whereas NO_X emissions were near-zero. Gross ISFC remained the same independent of loads at a constant speed for a given intake oxygen

mass fraction. More advanced combustion phasing and higher injection pressure reduced combustion variability at higher load but had no effect at lower load.

7. Higher unburned hydrocarbon emissions were more functions of in-cylinder oxygen concentration, in-cylinder temperature and combustion phasing rather than over-mixing at intermediate and high load operating conditions in high-EGR operation. Bulk quenching was hypothesized as the mechanism responsible for the high THC emissions in high-EGR LTC operation.

Chapter 5

OPTICAL ASSESSMENT OF HIGH-EGR DIESEL LTC AT VARIABLE INTAKE PRESSURE

5.1 Introduction

As discussed in Chapter 4, high-EGR LTC at medium load operating conditions has higher THC and CO emissions and inferior fuel economy compared to conventional diesel combustion. Increasing the in-cylinder oxygen concentration by increasing the intake air pressure was shown to reduce THC and CO emissions and improve fuel economy. These emissions are thought to be a result of local pockets of rich mixture that do not oxidize fully due to the retarded combustion phasing, low reaction-zone temperature and low oxygen concentration that lead to increased bulk quenching. The objective of the work presented in this chapter was to investigate these hypotheses by means of flame temperature measurements using two-colour pyrometry and gain further insight into the combustion phenomena through in-cylinder visualization.

5.2 Operating Conditions

The spray and combustion progression in both high-EGR LTC and conventional diesel combustion were visualized through a borescope and a camera at selected operating conditions in the single cylinder engine modified for optical access (as described in Chapter 3). It was seen in the previous chapter that high-EGR LTC at 2500 rpm engine speed was characterized by higher cyclic variability during LTC operation compared to 1500 rpm for a constant fuelling quantity (16 mg/cycle). It was difficult to hold the intake temperature constant during the EGR sweep at 2500 rpm. Therefore, it was imperative to have less cyclic variations to derive useful information from optical diagnostics (in-cylinder spray and flame visualization and flame temperature measurement by the two-colour pyrometry). Therefore, all further investigations are conducted at 1500 rpm engine speed. The operating conditions for the high-EGR LTC and conventional diesel combustion are listed in Table 5.1. The EGR levels in conventional diesel operation were set to 0%; however, the EGR levels given in Table 5.1 were due to experimental effects.

Note that the SOI timing (-27 ^{o}CA ATDC) used in the high-EGR LTC cases in this chapter were different from the SOI timing (-30 ^{o}CA ATDC) used in the previous chapter. This was to avoid optical window fouling due to spray impingement which was observed at -30 ^{o}CA ATDC. It may be recalled that a small clearance was provided in the piston lip to accommodate the protruding optical windows. The region inside the piston bowl covered under the field of view of the borescope at different crank angles is shown in Fig. 5.1. The field of view of the borescope and the spray under investigation are also shown in the figure. The grids and letters drawn on the piston bowl and the top land can be seen in the figure. Note that up to 30 ^{o}CA ATDC, only the piston bowl could be seen in

the FOV of the borescope, whereas beyond this crank angle, a part of the squish region (piston top land) was visible.

Table 5.1: Operating Conditions for Optical Assessment

Combustion strategy	**Conventional diesel**	**High-EGR LTC**
Engine speed	1500 rpm	1500 rpm
Fuel quantity	16±0.2 mg/cycle	16±0.2 mg/cycle
Fuel injection pressure	90 MPa	90 MPa
Start of Injection (SOI)	-6 ^{o}CA ATDC (Main SOI) -24 ^{o}CA ATDC (Pilot SOI)	-27 ^{o}CA ATDC (Main SOI) No pilot fuel
Intake pressure (absolute)	Ambient (100 kPa), 120 kPa and 150 kPa	Ambient (100 kPa), 120 kPa and 150 kPa
Intake temperature	50±2^{o}C	55±5^{o}C
EGR levels (% by vol.)	1 @100 kPa 4 @120 kPa 3 @150 kPa	57 @100 kPa 59 @120 kPa 63 @150 kPa

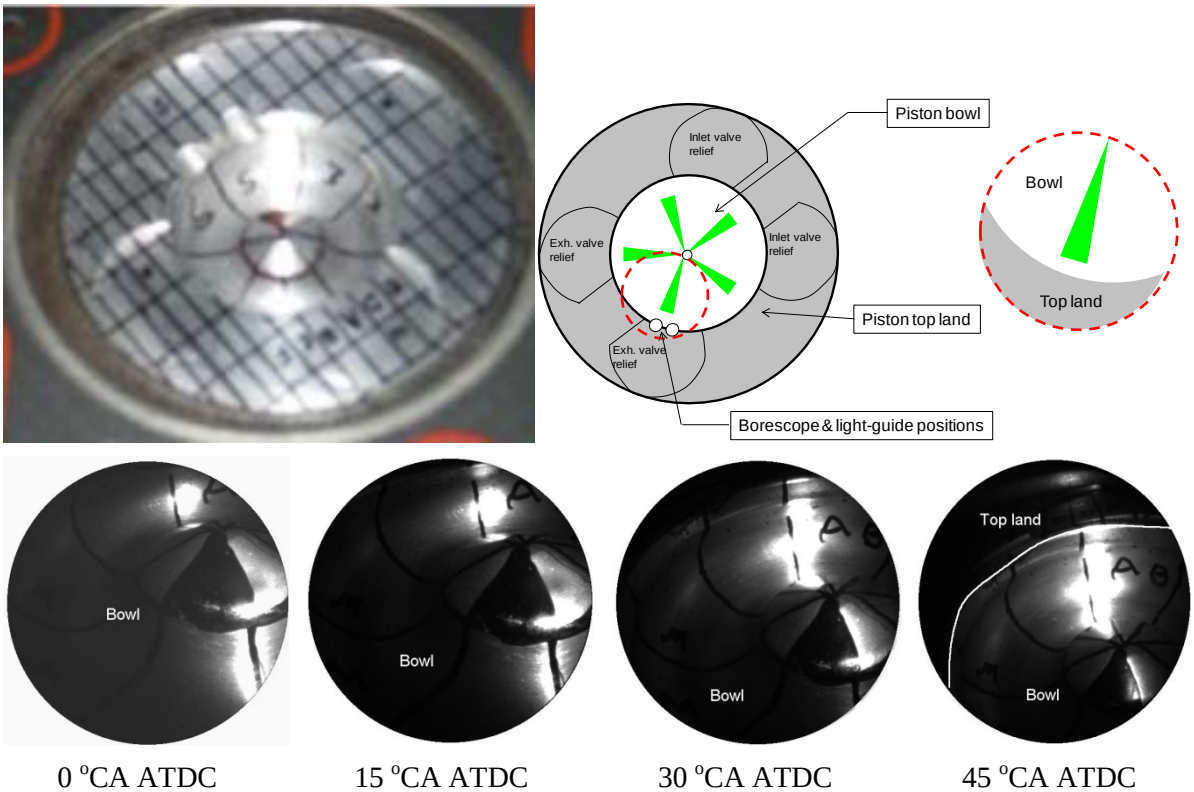

0 ^{o}CA ATDC 15 ^{o}CA ATDC 30 ^{o}CA ATDC 45 ^{o}CA ATDC

Fig. 5.1: Region of the piston bowl covered under the FOV of the 0^{o} borescope. Schematic of borescope field of view is also shown.

5.3 Optical Assessment of LTC and Conventional Diesel Combustion

In order to gain further insight into the combustion phenomena, a sequence of spray and flame images were obtained for both the high-EGR LTC and conventional diesel combustion strategies at 120 kPa intake pressure as shown in Fig. 5.2. The following points concerning the image sequences should be noted: 1) all image sequences were collected independently from the two-colour pyrometry data that will be presented later, 2) the images were taken over multiple cycles and 3) the conventional diesel combustion images were recorded with a camera gain of 20 dB whereas a gain of 30 dB was used in the LTC case. Thus, the raw image intensities shown in Fig. 6.2a are not directly comparable with those shown in Fig. 5.2b.

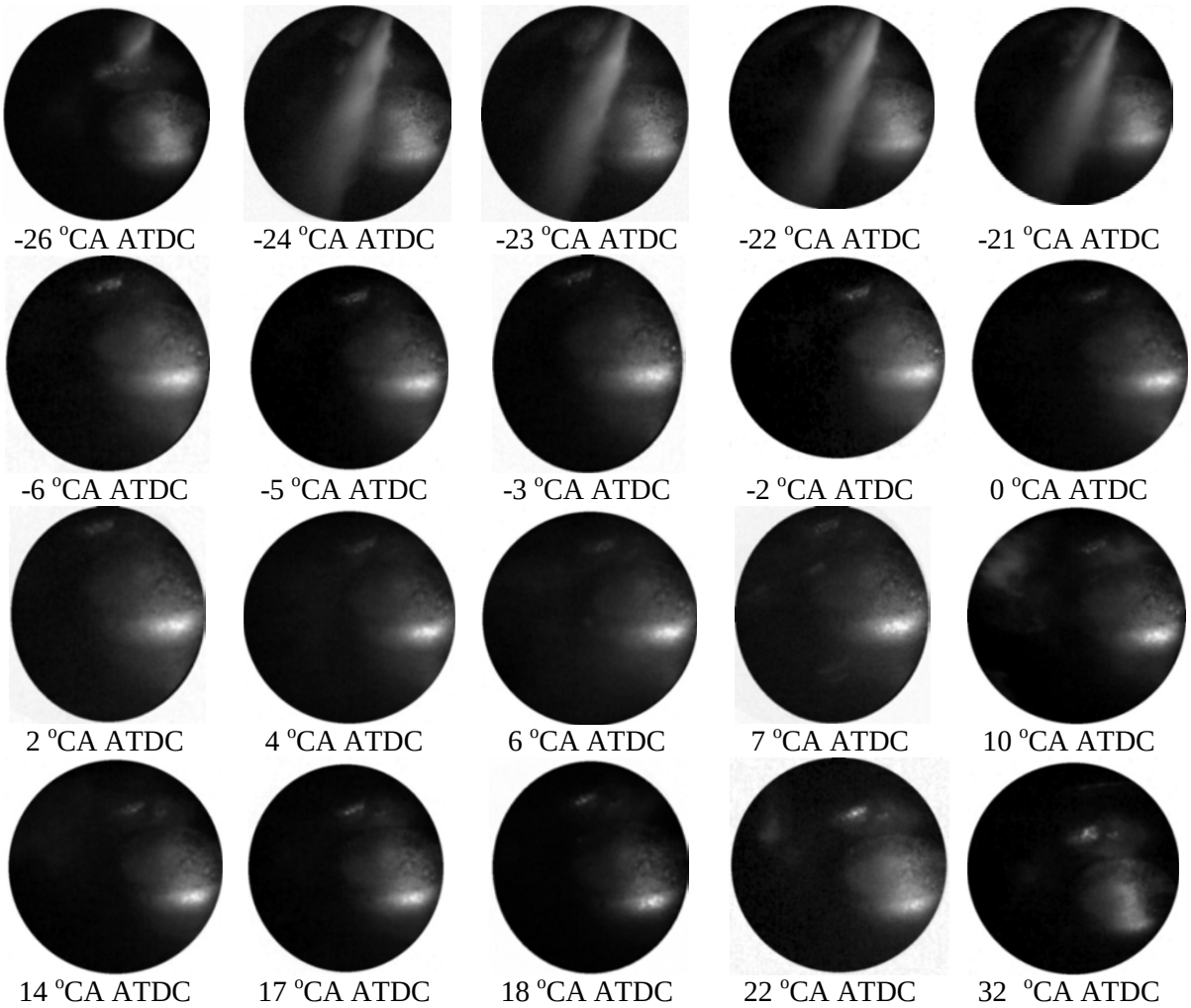

(a) High-EGR LTC at 120 kPa (absolute) intake pressure at 30 dB camera gain

Fig. 5.2a: Spray and flame images at 120 kPa (absolute) intake pressure in high-EGR LTC

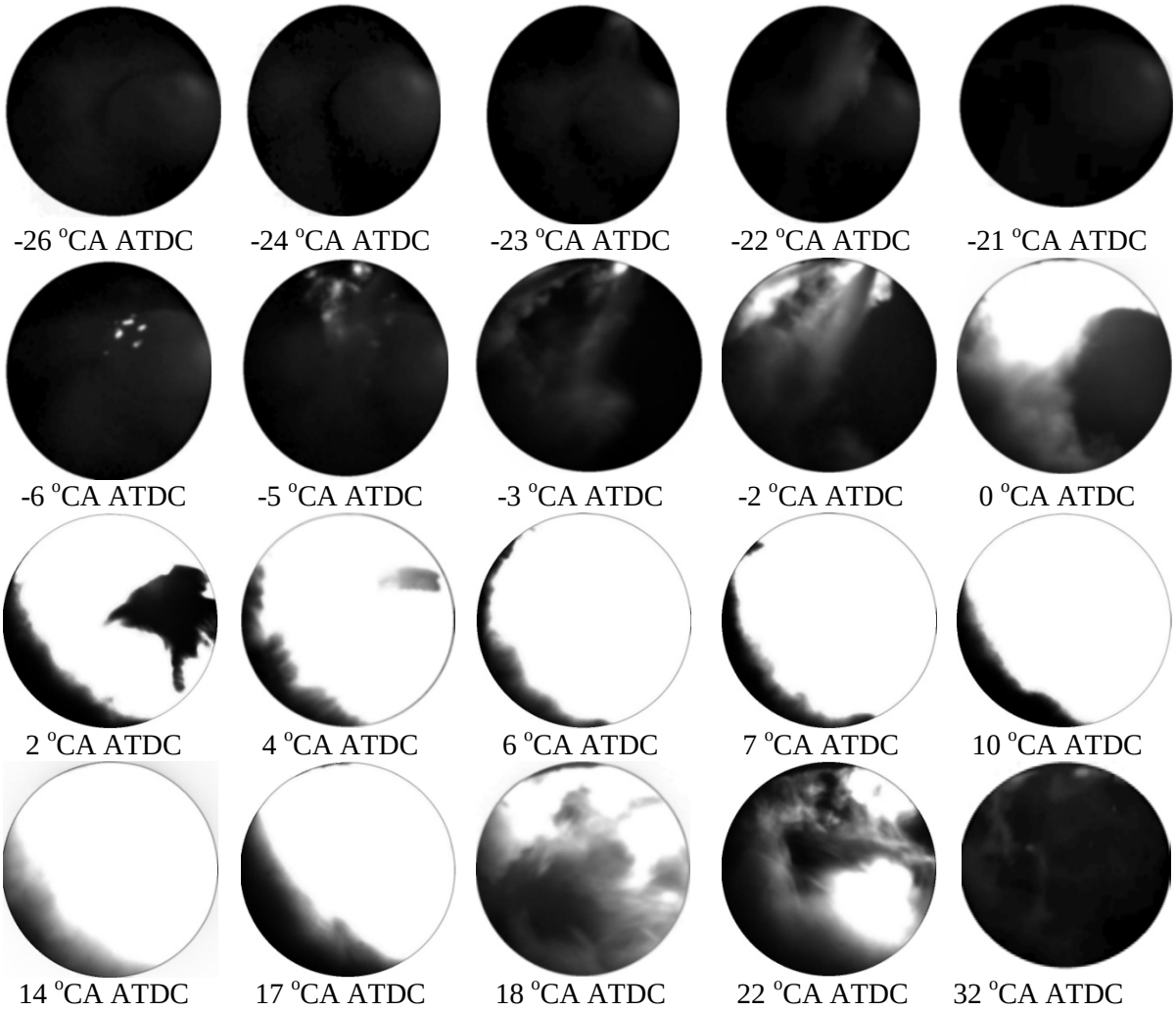

(b) Conventional diesel combustion at 120 kPa (absolute) intake pressure at 20 dB camera gain

Fig. 5.2b: Spray and flame images at 120 kPa (absolute) intake pressure in conventional diesel combustion

The combustion images for the high-EGR LTC case, shown in Fig. 5.2a, differ markedly from the conventional diesel case shown in Fig. 5.2b. In the high-EGR LTC case, the flame images are characterized by a lack of luminosity during combustion. Fuel injection in the high-EGR LTC case started at -27 °CA ATDC and continued through to -21 °CA ATDC. No luminous combustion is seen until 7 °CA ATDC indicating a long ignition delay. A very small area of luminosity is visible in the upper left quadrant of the 10 °CA ATDC combustion image. No clear soot luminosity can be seen after 10 °CA ATDC. The lack of soot luminosity in these images is unsurprising; previous research [Ogawa *et al*., 2007; Dec, 2009] has shown that soot formation in diesel engines is inhibited by very high levels of EGR. Also the combustion temperature is so low that whatever soot is formed would not radiate significantly. It could not be definitely identified which was the root cause in this case.

In the case of conventional diesel operation, a small pilot injection was used to control the rate of pressure rise within the cylinder. The pilot spray can be seen in the images acquired at -23 °CA

ATDC and -22 ^{o}CA ATDC (see Fig. 5.2b). Combustion of the pilot fuel is seen at -6 ^{o}CA ATDC. The main fuel injection started at -5 ^{o}CA ATDC and continued until -2 ^{o}CA ATDC. Combustion for the main fuel started almost immediately with a short ignition delay while the fuel was still being injected. Unlike the high-EGR LTC case, the spray penetration in conventional diesel combustion was much less due to near-TDC injection (high gas density and short ignition delay). The main combustion event in the conventional diesel operation is characterised by high levels of luminosity that fill a significant fraction of the borescope FOV and saturate the image (despite the reduced camera gain) over a period of approximately 15 °CA, from 2 °CA ATDC to 17 °CA ATDC. Luminous combustion continued up to 32 ^{o}CA ATDC. It is interesting to note that the peak soot luminosity in high-EGR LTC (refer to 10 ^{o}CA ATDC in Fig. 5.2a) is similar to the soot luminosity at 32 ^{o}CA ATDC in conventional diesel combustion (see Fig. 5.2b). However, the soot cloud late in the combustion phase in the conventional diesel case is widely distributed in the piston bowl compared to the narrow local luminosity seen in the high-EGR LTC case.

Also note that the spray images obtained for conventional diesel combustion (refer to Fig. 5.2b) were darker compared to the high-EGR LTC case because of quick fouling of the light guide tip by soot in conventional diesel operation; the borescope remained reasonably clean only for a few minutes. In contrast, the spray images in the high-EGR LTC operation were sharper due to minimum light guide tip fouling because of less soot formation. It was observed that the engine could be operated over an hour in the high-EGR LTC operation compared to a few minutes in the conventional diesel operation without window fouling. This demonstrates a significant difference between the two modes of combustion.

The effect of higher intake pressure on high-EGR LTC was investigated optically through a sequence of spray and flame images obtained at 150 kPa intake pressure as shown in Fig. 5.3 at the same instances as those of the high-EGR LTC at 120 kPa intake pressure shown in Fig. 5.2a. No visible difference could be seen in the spray images with the higher intake pressure. The high-EGR LTC strategy at 150 kPa intake pressure was characterized by a shorter ignition delay compared to the 120 kPa intake pressure as discussed in Chapter 4 (refer to Fig. 4.7b) which can also be verified from the images. Note the advanced location of the visible luminous combustion at 150 kPa at 2 ^{o}CA ATDC shown in Fig. 5.3 compared to 10 ^{o}CA ATDC at 120 kPa shown in Fig. 5.2a. Again, the high-EGR LTC at higher intake pressure was characterized by longer luminosity duration (15 ^{o}CA between 2 and 17 ^{o}CA ATDC). This also supports the earlier observation of longer combustion duration with higher intake pressure in the high-EGR LTC strategy reported in Chapter 4 (refer to Fig. 4.7b). Unlike the 120 kPa intake pressure case, some spatial variations of flame luminosity covering a wider region in the piston bowl can also be seen at 150 kPa intake pressure. It is interesting to note that the luminous intensity at 10 ^{o}CA ATDC at 120 kPa intake pressure (refer to Fig. 5.2a) approximately coincides with the luminosity at 17 ^{o}CA ATDC at 150 kPa intake pressure (refer to Fig. 5.3).

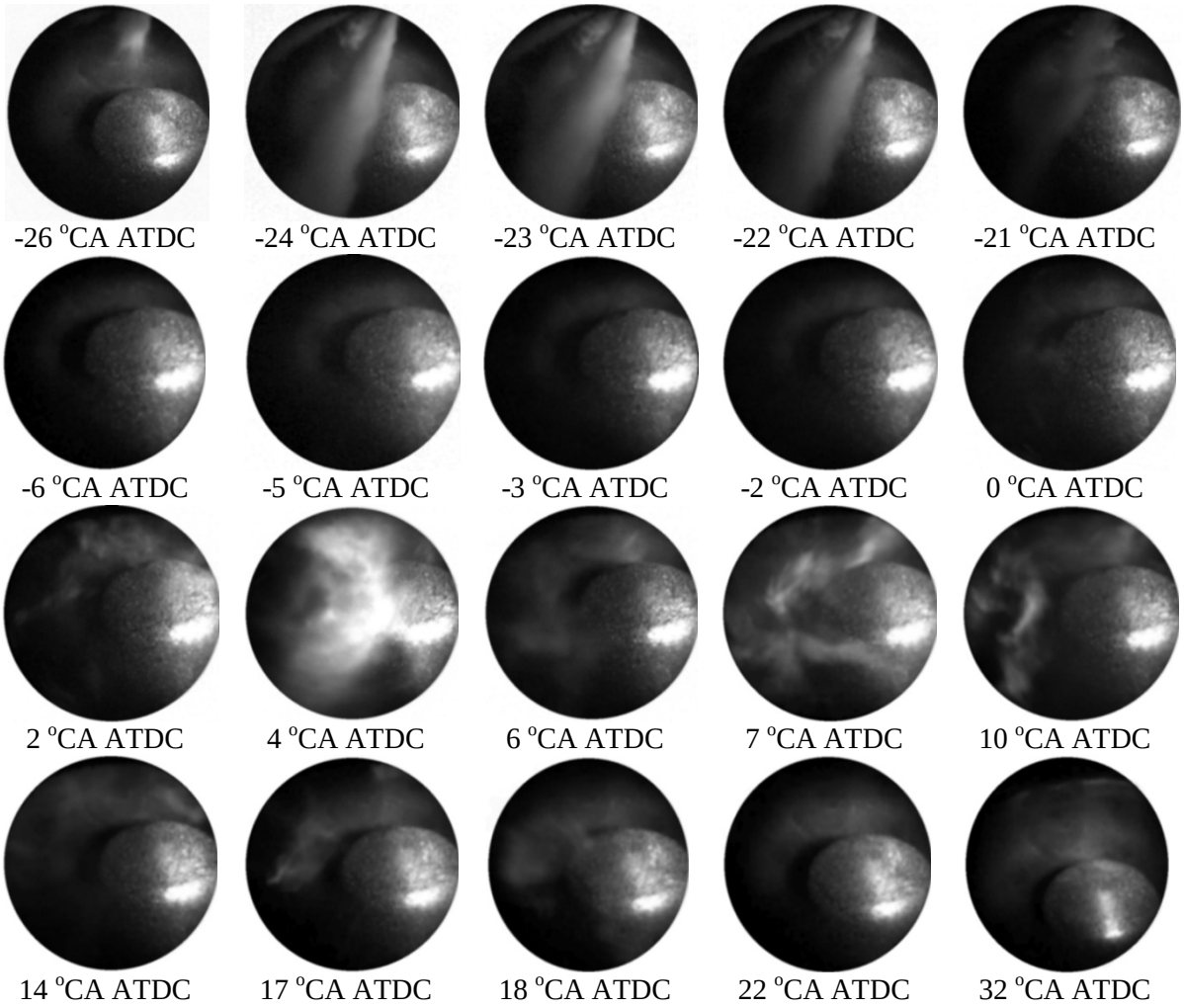

Fig. 5.3: Spray and flame images at 150 kPa (absolute) intake pressure at 30 dB camera gain

5.4 Spray Penetration at Different Intake Pressure

Due to the limitation of the FOV of the borescope, spray impingement on the piston bowl wall could not be seen; therefore, a modelling approach was adapted to find out the effects of variable intake pressure on spray penetration length and wall impingement. The spray penetration models of Dent [1971], Hiroyasu and Arai [1990] and Naber and Siebers [1996] were employed to calculate the spray penetration length as a function of time (in °CA) for 100 kPa (ambient) and 150 kPa intake pressure conditions; these are shown in Fig. 5.4. The equations used to calculate the spray penetration length with the above three models are given in Appendix A5. Spray penetration length was determined with the experimental in-cylinder pressure, injection pressure and the estimated mass averaged bulk gas temperature (obtained from in-cylinder pressure and volume as outlined in Sec. 3.4.1 in Chapter 3) at SOI. Note that this evaluation was not intended to verify or validate any of the spray penetration models in this work, but rather to give an overall idea regarding the spray penetration length and any possible wall impingement with the advanced SOI timings used in the high-EGR LTC strategy. The horizontal dotted line in Fig. 5.4 represents the distance from the

injector tip to the piston lip 1.5 ^{o}CA (~167 μs at 1500 rpm) after the commanded SOI timing (-27 ^{o}CA ATDC). From Fig. 5.4, it is apparent that irrespective of the spray penetration models, lip impingement would take place 1 ^{o}CA and 1.5 ^{o}CA after the commanded SOI timing at 100 kPa and 150 kPa intake pressures respectively.

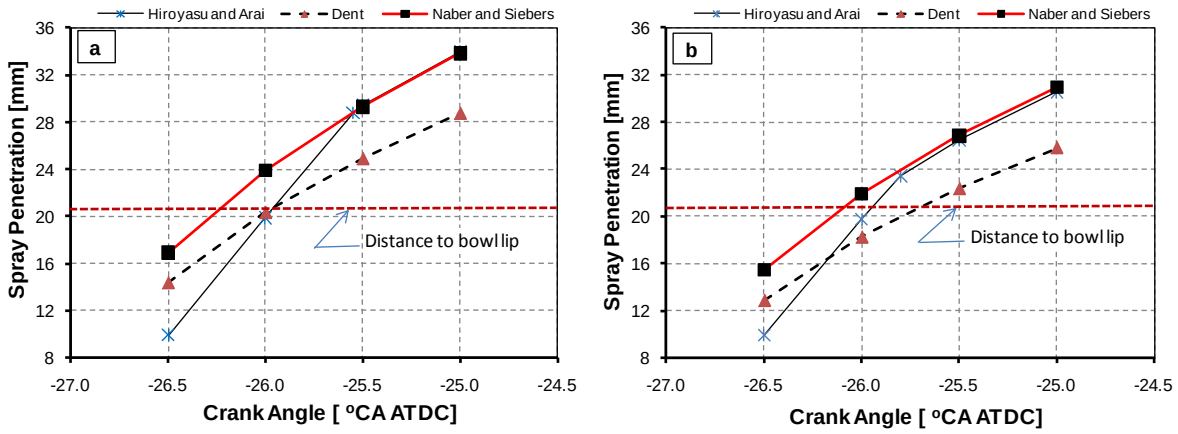

Fig. 5.4: Spray penetration length; a. Ambient pressure (100 kPa, abs), b. 150 kPa (abs) intake pressure

A graphical representation shown in Fig. 5.5 indicates that the fuel would impinge on the piston lip 1.5^{o} CA after SOI even at 150 kPa intake pressure. Therefore, bowl impingement is not critical for changes in emissions seen in the previous chapter at different boost pressures. With higher intake pressure, oxygen entrainment into the spray would increase, thereby affecting the mixture strength and the emissions of combustion by-products as discussed in Chapter 4. In addition to the increased in-cylinder oxygen concentration and oxygen density with higher intake pressure, flame temperature would also significantly influence the emissions of combustion by-products in the high-EGR LTC strategy as discussed in the next section.

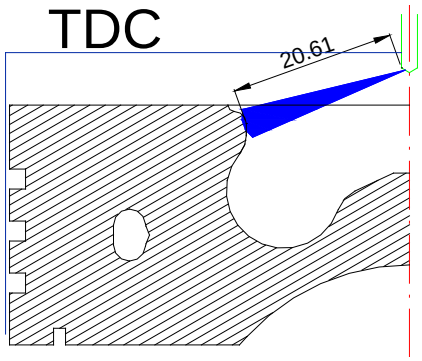

Fig. 5.5: Spray penetration analysis showing spray impingement on the piston lip 1.5 ^{o}CA after the commanded SOI timing at 150 kPa intake pressure. The distance from the injector to the spray tip is in mm.

5.5 Flame Temperature and Bulk Quenching

It was hypothesized in Chapter 4 that the onset of bulk quenching is delayed at higher intake pressure due to the advanced combustion phasing, higher in-cylinder temperature and higher in-cylinder oxygen concentration. With advanced combustion phasing, it is expected that the mixing rate of the partially burned/unburned fuel with in-cylinder oxygen molecules would be enhanced due to higher turbulence in the early combustion phase. In order to verify the hypothesis of bulk quenching, flame temperature was measured in the high-EGR LTC strategy at different intake pressures with the two-colour pyrometer described in detail in Sec. 3.7. Flame temperature was also measured in conventional diesel combustion. These results are shown in Fig. 5.6.

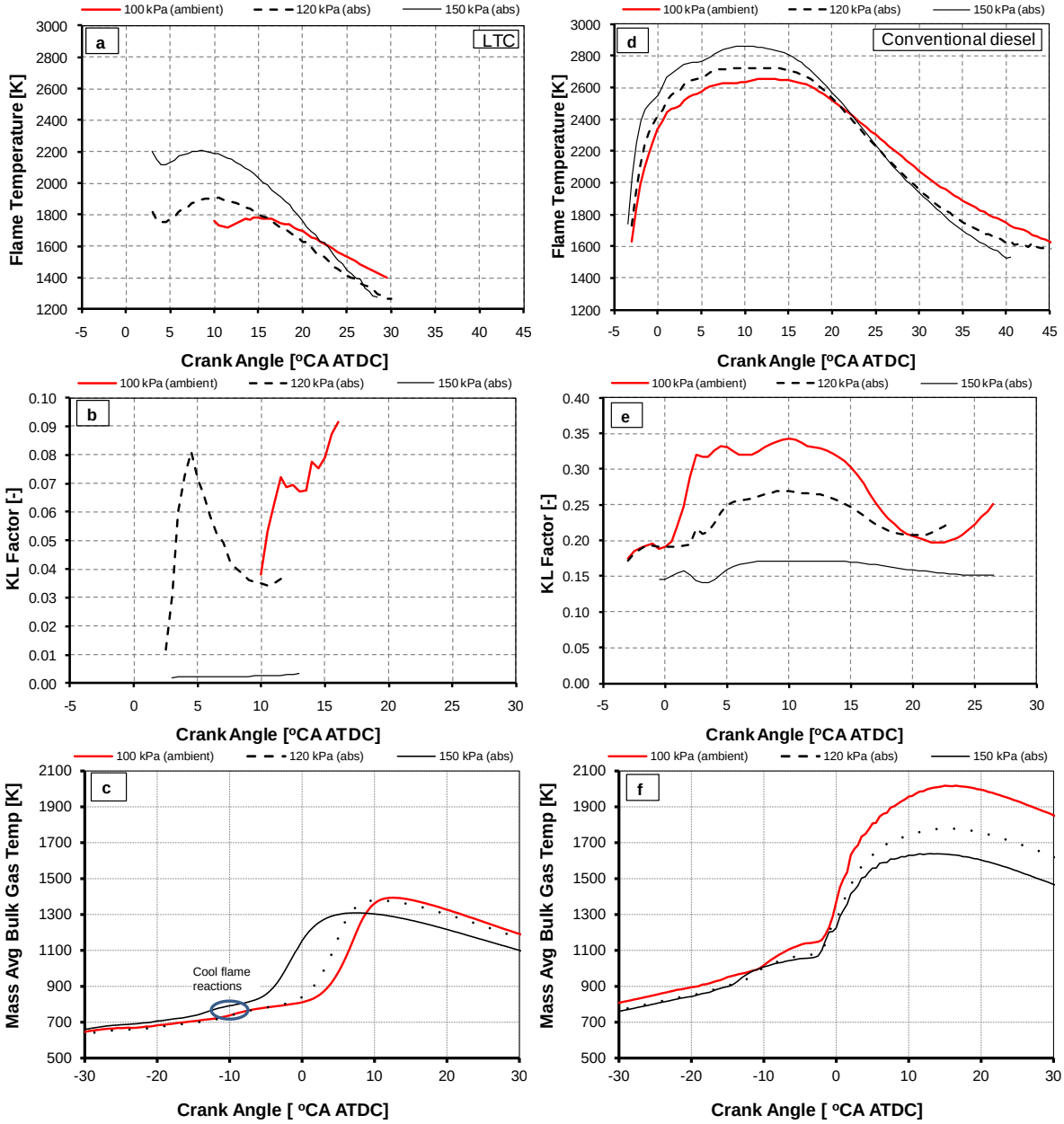

Fig. 5.6: Flame temperature, soot concentration and bulk gas temperature in high-EGR LTC and conventional diesel combustion. (a-c): High-EGR LTC; (d-f): Conventional diesel combustion

Peak flame temperatures are seen to decrease with the increased EGR fraction as expected, from a value of approximately 2800 K for the conventional diesel case (3% EGR) at 150 kPa intake pressure down to approximately 2200 K for the high-EGR LTC case (63% EGR). One notable feature of the results shown in Fig. 5.6d is the relatively long period (~15 °CA) during which the measured flame temperature in conventional diesel combustion is within a few percent of its peak value. With the high-EGR LTC strategy, the period of residency close to peak flame temperature is reduced.

In both conventional diesel combustion and LTC, the peak reaction zone flame temperatures are seen to be substantially higher for 150 kPa intake pressure. This higher temperature is maintained for the bulk part of the combustion event (up to 22 ^{o}CA ATDC) compared to lower intake pressure cases in the high-EGR LTC strategy. The higher reaction zone temperature at 150 kPa intake pressure shown in Fig. 5.6a is expected to include contributions from both higher mass averaged cylinder temperature (during the early part of combustion close to TDC as shown in Fig. 5.6c) and oxygen concentration effect. It was discussed in Chapter 4 that in the high-EGR LTC strategy, combustion phasing was advanced at higher intake pressure (refer to Fig. 4.2b in Chapter 4) for a constant SOI timing. This advanced combustion phasing resulted in the earlier occurrence of the peak flame temperature at higher charge pressures shown in Fig. 5.6a.

From the flame temperature measurement and the in-cylinder imaging both in conventional diesel combustion and high-EGR LTC, it was verified that flame temperature increased at higher intake pressure (consistent with the trends reported in the literature for conventional diesel combustion [Yan and Borman, 1988; Payri *et al*., 2007]) with the bulk of the combustion occurring close to TDC. This supports the earlier hypothesis of the delayed onset of bulk quenching at higher intake pressure as a result of the advanced combustion phasing, higher flame temperature and higher in-cylinder oxygen concentration.

The figure also shows the calculated *KL* factors (up to CA90) for the high-EGR LTC and conventional diesel combustion strategies at different intake pressures, shown in Figs. 5.6b and 5.6e respectively. Note that the ordinate of Fig. 5.6b is different from Fig. 5.6e. It may be recalled that the predicted *KL* factors for the low-load (8 mg/cycle fuelling quantity) conditions reported in Chapter 3 (refer to Fig. 3.15b) exhibited wholly unrealistic trends for the high-EGR LTC test points due, it was hypothesised, to low soot concentrations within the measurement volume. This behaviour is not observed in the medium-load data plotted in Fig. 5.6b. The calculated *KL* factors for the medium-load high-EGR operating conditions show trends of soot formation followed by soot oxidation (shown clearly at 120 kPa intake pressure), which would suggest that the soot concentrations within the pyrometer's measurement volume during medium-load LTC combustion were: 1) greater than those observed in low-load LTC, and 2) sufficient for measurement purposes. This can also be verified by the uncertainties due to random errors (corresponding to a 95% confidence interval as discussed in detail in Sec. 3.5 in Chapter 3 and in Appendix A2) in the measured flame temperature

and the *KL* factors shown in Fig. 5.7. The level of uncertainty in the flame temperature measurements for the medium-load operating points is similar to that of the low-load operating points shown in Chapter 3 (refer to Fig. 3.16b). With regard to the level of uncertainty in the calculated values of the *KL* factor, a comparison of the results shown in Figs. 5.7 and 3.16b indicate that the uncertainty in the *KL* factor is reduced at medium-load. This is consistent with an increased soot concentration at the higher load condition.

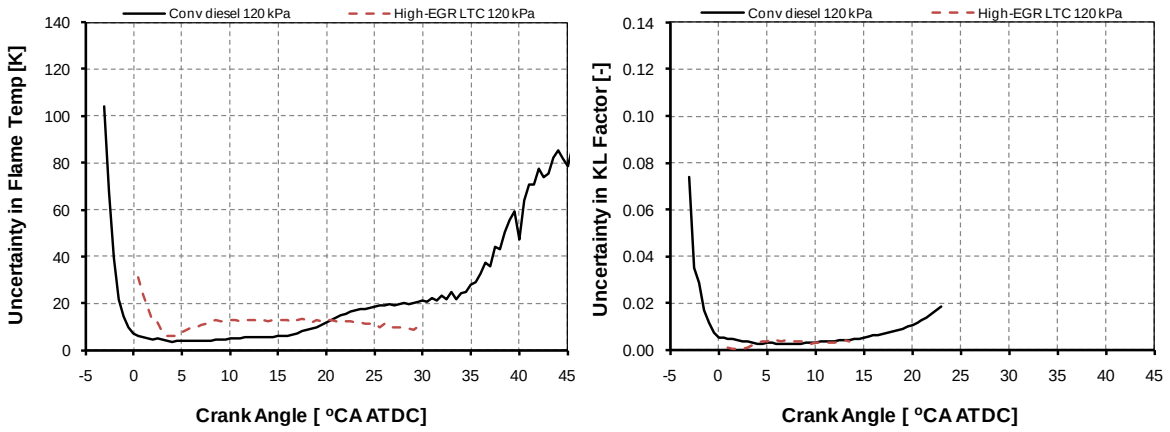

Fig. 5.7: Uncertainty (95% confidence interval) in flame temperature (left hand figure) and *KL* factor (right hand figure) for the 120 kPa intake pressure case for both conventional diesel and high-EGR LTC operation shown in Fig. 5.6

Now returning to Fig. 5.6, it can be seen that the *KL* factor calculated for the conventional diesel cases at different boost pressure is approximately constant (refer to Fig. 5.6e) through the bulk of the combustion event (5-15 ^{o}CA ATDC). After 20 ^{o}CA ATDC, the *KL* factor in the conventional diesel cases at 100 kPa and 120 kPa intake pressures show a steady increase until the calculation was terminated according to the SNR and variance criteria outlined in Sec. 3.7 in Chapter 3. In general, the increased intake pressure reduced the *KL* factor in the conventional diesel cases due to the higher flame temperature and the higher partial pressure of oxygen oxidizing the soot faster. This is consistent with the results reported by Yan and Borman [1988]. The magnitudes of the calculated *KL* factors for the high-EGR LTC cases were much lower than the conventional diesel cases indicating low soot formation. The *KL* factor in the high-EGR LTC regimes did not show any clear trend of soot oxidation at 100 kPa and 150 kPa intake pressures. The most probable cause of this was either due to very low soot formation or low soot concentration observed under the FOV of the borescope. The *KL* factor at 120 kPa pressure showed an earlier soot formation with rapid soot oxidation trend compared to the 100 kPa intake pressure case. The reason for the observed trend at 150 kPa intake pressure in the high-EGR LTC strategy could be because of low SNR; this could not be explained with the data obtained in this work and is a potential future work. Interestingly, the engine-out smoke emission at 150 kPa intake pressure in the high-EGR LTC strategy had a very low value of

smoke emission (0.02 FSN) compared to 0.45 FSN and 0.42 FSN at 100 kPa and 120 kPa intake pressures respectively.

Comparison of the trends in the *KL* factors shown in Figs. 5.6b and 5.6e with the corresponding combustion images from Fig. 5.2 yields good qualitative agreement for both the conventional diesel and high-EGR LTC cases. The behaviour of the calculated *KL* factor (and flame temperature) for the conventional diesel case (at 120 kPa intake pressure) is generally well matched to the observed combustion characteristics. Note that the pilot combustion event is not captured in the pyrometry data due to the low PMT gain setting used during conventional diesel operation; the calculated *KL* factor data then starts at around the time of start of combustion for the main fuel spray at approximately -2 °CA ATDC. The *KL* factor increases at around 2 °CA ATDC, which coincides with a marked increase in soot luminosity in the combustion images. From this point on, the *KL* factor data suggests a similarly extended period in which significant soot is present in the measurement volume, as do the combustion images with the maximum value of *KL* factor being reached at approximately 10 °CA ATDC, i.e. approximately at the mid-point of the observed period of high soot luminosity. The calculated *KL* factor is then seen to increase beyond 20 °CA ATDC before the calculation is terminated at CA90 (~23 °CA ATDC) according to the previously mentioned criteria (as discussed in Sec. 3.7 in Chapter 3). The flame temperature results indicate that there was measurable soot present in the cylinder during the high-EGR LTC operation that was not visible by means of combustion imaging. The results therefore demonstrate the benefits of a PMT based two-colour pyrometry system for low-temperature and low-soot engine applications.

5.6 Determination of Local Equivalence Ratio

Local equivalence ratio in addition to the local flame temperature would influence the oxidation of the partially burned hydrocarbon, unburned fuel, CO and soot. Therefore, the local equivalence ratio at the peak flame temperature location was determined by a theoretical calculation with the assumption that the local equivalence ratio before and after the occurrence of peak flame temperature would be richer and leaner respectively than the theoretical equivalence ratio corresponding to the peak flame temperature. Measured in-cylinder pressure and the calculated mass averaged bulk gas temperature at TDC (as shown in Figs. 5.6c and 5.6f) were the ambient conditions for estimating the adiabatic flame temperatures. In the work presented in this section, the actual local flame temperature was assumed to be 50 K higher than the measured flame temperature by the two-colour pyrometry system to account for the radiation heat transfer losses [Musculus, 2005]. Accordingly, two local equivalence ratios were determined theoretically to match the two flame temperatures: (1) peak two-colour flame temperature and (2) actual peak flame temperature with an increment of 50 K. Therefore, the local equivalence ratios are represented by a unidirectional error bar (towards a leaner equivalence ratio) in the ϕ–T map shown in Fig. 5.8 as the local equivalence ratio would only be leaner to match a higher local flame temperature.

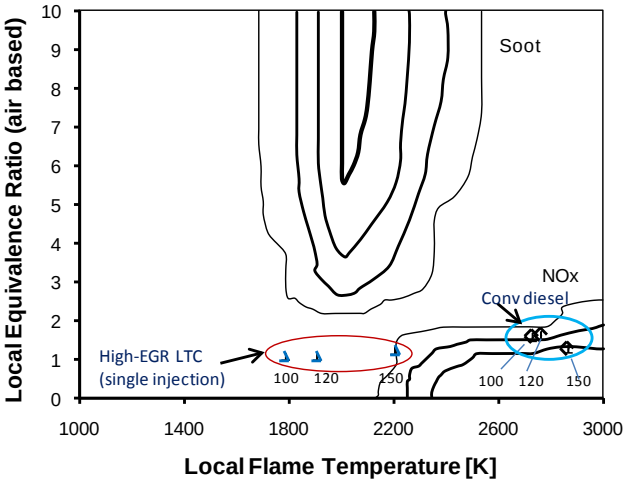

Fig. 5.8: Peak measured flame temperature and the theoretically determined local equivalence ratio (air-fuel ratio based) for single injection high-EGR LTC and conventional diesel combustion (pilot + main fuel injection) at different intake pressures (100, 120 and 150 kPa) at a fixed operating condition (i.e. 16 mg/cycle fuelling quantity and 1500 rpm engine speed). The numbered symbols in the plot indicate absolute intake pressure in kPa. Soot and NO_X formation islands in the ϕ–T map: Adapted from SAE Paper No. 2006-01-3386.

The intake oxygen mass flow rate for the high-EGR LTC cases at different boost pressures (taking into account the oxygen in the fresh air and the oxygen in the exhaust) were normalized by the intake oxygen mass flow rate at 100 kPa (absolute) intake pressure without intake charge dilution. The residual gas fraction (*RGF*, indicative of the actual intake charge dilution level) for different boost pressure cases was then determined by:

$$RGF = 1 - \frac{[m_{O2}]_{boost,EGR\ dilution}}{[m_{O2}]_{amb,no\ dilution}} \qquad (5.1)$$

where $[m_{O2}]_{boost,EGR\ dilution}$ indicates intake oxygen mass flow rate at a given boost pressure with intake charge dilution and $[m_{O2}]_{amb,no\ dilution}$ indicates intake oxygen mass flow rate at 100 kPa intake pressure (ambient) without intake charge dilution.

Adiabatic flame temperature was computed by setting the specific enthalpies of the reactants and the products to be equal. The specific enthalpy and specific heat of the reactants (fuel, EGR and fresh air) was determined by the curve fitted polynomial empirical correlations from the JANAF thermochemical data [Ferguson, 1986]. Ten equilibrium combustion products (CO_2, H_2O, N_2, O_2, CO, H_2, H, O, OH and NO) were considered with the assumption that for ϕ <3, the only species of importance because of dissociation are O, H, OH and NO. When the equivalence ratio is greater than 4, solid carbon C(s), hydrogen cyanide HCN, acetylene C_2H_2 and methane CH_4 need to be included with the above 10 equilibrium combustion products. In this work however, only 10 equilibrium combustion products have been considered, since it is expected that the equivalence

ratio at the peak flame temperature location will be less than 3. The mole fractions of the 10 equilibrium combustion products were determined by considering atom balancing and by introducing six equilibrium constants (dependent on pressure and temperature). Equilibrium constants were determined by the curve fitted polynomial empirical correlations from the JANAF thermochemical data [Ferguson, 1986]. The specific enthalpy and specific heat of the equilibrium combustion products were determined by determining the mole fractions of the equilibrium combustion products. The formulation and solution methodology for determining the thermodynamic properties of the reactants and the equilibrium combustion products are discussed in detail by Ferguson [1986].

The theoretical equivalence ratios determined from the method described above along with the measured peak flame temperature can be used to represent different combustion strategies in the local equivalence ratio ($\phi_{, \text{air-fuel}}$ based)-local flame temperature (T) map. Peak flame temperature and the corresponding local equivalence ratio with high-EGR single injection LTC and conventional diesel combustion (no EGR) at various intake pressures at a fixed operating condition (i.e. fuelling quantity 16 mg/cycle and engine speed of 1500 rpm) are shown in the ϕ–T map in Fig. 5.8. It should be noted that the single point represented in the ϕ-T map corresponds to the local peak flame temperature and the corresponding local equivalence ratio during the mixing controlled combustion phase in a cycle. It, however, does not represent the full true complexity of the combustion process, which will involve a wide range of local equivalence ratio and local temperature conditions, varying both spatially and temporally within the combustion chamber in a single cycle as discussed in detail in Sec. 2.5.1 in Chapter 2. Note that ϕ and T vary significantly during a cycle (ϕ and T vary between 6 and 0.5 and 1000 and 3000 K respectively) depending on the combustion strategy [Bittle *et al.*, 2011]. Illustrative routes for conventional diesel combustion and high-EGR LTC were shown earlier in Fig. 2.3 in Chapter 2. Similar 'routes' may or may not be applicable to the current LTC strategy, determination of which is beyond the scope of the current work. It should be noted that the peak flame temperature and the local equivalence ratio represented in the ϕ–T map by a single point during the mixing-controlled combustion phase in a cycle is still very relevant as it is indicative of the bulk of the high temperature mixing controlled combustion condition encountered during the combustion event. Note that these high temperature reactions during the mixing controlled combustion phase influence both the engine-out smoke, THC, CO and NO_X emissions.

The triangles shown in the ϕ-T map (Fig. 5.8) represent the peak flame temperatures and the local equivalence ratios in high-EGR LTC (Y_{O2} varying between 7% and 9%) at various intake pressures as given in Table 5.1 (intake pressure increasing from the left triangle at 100 kPa to the right most triangle at 150 kPa). Similarly, the diamonds on the right hand side of the ϕ-T map (inside the NO_X island) represent the peak flame temperatures and the local equivalence ratios in

conventional diesel combustion without any EGR at various intake pressures (intake pressure increasing from left to right: 100 kPa to 150 kPa).

It is well known that soot formation is very high in conventional diesel combustion; however, most of the soot gets oxidized during the mixing controlled combustion phase because of high flame temperature and high oxygen concentration [Dec, 1997]. It should be noted that the points shown in Fig. 5.8 for conventional diesel combustion lie outside of the soot formation island and they do not show the soot formation mechanism which would be at lower temperatures and at richer equivalence ratios than the points shown on the ϕ–T map. In the work reported here, low engine-out smoke emissions in conventional diesel operation (~0.5 FSN) were found. NO_X emissions were very high (43-49 g/kg of fuel) in conventional diesel combustion as the peak temperature (~2700 K) occurred at a near-stoichiometric local equivalence ratio ($1 < \phi < 2$), and due to the long high-temperature residence time.

In the high-EGR single injection LTC strategy, the local flame temperature (1800 K <T <2200 K) and the local equivalence ratio ($\phi \sim 1$) were reduced compared to conventional diesel combustion. This reduced soot and NO_X formation simultaneously (smoke emissions ~0.5 FSN, similar to the smoke levels in conventional diesel combustion and near-zero NO_X emissions ~0.3 g/kg of fuel). The near-stoichiometric values of ϕ corresponding to the peak flame temperatures in the high-EGR LTC strategy agree with the hypothesized LTC combustion route shown in Fig. 2.3 in Chapter 2 which was adapted from Bittle *et al.* [2011].

In the high-EGR LTC strategy, the local equivalence ratio corresponding to the peak flame temperature location did not change significantly. It is expected that the local equivalence ratio would decrease in the later part of the mixing-controlled phase (the path followed in the ϕ–T map will be towards the left with falling flame temperatures and lower local equivalence ratios as was shown earlier in Fig. 2.3 in Chapter 2). Kook *et al*. [2005] suggested that 1400 K is the limiting temperature above which CO oxidation would increase provided adequate levels of fuel-air mixing take place. In the high-EGR LTC strategy, it is expected that CO oxidation would be inhibited due to the reduced oxygen concentration, lower in-cylinder temperature and slow rate of fuel-air mixing (due to the retarded combustion phasing) that would eventually quench later in the expansion stroke. Similarly, the limiting temperature for hydrocarbon oxidation has been reported to vary between 1700 K and 1900 K [Warnatz *et al*., 2000; Flynn *et al*., 2000]. Therefore, it is expected that the longer high-temperature residence time and the higher oxygen concentration at higher intake pressure would enhance both THC and CO oxidation.

5.7 Conclusions

In this chapter, the effect of variable intake pressure was investigated optically for both high-EGR LTC and conventional diesel combustion conditions. In-cylinder spray and flame images were

obtained at different operating conditions along with flame temperature measurements by the two-colour method. It was found that:

1. Peak flame temperature increased at higher intake pressure in the high-EGR LTC strategy. The peak flame temperature location was close to TDC due to the advanced combustion phasing at higher intake pressure. Advanced combustion phasing also ensured that the in-cylinder mass averaged bulk gas temperature remained high before the commencement of the mixing-controlled phase of combustion.
2. Longer residence time of the high temperature reactions at higher intake pressure combined with higher in-cylinder oxygen concentration reduced THC and CO emissions. The hypothesis of the delayed onset of bulk quenching in the high-EGR LTC strategy at higher intake pressure was also verified.
3. High-EGR LTC at higher intake pressure was characterized by earlier and longer combustion luminosity duration compared to lower intake pressure. Again, a higher flame luminosity occupying a large region in the piston bowl was seen at higher intake pressure, indicating bulk combustion at higher intake pressure. At lower intake pressure, very little soot luminosity could be seen occupying only a small region in the piston bowl, suggesting that either soot formation is reduced due to low flame temperature and improved air-fuel mixing or the flame temperature is so low that there is little radiation.

These conclusions suggest that high combustion efficiency (low THC and CO emissions) with acceptable smoke and NO_X emissions can be obtained by marginally increasing the flame temperature and the in-cylinder oxygen concentration with a higher intake oxygen mass fraction (i.e., reduced EGR levels) compared to the low intake oxygen mass fraction used in Chapter 4 to achieve LTC, provided a long ignition delay time can be maintained. It is expected that long ignition delay would reduce soot formation and high intake oxygen concentration, high flame temperature with advanced combustion phasing would enhance soot, THC and CO oxidation without significantly influencing NO_X formation. This can possibly be achieved by a split fuel injection strategy. The split fuel injection strategy at higher intake oxygen mass fraction (reduced/moderate EGR levels) is reported in the next chapter.

Chapter 6
EFFECTS OF SPLIT INJECTIONS ON LTC WITH MODERATE EGR LEVELS

6.1 Introduction

Although the potential benefits of diesel LTC are clear, a practical diesel LTC system has yet to be implemented in a production engine. One of the main barriers has been the requirement for EGR levels that can exceed 65% by volume (depending on operating condition). These EGR levels are much greater than the 40-50% by volume needed to achieve near-zero NO_X emissions (the specific EGR levels and the associated NO_X and smoke response depend strongly on the operating conditions of an engine). However, at 40-50% EGR levels, smoke emissions are substantially above conventional diesel engine-out levels. It was shown in Chapter 4 that with a single fuel injection event, high levels of EGR (often >60% by volume depending on load and intake pressure) are needed to reduce smoke emissions. At these EGR levels, fuel efficiency is typically impaired, partial combustion by-product emissions increase, and the combustion event becomes very sensitive to small changes in operating parameters. With EGR levels greater than 50%, the traditional smoke-NO_X trade-off seen in a conventional diesel engine is replaced by a smoke-THC trade-off. Furthermore, the ability of the engine to respond to transients is compromised. This chapter, therefore, aims to demonstrate that near-zero smoke and NO_X emissions can be achieved with a split fuel injection strategy at EGR levels significantly lower than those required in the single injection high-EGR LTC strategy.

6.2 Objectives

From the literature review presented in Sec. 2.8 in Chapter 2, it is clear that split injection strategy has been used with very high levels of EGR (up to 67% by mass, depending on the engine specification, operating conditions and fuel injection timings). A technique that reduces the EGR requirements for LTC operation at medium load could make LTC a more appealing technology. Although retarded injection timings and lower compression ratio reduce the EGR requirement, THC and CO emissions, cyclic variability and GISFC still remain excessive [Colban *et al.*, 2007]. In this chapter, the potential to achieve low-emission diesel operation with levels of EGR lower than required for a single fuel injection LTC strategy by using a split injection strategy and advanced injection timings is evaluated. This aims to control THC and CO emissions, while achieving near-zero NO_X at smoke emissions and fuel efficiency comparable to conventional diesel combustion. The sensitivity of the split injection strategy to the variations of operating parameters (i.e. EGR levels, intake pressure, injection pressure injection timing and fuel split ratio) on emissions and fuel economy are also investigated in this chapter. Deeper insights into the combustion phenomena are obtained with in-cylinder optical investigations.

6.3 Experimental Methodology

The work reported in this chapter focused on EGR levels of ~52±0.5% by volume at a fixed intake pressure of 120 kPa (absolute). It should be noted that although the EGR rate was held constant, owing to the varying amount of oxygen in the exhaust, the intake oxygen mass fraction was variable (11.5±0.5%). To provide a baseline over the full sweep from conventional diesel combustion to LTC regime, a set of single injection tests were conducted (as reported in Chapter 4) where the EGR was varied from 0 to 62% by volume at 120 kPa intake pressure. The operating conditions with the split injection strategy are specified in Table 6.1. The operating conditions corresponding to the variations of operating parameters (i.e. EGR levels, intake pressure, injection pressure, injection timing and fuel split ratio) are listed in Table 6.2. For selected operating conditions, cycle resolved spray and combustion processes are visualized along with flame temperature and soot concentration measurements.

Table 6.1: Engine Operating Conditions

Engine speed	1500 rpm
Fuel quantity	15.6±0.2 mg/cycle
Global equivalence ratio (O_2 based)	0.72±0.04
1st start of injection (SOI1) timing	Refer to Fig. 6.1
2nd start of injection (SOI2) timing	-15 °CA ATDC
Intake pressure (absolute)	120 kPa
Intake temperature	67±3°C
Fuel injection pressure	90 MPa
EGR levels (by volume)	52±0.5%
Intake oxygen mass fraction	11.5±0.5%
Commanded fuel split fraction	50:50

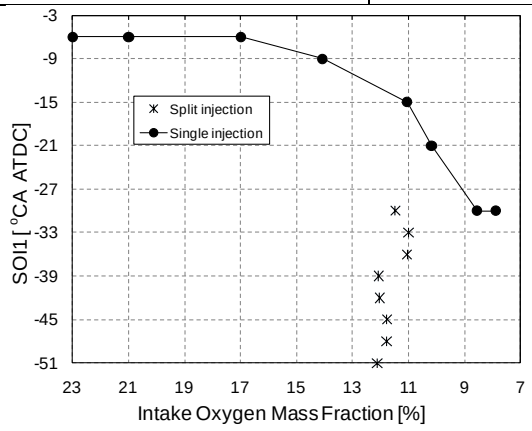

Fig. 6.1: Fuel injection timing vs. intake oxygen mass fraction for the single injection and split injection cases

Table 6.2: Engine Operating Conditions for Sensitivity Analysis

Engine speed	1500 rpm			
Fuel quantity	15.6±0.2 mg/cycle			
Split injection cases	Variable intake oxygen mass fractions	Variable injection pressures	Variable intake pressures	Variable fuel split ratios
Commanded fuel split fraction (by mass)	50:50	50:50	50:50	25:75 50:50
EGR (% by volume)	52±0.5, 54±0.5	52.5±1	52±0.5 (120 kPa) 55±1.0 (150 kPa)	54±1
Absolute intake pressure (kPa)	120	120	120, 150	120
Global equivalence ratio (oxygen based)	0.71±0.04 (52% EGR) 0.84±0.04 (54% EGR)	0.71±0.04 (90 MPa) 0.75±0.02 (110 MPa)	0.71±0.04 (120 kPa) 0.55±0.05 (150 kPa)	0.75±0.02 (25:75) 0.84±0.04 (50:50)
Fuel injection pressure (MPa)	90	90, 110	90	90
2^{nd} start of injection (SOI2) (^{o}CA ATDC)	-15 (52% EGR) -18 (54% EGR)	-15	-12 (150 kPa) -15 (120 and 150 kPa) -18 (150 kPa)	-21 (25:75) -18 (50:50)

The fuelling quantity of 15.6±0.2 mg/cycle at 52% EGR levels for the single-injection case generated a GIMEP of 500 kPa. For the split injection cases, two injections per cycle with a 50:50 split were used. Although the commanded fuel quantity was fixed for the two injections, the power output varied for the split injection cases. So as to achieve an even split of fuel between the two injection events in the 50:50 split injection case, the commanded 1^{st} fuel injection pulse duration (PW1) was kept constant and the commanded 2^{nd} fuel injection pulse duration (PW2) was adjusted to maintain the fuel flow rate at the desired level. Previous work on this engine has shown that the major influences of the pressure pulsations are on the quantity of fuel in the second injection; as a result, varying this provided the best estimate for maintaining equal fuel masses in the two injections [Michailidis *et al*., 2010]. This was also verified by measuring the fuel volume distribution between the two injection events with a rate tube at 750 rpm engine speed. More details regarding the fuel volume distribution between the two injection events are provided in Appendix A6. It was found that depending on the SOI1 and SOI2 timings, the fraction of the fuel injected between the two injection events varied only by ±4%. Therefore, it is expected that this variation would have an insignificant effect on the results presented in this chapter. From the rate tube measurement, it was also seen that

the delay between the injector drive current signal and the commanded start of injection timing was 3 ^{o}CA at 1500 rpm. Note that the measured delay (actual SOI was retarded compared to the injector drive current signal) was 1.5 ^{o}CA at 750 rpm as shown in Fig. A6.1b in Appendix A6.

The basic fuel injection scheme is shown in Fig. 6.2. With regard to fuel injection timing for split injection operation of the engine, SOI1 timing was varied between -51 and -30 ^{o}CA ATDC. SOI2 was adjusted for the 'maximum advance for best indicated torque' (MBT fuel injection strategy) to improve combustion efficiency.

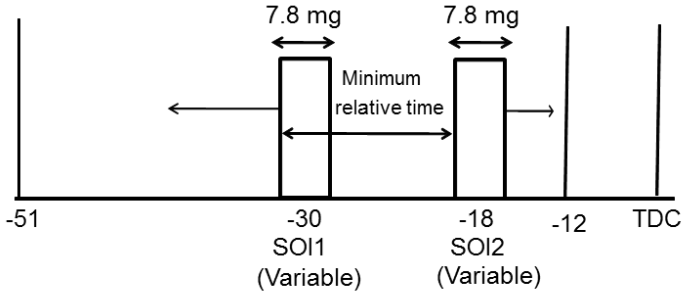

Fig. 6.2: Schematic of injection timings with split injection strategy during the compression stroke. Injection timings and injection duration (PW1 and PW2 in terms of commanded mass in mg) are shown. Relative time (variable between 15 and 36 ^{o}CA) is the difference in time between SOI1 and SOI2.

It was found that for SOI1 timings earlier than -51 ^{o}CA ATDC, THC emissions and GISFC increased significantly, most likely due to poor fuel evaporation (assuming a constant specific heat ratio, γ = 1.33 and an initial temperature at the beginning of the compression stroke to be 65^{o}C, the average in-cylinder gas temperature at -60 ^{o}CA ATDC during the compression stroke is estimated to be ~375^{o}C, which is close to the final boiling point of a conventional diesel blend (360^{o}C: temperature corresponding to the 95% volume of the distillate collected)). A spray penetration analysis using the Hiroyasu and Arai [1990] model suggests that for SOI1 timings earlier than -51 ^{o}CA ATDC, the spray might impinge on the cylinder liner and dilute the lubricating oil.

6.4 Comparison of Split Injection LTC at Reduced EGR with Single Injection High-EGR LTC

In this section, the split fuel injection strategy (50:50 by mass) was investigated at a higher intake oxygen mass fraction (Y_{O2} ~12%) and a comparison was made with the single injection strategy covering EGR levels from 0-62% by volume at 120 kPa intake pressure. The injection pressure was maintained constant at 90 MPa for both the fuel injection strategies. This EGR sweep with the single injection strategy resulted in intake charge dilution ranging from 23-8%. The objective of the work presented in this section was to demonstrate that the split injection strategy with reduced EGR level can reduce smoke emissions without affecting NO_X emissions. The effects

of variable SOI1 and SOI2 timings with the split injection strategy at reduced EGR levels on THC, CO emissions and GISFC are also reported in this section. The error bars shown in selected figures for CO and THC emissions represent the combined instrument error associated with the air, fuel and emissions measurement systems. Similarly, the error bars shown for GISFC are the combined instrumentation errors associated with fuel flow and cylinder pressure measurements. The error bars for smoke emissions represent the instrument error of the smoke measurement system. In all cases, the scatter in the data is significantly less than the calculated instrument error.

6.4.1 Effects of SOI1 Timing on Smoke and NO_X Emissions

With regard to fuel injection timing for split injection operation of the engine, as mentioned earlier, SOI1 timing was varied between -51 to -30 ^{o}CA ATDC, while the start of injection timing for the second fuel mass was kept constant (SOI2 -15 ^{o}CA ATDC). MBT SOI timing was used for the single injection strategy during the EGR sweep as shown in Fig. 6.1. The smoke and NO_X emissions results for both the fuel injection strategies are shown in Figs. 6.3 and 6.4 respectively. Note that the split injection results shown in black crosses in the figures correspond to tests at different SOI1 timings. The trends with SOI1 timings have been shown, wherever applicable.

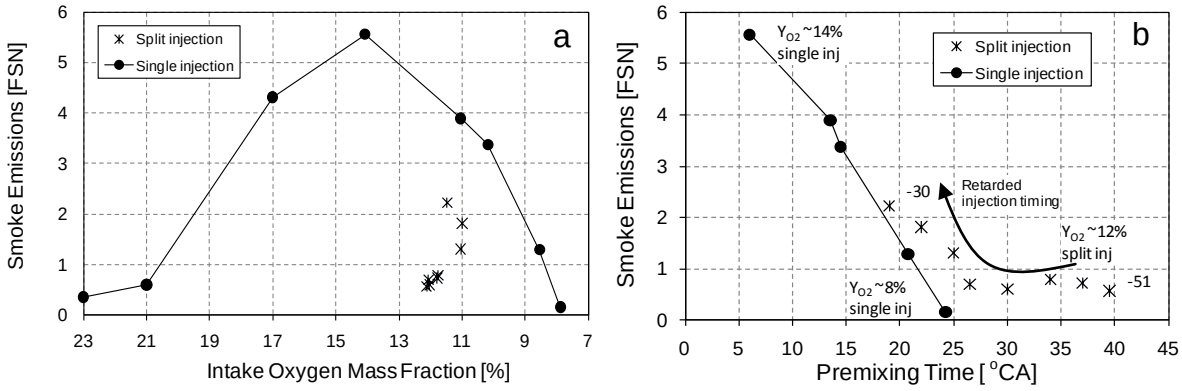

Fig. 6.3: The effects of different SOI1 operating points on smoke emissions; a. smoke emissions with intake oxygen mass fraction with split and single injections, b. smoke emissions with premixing time with split (Y_{O2} ~11-12%) and single injections (Y_{O2} ~8-14%), the numbers in the plot indicate SOI1 in ^{o}CA ATDC

The results shown in Fig. 6.3 suggest that smoke emissions in the split injection cases are significantly influenced by the premixing time (SOC-SOI1; SOC is defined in Sec. 3.4 in Chapter 3) available to the first injected fuel mass. As shown in Fig. 6.3b, smoke emissions were lower at high EGR rates (Y_{O2} <9%) with the single main injection; this is attributed to the increased premixing time (SOC-SOI) available to the fuel and is one of the key reasons for the reduction in smoke emissions in the single injection high-EGR LTC as discussed in Chapter 4. Similar behaviour is seen in the split main injection results shown in Fig. 6.3b; with SOI1 timing more advanced than -36 ^{o}CA

ATDC, the premixing time was greater than 25 ^{o}CA resulting in low smoke emissions (<1 FSN) due to the increased degree of premixing prior to the SOC.

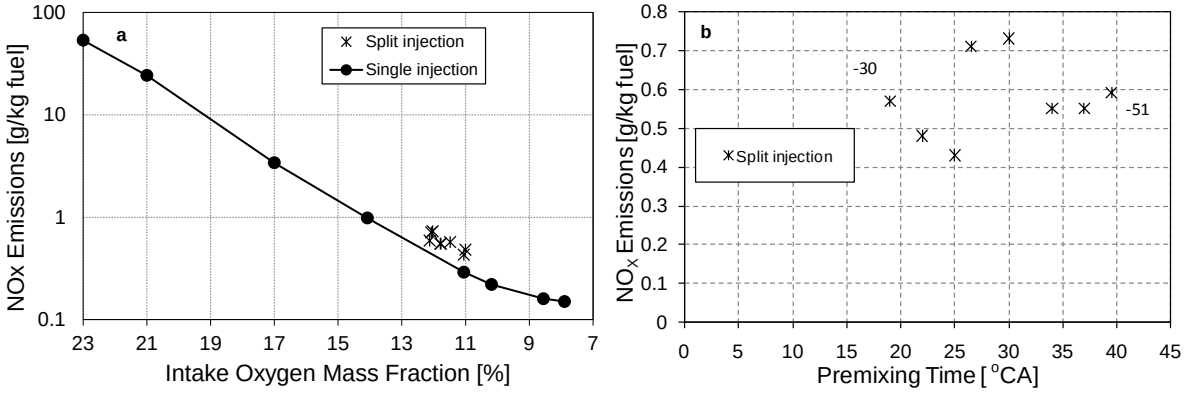

Fig. 6.4: The effect of split injections on NO_X emissions

The data shown in Fig. 6.3 suggests that a split main injection strategy, with appropriate injection timings, can reduce smoke emissions substantially at a given intake oxygen mass fraction. The corresponding NO_X emissions are shown in Fig. 6.4 (note that NO_X emissions are plotted on a logarithmic ordinate, Fig. 6.4a). A relatively small increase in NO_X emissions is seen in all split main injection cases compared to the single main injection case at the investigated Y_{O2}, probably because of the increased in-cylinder temperature due to an earlier SOC (not shown here). However, no trend in the NO_X emissions was seen with different premixing time, Fig. 6.4b. Most significantly, NO_X emissions remained at a very low level (i.e. <1g/kg fuel). Therefore, considering the corresponding reduction in soot emissions shown in Fig. 6.3, the overall effect of the split main injection strategy could be regarded as enabling LTC (or at least LTC-like combustion) at a higher intake oxygen mass fraction (i.e. reduced EGR levels) than was possible with the single injection strategy.

6.4.2 Effects of SOI2 Timing on Smoke Emissions in Reduced EGR LTC

A retarded SOI2 injection timing (-12 ^{o}CA) compared to the baseline SOI2 timing of -15 ^{o}CA ATDC was investigated at reduced EGR levels. It was found that retarding SOI2 beyond -15 ^{o}CA ATDC at Y_{O2} ~12%, resulted in high smoke emissions—a result that may be explained by considering the energy release plots shown in Fig. 6.5 at two SOI2 timings (-12 ^{o}CA and -15 ^{o}CA ATDC, Figs. 6.5a and 6.5b respectively). Note that the energy release plot at Y_{O2} ~11% with SOI timing at -15 ^{o}CA ATDC with a single main injection per cycle is also plotted for a comparison (Fig. 6.5c) and that the injector drive current signals (average of 200 consecutive cycles) indicating the start and the end of injection events are also shown in the figures. Note that the actual fuel injection started 3 ^{o}CA after the injector drive current signals shown in the figures.

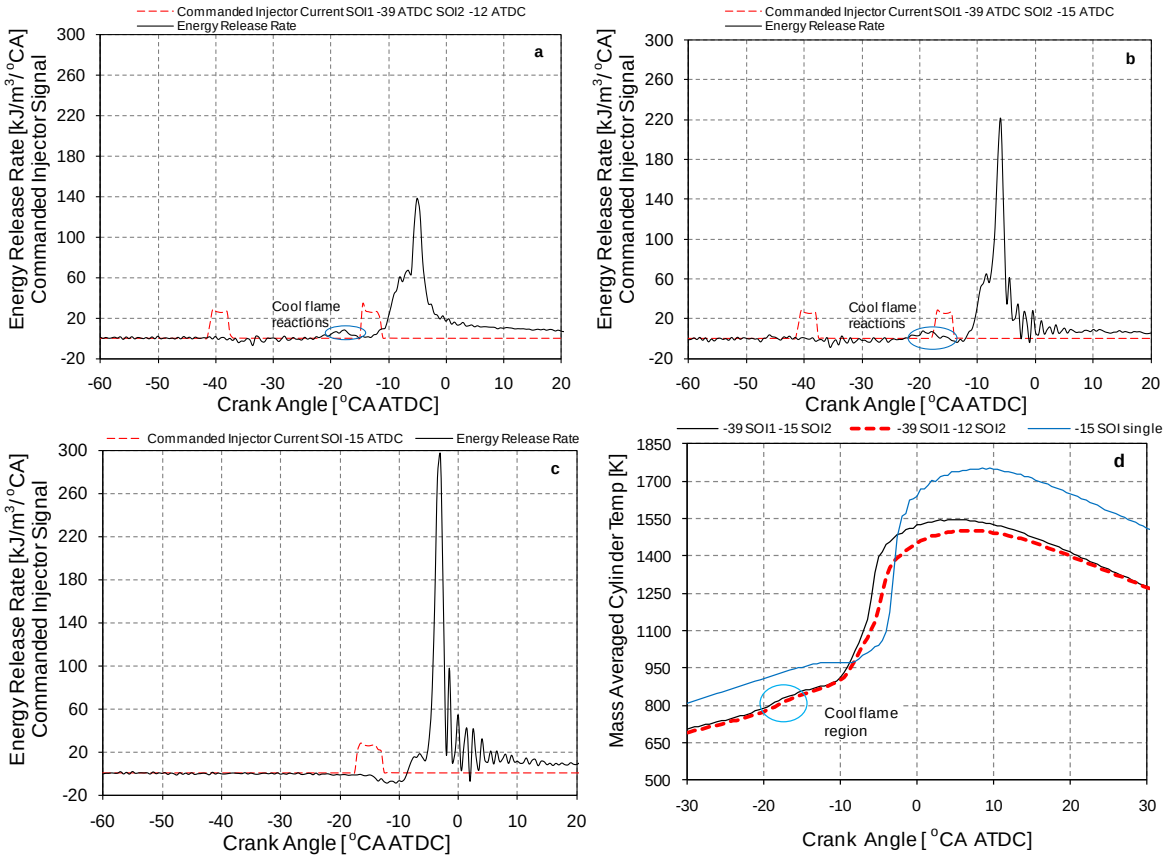

Fig. 6.5: Energy release rate and commanded injector current signals (arbitrary units) (average of 200 consecutive cycles); a. split injections, Y_{O2} ~12%, smoke emissions: 2.7 FSN; b. split injections, Y_{O2} ~12%, smoke emissions: 0.7 FSN; c. single injection, Y_{O2} ~11%, smoke emissions: 3.9 FSN; d. mass averaged in-cylinder bulk gas temperature for the cases shown in Figs. 6.5a-6.5c

Figs. 6.5a and 6.5b show the cool-flame reactions characteristics of LTC, starting approximately 17 ^{o}CA after the SOI1 timing. These reactions cause the energy release rate to rise briefly (at approximately -23 ^{o}CA ATDC) to a low peak (at approximately -19 ^{o}CA ATDC) and then decline to a near-zero level as the cool-flame combustion reaches the region of negative temperature coefficient (NTC). The details of the low temperature cool-flame and NTC reactions are discussed in Sec. 2.6 in Chapter 2. The cool-flame reactions shown in Figs. 6.5a and 6.5b are then closely followed by the main high-temperature energy release reactions. No cool-flame reactions were observed for the 2nd part of the injected fuel and the high-temperature reactions for all the injected fuel took place together. Unlike the split injection cases shown in Figs. 6.5a and 6.5b, no distinct cool flame reaction was seen at this intake oxygen mass fraction (11% Y_{O2}) with the single injection strategy at SOI timing of -15 ^{o}CA ATDC (refer to Fig. 6.5c). It should be noted that the low magnitude of energy release reactions seen between -9 ^{o}CA ATDC to -6 ^{o}CA ATDC in Fig. 6.5c for the single injection case do not represent the low temperature cool flame reactions. Instead, it is more indicative of the intermediate temperature reactions (occurring between the low temperature

and high temperature reactions) corresponding to the bulk gas temperatures of 950-1170 K as shown in Fig. 6.5d. Also note that bulk gas temperatures of 760-880 K correspond to cool flame reactions as shown in Fig. 7.5d for the two split injection cases. The details of the low, intermediate and high-temperature reactions stages are reported by Hwang *et al.* [2008] in an HCCI combustion strategy.

The key difference in the results shown in Figs. 6.5a and 6.5b is the timing of the 2nd injection event with respect to the cool flame reactions. It is apparent from Fig. 6.5a that the 2nd injection event occurs after the cool-flame reaction period. Indeed, part of the fuel from the 2nd injection (SOI2 at -12 ^{o}CA ATDC) is injected into the main high-temperature combustion reactions. In this case it is to be expected that soot formation would increase because of the localized high in-cylinder temperature and the reduced ignition delay (leading to a potentially rich local equivalence ratio) of the fuel injected during the second injection event; this led to smoke levels approaching 3 FSN. Other cases at this intake oxygen mass fraction with injection timings more retarded than -12 ^{o}CA ATDC (not shown here) showed similar effects. On the other hand, with SOI2 at -15 ^{o}CA ATDC (Fig. 6.5b), the 2nd injection is timed such that the fuel is injected into the NTC region of the cool-flame reactions from the 1st injected fuel mass. In this case, smoke emissions were 75% lower than the earlier case. This result is consistent with the results reported by Lee and Lida [2001] and Kanda *et al*. [2005] indicating that when diesel fuel was injected either prior to or during the low temperature reactions, soot formation was restrained. It was assumed that the intermediate products i.e. hydrogen peroxide (H_2O_2) and formaldehyde (CH_2O) formed during the low temperature oxidation reactions had a reducing effect on soot formation [Lee and Lida, 2001]. Musculus [2006] suggested that proper phasing of the cool flame event relative to fuel injection could also help vaporizing the liquid fuel. The results from the current work support the view that fuel injection during the NTC region of a cool-flame reaction is a technique that can be used to suppress soot formation from a subsequent injection event; however, the results obtained in this investigation do not elucidate the mechanism of soot reduction and further detailed investigation in this area is required. Similar phenomena were observed with all of the energy release plots with SOI1 timings variable between -51 to -30 ^{o}CA ATDC for a fixed SOI2 timing at -15 ^{o}CA ATDC. Further investigations regarding the effect of variable SOI2 timings on combustion and emissions with the 50:50 split injection strategy at a higher intake pressure (150 kPa) are reported in more detail in Sec. 6.5.3.

It can be concluded that the soot emissions in the split injection strategy are significantly influenced by both the SOI1 and SOI2 timings without any noticeable effect on NO_X emissions. It is also found that less flexibility in terms of varying the SOI2 timing at the investigated Y_{O2} was available due to its effect on smoke emissions. On the other hand, for a fixed SOI2 timing, SOI1 timing affected the smoke emissions by influencing the fuel-air premixing for the fuel mass injected during the 1st injection. Therefore, SOI1 timing is used as the variable to compare the combustion and emission parameters at different operating conditions investigated and reported in this chapter.

6.4.3 Effects of Split Injections on Combustion By-Products Emissions

Implementing the split main injection strategy at intake oxygen mass fractions between 11% and 12% increased THC emissions compared with the single injection strategy at the same intake oxygen mass fraction as shown in Fig. 6.6a. This is likely a result of, in the 50:50 fuel split case, a proportion of the fuel injected during the 1st injection event entering into the squish region. Although part of it may get oxidized during the mixing-controlled or late cycle burn out phase during the expansion stroke, a part of it may still reside in the crevice volumes and other parts of the squish region and escapes combustion, thus contributing to higher THC emissions. It is also hypothesized that either over-mixing (longer premixing time may lead to lean mixtures for the mass of fuel in the 1st injection event) or spray impingement on the combustion chamber walls (due to advanced SOI1 timing) might contribute to the high THC emissions. However, it is noteworthy that compared to the case of 8% intake oxygen mass fraction with single injection, where Y_{O2} ~8% is the intake oxygen mass fraction required to give acceptable NO_X and smoke emissions in the single injection mode, the split main injection strategy yields an almost 50% reduction in THC emissions. The mechanisms by which these emissions are changed at constant Y_{O2} are discussed in more detail in the next section.

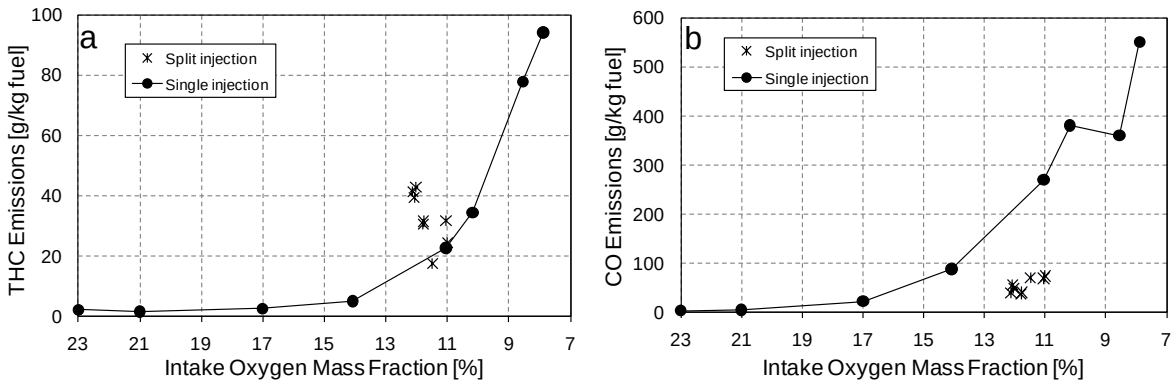

Fig. 6.6: Effects of split and single injections on THC and CO emissions

Fig. 6.6b shows the experimental data for CO emissions for the single injection and split main injection cases. CO emissions are seen to be reduced significantly by the split main injection strategy at Y_{O2} ~12% compared to the single injection case at the same intake oxygen mass fraction. It is thought that this is primarily due to better premixing of the fuel-air charge before the SOC, thereby minimizing rich pockets of fuel-oxygen charge in the combustion chamber. Reduced CO emissions at 50:50 fuel split case roughly coincided with the increase in THC emissions in some cases (note that the combustion of 1 kg of fuel with air produces approximately 2 kg of CO). However, it should be recognized that whilst the engine-out CO emissions are higher than the current legislated limits it is expected that the high CO emissions can be treated relatively easily with a DOC.

As regards the significant reduction in THC and CO emissions between the ~8% Y_{O2} single injection case and the 11-12% Y_{O2} split main injection cases observed in Fig. 6.6, this is thought to

be due to a reduction in the rich mixture zones within the cylinder and a delay in the onset of bulk quenching of the end gases. The delayed onset of bulk quenching in the present work is indicated by the long combustion duration (CA5-CA95) and advanced CA50 data shown in Fig. 6.7. Longer combustion durations are seen with the split main injection strategy compared to those found with a single injection event at the same intake oxygen mass fraction (Fig. 6.7a). Longer combustion durations are also indicated at higher intake oxygen mass fractions (Y_{O2} >12%) with the single injection strategy. This split injection strategy also results in an earlier combustion phasing, as demonstrated by the advanced CA50, shown in Fig. 6.7b. The net effects of the advanced combustion phasing and the longer combustion durations suggest that more of the fuel and CO will be oxidized before bulk quenching occurs compared to the case of the 8% intake oxygen mass fraction with a single injection. In turn, this is expected to result in lower THC and CO emissions.

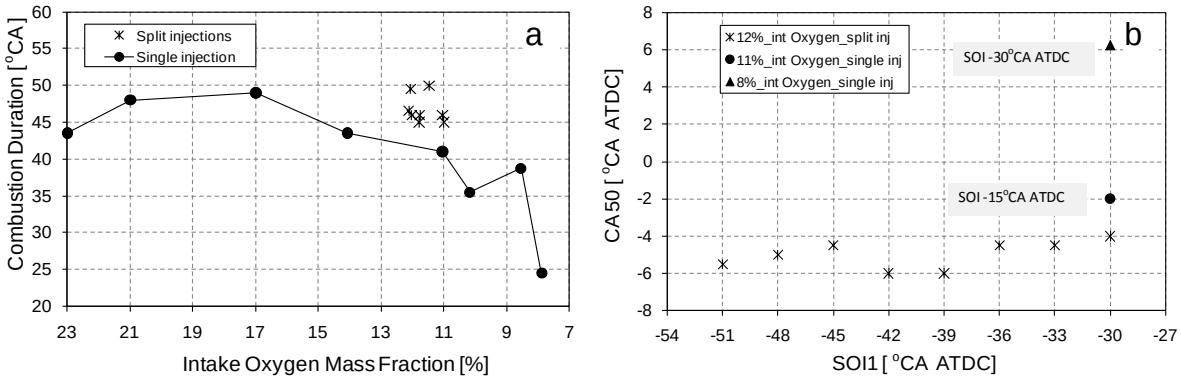

Fig. 6.7: Effects of split and single injections on combustion duration and combustion phasing. The combustion phasing (CA50) at 8% (SOI at -30 °CA ATDC) and 12% (SOI at -15 °CA ATDC) intake oxygen mass fractions with single injection are also plotted in Fig. 6.7b for comparison.

As mentioned earlier, the fuelling quantity was maintained constant. As a result, the power generated as indicated by the GIMEP varied between 500 and 550 kPa, depending on the timing of SOI1 and Y_{O2} with split injections. It should be noted that the COV of GIMEP were <2% for all the split injection cases and no misfiring cycles were seen. The data on GISFC with the split and single injection strategies are shown in Fig. 6.8. It can be seen from the figure that GISFC at Y_{O2} ~12% with split injections was increased compared to single injection operation at the same intake oxygen mass fraction. The increased GISFC (depending on SOI1 timing) at Y_{O2} ~12% may be attributed partly to the advanced combustion phasing (see Fig. 6.7b), which is likely to increase heat transfer losses and compression work and partly to lower combustion efficiency (see Fig. 6.9) because of increased THC emissions. Nonetheless, it is significant that the GISFC for all the split injection cases at Y_{O2} ~12% are substantially lower than the GISFC at Y_{O2} ~8% with a single main injection. Interestingly, Fig. 6.9 clearly shows an inverse relationship between combustion efficiency and

GISFC, indicating that combustion efficiency is the largest influence on thermal efficiency at these conditions.

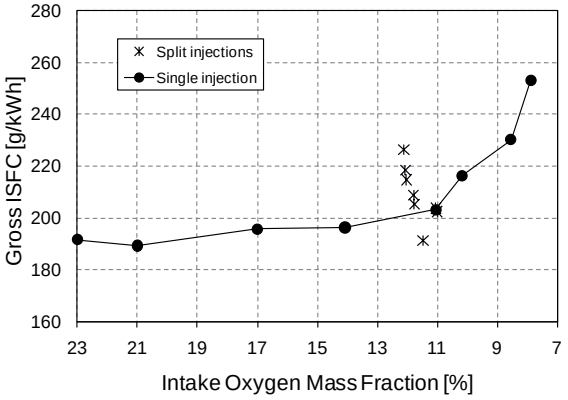

Fig. 6.8: Effect of split and single injections on GISFC

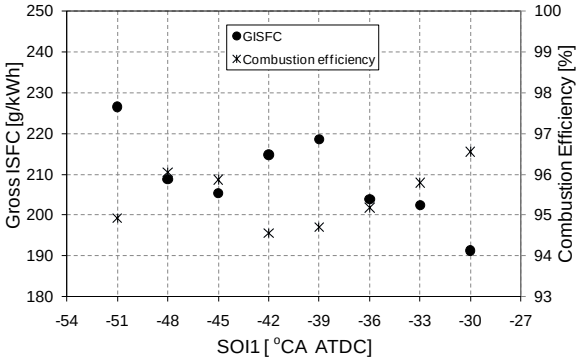

Fig. 6.9: The effect of different SOI1 timings (with -15 °CA ATDC SOI2 timing) on GISFC and combustion efficiency

A comparison has been made to illustrate the effects of 50:50 split main injection with single injection at the same intake oxygen mass fraction (Y_{O2} ~11%) and with high-EGR LTC at much lower intake oxygen mass fraction (Y_{O2} ~8%). For this comparison, the 'best SOI1 split injection' (SOI1 -45 °CA ATDC at Y_{O2} ~11.5%) has been selected which corresponds to a smoke emission <1 FSN with low THC and CO emissions as well as low GISFC. NO_X emission was very low at ~0.6 g/kg of fuel with the split injection strategy at all SOI1 timings. Smoke, NO_X, THC and CO emissions have been plotted along with GIMEP and GISFC as shown in Fig. 6.10. Although the GIMEP was higher at 11% Y_{O2} with the single injection strategy compared to the split injection strategy at 11.5% Y_{O2}, GISFC for both the cases were the same; this is due to a marginally higher fuel flow rate with the single injection case compared to the split injection strategy. In general, Fig. 6.10 demonstrates the potential of the split injection strategy in terms of reducing smoke and CO emissions, although NO_X and THC emissions increased marginally compared to single injection at the same intake oxygen mass fraction. However, as has been previously discussed, THC, CO

emissions and GISFC reduced significantly compared to single injection at 8% intake oxygen mass fraction.

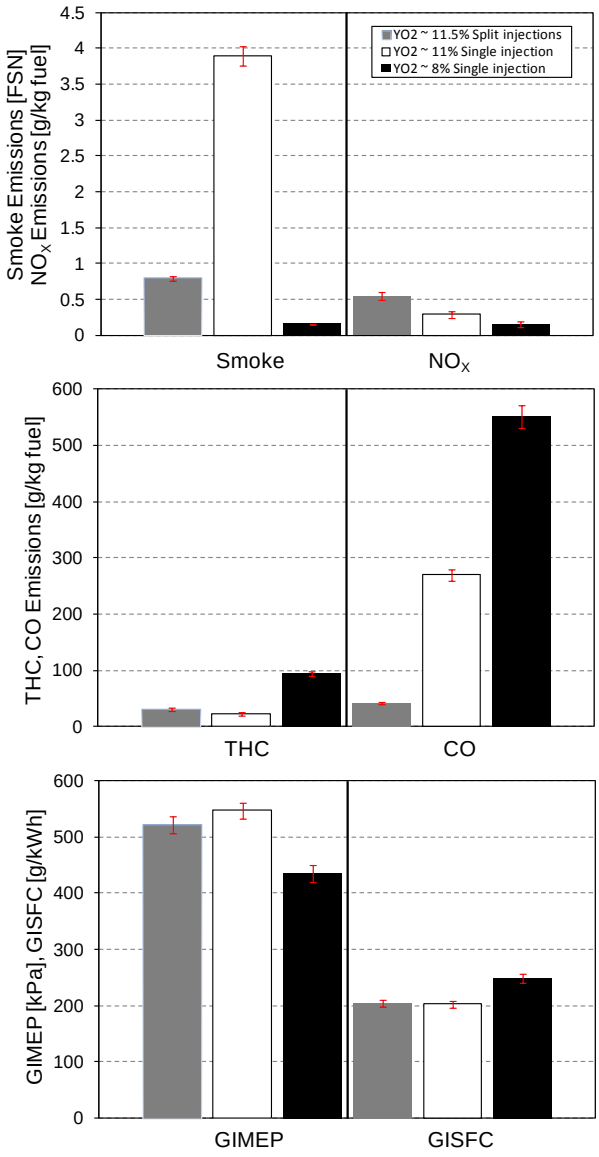

Fig. 6.10: Comparison of emissions and performance at 'best SOI1' split injection (SOI1 -45 ^{o}CA ATDC, SOI2 -15 ^{o}CA ATDC) with single injection

6.5 Effects of Operating Parameters on Split Injection LTC

The previous section demonstrated that split injection in LTC offers significant benefits over single injection LTC, and showed that both SOI1 and SOI2 timings influenced smoke emissions and the combustion event. The objective of this section is to investigate the sensitivity of the split injection strategy to variations of operating parameters (i.e. EGR levels, intake pressures, injection pressures, injection timings and fuel split ratios) on emissions and fuel economy. The effects of variable injection pressures (90 MPa and 110 MPa) and variable intake pressures (120 kPa and 150 kPa, absolute) on diesel LTC with the 50:50 split injection strategy are presented. The potential of

reducing the fraction of the fuel in the 1st injection event (25:75 fuel split ratio) on emissions and fuel economy with the split injection strategy is also investigated. The operating conditions are listed in Table 6.2. The investigated operating parameters are likely to be encountered by an engine while following a legislated drive cycle.

The results are subdivided into four sub-sections to provide a more focussed investigation of the effects of split injections on emissions and other related combustion parameters:

I. Effects of variable intake oxygen mass fractions at a constant intake pressure
II. Effects of variable injection pressures at a constant intake pressure
III. Effects of variable intake pressures at a constant intake oxygen mass fraction
IV. Effects of variable fuel split ratios at a constant intake oxygen mass fraction.

6.5.1 Effects of Variable Intake Oxygen Mass Fractions at a Constant Intake Pressure

The experimental results for smoke, CO and THC emissions and GISFC for the engine operating with two different intake oxygen mass fractions (10.5% and 12%) at an intake pressure of 120 kPa (absolute) using a split main injection strategy are shown in Fig. 6.11. Results are reported as a function of SOI1 timing—SOI2 timings are held constant at values of -18 and -15 ^{o}CA ATDC respectively, corresponding to MBT injection timings. For the purposes of comparison, emissions and GISFC levels corresponding to a single injection strategy with an identical injected fuel mass at MBT fuel injection timing and an intake oxygen mass fraction of 11% are shown in the figures by a solid horizontal line. NO_X emissions were less than 1 g/kg of fuel for all the cases investigated and hence, are not reported.

The results show CO, THC and GISFC to be consistently higher in the case of the 10.5% intake oxygen mass faction than for the 12% intake oxygen mass fraction case, Figs. 6.11b – 6.11d. This is in agreement with earlier studies performed on the same engine using a single pulse injection strategy [Cong, 2011]. Smoke emissions, Fig. 6.11a, are shown to be relatively insensitive to intake oxygen mass fraction for SOI1 timings between -51 and -39 ^{o}CA ATDC (in all the cases the emissions are less than 1 FSN). At first glance the results do seem to indicate some sensitivity to intake oxygen mass fraction at a SOI1 timing of -36 ^{o}CA ATDC, where the smoke emissions for the 10.5% case are markedly higher than for the 12% case. However, considering the experimental results for smoke in conjunction with the CO, THC and GISFC data collected at this same SOI1 timing and accounting for the combustion chamber geometry, the results suggest that emissions and fuel consumption at this timing are strongly affected by spray-wall interactions.

A graphical investigation using the spray penetration model of Hiroyasu and Arai [1990] (see Appendix A5 for the details) indicates that fuel from the 1st injection event would likely impinge on the lip of the piston bowl for SOI1 timings between -30 to -36 ^{o}CA ATDC. Fig. 6.12 shows the case of SOI1 at -36 ^{o}CA ATDC. As this simple geometric approach does not take the effects of swirl or

changing cylinder pressure into consideration, this hypothesis was investigated by in-cylinder imaging using the borescope, discussed in Sec. 3.6 in Chapter 3. Fig. 6.13 shows a sequence of spray images showing details of the first injection event (upper row) and the second injection event (lower row) for SOI1 timing of -39 ^{o}CA ATDC and a SOI2 timing of -15 ^{o}CA ATDC.

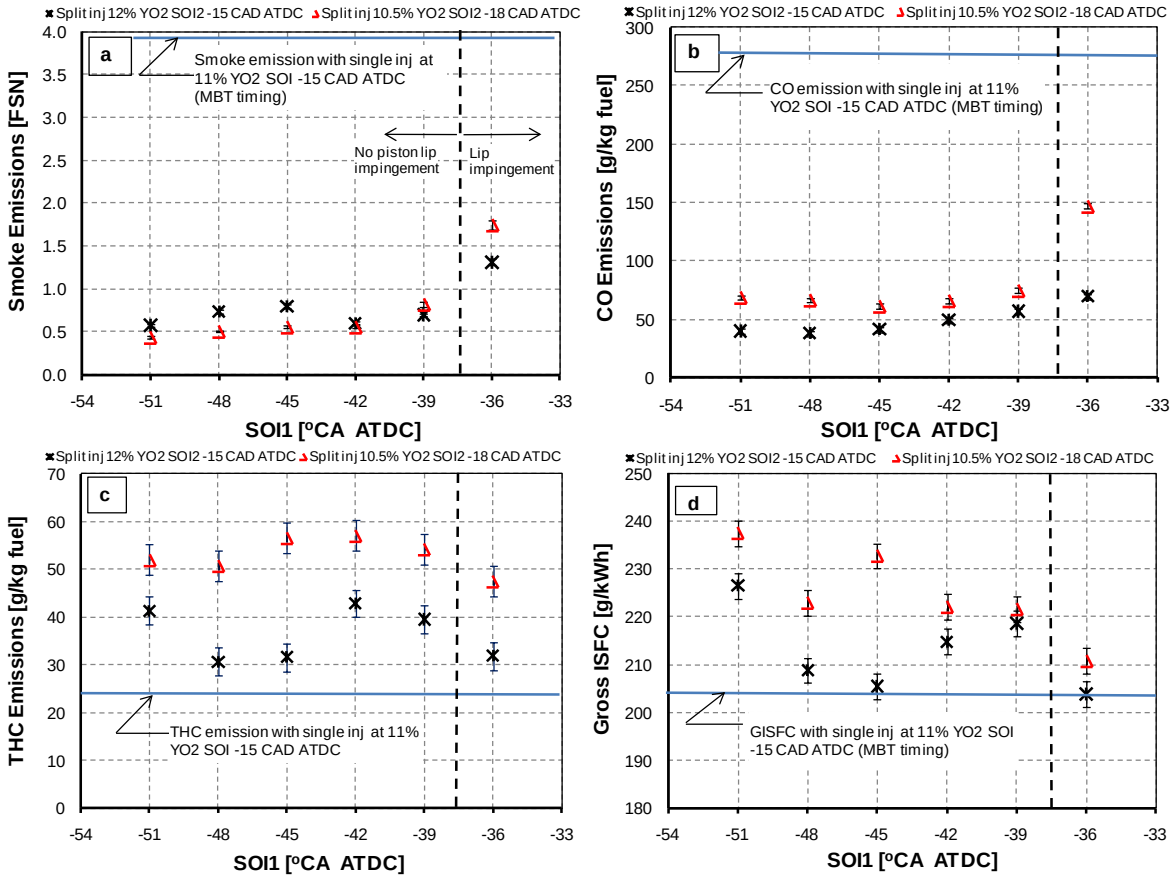

Fig. 6.11: Smoke, CO and THC emissions and gross ISFC at different SOI1 operating conditions at various intake oxygen mass fractions at 120 kPa intake pressure

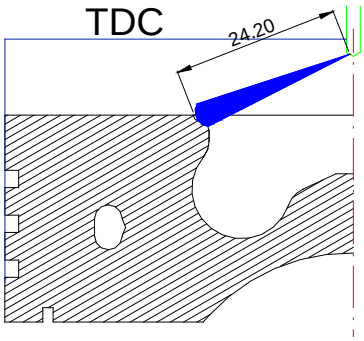

Fig. 6.12: Spray penetration analysis showing spray impingement on the piston lip for the fraction of fuel injected during the 1st injection event; SOI1 -36 ^{o}CA ATDC, positions of the piston and the spray are shown 2 ^{o}CA after SOI1. The distance from the injector to the spray tip is in mm.

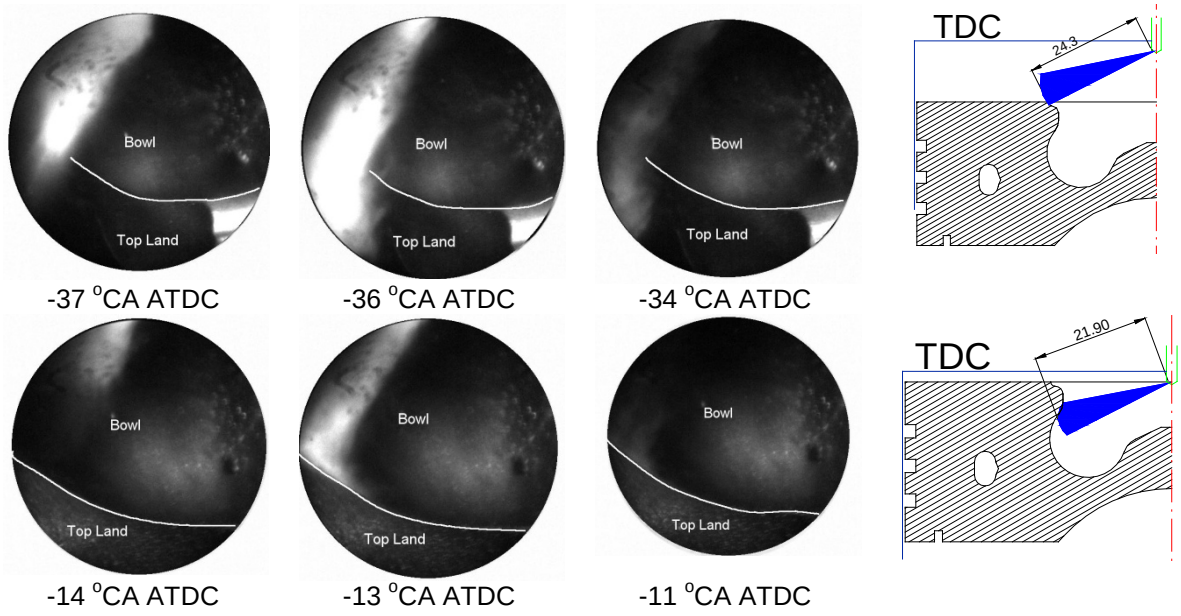

Fig. 6.13: Spray images showing spray impingement for the fuel spray during the 1st and 2nd injection events in the squish region and piston bowl respectively; upper row: 1st injection event, bottom row: 2nd injection event; SOI1 -39 °CA ATDC, SOI2 -15 °CA ATDC. Camera gain: 25 dB. The schematic in the right hand side shows spray impingement locations with the two injection events calculated with the Hiroyasu and Arai [1990] spray penetration model. The distance from the injector to the spray tip is in mm.

The images clearly show fuel from the 1st injection event missing the piston bowl and entering the squish region at crank angles earlier than -36 °CA ATDC. At -36 °CA ATDC, the fuel is seen to impinge on the piston top land. Continued spray impingement on the piston top land/bowl lip region was observed until -34 °CA ATDC during the 1st injection event. This shows that the fuel distribution from the 1st injection pulse will differ markedly between SOI1 timings occurring before -39 °CA ATDC, in which case all of the fuel is expected to be distributed in the squish region, and those occurring after -39 °CA ATDC, where some (unknown) fraction of the fuel is expected to be deposited on the piston top land and in the piston bowl—note that in all cases the fuel injected in the second injection event is wholly contained within the piston bowl. The uneven distribution of the fuel between the piston bowl and the squish region would change the local equivalence ratio, thus, influencing the emissions for SOI1 timing after -39 °CA ATDC.

Although the results indicate that the final level of smoke emission is insensitive to intake oxygen mass fraction in the range examined, there is evidence to suggest that the temporal development of the in-cylinder soot production is affected by Y_{O2}. Fig. 6.14 shows reaction zone flame temperatures (Fig. 6.14a) and *KL* factors (soot concentrations shown in Fig. 7.14b) as a function of crank angle for the two intake oxygen mass fraction cases under investigation. Not only is the peak reaction zone temperature seen to be substantially higher for the 12% intake oxygen mass

fraction case than for the 10.5% case, but a higher temperature is maintained throughout the combustion event. An increase in intake oxygen mass fraction also resulted in the peak energy release rate occurring earlier (advanced combustion phasing, CA50) at 12% Y_{O2} as shown in Fig. 6.14c. Accordingly, the higher reaction zone temperatures for the 12% intake oxygen mass fraction shown in Fig. 6.14a is expected to include contributions from both the mass averaged cylinder temperature (Fig. 6.14d) and the oxygen concentration effect (local equivalence ratio). Note the occurrence of the cool flame reactions at ~800 K (Fig. 6.14d) consistent with the values (760-880 K) reported in literature [Sjoberg and Dec, 2007].

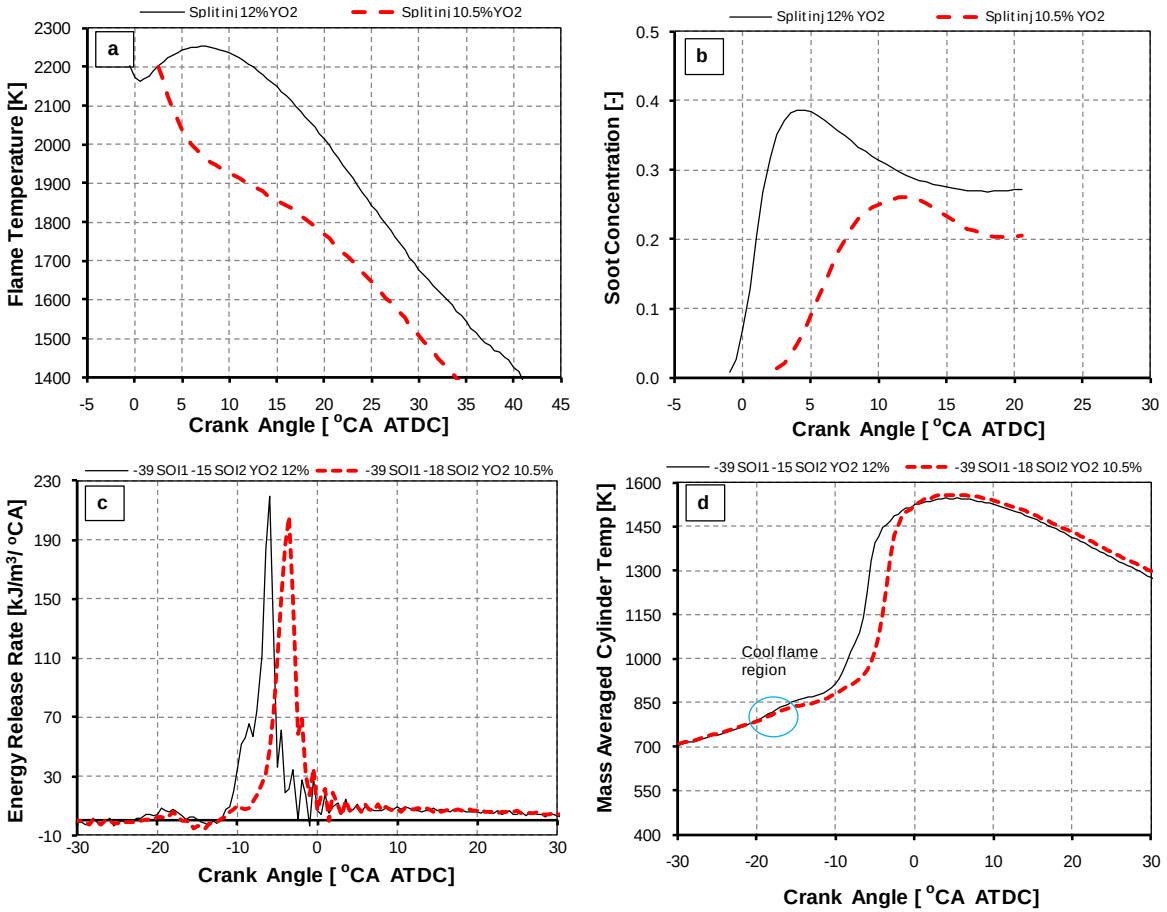

Fig. 6.14: a. Flame temperature, b. Soot concentration, c. Energy release rate, d. Mass averaged cylinder temperature at various intake oxygen mass fractions

In turn, the temperature and local equivalence ratio can be expected to affect both soot formation and any subsequent soot oxidation. This is evident in the data presented in Fig. 6.14b which show that soot production occurs earlier in the cycle, is more rapid, and reaches a higher peak value in the 12% intake oxygen mass fraction case. Subsequently, the results indicate that soot oxidation is relatively more rapid in the 12% case. Both of these observations are consistent with a higher local flame temperature and are further supported by the sequence of images shown in Figs. 6.15 and 6.16.

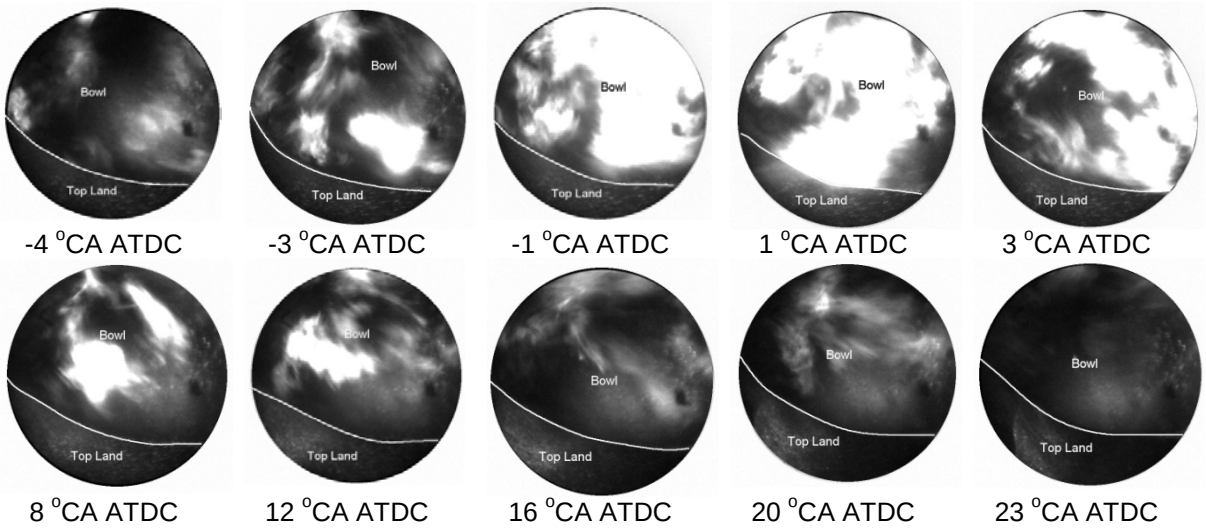

Fig. 6.15: Combustion images at different crank angles at 12% intake oxygen mass fraction; SOI1 -39 °CA ATDC, SOI2 -15 °CA ATDC. Camera gain: 25 dB

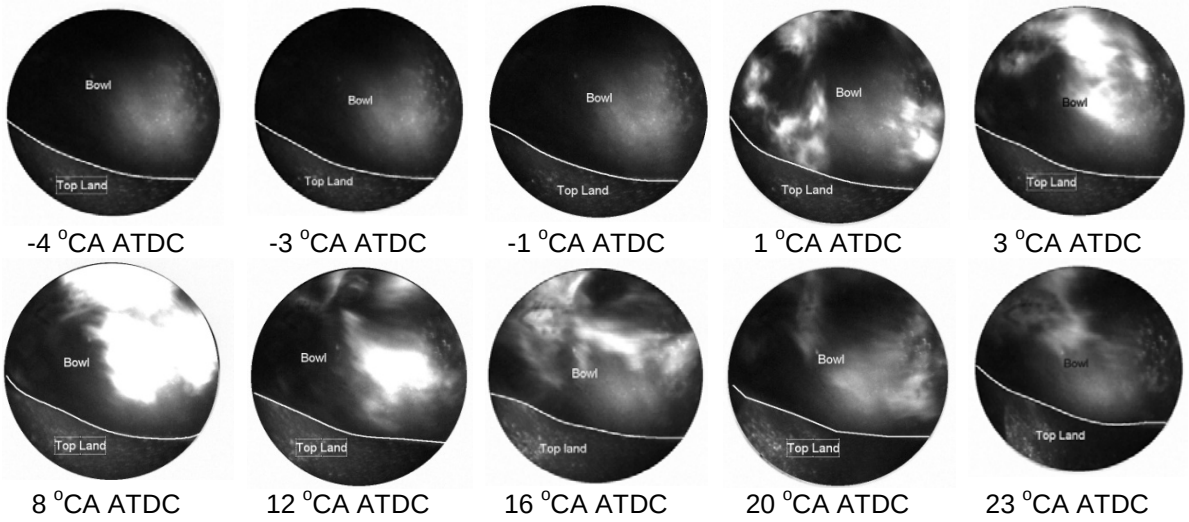

Fig. 6.16: Combustion images at different crank angles at 10.5% intake oxygen mass fraction; SOI1 -39 °CA ATDC, SOI2 -18 °CA ATDC. Camera gain: 25 dB

In Fig. 6.15 (12% Y_{O2}), significant luminosity, attributed to broadband soot incandescence, is visible at an image acquisition time of -3 °CA ATDC. The area of luminosity is extensive, filling a large fraction of the visible piston bowl. Substantial soot luminosity continues through to 3 °CA ATDC. This behaviour differs from that shown in Fig. 6.16 (10.5% Y_{O2}) where substantial soot luminosity is not seen until approximately 3 °CA ATDC, i.e. 6 °CA later in the cycle than for the higher intake oxygen mass fraction case. Note also the similarity between the two cases at an image acquisition time of 12 °CA ATDC; this is consistent with the earlier observation from Fig. 6.14b that indicates similar final levels of soot emission for the two intake oxygen mass fraction cases. It agrees with the measured smoke emissions (FSN) that were essentially the same (refer to Fig. 6.11a

at -39^{o} CA ATDC SOI1 timing). Significantly, these images and the associated two-colour pyrometry results clearly demonstrate that soot production in this twin injection 'mixing-controlled' LTC mode involves both significant soot formation and oxidation. This contrasts with many alternative LTC strategies such as HCCI, MK and single injection high-EGR LTC (shown in Fig. 5.2a in Chapter 5) where no visible soot incandescence is seen, i.e. the low soot emissions in these modes are the result of low formation rates. This result further validates the use of two-colour pyrometry in this application because the pyrometry technique is dependent on visible soot luminosity.

Returning now to the effect of intake oxygen mass fraction on the CO and THC emissions and the fuel consumption of the engine as shown in Figs. 6.11b – 6.11d, it was previously hypothesised that an increase in THC and CO emissions seen at reduced intake oxygen mass fraction with a single injection strategy is due to increased bulk quenching (a result of a reduced in-cylinder oxygen concentration and local in-cylinder temperature). The results of the two-colour pyrometry shown in Fig. 6.14a, suggest that this same bulk quenching mechanism is responsible for the increased CO and THC emissions seen for the lower intake oxygen mass fraction case in the split injection strategy also, see Figs. 6.11b and 6.11c. The increase in GISFC at 10.5% Y_{O2} shown in Fig. 6.11d is consistent with the reduction in combustion efficiency as indicated by the increased THC and CO emissions (Figs. 6.11b and 6.11c). It is interesting to note that GISFC with the split injection strategy can be maintained very similar to the single injection event through careful selection of injection timings and dwell timings (as shown at the SOI1 timings of -36 ^{o}CA ATDC and -45 ^{o}CA ATDC with SOI2 at -15 ^{o}CA ATDC at 12% Y_{O2} in Fig. 6.11d).

6.5.2 Effects of Variable Injection Pressures at a Constant Intake Pressure

Injection pressure was shown in Chapter 4 to have significant influence on single injection high-EGR LTC. To evaluate its influence on split injection LTC, a comparison was made between the emissions and fuel consumption using two injection pressures (90 and 110 MPa) at a constant intake pressure (120 kPa) with -15 ^{o}CA ATDC SOI2 timing. Note that no lower injection pressures were investigated as previous work had shown that combustion stability and fuel economy were much reduced for P_{inj} <90 MPa [Cong *et al*., 2010; Cong *et al*., 2011b]. The upper limit to the injection pressures examined was dictated by the need to restrict the rate of pressure rise below 1 MPa/^{o}CA while maintaining a constant SOI2 injection timing. It was found that as injection pressure was increased, higher levels of EGR were required to satisfy these constraints—directly affecting the intake oxygen mass fraction and complicating the comparison of experimental results. The change in intake oxygen mass fraction at the chosen injection pressure of 110 MPa was considered to be the maximum acceptable value in the work reported in this chapter. The results for smoke emissions and GISFC are plotted as a function of SOI1 timing in Figs. 6.17a and 6.17b, respectively. Smoke

emissions and GISFC levels corresponding to the single injection strategy at 110 MPa injection pressure with MBT injection timing at 11% Y_{O2} are also compared in the figures.

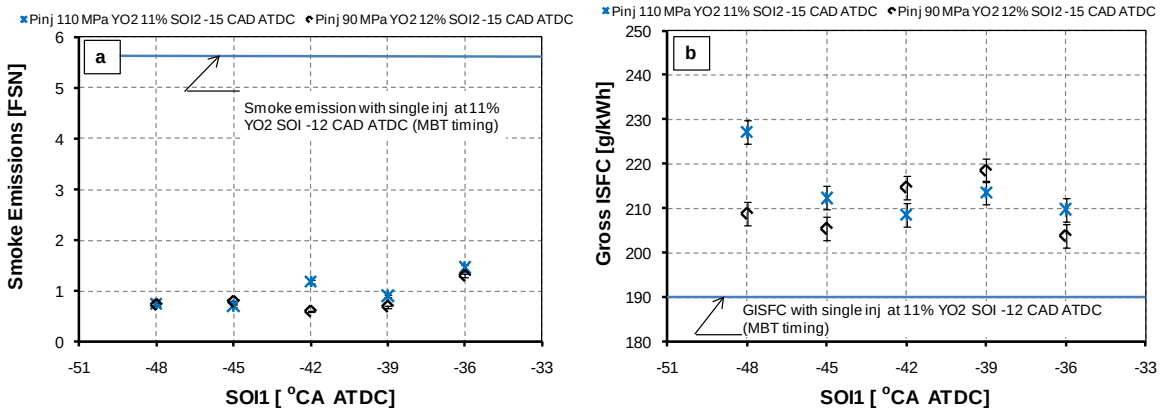

Fig. 6.17: (a) Smoke emissions and (b) GISFC at two injection pressures (90 and 110 MPa)—intake oxygen mass fractions and SOI2 for the two cases are given in the legend

As shown in Fig. 6.17a, smoke emissions did not show any significant variation with injection pressure or SOI1 timing with the split injection strategy. This is contrary to conventional diesel combustion and high-EGR (67% by mass, 7.5% Y_{O2}) split injection LTC strategy reported by Koci *et al*. [2009], where higher injection pressure reduces smoke emissions due to better atomization and vaporization of the fuel (spray penetration is also expected to increase with higher injection pressure by a factor of $P_{inj}^{0.25}$ [Hiroyasu and Arai, 1990] which may affect impingement) without any significant impact on THC and CO emissions. The smoke results reported here are likely confounded by the effects of intake oxygen mass fraction. In order to maintain a fixed SOI2 timing for both the injection pressure cases examined here, a higher EGR rate (53%) was found necessary at the higher injection pressure to limit the rate of pressure rise. It is hypothesized that the higher injection pressure case (giving better fuel atomization and vaporization) at the lower intake oxygen mass fraction result in a local equivalence ratio at the SOC that is not significantly different to the lower injection pressure case at the higher intake oxygen mass fraction, thus, leading to similar levels of smoke emissions seen in Fig. 6.17a.

With regard to THC and CO emissions, variation of injection pressure in the range tested was found to have only minor influence on THC and CO emissions (not shown here), affecting GISFC as shown in Fig. 6.17b. However, no clear trend is seen in the results. It was notable, however, that GISFC increased significantly at the higher injection pressure when SOI1 was advanced beyond -45° CA ATDC.

6.5.3 Effects of Variable Intake Pressures at a Constant Intake Oxygen Mass Fraction

Intake pressure was shown in Chapter 4 to have significant influence on single injection high-EGR LTC. To evaluate its influence on the split injection LTC, a comparison was made between the emissions and fuel consumption with two intake pressures (120 and 150 kPa) at a constant intake oxygen mass fraction of 12%; these results are shown in Fig. 6.18 as a function of SOI1 timing (with a constant SOI2 timing of -15 ^{o}CA ATDC). Emissions and GISFC levels corresponding to the single injection strategy at 150 kPa intake pressure with MBT injection timing at an intake oxygen mass fraction of 12% are also shown in the figures. The results show CO, THC and GISFC to be consistently lower in the case of 150 kPa intake pressure than for the 120 kPa intake pressure case, Fig. 6.18 (b-d). This is in agreement with the earlier studies with a single injection strategy as discussed in Chapter 4. The trend in smoke emissions with varying intake pressure at different SOI1 timings is less clear; however, it is noteworthy that in both cases the smoke emissions are <1 FSN with the split injection strategy.

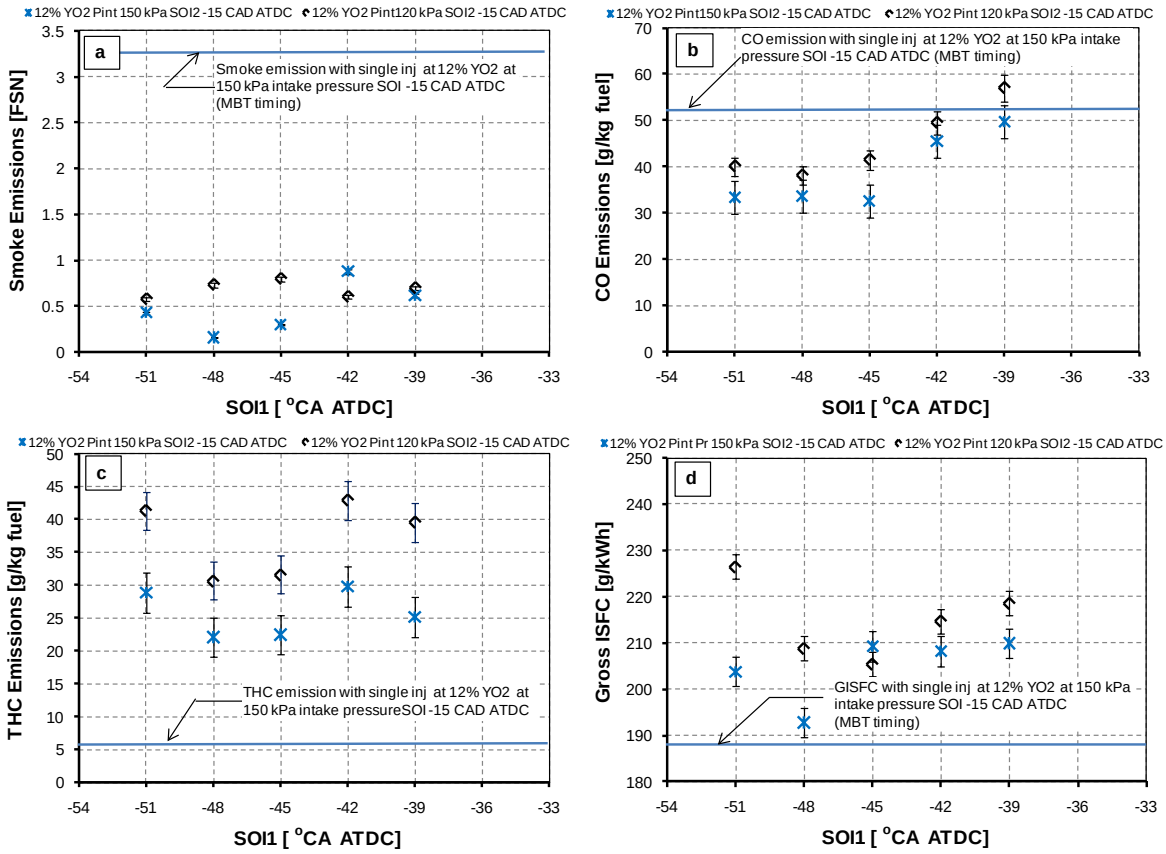

Fig. 6.18: (a) Smoke emissions, (b) CO emissions, (c) THC emissions, (d) gross ISFC at various intake pressures

The calculated energy release rates, the combustion durations and the corresponding two colour pyrometry results for local temperature and soot concentration for the two intake pressures

under investigation are shown in Figs. 6.19a – 6.19d respectively. It is interesting to note that there are no significant differences in the peak reaction zone temperatures for the two cases (although the flame temperature decreases more rapidly for the higher intake pressure experiments); see Fig. 6.19c. However, substantial differences are shown in the soot concentration as a function of crank angle (Fig. 6.19d) for the two cases—suggesting that soot production under these two operating conditions is strongly influenced by the local equivalence ratio.

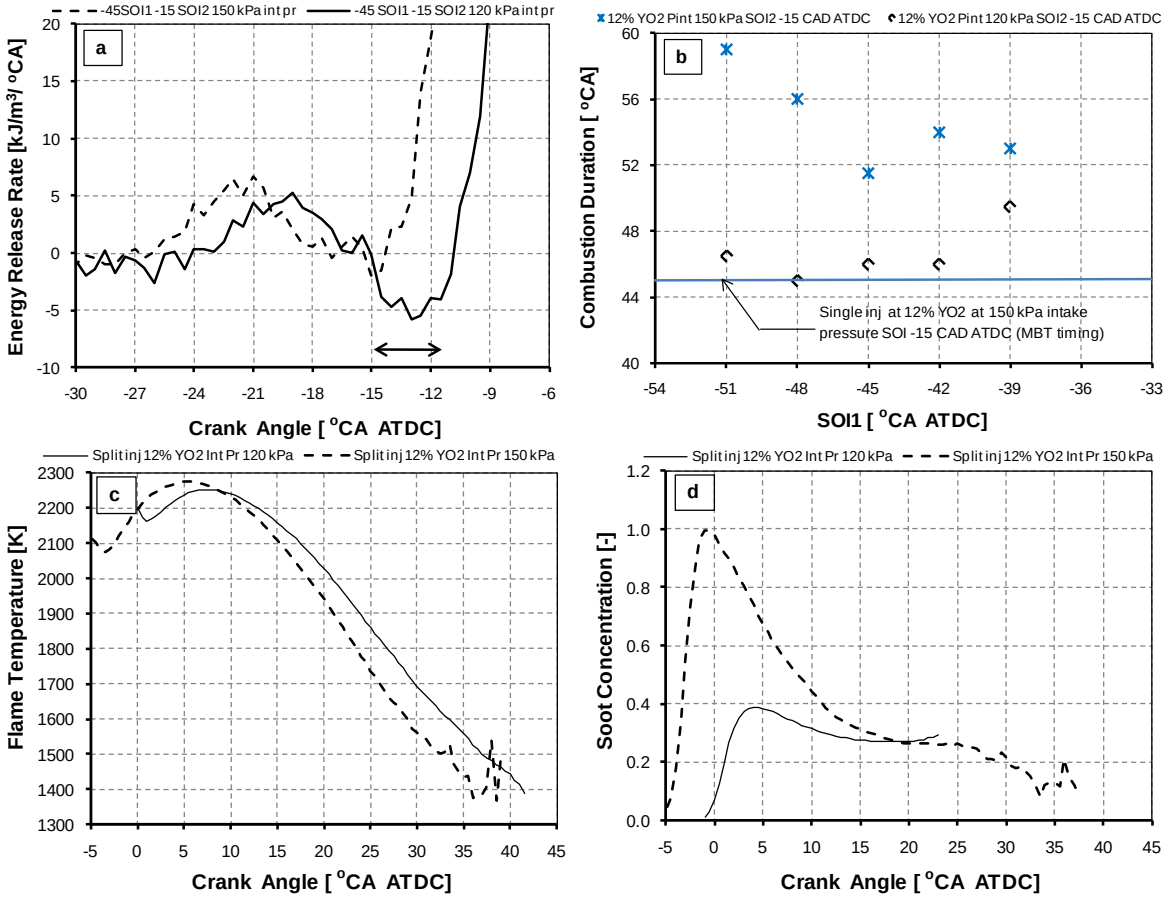

Fig. 6.19: (a) Low temperature cool flame reactions at various intake pressures, representative SOI2 timing and injection duration is shown by the arrow; (b) Combustion duration at various intake pressures; (c) Flame temperature; (d) Soot concentration at various intake pressures. SOI1: -45 ^{o}CA ATDC, SOI2: -15 ^{o}CA ATDC

Fig. 6.19a shows the timing of the 2nd injection event with respect to energy release rate. It can be seen that whereas in the lower intake pressure case the second fuel mass is injected into the NTC region of the cool flame reactions, in the higher intake pressure case the second injection event occurs during a period of high energy release as the main combustion reaction is in progress. This is expected to reduce the ignition delay of the second injected fuel mass in the 150 kPa intake case compared to the 120 kPa case; thus, yielding a richer local equivalence ratio and the substantially

increased peak smoke concentrations shown in Fig. 6.19d. Subsequently, the results indicate that soot oxidation is relatively more rapid and more complete in the 150 kPa intake pressure case. The higher oxygen concentration (per unit volume) for the 150 kPa intake pressure case clearly favours soot oxidation during the high temperature mixing-controlled phase of combustion. Furthermore, Fig. 6.19b shows that combustion duration is increased at the higher intake pressure. The increased combustion duration is reflected in the observation of continued soot oxidation late in the expansion stroke at higher intake pressure (see Fig. 6.19d) ultimately reaching a soot concentration level significantly lower than for the 120 kPa intake pressure case. This also agrees with the engine-out smoke emission (0.3 FSN) at -45 ^{o}CA ATDC SOI2 timing (refer to Fig. 6.18a).

The smoke trend observed in this split injection strategy at 12% Y_{O2} is contrary to that reported by Koci *et al*. [2009] at 7.5% Y_{O2}. It was shown in the cited work that PM emissions increased at higher intake pressure due to reduced ignition delay for the mass of fuel injected during the 2nd injection event. In the cited work, it was hypothesized that soot formation and engine-out smoke emissions increased due to a reduced ignition delay and soot oxidation was not enhanced due to lower flame temperature and lower in-cylinder oxygen concentration compared to the 12% Y_{O2} used in the work reported in this chapter. The soot reduction mechanism discussed above in the present split injection strategy at 12% Y_{O2} is very different from those reported in literature at 7.5% $Y_{O2.}$

Returning to the effect of intake pressure on THC and CO emissions, as expected THC emissions reduced, whereas surprisingly there was only a marginal reduction in CO emissions at higher intake pressure (refer to Figs. 6.18b and 6.18c). This indicates that CO oxidation was not enhanced further at higher intake pressure. The fact that THC emissions were reduced with higher intake pressure (and hence higher volumetric oxygen concentration) suggests that the oxidation of hydrocarbon is oxygen limited. That the CO emissions did not increase indicates that more hydrocarbons were getting converted to CO_2 with higher intake pressure, but still leaving generally the same amount of CO; however, this is speculative. GISFC marginally reduced at higher intake pressure (refer to Fig. 6.18d) consistent with the THC emissions trend.

Effects of SOI2 timing at a constant intake pressure and intake oxygen mass fraction

The effects of SOI2 timings on smoke emissions were reported at 120 kPa intake pressure in Sec. 6.4.2. It was shown that SOI2 timing when retarded from the MBT injection timing resulted in high smoke emissions, as a part of the fuel during the 2nd injection event was injected into the high temperature gases. It was also discussed in Sec. 6.4.2 that injecting some fuel into the NTC region of the fuel from the 1st injection event may reduce soot formation. Therefore, to study these effects further, investigation was conducted at 150 kPa intake pressure at 12% intake oxygen mass fraction; higher intake pressure was chosen as it is expected that the increased in-cylinder oxygen concentration at higher intake pressure may enhance soot oxidation, so that engine-out smoke

emissions would be low to enable optical investigation. In this sub-section, an advanced (-18° CA ATDC) and a retarded (-12° CA ATDC) SOI2 timing compared to the baseline condition of -15° CA ATDC were investigated. It was shown earlier that at this baseline condition, the fuel from the 2nd injection event was injecting into the high temperature gases (refer to Fig. 6.19a). With a retarded SOI2 timing (-12 °CA ATDC), fuel from the second injection was injected into gases that were at a higher temperature than the baseline condition and as expected (for the reason presented earlier) smoke emissions increased (>1 FSN) as shown in Fig. 6.20a.

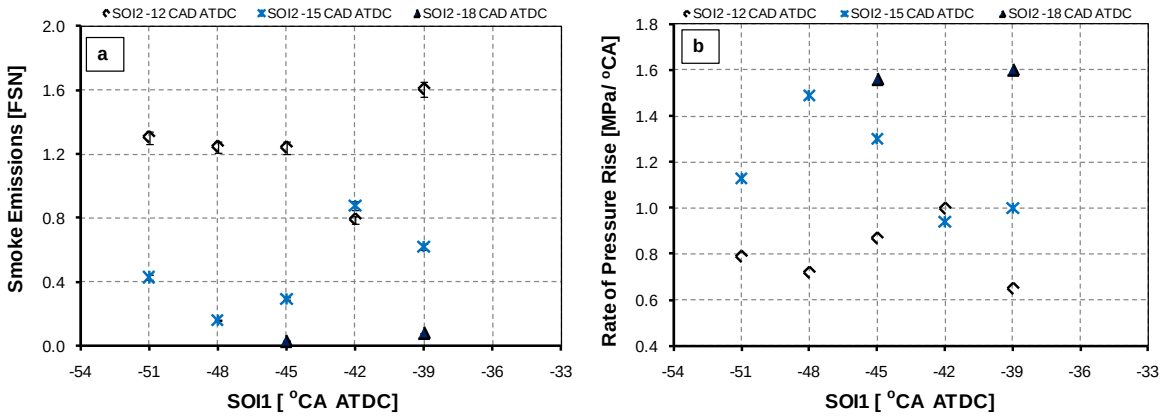

Fig. 6.20: (a) Smoke emissions at different SOI1 operating conditions with split injections at various SOI2 timings at 150 kPa intake pressure and 12% intake oxygen mass fraction; (b) Rate of pressure rise at different SOI1 operating points with split injections at various SOI2 timings at 150 kPa intake pressure and 12% intake oxygen mass fraction

With the advanced SOI2 timing (-18 °CA ATDC), fuel from the 2nd injection event was injected into the NTC phase of the low temperature cool flame reactions (as shown in Figs. 6.21a and 6.21b) and smoke emissions were nearly zero (see Fig. 6.20a). With the retarded SOI2 timing (-12 °CA ATDC), higher smoke emission was seen at -39 °CA ATDC SOI1 timing compared to other SOI1 timings shown in Fig. 6.20a. This can be attributed to the timing of the 2nd injection event with respect to the magnitude of the energy release rate of the fuel from the 1st injection event, where the fuel during the 2nd injection event was injected into the gases at higher temperatures (indicated by the higher magnitude of the energy release rate at SOI2 timing shown in Fig. 6.21a compared to -45 °CA ATDC SOI1 case shown in Fig. 6.21b). These observations are further supported by the flame temperature and *KL* factor (soot concentration) results obtained through the two-colour pyrometry (refer to Figs. 6.21c and 6.21d). Although the local reaction zone flame temperatures are similar at -15 and -18 °CA ATDC SOI2 timings, the results plotted in Fig. 6.21d show marked differences in crank-angle resolved soot concentrations. Advanced SOI2 timing (with the fuel from the 2nd injection event being injected into the cool flame reactions) not only reduced the peak soot concentration, but also resulted in near-zero soot concentration. This supports the

earlier hypothesis that smoke emissions are significantly reduced when the fuel from the 2nd injection is injected into the cool flame reactions of the fuel injected during the 1st injection event, despite there being a lower ignition delay for the 2nd injected fuel mass.

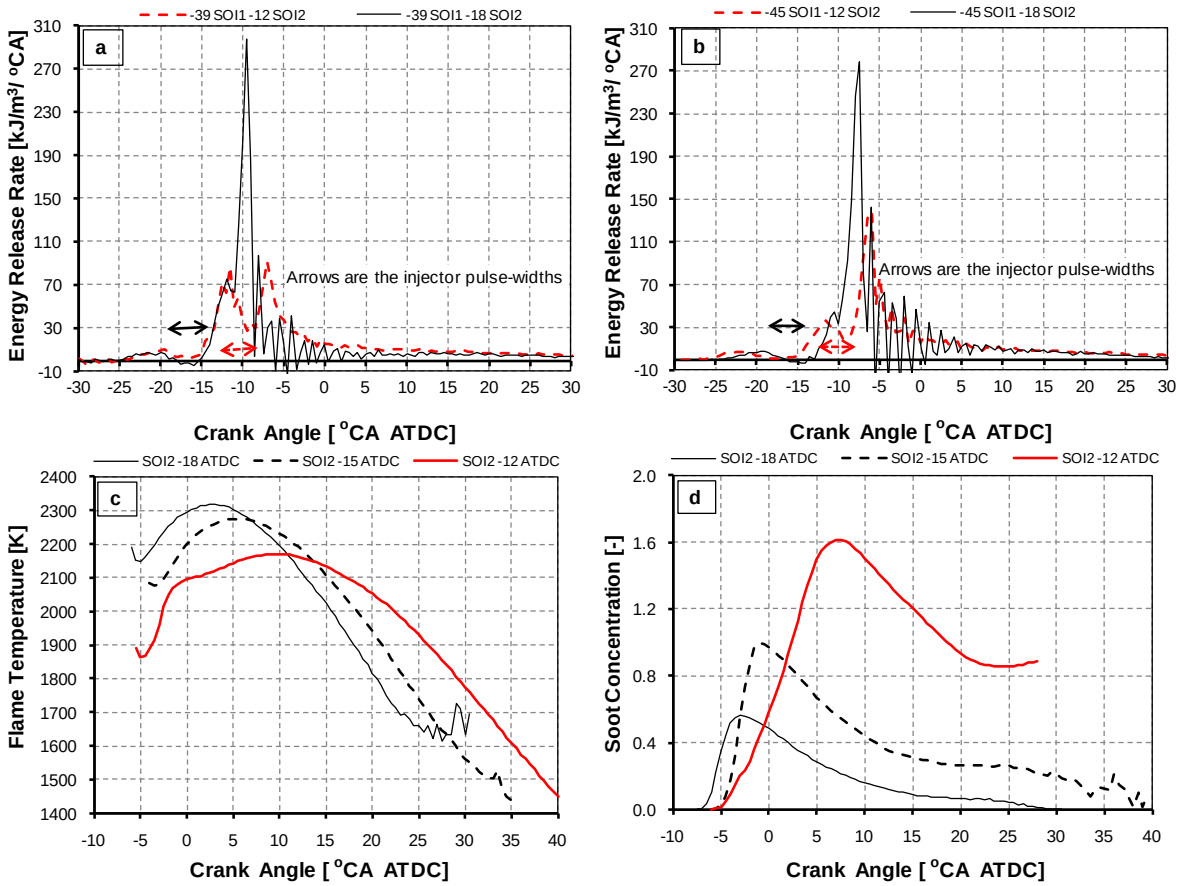

Fig. 6.21: (a) Energy release rate at different SOI2 timings at -39 °CA ATDC SOI1 timing; (b) Energy release rate at different SOI2 timings at -45 °CA ATDC SOI1 timing; (c) Flame temperature at different SOI2 timings; (d) Soot concentration at different SOI2 timings

It should be noted that the rate of pressure rise was very high with -18 °CA ATDC SOI2 timing (~1.6 MPa/°CA shown in Fig. 6.20b); hence, this advanced SOI2 timing was not investigated at other SOI1 timings. The rate of pressure rise with -12 °CA ATDC SOI2 timing was ~0.8 MPa/°CA. This demonstrates an interesting trade-off between the rate of pressure rise and smoke emissions (refer to Fig. 6.20). Combustion rate shaping due to the overlapping 2nd injection event and premixed combustion at retarded SOI2 timing reduced the rate of pressure rise. It is expected that with retarded SOI2 timing, the fuel injected into the high temperature gases would cause cooling effects on the combustion products and these cooler gases would then be entrained into the spray. Hence, the subsequent partially premixed energy release reactions would take place slowly, thereby reducing the rate of pressure rise. Also, it is expected that due to the near-TDC 2nd injection timing, in-cylinder temperatures would be higher enhancing fuel vaporization for the mass of fuel injected

during the 2nd injection event. Retarding or advancing the SOI2 timing had marginal effect on THC and CO emissions (not shown here); however, GISFC did not show any clear trend with SOI2 timing and varied indiscernibly with SOI1 timings as shown in Fig. 6.22. It should be noted that there is a significant reduction in GISFC at certain fuel injection and dwell timings.

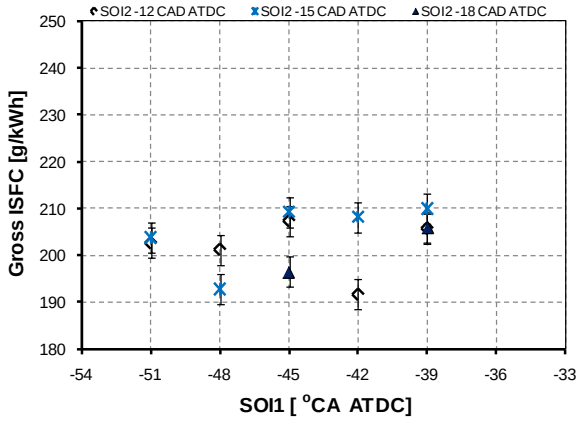

Fig. 6.22: Gross ISFC at different SOI1 operating conditions with split injections at various SOI2 timings at 150 kPa intake pressure

6.5.4 Effects of Variable Fuel Split Ratio at a Constant Intake Oxygen Mass Fraction

Splitting the fuel evenly between the squish region and piston bowl influenced the emissions and the GISFC as discussed in the previous sections. Various optimized fuel split ratios have been reported in the literature with the high-EGR LTC strategy (7.5% Y_{O2}) [Koci *et al*., 2009] to reduce emissions and improve fuel economy. To study the effects of various fuel split ratios on emissions and GISFC, two fuel split ratio cases (25:75 and 50:50) were investigated at a constant intake pressure (120 kPa) at ~10.5% Y_{O2} (corresponding to ~54% EGR levels). SOI1 timing was variable between -30 and -51 °CA ATDC, whereas SOI2 timing was fixed at -21 and -18 °CA ATDC (MBT fuel injection timings) for the 25:75 and 50:50 fuel split ratio cases respectively. However, the lower fuel split ratio (25:75) case was investigated at only three SOI1 timings (compared to the 50:50 fuel split ratio case) because of high smoke emissions. It should be noted that optimizing the fuel split ratio was not a specific objective of this work; this section aims simply to elucidate the potential of this parameter for controlling emissions and performance. The experimental results for the smoke, CO, THC emissions and GISFC for the two fuel split ratios are shown in Fig. 6.23. Emissions and GISFC levels corresponding to the single injection strategy with the MBT injection timing at ~10.5% Y_{O2} are also shown in the figures.

The results show smoke emissions to be consistently higher with the 25:75 fuel split ratio case compared to the 50:50 fuel split ratio case as shown in Fig. 6.23a. The 1st premixing time (SOC-SOI1) for the fraction of the fuel injected during the 1st injection event for the 50:50 fuel split ratio case was marginally longer (22-39 °CA, increasing with advanced SOI1 timings) compared to the

19-37 ^{o}CA in the 25:75 fuel split ratio case, whereas the 2nd premixing time (SOC-SOI2) for the mass of the fuel injected during the 2nd injection event was approximately the same (6-7 ^{o}CA) for both the fuel split ratio cases (not shown here). It is expected that in the 25:75 fuel split ratio case, the equivalence ratio in the squish region at SOC will be much lower (due to lower fuel mass in the squish region and similar premixing time) compared to the 50:50 fuel split ratio case. On the other hand, the spatial distribution of equivalence ratios in the piston bowl in the 25:75 fuel split ratio case will be richer compared to the 50:50 fuel split ratio case (due to higher mass of fuel in the 2nd injection event with the 25:75 fuel split ratio case compared to the 50:50 fuel split ratio case with almost the same ignition delay/2nd premixing time for both the cases). This is expected to increase soot formation for the 25:75 fuel split ratio case.

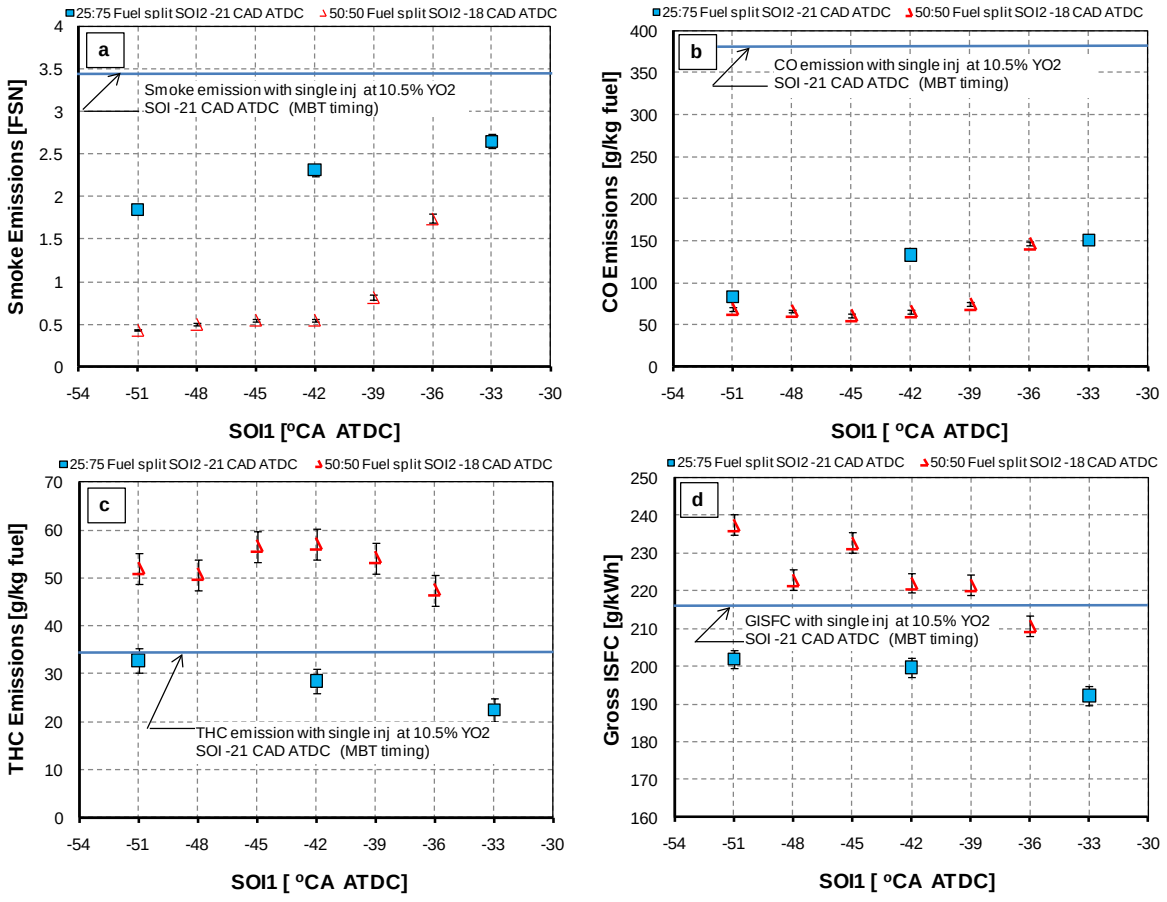

Fig. 6.23: (a) Smoke emissions, (b) CO emissions (c) THC emissions, (d) gross ISFC at various fuel split ratio cases

The energy release rate plot, Fig. 6.24, shows an advanced combustion phasing and a higher peak energy release rate for the 25:75 fuel split ratio case. The advanced combustion phasing and the rapid rise in the energy release rate is expected to increase the flame temperature marginally in the 25:75 fuel split ratio case compared to the 50:50 fuel split ratio case. The increased flame

temperature with a rich equivalence ratio in the 25:75 fuel split ratio case is expected to increase soot formation. It is hypothesized that soot oxidation rate would remain the same for both the cases due to the same intake oxygen mass fraction. It should be noted that no distinct cool reactions can be seen for the 25:75 fuel split ratio case. Distinct cool flame reactions can be seen in the energy release plot shown in Fig. 6.24b for the 50:50 fuel split case. Due to higher fraction of fuel in the 1st injection event with the 50:50 fuel split ratio case, it is likely that more intermediate radicals were formed, thereby showing the distinct cool flame reactions. These intermediate radicals may also influence soot formation as discussed in Sec. 6.4.2. Note that the 'cool flame like' energy release rate for the 25:75 fuel split ratio case and the 'cool flame like' energy release rate after the initial cool flame reactions in the 50:50 fuel split ratio case shown in Fig. 6.24b correspond to the intermediate temperature reactions as discussed earlier in Sec. 6.4.2 and in Chapter 2.

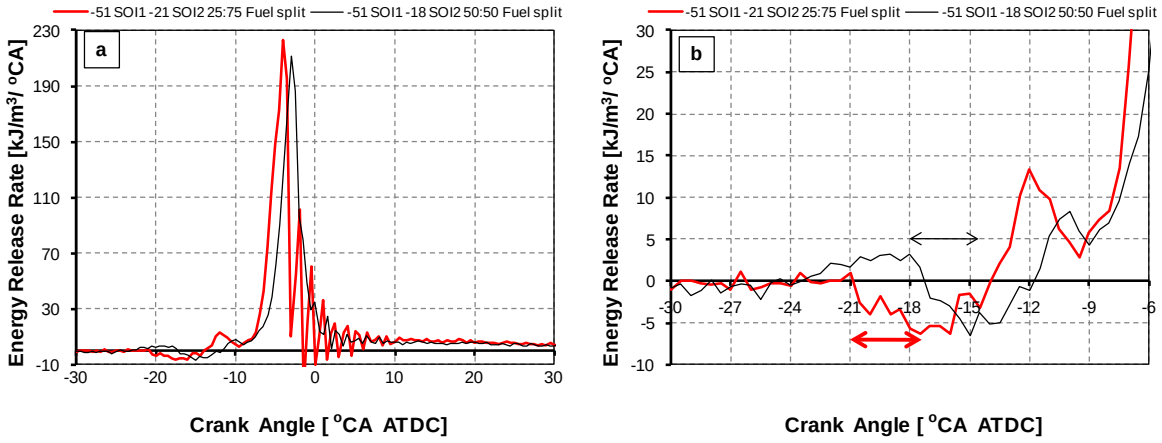

Fig. 6.24: Energy release rate at various fuel split ratios. Representative SOI2 timing and injection durations are shown by the arrows.

The THC emissions results shown in Fig. 6.23c indicate that with reduced fraction of fuel in the 1st injection event (25:75), THC emissions reduced marginally compared to the single injection case and significantly compared to the 50:50 fuel split ratio case. Better oxygen utilization along with higher flame temperature is expected to reduce THC emissions in the 25:75 fuel split ratio case. Also, unlike the 50:50 fuel split ratio case, where most of the fuel mass during the 1st injection event was completely missing the piston bowl and entering the squish region (refer to Fig. 6.13), the reduced mass of the fuel in the 1st injection event with the 25:75 fuel split ratio case reduced THC emissions. The fact that both THC and CO emissions were reduced with the 25:75 fuel split ratio case suggests that the combustion process is more complete.

It is expected that with the split injection strategy, the probability of rich pockets of fuel-air mixture in the cylinder was reduced thus resulting in reduced CO emissions (refer to Fig. 6.23b). Also, the utilization of the oxygen in the squish region improved CO oxidation, thereby significantly reducing CO emissions compared to the single injection case. THC and CO emissions

influenced combustion efficiency, thereby affecting GISFC for both the fuel split ratio cases as shown in Fig. 6.23d. GISFC reduced significantly with the 25:75 fuel split ratio case compared to the 50:50 fuel split ratio and single injection cases. Interestingly, the lower fuel split ratio case (25:75) indicates an interesting THC-smoke (or GISFC-smoke) trade-off (see Figs. 6.23a and 6.23c).

6.6 Determination of Local Equivalence Ratio with the Split Injection Strategy

The theoretical calculation to determine the local equivalence ratio (air-fuel ratio based) matching the measured peak flame temperature discussed in Sec. 5.6 in Chapter 5 was repeated for a selected 50:50 split injection cases. As discussed in Chapter 5, the measured in-cylinder pressure and the calculated mass averaged bulk gas temperature at TDC were taken as the ambient conditions for estimating the adiabatic flame temperature. The actual local flame temperature was assumed to be 50 K higher than the measured flame temperature to account for the radiation heat transfer losses [Musculus, 2005] similar to the approach in Sec. 5.6. The peak flame temperature and the corresponding local equivalence ratio with the split injection strategy at reduced EGR levels at various intake pressures at a fixed operating condition (i.e. fuelling quantity ~16 mg/cycle and an engine speed of 1500 rpm) are shown in Fig. 6.25. Conventional diesel combustion and high-EGR single injection LTC operating points are also plotted in the figure. Conventional diesel and single injection high-EGR LTC operating points were discussed in more detail in Sec. 5.6 in Chapter 5.

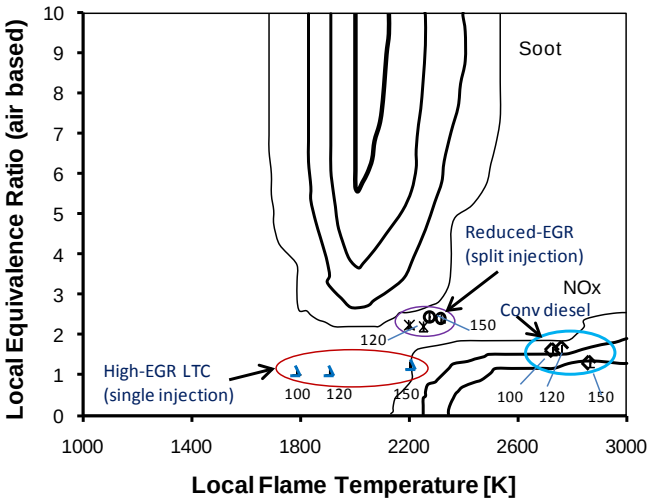

Fig. 6.25: Peak measured flame temperature and the theoretically determined local equivalence ratio (air-fuel ratio based) for different LTC strategies (single injection high-EGR LTC and reduced EGR split injection LTC) and conventional diesel combustion at different intake pressures (100, 120, and 150 kPa) at a fixed operating condition (i.e. 16 mg/cycle fuelling quantity and 1500 rpm engine speed). The numbers in the plot next to symbols indicate absolute intake pressure. Soot and NO_X formation islands in the ϕ–T map: Adapted from SAE Paper No. 2006-01-3386.

As discussed earlier in the previous sections, the net engine-out smoke emissions in the split injection strategy at reduced EGR levels is a result of soot formation and subsequent soot oxidation due to high flame temperature and high in-cylinder oxygen concentration; these mechanisms are not indicated by the single point plotted in the ϕ–T map for the split injection cases. It should be noted that similar to the high-EGR single injection LTC strategy (Y_{O2} ~8%), split injection at reduced EGR levels (Y_{O2} ~12%) resulted in low smoke emissions (<0.5 FSN). However, the increased flame temperature at reduced EGR levels did not necessarily increase NO_X emissions significantly with the split injection strategy due probably to the richer local equivalence ratios (ϕ ~2) compared to the near-stoichiometric local equivalence ratios in the high-EGR single injection LTC and conventional diesel combustion strategies. NO_X emissions increased only marginally in the split injection cases (~0.8 g/kg of fuel). Looking at the relative locations of the various points plotted in the ϕ–T map, the split injection operating points represent an interesting transition route (through the minimum soot and NO_X islands) from the high-EGR single injection LTC operation to conventional diesel operation or *vice-versa*.

6.7 Conclusions

The work reported in this chapter investigated the effects of a split main injection strategy under LTC conditions with the aim of achieving low-emission combustion with practical levels of EGR. This work also investigated the effects of various operating parameters (i.e. variable intake oxygen mass fractions, injection pressures, intake pressures, injection timings and fuel split ratios) with the split injection strategy. At selected operating conditions, in-cylinder visualization and two-colour pyrometry were carried out. It was found that:

1. With the split main injection strategy, smoke emissions were reduced to <1 FSN at 12% intake oxygen mass fraction, similar to the levels with 8% intake oxygen mass fraction with single main injection, with little effect on NO_X emissions which remain well below legislated limits. THC, CO emissions and GISFC were reduced significantly with split injection at 12% intake oxygen mass fraction compared to the single main injection at 8% intake oxygen mass fraction. The split main injection strategy, therefore, effectively achieves one of the key benefits of LTC at reasonable thermal efficiency and practical EGR levels. In-cylinder optical investigation revealed that higher flame temperature at higher oxygen concentration enhanced THC, CO and soot oxidation. Higher injection pressure, however, had an indiscernible effect on THC, CO, smoke and GISFC in the split injection strategy.
2. The split injection strategy was very sensitive to injection and dwell timings and hence, needs to be carefully calibrated. With optimum injection timings and dwell timings, partial combustion by-product emissions as well as GISFC with the split injection strategy can be maintained very similar to the single injection strategy.

3. The engine-out emissions from the reduced-EGR split-injection LTC operation are relatively insensitive to changes in key engine and fuel system operating parameters; the only major sensitivity being those of THC emissions and fuel consumption to intake oxygen mass fractions.
4. Smoke emissions were reduced significantly when the fuel from the 2nd injection was injected into the cool flame reactions of the fuel injected during the 1st injection event. Although soot formation took place from the 2nd fuel injection event, most of it was subsequently oxidized, as shown in the optical assessment of the combustion event.
5. CO emissions with split injections at 12% intake oxygen mass fraction reduced significantly compared to 12% intake oxygen mass fractions with single main injection. This was attributed primarily to the increased premixing time, which minimized the rich fuel-oxygen zones in the combustion chamber and to the increased in-cylinder temperature which enhanced CO oxidation. However, THC emissions and GISFC with the split main injection were higher than the single injection case in certain injection timings at the corresponding intake oxygen mass fraction. In certain cases, the increased THC emissions with split injection strategy approximately coincided with the reduced CO emissions.
6. At higher intake pressure, injecting fuel from the 2nd injection event into the high temperature gases reduced the rate of pressure rise. However, the retarded SOI2 timing increased smoke emission marginally (a trade-off between rate of pressure rise and smoke emission) without any significant impact on THC and CO emissions and GISFC.
7. The best performance engine operating boundary condition for the split injection strategy, with respect to fuel economy and total emissions, was found to be at a SOI1 timing of -42 ^{o}CA ATDC with SOI2 timing at -12 ^{o}CA ATDC, 150 kPa intake pressure and 12% intake oxygen mass fraction. These operating conditions produced a GISFC of 192 g/kWh with smoke emissions <1 FSN, NO_X emissions <1 g/kg of fuel, with THC and CO emissions of 19 and 39 g/kg of fuel respectively.

The results of the present study have shown that THC and CO emissions still remain high in the split injection strategy and warrant further research. Nevertheless, it is expected that the reduced EGR requirements will extend the LTC load boundary at a given engine intake pressure. It is also observed that this split injection strategy should make the combustion mode transition easier between LTC and conventional diesel operation with low soot and NO_X emissions. The next chapter will discuss some typical transient routes (LTC to conventional diesel and *vice-versa*) encountered in a passenger vehicle (with a 2 litre turbocharged diesel engine) while following the NEDC driving cycle.

Chapter 7

MODE TRANSITION BETWEEN HIGH-EGR LTC AND CONVENTIONAL DIESEL COMBUSTION

7.1 Introduction

The potential benefits of high-EGR LTC to reduce smoke and NO_X emissions simultaneously have been reported widely in the literature at steady-state operating conditions. However, due to the reduced in-cylinder oxygen concentration at medium load, emissions of partial combustion by-products remain excessive with reduced thermal efficiency. Therefore, high-EGR LTC strategy is currently limited to medium load operating conditions. In order to implement the high-EGR LTC strategy in a passenger vehicle, a transition to conventional diesel operation is required to satisfy the expected high load and high speed demands of the engine. Similarly, a transition is required from conventional diesel to high-EGR LTC for low and medium load operation. These transitions must be carefully managed to ensure smooth engine operation while avoiding excessive pollutant emissions. The performance and emissions of an engine during two typical combustion mode transitions (from LTC to conventional diesel and *vice-versa*) have been investigated and are reported in this chapter.

Most of the operation of an automotive engine occurs under transient operating conditions, where speed and load vary continuously. Transient engine operation contributes much more to the total amount of emissions over a drive cycle compared to the steady-state operation; it was reported that transient spikes of soot and NO may contribute to 53% and 16% of the total emissions respectively during a city driving condition [Hagena *et al*., 2011]. The different response time-scales of the engine's turbocharger, EGR and fuelling systems are the main reasons for the deviations between the steady-state and transient performance and emissions.

Transient response of the turbocharger is the critical parameter influencing the delay in the increase of speed or load in a turbocharged diesel engine. This is primarily due to the inertia of the turbocharger rotor which requires a significant fraction of the exhaust energy while accelerating. In addition, pressure pulses, gas friction and flow inertia contribute to the delay in the response time [Benajes *et al*., 2002]. Although the exhaust energy can be increased by injecting more fuel into the combustion chamber, the limiting factor is the fuel-air ratio which influences soot emissions. This limiting fuel-air ratio restricts the torque developed by the engine while following a drive cycle.

The transient performance of the turbocharger is also affected by EGR strategy. Slow response of the EGR system combined with its interaction with the turbocharger lead to unpredictable and unfavourable EGR rates compared to the air flow rates. This causes high NO_X or smoke emissions depending on EGR rate and air-fuel ratio in conventional diesel operation. Note that the EGR flow rate is controlled through the modulation of the EGR valve and the setting of the vane position of the variable geometry turbocharger (VGT). NO_X and smoke emissions also depend on the load ramp-up time. An instantaneous load ramp-up makes the VGT vanes open up

immediately while closing the EGR valve position. This reduces the EGR rate, thereby causing the NO_X spike at the beginning of an acceleration event of the vehicle. On the contrary, with a gradual load ramp-up, the VGT vanes move gradually to their steady-state position and the EGR valve opens and closes steadily, thereby reducing the NO_X and smoke spikes [Kang and Farrell, 2005; Hagena *et al*., 2006]. Although the 2nd approach is more favourable to reduce the smoke and NO_X spikes during a load transient, it results in a slow rise in the engine torque and a therefore a driveability penalty [Kang and Farrell, 2005; Hagena *et al*., 2006].

The mismatched response of the injection system (injection pressure compared to fuel quantity and injection timing) and the turbocharger during a transient contributes to high emissions. With faster rise of injection pressure compared to boost pressure, over-penetration of the fuel jet may occur in the combustion chamber causing wall impingement with high smoke, CO and THC emissions. Higher injection pressure also increases NO_X emissions during the transient similar to steady-state operation [Hagena *et al*., 2006]. A slow rise of injection pressure influences injection duration, fuel-air mixing and hence, combustion and emissions. Therefore, a careful optimization is required between fast response/driveability and emissions trade-off [Hagena *et al*., 2011]. High fraction of premixed combustion and high localized temperatures at the inception of a tip-in (a rapid increase in engine command from low speed/low load to high load) contribute to high NO_X and PM emissions due to over-fuelling [Hagena *et al*., 2011] in conventional diesel operation. However, the flexibility of the current high pressure common rail fuel injection system allows the injection parameters to be adapted to the actual in-cylinder conditions during the transient, provided they are known. Therefore, it is the air handling system that limits the performance of the engine.

Thermal transient is generally longer than the turbocharger acceleration transient and is an additional reason for the delay for the required air flow rate. In turbocharged engines, the walls of the exhaust pipes and cylinder walls are expected to be colder than the gases, and they would absorb some energy, thus reducing energy transfer to the turbine [Benajes *et al*., 2002]. It is reported that the thermal transient would have a significant effect during a cold start until the engine and the turbocharger reach steady-state temperatures [Rakopolous *et al*., 2010]. Cold starting is characterized by combustion instability, excessive smoke and increased combustion noise [Rakopolous *et al*., 2010]. However, the thermal inertia is still secondary to the response of the air handling system.

The difficulties of ‘turbo-lag’ and the mismatched response time of different engine’s subsystems discussed above during a load transient in conventional diesel operation are expected to exacerbate during a combustion mode shift from high-EGR LTC to conventional diesel operation. High EGR rates tend to reduce the available exhaust enthalpy by reducing combustion temperature and diverting gas flow away from the exhaust turbine. High-EGR LTC is characterized by high THC and CO emissions even during steady-state operation and the transients are expected to increase these emissions further. The intermediate EGR levels likely to be experienced by the engine during a

mode transition from high-EGR LTC to low EGR conventional diesel combustion or *vice-versa* are expected to increase smoke emissions significantly. Intermediate EGR levels here implies EGR levels that are above those required for NO_X control in conventional diesel mode but below the levels required to inhibit soot formation in LTC operation.

Cong [2011] investigated mode transition from high-EGR LTC to conventional diesel combustion with a short load ramp-up period during the NEDC test cycle. The selected operating conditions (intake air pressure, EGR rate), representing transition from LTC to conventional diesel combustion, were derived from the combination of a one-dimensional Ricardo WAVE model and transient test data for a 2 litre turbocharged diesel engine. These operating conditions were tested in the same AVL single cylinder diesel engine under consideration in this work (as described in Chapter 3) under steady-state. In the work reported by Cong, the limiting fuelling quantity considered for LTC operation was very high (20 mg/cycle fuelling quantity corresponding to 600 kPa GIMEP). It is expected that this fuelling quantity would produce high smoke emissions during a transient in LTC due to the limited boost pressure availability. By using a retarded fuel injection timing and reduced fuel injection pressure, Cong [2011] showed that smoke emissions in the transient could be reduced, albeit with a thermal efficiency penalty. The objective of the work reported in this chapter is to investigate the effects of the same transition on combustion and emissions subject to an appropriate LTC fuelling quantity limit matched to the achievable boost pressure during the selected transient. The use of an alternative fuel injection strategy (i.e. split injection) for a smooth combustion mode transition is reported also.

7.2 Research Methodology

Manufacturer's data from a production vehicle powered by a four-cylinder 2 litre turbocharged diesel engine was used to elucidate real-life transient behaviour over the NEDC test cycle. Note that the NEDC test cycle, which is used for the certification of light-duty vehicles in Europe, is performed on a chassis dynamometer. The test cycle consists of four repeated phases representing urban driving (ECE15) followed by a single phase representing the 'Extra Urban Driving Cycle' (EUDC). The ECE15 cycle, which represents city driving conditions, is characterized by low vehicle speed (maximum speed limited to 50 km/h), low engine load and low exhaust gas temperature for a total duration of 780 s covering a distance of 4.052 km. The EUDC phase, on the other hand, is a more aggressive, high speed (maximum vehicle speed of 120 km/h) driving mode for a total duration of 400 s covering a distance of 6.955 km [DieselNet, 2012]. Note that meeting the vehicle speed at a certain acceleration level is also a critical requirement for the legislated driving cycle under consideration. The speed profile of the vehicle during this drive cycle is shown in Fig. 7.1. Analysing corresponding engine speed and fuel quantity data provide interesting insight into engine behaviour during the NEDC drive cycle. These data are shown in Fig. 7.2.

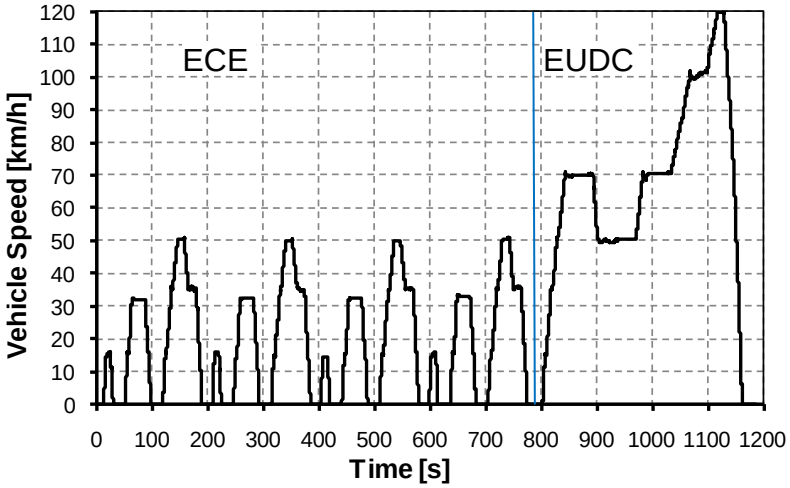

Fig. 7.1: Vehicle speed profile during the NEDC driving cycle [DieselNet, 2012]

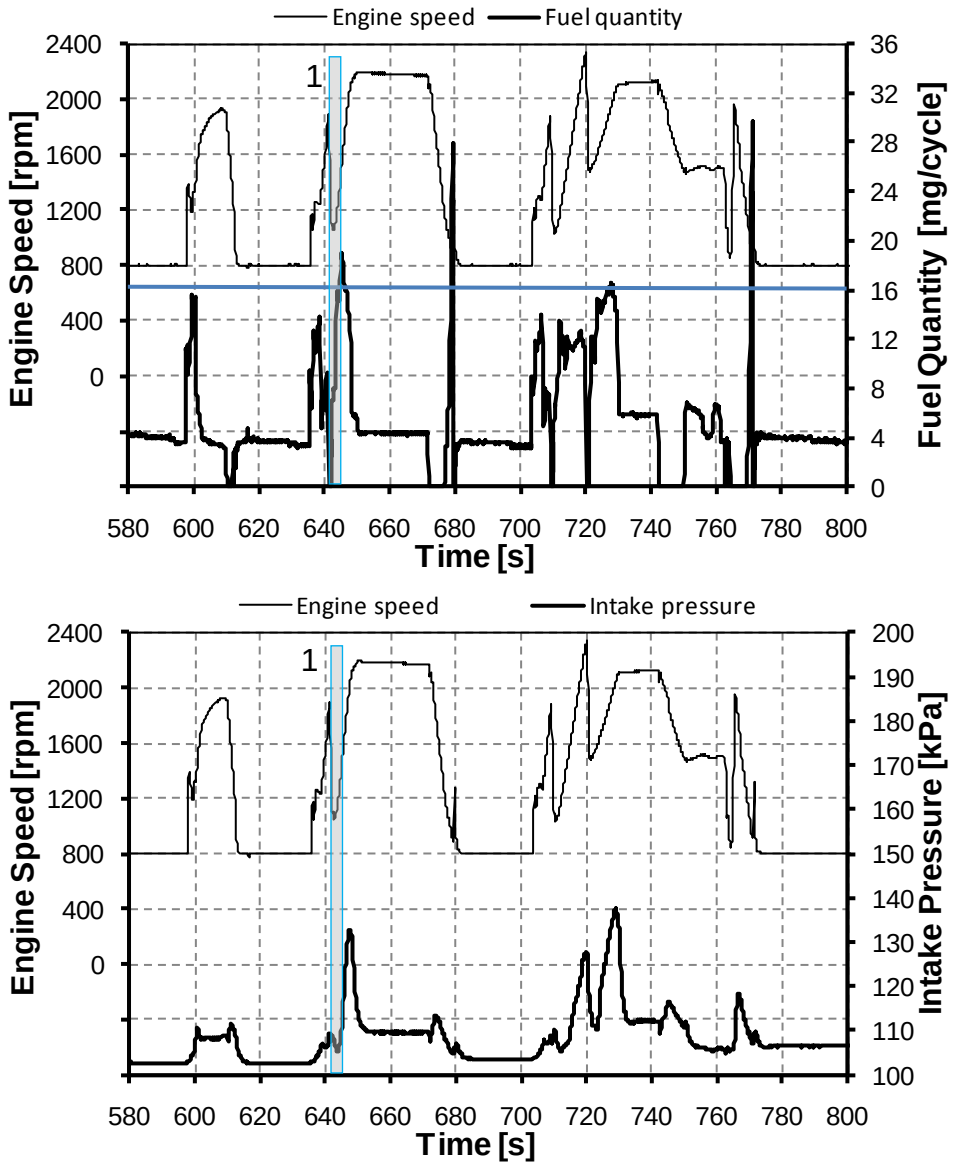

Fig. 7.2: Engine speed, fuelling quantity and intake pressure during the urban cycle of the NEDC driving cycle [Derived from manufacturer's drive cycle test data]

It should be noted that it may be difficult to implement the high-EGR LTC strategy prior to the 4th replication of the urban drive cycle due to low coolant temperature which may lead to engine misfiring and instability. Therefore, we can consider that the cycle shown in Fig. 7.2 represents engine operating conditions corresponding to the 4th replication of the urban drive cycle, where manufacturer's drive cycle test data have shown that the coolant temperature will be at its full operating level.

The data shown in Fig. 7.2 indicated that the maximum achievable intake pressure for this engine during an instantaneous load ramp-up corresponding to a fuelling quantity ramp of 8 to 19 mg/cycle (marked as 1 in Fig. 7.2) was limited to 112 kPa (absolute) during the urban (ECE15) driving cycle. Also noteworthy are the distinct fuelling spikes at ~679 s and 771 s in the urban drive cycle. These fuelling spikes might need an air-fuel limiter in LTC; as there is so little excess air in LTC, injecting extra fuel would only increase emissions without any improvement in engine performance. This would have an impact on the driveability. It was reported in Chapter 4 that high-load LTC (corresponding to 21 mg/cycle fuel quantity) can be achieved with high boost pressure (200 kPa, absolute). In the naturally aspirated mode of operation the fuel quantity for LTC operation was limited to 16 mg/cycle. It was also shown in Chapter 4 that high-EGR LTC corresponding to 16 mg/cycle fuel quantity was achievable both at 1500 rpm and 2500 rpm engine speeds. Thus, the engine speed requirements of the NEDC driving cycle can be met wholly within the LTC operational regime. In the present investigation, the fuel quantity of 16 mg/cycle was taken as the limiting load for LTC operation; it follows therefore that a combustion mode shift is required to meet the high drive cycle load demand. It should be noted that 16 mg/cycle fuelling quantity is very engine dependent; but the overall concepts remain the same separate from the actual LTC load limit chosen. A higher fuelling quantity limit would require fewer combustion mode shifts, which is better. It can also be seen from Fig. 7.2 that the majority of the urban drive cycle can be covered under LTC regime except the highlighted region marked as 1, where a mode transition would be required to conventional diesel operation.

In the EUDC phase of the drive cycle, there are frequent and rapid load ramp-ups as shown in Fig. 7.3 which would require frequent combustion mode transition between LTC and conventional diesel operation. The three speed and load transients (2-4) in the EUDC drive cycle that would require a combustion mode shift are also shown in the figure: (2) load and speed transients crossing combustion modes (LTC to conventional diesel), (3) load transient crossing combustion mode at a constant speed (LTC to conventional diesel) and (4) load transient crossing combustion mode at a constant speed (LTC to conventional diesel operation and *vice-versa*). Intake pressure and gear ratio during these transitions are also shown in the figure. The four transients considered here are listed in Table 7.1.

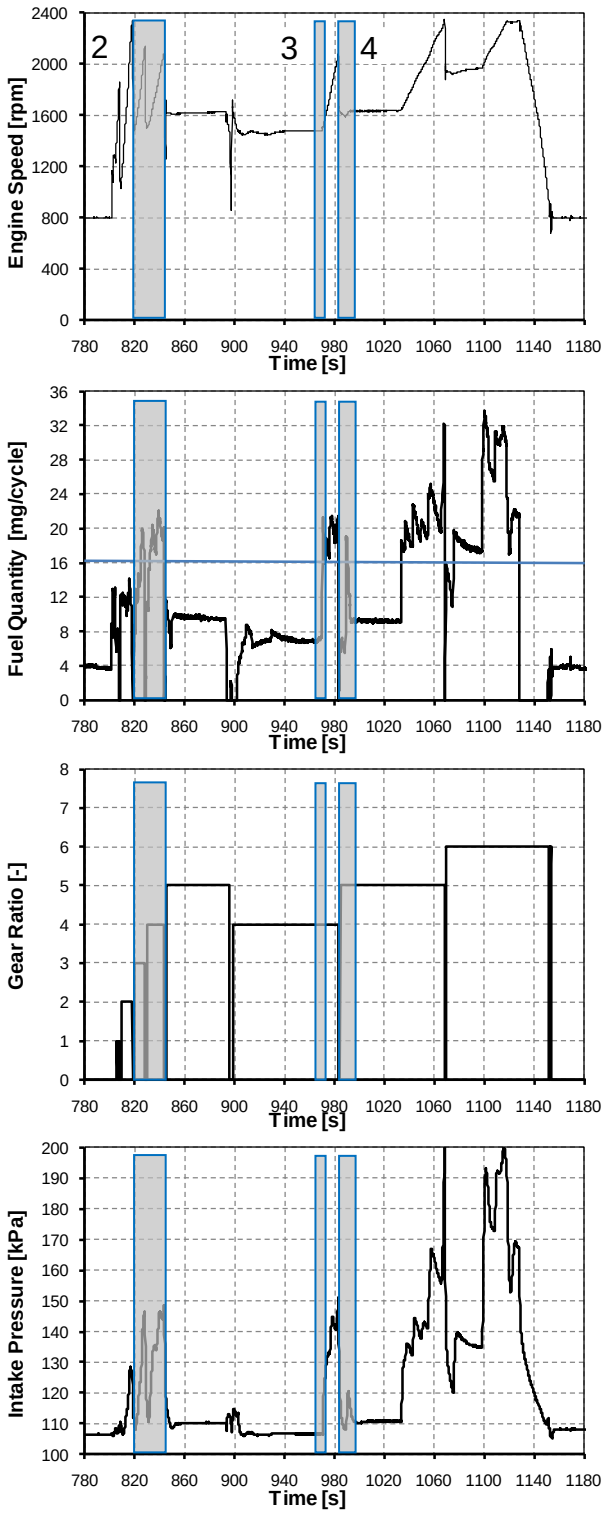

Fig. 7.3: Engine speed, fuelling quantity, gear ratio and intake pressure during the EUDC phase of the NEDC driving cycle [Derived from manufacturer's drive cycle test data]

Table 7.1: Selected Transient Routes

Transient Route		Time (s)	Engine speed (rpm)	Fuel quantity (mg/cycle)	EGR rate (%)	Intake pressure (kPa)	Gear ratio
1) Load and speed transient crossing combustion modes (LTC to conventional diesel)	Initial	643.12	1081	7.9	62	106	0 (Neutral)
	Final	645.22	1501	18.9	20	112	2
2) Load and speed transient crossing combustion modes (LTC to conventional diesel)	Initial	820.21	1508	7.8	62	108	3
	Final	834.21	1653	20.4	20	132	4
3) Load transient crossing combustion modes (LTC to conventional diesel)	Initial	969.9	1481	7.4	62	106	4
	Final	970.5	1508	21.4	21	108	4
4) Load transient crossing combustion modes (LTC to conventional diesel and *vice-versa*)	Initial	984.9	1618	6 to 19	62	115	5
	Final	991.9	1630	19 to 12	60	118	5

Note that the data listed in Table 7.1 (except the EGR rate) were derived from manufacturer's test data. EGR rates for high-EGR LTC operation were chosen from Chapter 4 of this thesis, whereas the EGR levels in conventional diesel operation were based on the current low EGR levels used in a production engine. It is acknowledged that the load transients at 1600 rpm and 1900 rpm at 1033 s and 1075 s respectively are also critical; however, they have not been considered in the work reported in this chapter as they are essentially similar to 'Transient 3', the exception being only engine speeds. Fig. 7.4 shows NO_X emissions during these transients in conventional diesel operation normalized with respect to the drive cycle maximum value. Note that although 'Transient 4' is not particularly relevant during a conventional diesel transient, it is reported in the literature that mode transition from conventional diesel to LTC operation increases NO_X emissions [Burton *et al*., 2009; Tanabe *et al.*, 2010] and hence, this transient is considered in this investigation.

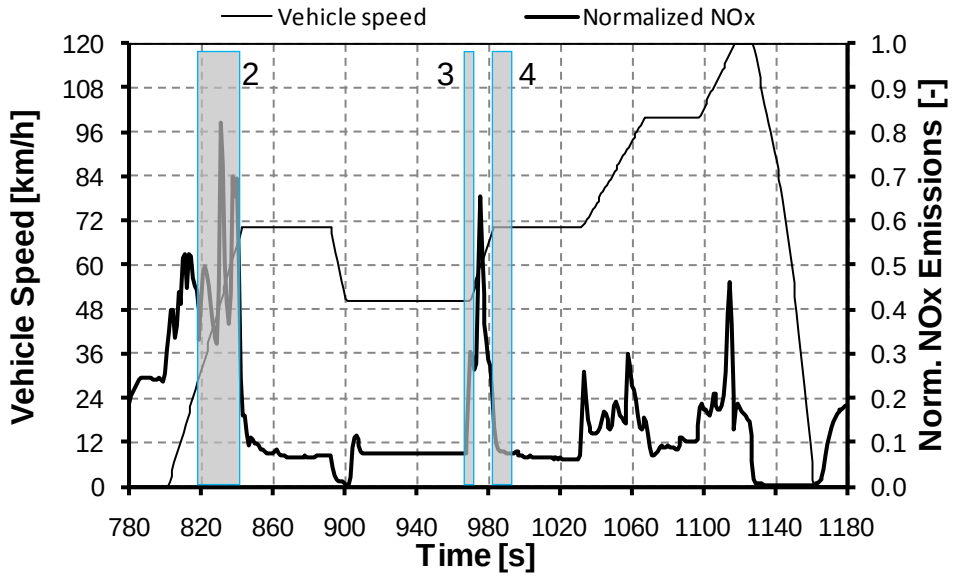

Fig. 7.4: NO_X emissions and vehicle speed during the EUDC phase of the NEDC driving cycle [Derived from manufacturer's drive cycle test data]

Among the different transient conditions, a load transient at a constant engine speed is considered to be the most representative of the engine response [Benajes *et al*., 2002]. A load transient is generally encountered when a vehicle climbs a hill or when engaging the clutch after a gear change. Engine speed accelerations generally experience less turbo-lag and hence are considered easier to control [Watson and Janota, 1982; Rakopolous and Giakoumis, 2006] compared to load transients. A careful examination of the NO_X emissions data during vehicle acceleration event showed peak NO_X emissions to occur at a fixed engine speed during a gear shift (refer to 'Transient 2' in Figs. 7.3 and 7.4) which includes engaging and disengaging the clutch and changing the gear. 'Transient 2' could also be seen as a 4-gear transient event. While the gear change is underway, the vehicle coasts under its own inertia. Once the new gear is selected and the clutch is re-engaged, the vehicle attempts to regain the drive-cycle speed. During this event the fuel quantity is increased very quickly (refer to Fig. 7.3): equivalent to the case of a load transient at a fixed engine speed. Although this transient is critical to the reduction of NO_X emissions during a driving cycle, this was considered to be more of a control issue, and was beyond the scope of this work. Therefore, in this study, only the load transients ('Transient 3' and 'Transient 4') were investigated. More details of these two transients are shown in Fig. 7.5. Note that real-world usage might differ substantially from this drive cycle [Pelkmans and Debal, 2006] and performance needs to be maintained and emissions need to be kept to reasonable levels.

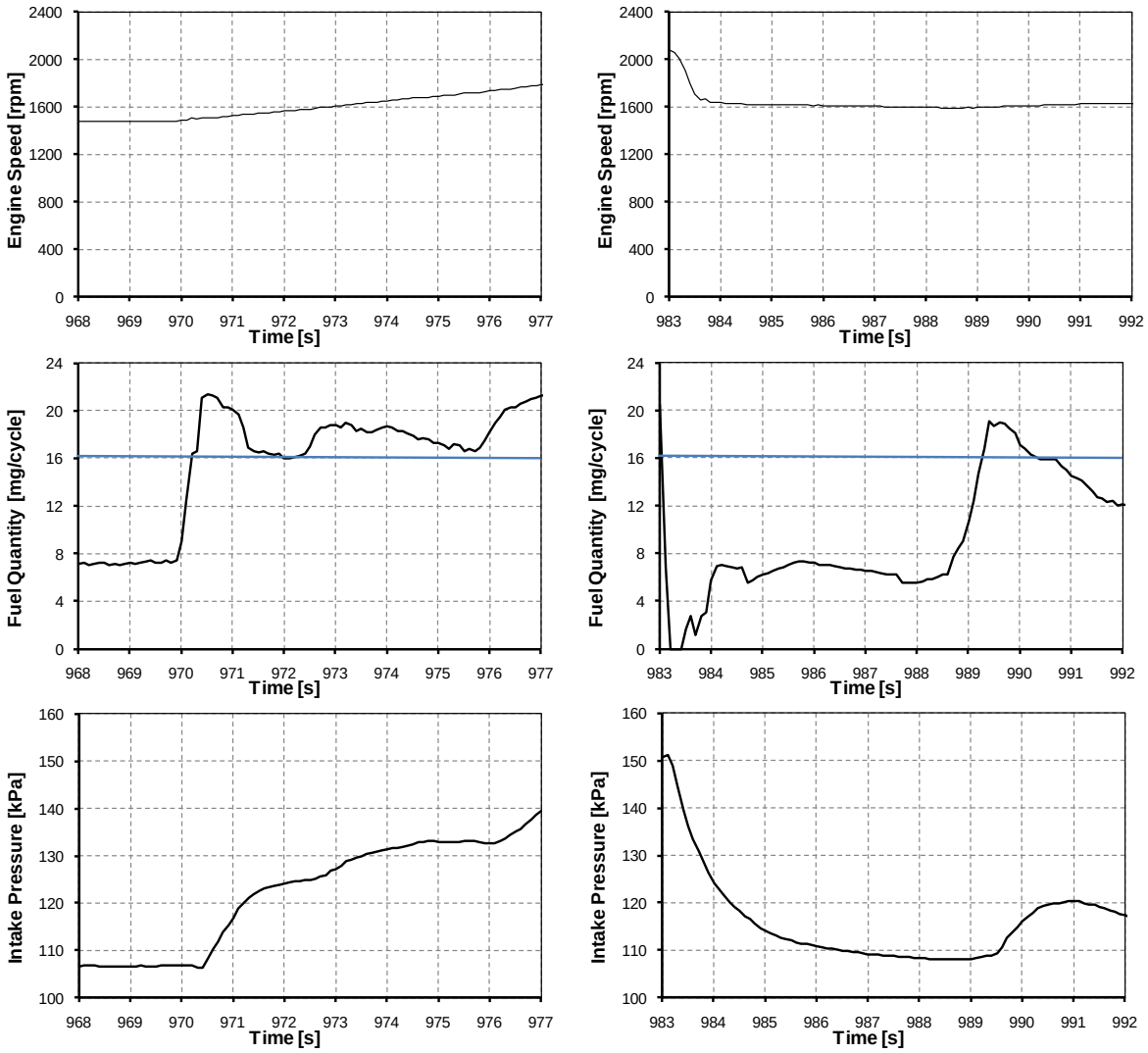

Fig. 7.5: Engine speed, fuelling quantity and intake pressure during the transients under investigation [left hand column: 'Transient 3'; right hand column: 'Transient 4']

7.3 Modelling of the Transients

A baseline one-dimensional Ricardo WAVE model for a four-cylinder 2 litre turbocharged diesel engine was provided by a project partner to help evaluate the performance of the engine during a transient. The original model had a PID controller to control the EGR valve opening and another PID controller for VGT vane position to get the desired intake pressure and EGR rates. For the purpose of this study, the original model was modified to operate in high-EGR LTC condition. A new PID controller based on EGR rate sensing was set up to get the desired EGR level. The model was first modified by a previous Loughborough researcher [Cong, 2011] and has been further modified in this work by replacing the built-in SOC controller in the original model with a CA50 controller, as CA50 would be a better control parameter than the SOC, especially in high-EGR operation of the engine. The turbocharger maps for a production 2 litre diesel engine were used in the model.

The main objective of this investigation was to evaluate the engine operating conditions likely to be encountered during combustion mode transitions from LTC to conventional diesel operation and *vice-versa*. Therefore, an important aspect of the transient modelling is the correct prediction of engine combustion behaviour so that the in-cylinder performance (i.e. IMEP), exhaust gas energy (i.e. exhaust gas pressure and temperature at exhaust valve opening) and the turbocharger response can be evaluated accurately. In the absence of experimental cylinder pressure data, the energy release rates were not available to be used in the combustion model. Therefore, WAVE's diesel Wiebe model was used. This model depends on engine speed, air flow rate, fuel injection quantity and fuel injection timing. Fuel injection timings were specified to achieve a desired CA50 strategy. Near-TDC and retarded CA50s were set in the model for high-EGR LTC and conventional diesel operation respectively and accordingly SOI timings were specified. Advanced injection timings were used in high-EGR LTC operation as reported in Chapter 4, whereas retarded injection timings were used for conventional diesel operation at low EGR levels. Fuel injection pressures similar to those used in the recorded data of the manufacturer were used. The model can predict the intake pressure (based on the maps of the turbocharger) and the EGR flow rate which are the critical parameters for the evaluation of transient performance and emissions.

Fuel quantity, intake pressure and transient duration obtained from the drive cycle test data at a specific engine speed were fed into the model for the transient simulation. The start and end positions of the EGR valve were fixed in advance during the transition. Intake pressure in the model was controlled with a PID controller by adjusting the VGT vane position. Note that getting the desired EGR levels at the beginning and at the end of the transient simulation was the prime requirement in this work and therefore, depending on the exhaust enthalpy, the intake pressure obtained from the simulation varied from the targeted intake pressure during the transient. EGR valve position and the desired intake pressure profiles followed the commanded fuel quantity and engine speed as is the case in a typical engine control system. The model was initially allowed to run for 20 s at steady-state before the transient simulation started. This was done to ensure that the model had converged before the start of the transient simulation. Similarly, at the end of the transient simulation, the model was allowed to run until the final transient point reached the steady-state condition. As expected, due to the inherent delays in the response time of the EGR valve and the turbocharger, the EGR rate and the intake pressure during the transient were different from the steady-state operating conditions. The details of the simulation procedure were previously reported by Cong [2011]. From this simulation, the predicted EGR rate and the intake pressure during the transient were obtained on a cycle-by-cycle basis along with the fuel quantity at a specific engine speed. These parameters can define the engine operating conditions at every cycle during the transient under consideration. These individual transient operating conditions at each cycle obtained from the driving cycle test data and the 1-D simulation are referred to as 'pseudo-transient' operating conditions. It should be noted that due to the crude combustion model used in this study,

no claims are made with respect to the prediction of the engine performance and emissions of the WAVE model and the model results are not validated against any empirical performance data.

7.4 Selection of Pseudo-transient Operating Conditions

Combustion mode transition from LTC to conventional diesel operation at a constant engine speed of 1500 rpm was simulated for 'Transient 3' (refer to Table 7.1). Similarly, 'Transient 4' dealing with the mode transition from LTC to conventional diesel operation and *vice-versa* at 1600 rpm engine speed was also simulated to identify the pseudo-transient operating conditions. The EGR rate, intake manifold pressure and the fuel quantity determined from the simulation results during 'Transient 3' and 'Transient 4' are shown by the solid lines in Figs. 7.6 and 7.7 respectively. Note that the dashed lines in Figs. 7.6 and 7.7 represent the EGR levels and the intake pressures derived from the manufacturer's NEDC test data during a load transient in conventional diesel operation. In the figures, pseudo-transient operating conditions are represented by filled diamonds, whereas open triangles represent transients occurring in conventional diesel operation. The basis of selection of the tested pseudo-transient operating conditions is discussed in the next paragraph. Note that in some cases, the tested intake pressures were marginally different (~1 kPa) from the WAVE simulated values (refer to the first two cycles in Fig. 7.6, for example) which were experimental testing effects due to control difficulties. This difference is expected not to have a notable influence on combustion and emissions in the high-EGR LTC operation.

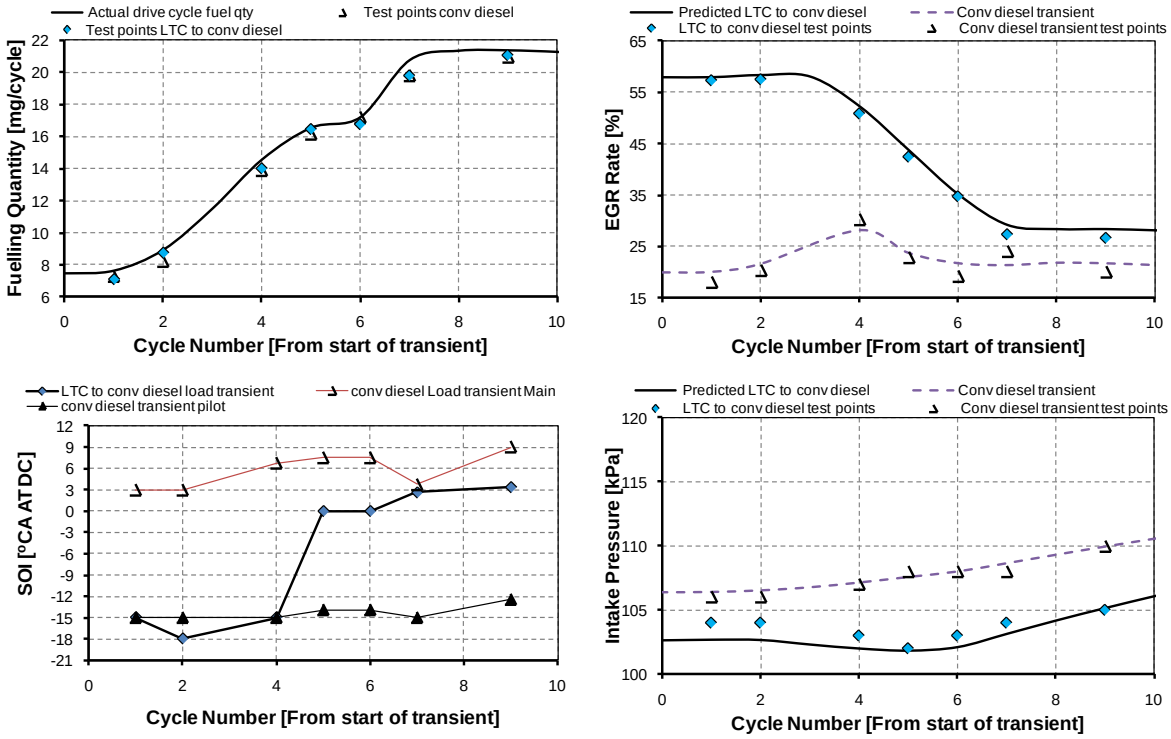

Fig. 7.6: Fuelling quantity, SOI timing, EGR rate and intake pressure during 'Transient 3' and the investigated pseudo-transient operating conditions

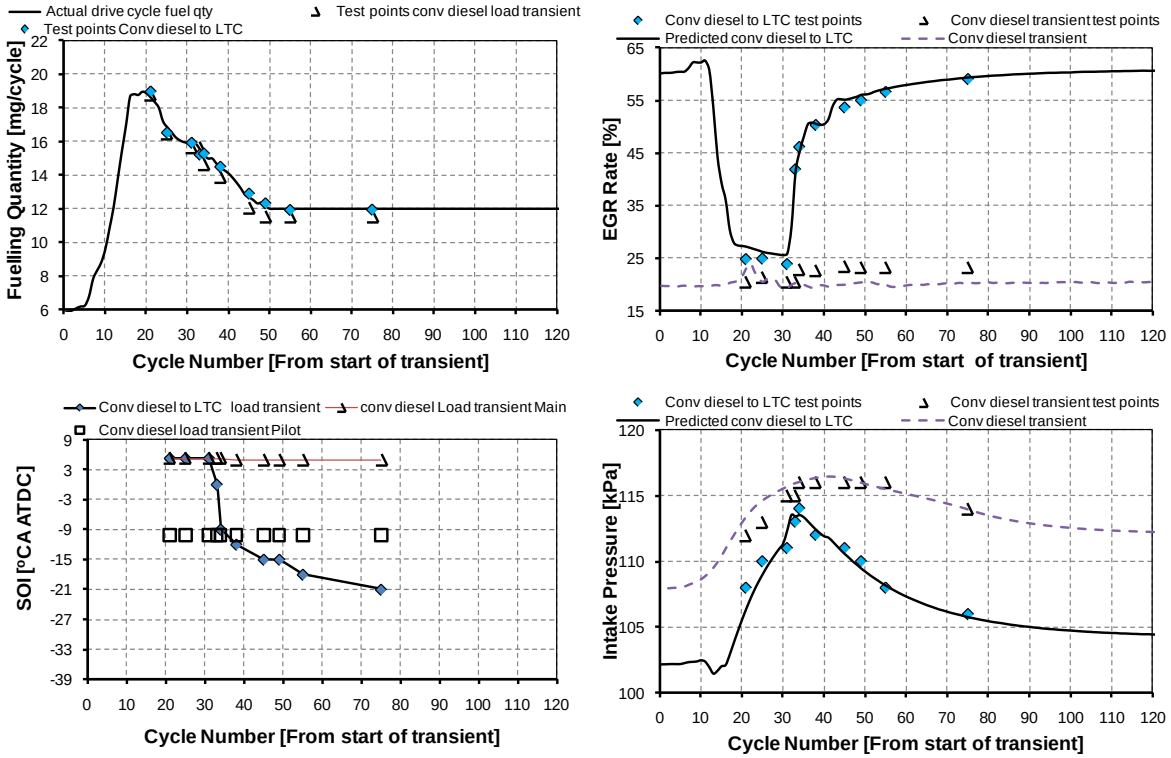

Fig. 7.7: Fuelling quantity, SOI timing, EGR rate and intake pressure during 'Transient 4' and the investigated pseudo-transient operating conditions

Two pseudo-transient operating conditions were selected corresponding to the start and end of the transient. Typically the intake pressure did not reach the desired steady-state value by the end of the transient, although the desired fuel quantity and EGR rates were achieved. This highlights the slow response of the air system, consistent with previous publications [Burton *et al*., 2009; Tanabe *et al*., 2010]. It is also due to the feedback controller configuration in the model used in this work which was configured to first supply the targeted EGR levels and then the VGT position was controlled to achieve the targeted boost pressure. Note that the WAVE model used in this work was specially adapted for high EGR operation and did not replicate the operating strategy to control the EGR levels and boost pressures in the production engine. Some intermediate pseudo-transient operating conditions considered most likely to impose difficulties in terms of performance and emissions were also selected for investigation so that the entire transient event can be represented by a set of pseudo-transient operating conditions. Pseudo-transient operating conditions were also identified at the corresponding cycles during the load transient in conventional diesel operation so that a comparison of performance and emissions can be made between these two transients. The pseudo-transient operating conditions corresponding to 'Transient 3' (combustion mode transition from LTC to conventional diesel operation) and 'Transient 4' (combustion mode transition from conventional diesel to LTC) are listed in Tables 7.2 and 7.3 respectively.

Table 7.2: Pseudo-transient Operating Conditions ['Transient 3']

Transition Case	LTC to conventional diesel	Conventional diesel
Engine speed (rpm)	1500	
Fuelling quantity (mg/cycle)	7.4-21.4 (see Fig. 7.6)	
Intake pressure (kPa)	102-105 (see Fig. 7.6)	106-110 (see Fig. 7.6)
EGR level (%)	58-26 (see Fig. 7.6)	18-30 (see Fig. 7.6)
Fuel injection pressure (MPa)	65 to 120 (increased with increasing fuelling quantity)	
SOI timing (^{o}CA ATDC)	-18 to 4 (see Fig. 7.6)	Main injection: 3 to 9; Pilot injection: -12 to -15 (see Fig. 7.6)
Intake temperature (^{o}C)	55±10	50±10

Table 7.3: Pseudo-transient Operating Conditions ['Transient 4']

Transition Case	Conventional diesel to LTC	Conventional diesel
Engine speed (rpm)	1600	
Fuelling quantity (mg/cycle)	18.8-12 (see Fig. 7.7)	
Intake pressure (kPa)	113-105 (see Fig. 7.7)	116-113 (see Fig. 7.7)
EGR level (%)	27-60 (see Fig. 7.7)	20-25 (see Fig. 7.7)
Fuel injection pressure (MPa)	120 to 80 (decreased with decreasing fuelling quantity)	
SOI (^{o}CA ATDC)	4 to -21 (see Fig. 7.7)	Main injection: ~5; Pilot injection: -10 (see Fig. 7.7)
Intake temperature (^{o}C)	60±20	40±10

Note that 'Transient 4' involved combustion mode transition from LTC to conventional diesel operation and *vice-versa* within the same transient. Although the entire transient operation was simulated, pseudo-transient operating conditions were selected during the combustion mode transition from conventional diesel to LTC operation only. It can be seen in Figs. 7.6 and 7.7 that combustion mode transition from LTC to conventional diesel operation follows similar routes for both the transient cases ('Transient 3' and 'Transient 4'), speed being the only exception (1500 rpm in 'Transient 3' and 1600 rpm in 'Transient 4'). It was reported in an earlier investigation that a ±5% variation in engine speed had an insignificant impact on LTC combustion and emissions [Cong, 2011]. Therefore, only the mode transition from conventional diesel to LTC operation was investigated during 'Transient 4'. It is acknowledged that such a rapid transition from LTC to conventional diesel operation and *vice-versa* in a single transient would make the combustion control strategy more difficult. Engine coolant and oil temperatures were maintained at 80^{o}C and 90^{o}C respectively, similar to the values during the EUDC phase of the driving cycle. The identified pseudo-transient operating conditions were investigated in the single cylinder AVL engine at steady-state with independently controllable EGR and boost systems as discussed in Chapter 3.

From the simulated transient intake pressure profile, it can be seen that all the cycles suffered from turbo-lag because of reduced exhaust enthalpy and there was a difference of ~5 kPa between

the target and the actual boost pressures throughout the transient (Figs. 7.6 and 7.7). Again, due to reduced exhaust gas mass flow rates, the turbine operated at its lowest efficiency zone. Thus, the ability of the turbine to spin faster was restricted which increased the turbo-lag and the possibility of delivering the targeted intake pressure. Note that the target boost pressure in the model was the same as the boost pressure during the load transient in conventional diesel operation ('conventional diesel transients' legends shown in Figs. 7.6 and 7.7). It is interesting to note that in 'Transient 4', overshooting of the intake pressure took place at the 20^{th} cycle, although the fuel quantity had started to decrease and EGR rate had increased up to 45% (refer to Fig. 7.7). At this condition, the turbocharger had started to pick up speed after the initial 'turbo-lag', which caused the boost pressure to overshoot. Intake pressure increased up to the 34^{th} cycle. From the 35^{th} cycle onwards, intake pressure decreased rapidly due to reduced exhaust enthalpy (because of reduced fuel quantity and high EGR levels) reaching a steady-state after the 80^{th} cycle, much later than the EGR levels and the fuel quantity had reached their steady states. This is due to the feedback controller configuration used to control the EGR valve position and VGT vane position, as would be experienced in a production engine.

7.5 Assessment of Mode Transition from LTC to Conventional Diesel Operation

The pseudo-transient operating points identified from the 1-D simulation corresponding to a mode transition from LTC to conventional diesel operation were investigated on the AVL single cylinder research engine to evaluate the combustion processes and their effects on emissions. GIMEP reported in this work was based on the engine load identified from the load transient in conventional diesel operation. The production engine used a pilot fuel injection to reduce noise and a retarded main injection timing to reduce NO_X emissions throughout the entire driving cycle. The retarded injection timing would also result in high exhaust temperature and pressure thereby increasing the exhaust enthalpy. Although a similar fuel injection strategy was used in this work to assess the load transient in conventional diesel operation, smoke emissions were higher than would be expected from a production engine. Note that the Euro 5 compliant production engine referenced in this work used an advanced fuel injection system with multiple fuel injection events (three or more fuel injections per cycle) and was carefully calibrated compared to only a pilot and a main fuel injection strategy used in the AVL single cylinder engine in this work. Also note that the production engine was fitted with a DPF, so smoke was not the most significant emission during calibration. Accordingly, the GIMEP corresponding to the pseudo-transient operating conditions during the conventional diesel transient were more relevant in this work to validate the drive cycle load requirement rather than a direct comparison of the emissions.

Some selected intermediate pseudo-transient operating conditions were also investigated at marginally higher intake pressures (3-5 kPa higher), just matching the manufacturer's test data, during the corresponding load transient in conventional diesel operation. It is expected that when the

LTC strategy is employed in a production diesel engine, the existing turbocharger may not be suitable to meet the demanded intake pressure. High boost pressure can be achieved by resizing the turbine or with different VGT positions. However, resizing the turbocharger may not necessarily meet the full load requirement (i.e. conventional diesel operation). Therefore, advanced turbocharger technology such as a twin-stage turbocharger (parallel or series sequential) or an electrically assisted turbocharger (e-turbo) may be required in a 'dual-mode' engine. However, they may also add cost, complexity, weight and packaging challenge to the engine [Arnold, 2004]. That only a 3-5 kPa higher intake pressure was considered, it is not unreasonable to assume that such a system would be available for the 'dual-mode' engine. SOI timing and the oxygen based equivalence ratio at both the intake pressures are shown in Fig. 7.8. It should be recalled that the symbols in the figures were the actual tested conditions and are not results obtained from the 1-D WAVE simulation.

Note that the SOI timings used in conventional diesel transient are not the manufacturer's control strategy. This is a control strategy reported in the literature [Charlton, 2005; Okude *et al*., 2007] and similar to what would be expected in a light-duty automotive production diesel engine. SOI timings in LTC were chosen based on an MBT timing strategy as described in detail in Chapter 4. It should be noted that the oxygen based equivalence ratio, shown in Fig. 7.8, was a calculated parameter based on the actual air flow rates, EGR levels and oxygen concentrations in the exhaust obtained from the experimental data.

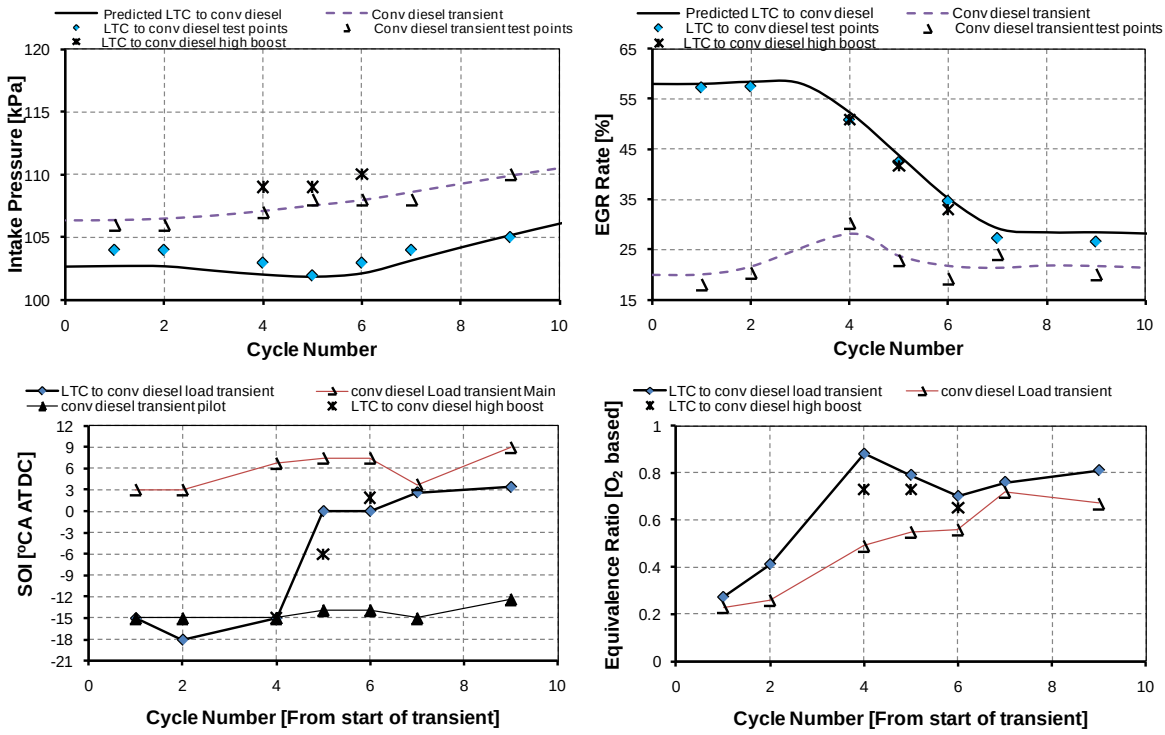

Fig. 7.8: Pseudo-transient operating conditions (intake pressure, EGR rate, SOI timing and oxygen based equivalence ratio) during 'Transient 3'

The in-cylinder performance in terms of GIMEP and the combustion parameters (ignition delay and CA50) are shown in Fig. 7.9. It should be recalled that fuel quantity from the manufacturer's test data was input to the WAVE model to predict the GIMEP. It is interesting to note that despite the crudeness of the combustion model used in the 1-D simulation, there was only a marginal difference between the predicted and the experimentally determined GIMEP (between the experimentally determined GIMEP and the predicted GIMEP in the conventional diesel transient shown in Fig. 7.9), the exception being at Cycles 6 and 7. The deviation of the GIMEP from the predicted value at Cycle 7 may be attributed to the slightly lower fuel quantity used during the test as shown in Fig. 7.6. The deviation seen in Cycle 6 may be due to a non-optimized combustion phasing. Note that Cycles 6 and 7 come under conventional diesel operation, which can be optimized with known techniques and is beyond the scope of this work.

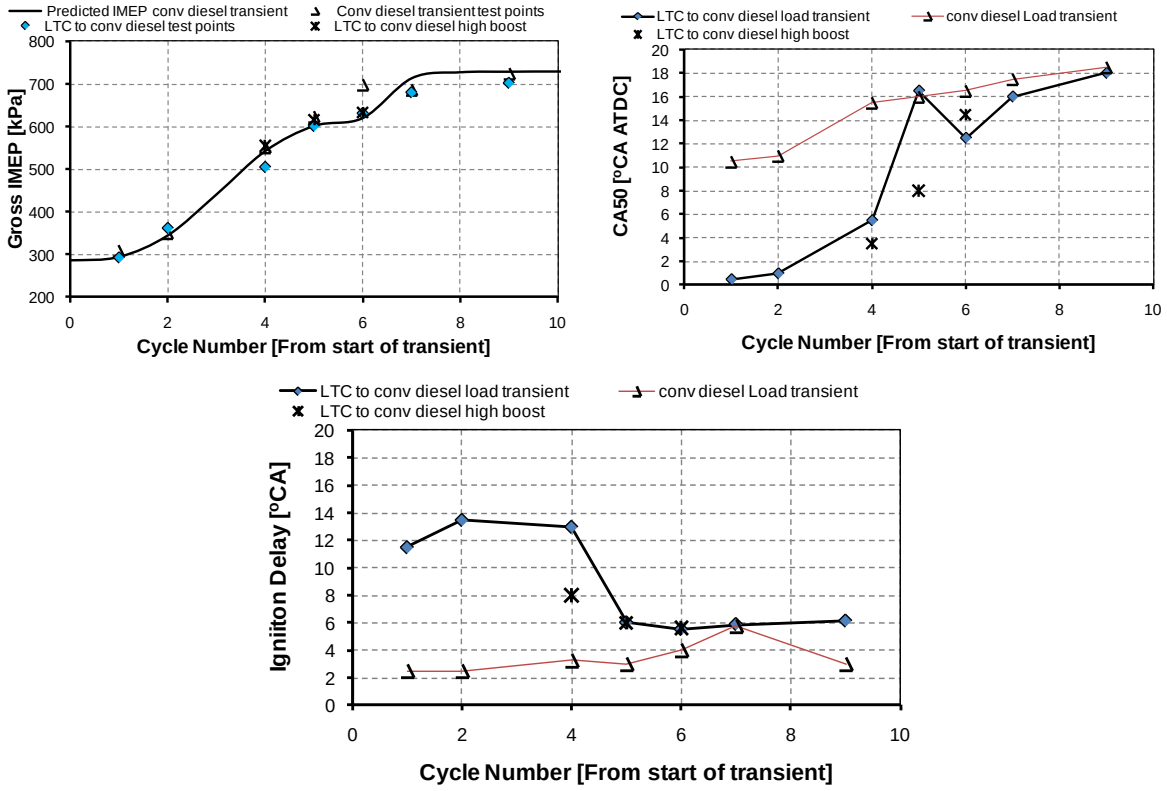

Fig. 7.9: Performance, combustion phasing and ignition delay corresponding to the pseudo-transient operating conditions during 'Transient 3'. The parameters shown in the figure are experimental data and not from WAVE.

It can be seen from Fig. 7.9 that during the mode transition from LTC to conventional diesel, the drive cycle demanded load could not be met at Cycle 4 due to increased THC and CO emissions resulting in low combustion efficiency and high GISFC (refer to Fig. 7.10). However, it is expected that a 10% reduction in the GIMEP in one cycle will not significantly affect the driving cycle under consideration. Note that an increase in the fuel quantity under this condition was not particularly

effective to increase GIMEP due to the limited in-cylinder oxygen availability which increased THC, CO and smoke emissions and GISFC further (not shown here) without increasing load. On the other hand, with a marginally increased intake pressure, the GIMEP increased at the intermediate cycles so that the engine would be able to follow the drive cycle load demand more closely as shown in Fig. 7.9 (refer to the 'cross symbols' corresponding to 'LTC to conventional diesel high boost' legend in the figure).

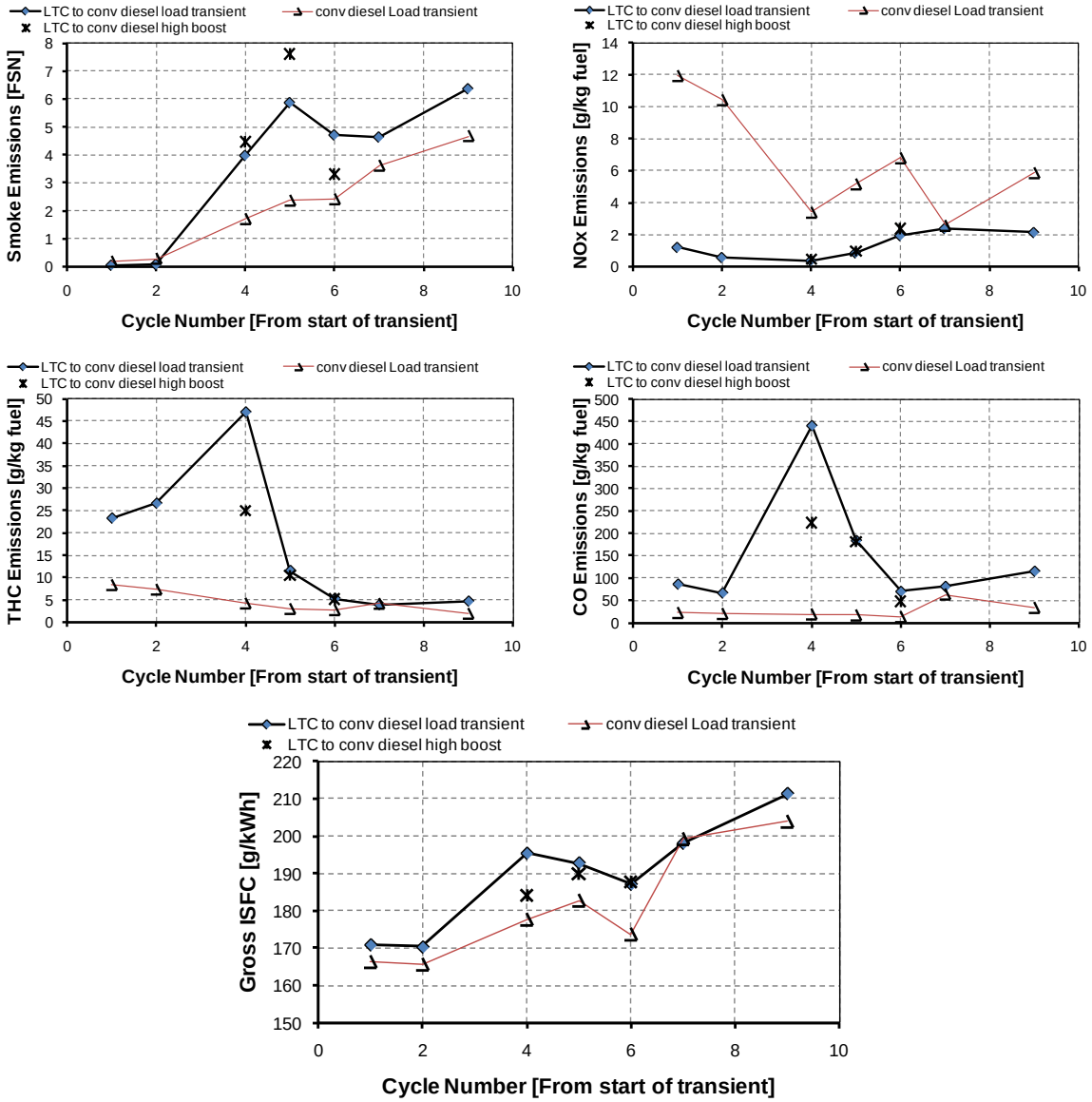

Fig. 7.10: Emissions and gross ISFC corresponding to the pseudo-transient operating conditions during 'Transient 3'. The parameters shown in the figures are experimental data and not from WAVE.

It should be recalled that retarded injection timings and low EGR levels were used in conventional diesel combustion, whereas advanced injection timings were used in LTC. As

discussed in the previous chapters of the thesis, near-TDC combustion phasing is desirable in high-EGR LTC operation to have maximum combustion efficiency. The combustion phasing (CA50) during the transition from LTC to conventional diesel operation, shown in Fig. 7.9, was particularly interesting as it represented a smooth transition from a near-TDC combustion phasing to a retarded combustion phasing (18 ^{o}CA ATDC) at higher intake pressures, the exception being at Cycle 5 at lower intake pressure. Since this cycle comes under conventional diesel operation, the retarded combustion phasing is expected to reduce NO_X emissions and increase smoke emissions without having any significant effects on THC and CO emissions. However, the spike in the CA50 data at Cycle 5 for the low boost pressure case is smoothed by the increase in intake pressure. Combustion mode transition from LTC to conventional diesel operation occurred after the 4th cycle as evident by the reduction in the ignition delay (refer to Fig. 7.9).

Now returning to the emissions data shown in Fig. 7.10, the potential benefit of LTC on NO_X reduction is evident, where NO_X levels were less than or equal to 2 g/kg of fuel during the combustion mode transition compared to the relatively high values of NO_X during the load transient in conventional diesel operation. Although smoke emissions were near-zero at the beginning of the transition, high levels of smoke were emitted in the intermediate cycles and at the end of the transition, exceeding the smoke levels during the load transient in conventional diesel operation. High smoke emissions in the intermediate cycles are attributed to the unfavourable intermediate EGR levels, consistent with the results reported in Chapter 4, where during an EGR sweep, peak smoke emissions occurred between 45% and 55% EGR levels depending on the intake pressure. High smoke emissions at the intermediate EGR levels are the net result of the competition between soot formation and oxidation, which is a function of flame temperature, in-cylinder oxygen concentration and residence time of high temperature combustion reactions, as reported in Chapters 4 and 5 of this thesis. Similarly, high smoke emissions at the end of the transition were because of the higher equivalence ratio (refer to Fig. 7.8). It was seen from the WAVE results that the boost pressure would get to the steady-state point at the 52nd cycle (not shown here).

Emissions of partial combustion by-products were very high during the combustion mode transition from LTC to conventional diesel operation (Cycles 1-4), similar to the values seen in the high-EGR LTC operation under steady-state operation as reported in Chapter 4 and by Cong *et al.* [2011a]. The increased combustion by-products emissions in high-EGR LTC operation were due to the reduced flame temperature and low in-cylinder oxygen concentration. It was discussed in Chapter 4 that high THC and CO emissions in high-EGR LTC operation were primarily because of bulk quenching due to the combination of reduced in-cylinder oxygen concentration, low flame temperature and retarded combustion phasing. This hypothesis was supported by optical investigations reported in Chapter 5; decreased flame temperature, retarded occurrence of peak flame temperature, short residence time of high-temperature reactions and combustion luminosity occurring in a small portion of the piston bowl contributed to the increased bulk quenching. High

THC emissions at the beginning of the transient (refer to Cycles 1 and 2 in Fig. 7.10) were due to over-mixing and lower flame temperatures [Dec, 2009; Cong, 2011]. High THC and CO emissions increased GISFC as shown in Fig. 7.10. It should be noted that THC and CO emissions and GISFC were much lower during the transient in conventional diesel operation compared to the combustion mode transition from LTC to conventional diesel operation. Exhaust temperatures in high-EGR LTC operation during the combustion mode transition were approximately 20-60^{o}C lower than the corresponding cycles in conventional diesel transient. This difference in the exhaust temperatures may have significant influences on the after-treatment conversion efficiency.

Methods to reduce emissions during combustion mode transition from high-EGR LTC to conventional diesel operation

It was shown that with increased intake pressure, the drive cycle load demand could be met during the combustion mode transition; however, THC, CO and smoke emissions as well as GISFC were particularly very high at the intermediate cycles. Increased intake pressure at the intermediate cycles increased smoke emissions (see Fig. 7.10) possibly due to advanced combustion phasing and reduced ignition delay (see Fig. 7.9). SOI timing was kept constant at the 4th cycle, whereas it was advanced in the 5th cycle with increased intake pressure. Combustion phasing had a significant effect on NO_X emissions in conventional diesel operation (Y_{O2} >13%); however, it did have little influence at high EGR levels (~50-55% EGR) as has been shown in the previous chapters of this thesis and elsewhere [Tanabe *et al*., 2010].

It was reported in Chapter 6 that a split fuel injection strategy with MBT injection timing was effective in reducing smoke emissions at moderate EGR levels compared to the single injection strategy. Therefore, the split fuel injection strategy was investigated at the intermediate pseudo-transient operating conditions to reduce smoke emissions. Pseudo-transient operating conditions at the 4th and 5th cycles were investigated only as these cycles had very high smoke emissions. Fuel split ratio of 50:50 and 35:65 were investigated at the 4th cycle, whereas only the 50:50 fuel split ratio was investigated at the 5th cycle. SOI1 timing for the 4th cycle were -36 and -33 ^{o}CA ATDC for the 50:50 and 35:65 fuel split ratios respectively, whereas the SOI1 timing for the 5th cycle was -36 ^{o}CA ATDC. SOI2 timings for the 4th and 5th cycles were -15 and -12 ^{o}CA ATDC respectively. These timings were based on injection timings investigated in Chapter 6. Emissions and in-cylinder performance at these two intermediate cycles with the split fuel injection strategy are shown in Fig. 7.11.

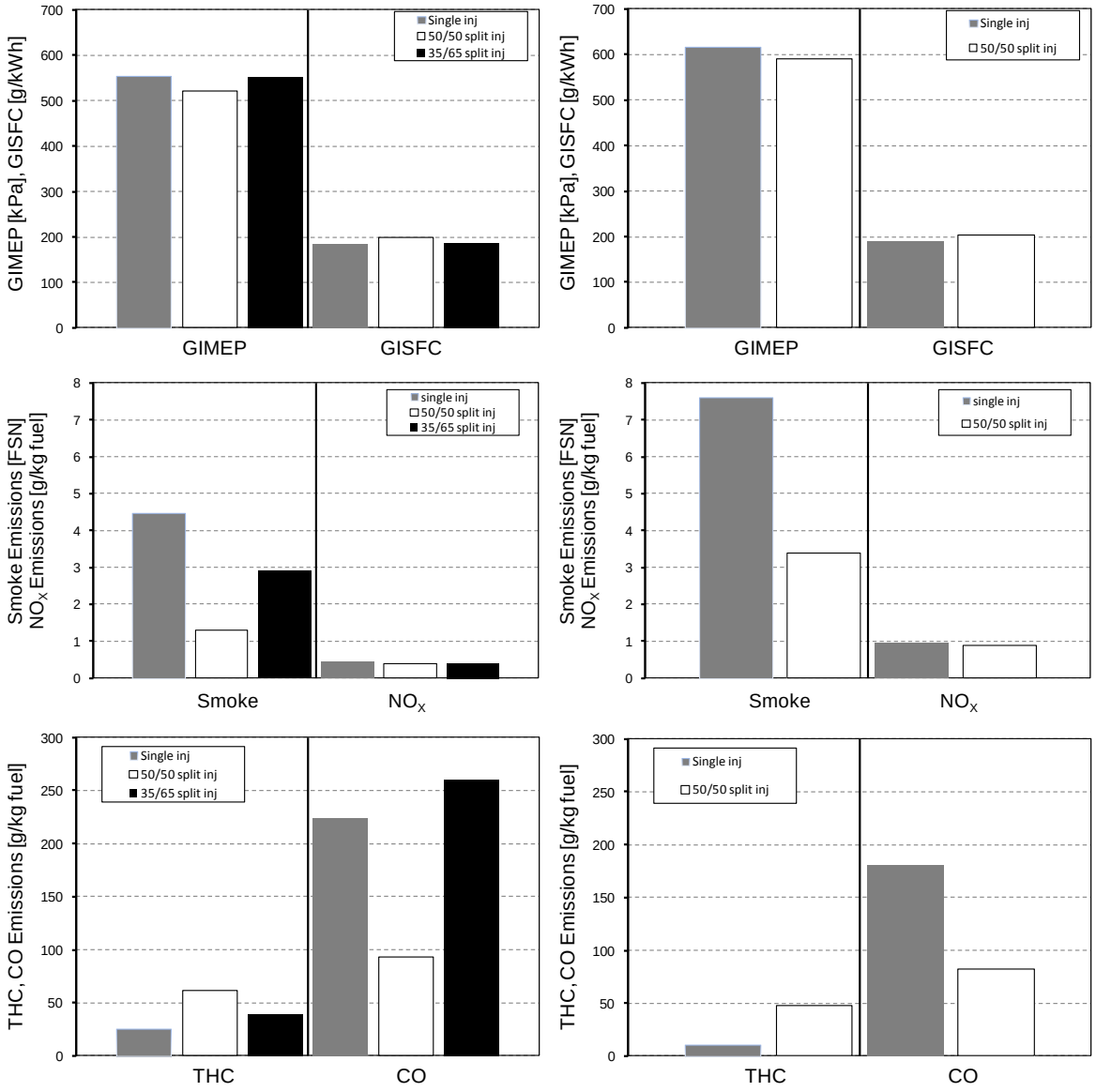

Fig. 7.11: In-cylinder performance and emissions with split and single fuel injection strategies (left hand column: 4th cycle; right hand column: 5th cycle)

Although the potential benefits of the split injection strategy on the reduction of smoke and CO emissions with little effect on NO_X emissions is evident from the figures above, it came at the expense of increased THC emissions. There was a reduction in the GIMEP with the 50:50 split fuel injection strategy at a given fuel quantity which is again undesirable in terms of meeting the required drive cycle load. An increase in the fuel quantity may increase GIMEP; however, it is expected that due to low in-cylinder oxygen concentration, it may adversely affect THC, CO and smoke emissions and hence, it was not investigated in this work. Instead, a different fuel split ratio (35:65) was investigated at the pseudo-transient operating condition corresponding to the 4th cycle so that GIMEP can be increased to meet the drive cycle load requirement. This strategy reduced THC emission and increased smoke emission as shown in Fig. 7.11. The net CO and THC emissions were

higher with the 35:65 fuel split ratio compared to the single injection strategy. 35:65 fuel split fraction was arbitrarily selected here to investigate the effect of the reduction of fuel quantity in the 1st injection event on smoke emissions and GIMEP. Note that it was not intended to carry out a set of different fuel split ratios at different injection timings to optimize the performance and emissions of the single cylinder engine during the combustion mode transition under consideration here. Note that CO and smoke emissions increased with the 35:65 fuel split ratio, compared to the 50:50 fuel split ratio and single injection strategies with insignificant effects on NO_X emissions as shown in Fig. 7.11. Energy release rates for the two intermediate cycles (4th and 5th) at higher boost pressure with different fuel injection strategies are shown in Fig. 7.12.

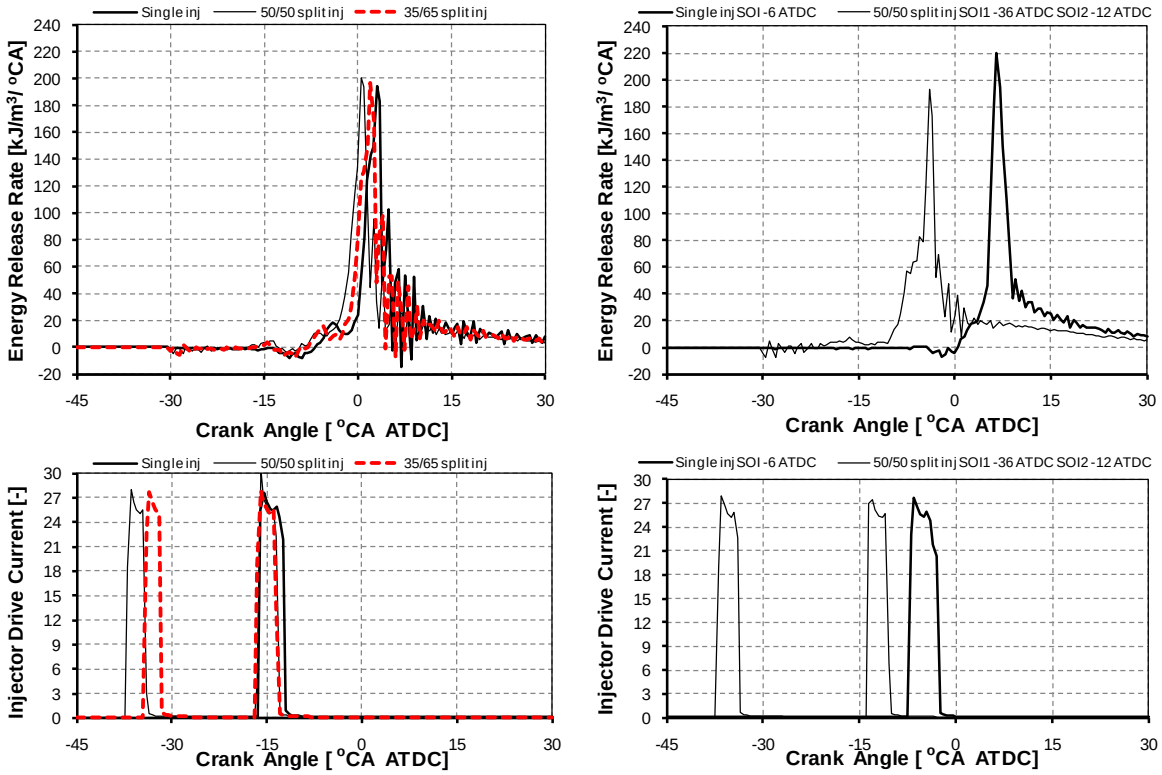

Fig. 7.12: Energy release rate and injector drive current at various fuel split ratios (left hand column: 4th cycle; right hand column: 5th cycle). Injector drive currents are represented in arbitrary units.

In the 4th cycle, the 1st premixing time (SOC-SOI1) for the fraction of the fuel injected during the 1st injection event was ~30 °CA with the split injection strategy, whereas the 2nd premixing time (SOC-SOI2) for the fraction of the fuel injected during the 2nd injection event was ~11 °CA. SOC was identified as described earlier in Sec. 3.4 in Chapter 3. These premixing times were much longer than the premixing duration (SOC-SOI) of 8 °CA in the single injection strategy, which influence soot formation. As discussed in Chapter 6, with the split injection strategy, the utilization of the available oxygen in the squish region improved CO oxidation. However, the fuel residing in the crevice volumes and other parts of the squish region escaped combustion and contributed to high

THC emissions. Similarly, in the 5th cycle, the premixing times with the 50:50 split injection strategy were 23.5 and 0.5 ^{o}CA respectively for the fraction of the fuel injected during the 1st and 2nd injection events compared to the premixing time (ignition delay) of 6 ^{o}CA with the single fuel injection strategy. Although the longer premixing time with the split injection strategy is expected to reduce smoke formation, in the 5th cycle, a fraction of the fuel from the 2nd injection event was injected into the high temperature gases which led to high smoke emissions (see right hand side of Fig. 7.12). Regarding high THC emissions with the split injection strategy in the 5th cycle, the same explanation holds good as explained for the 4th cycle. In summary, the split fuel injection strategy demonstrated that smoke emissions can be reduced; however, further optimization needs to be carried out to meet the drive cycle load requirement during the combustion mode transition.

7.6 Assessment of Transition from Conventional Diesel to LTC

The pseudo-transient operating conditions corresponding to 'Transient 4' dealing with a combustion mode transition from conventional diesel to LTC operation were investigated on the AVL single cylinder research engine. Intake pressure, EGR rate, SOI timing and the oxygen based equivalence ratio during the transition are shown in the left hand column of Fig. 7.13. Retarded injection timing strategy similar to the previous section was used during the transient in conventional diesel operation to reduce NO_X emissions, whereas gradual advanced injection timings (similar to the MBT strategy used in high-EGR LTC operation in Chapter 4) were used in the intermediate cycles and in high-EGR LTC operation during the combustion mode transition from conventional diesel to LTC. It should be noted that the fuel injection timing during the load transient in conventional diesel operation did not necessarily replicate the production engine's test data referenced in this work. The intake pressure during the combustion mode transition in 'Transient 4' was higher compared to 'Transient 3'. However, the intake pressure was lower than the targeted values to start with. It should be recalled that 'Transient 4' involved two combustion mode transitions: (1) LTC to conventional diesel and (2) conventional diesel to LTC. Although only the mode transition from conventional diesel to LTC operation was investigated for 'Transient 4', simulation was carried out for the entire transient (LTC to conventional diesel and *vice-versa*). Because of high EGR requirements in LTC, exhaust enthalpy was reduced and therefore, there was a reduction in boost pressure at the beginning of the transient. Similar to the previous section, intake pressure was increased at the intermediate cycles during the combustion mode transition to match the target intake pressure as shown in the right hand column of Fig. 7.13 to investigate their effects on engine performance, combustion and emissions.

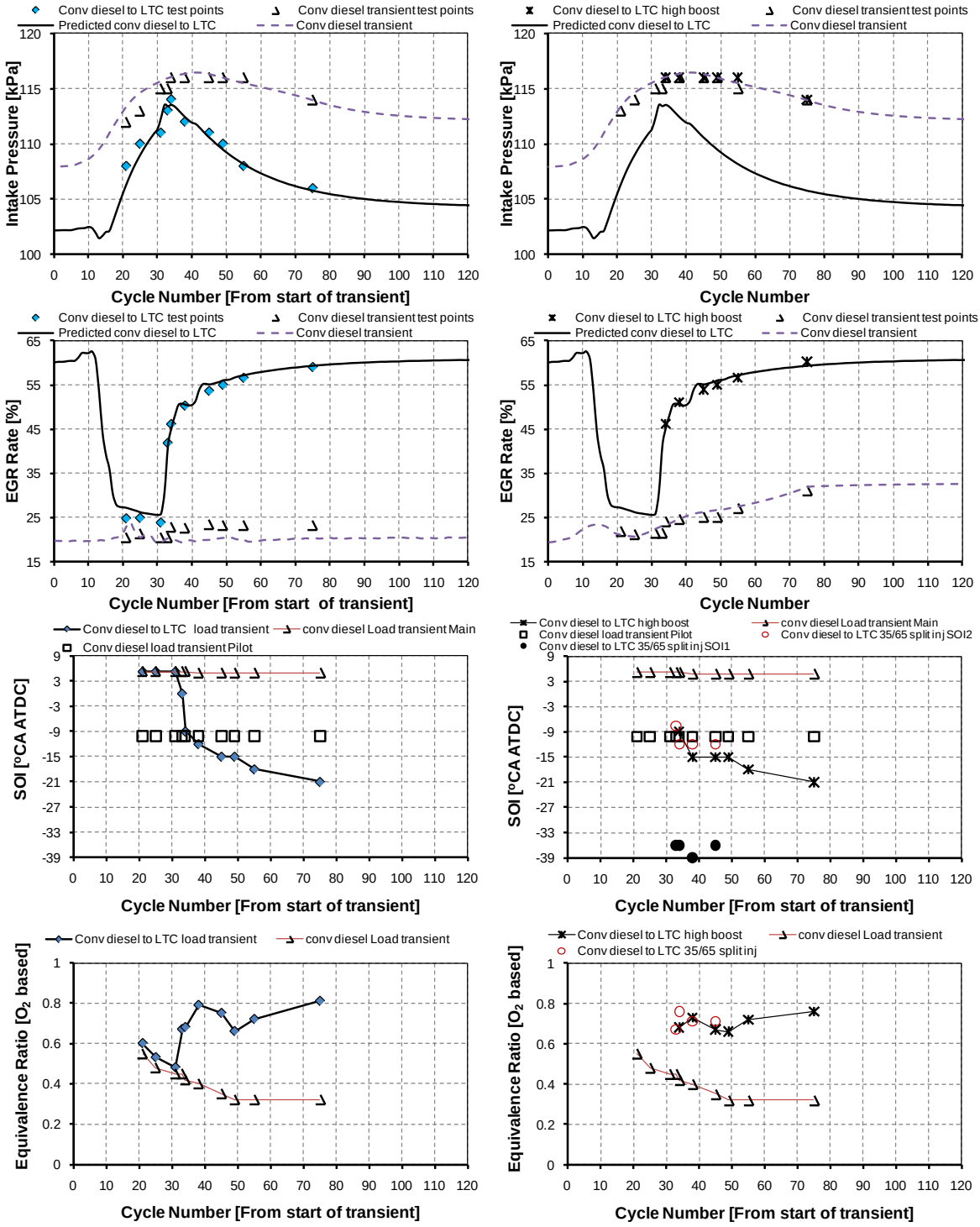

Fig. 7.13: Pseudo-transient operating conditions (intake pressure, EGR level, SOI timing and oxygen based equivalence ratio) during 'Transient 4' (left hand column: lower intake pressure; right hand column: higher intake pressure)

The in-cylinder performance in terms of GIMEP obtained from the steady-state evaluation of the pseudo-transient operating conditions during the combustion mode transition from conventional diesel to LTC is shown in Fig. 7.14. As discussed earlier, GIMEP obtained from the pseudo-

transient operating conditions corresponding to the load transient in conventional diesel operation were taken as the actual load of the engine while following the drive cycle. It is worth mentioning that despite the crudeness of the combustion model (i.e. a diesel Wiebe function where engine reference speed and SOC were specified), the predicted GIMEP during the combustion mode transition matched well with the experimental GIMEP values obtained from the AVL single cylinder engine. Combustion phasing (CA50) and the ignition delay derived from the energy release rates are also shown in the figure. Note that the increased intake pressure did not have a significant effect on GIMEP as shown on the right hand column of Fig. 7.14. Higher intake pressure was investigated during this transient to reduce the emissions of partial combustion by-products and smoke.

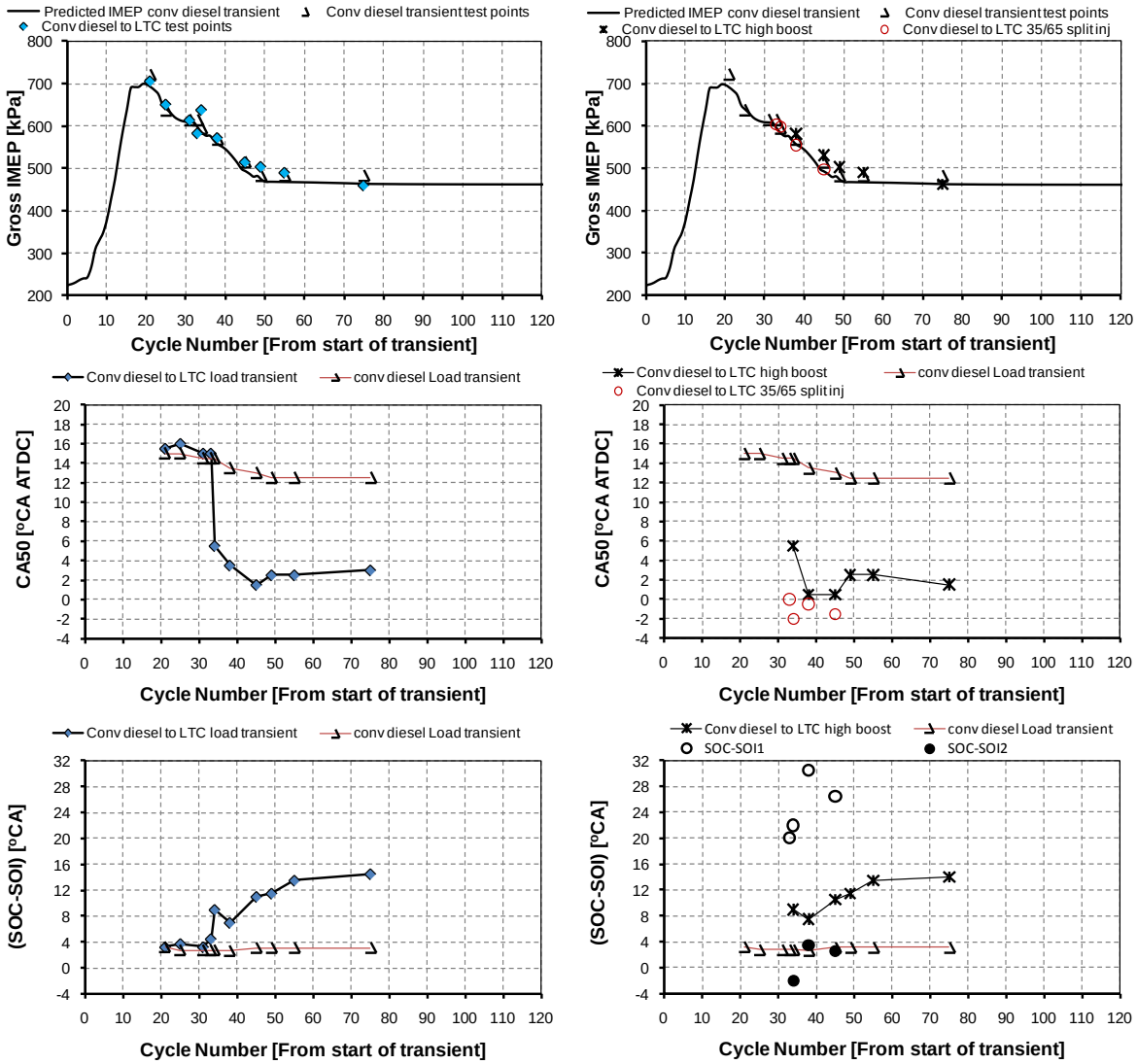

Fig. 7.14: Performance, combustion phasing and ignition delay corresponding to the pseudo-transient operating conditions during 'Transient 4' (left hand column: lower intake pressure with single injection, right hand column: higher intake pressure with single injection and split injections)

From the two transients (mode transition from conventional diesel to LTC and load transient in conventional diesel operation), it can be seen that the combustion phasing during the combustion mode transition changed from a retarded CA50 (~16 ^{o}CA ATDC) in conventional diesel operation to a near-TDC CA50 (~2 ^{o}CA ATDC) in LTC operation. The transition of CA50 from a retarded position to a near-TDC position indicates that it may be used as a control parameter during combustion mode transition and accordingly, SOI timing may be adjusted. A smooth transition of CA50 is desirable during the combustion mode transition to maintain combustion stability while avoiding destabilizing step-changes in combustion. Combustion mode transition occurred at the 49th cycle as indicated by the increased ignition delay (SOC-SOI) from 4 ^{o}CA in conventional diesel operation to ~12 ^{o}CA in high-EGR LTC operation as shown in Fig. 7.14.

As expected, NO_X emissions reduced during the transition from conventional diesel to LTC as shown in Fig. 7.15. The initial high NO_X emissions, shown in Fig. 7.15, in conventional diesel operation were due to the overshooting intake pressure (low equivalence ratio) and low EGR levels (~25%) as shown in Fig. 7.13. Transition into LTC reduced NO_X emissions significantly, with advanced combustion phasing (see Fig. 7.14) showing little effect. The load transient in conventional diesel operation showed the opposite trend, where NO_X emissions were high due to lean equivalence ratios and low EGR levels despite retarded injection timings. Due to fuel-rich oxygen based equivalence ratios (i.e. high EGR levels) and short ignition delay, smoke emissions during the mode transition from conventional diesel to LTC operation were unacceptably high at the intermediate cycles. With the transition of combustion into high-EGR LTC operation, smoke emissions decreased and were similar to those in conventional diesel operation. Smoke emissions in the conventional diesel load transient were low due to low oxygen based equivalence ratios (see Fig. 7.13) and high flame temperatures. As discussed earlier, the emissions data presented in the figure do not necessarily represent the emission levels in the production engine referenced in this work due to an advanced fuel injection system and careful engine calibration.

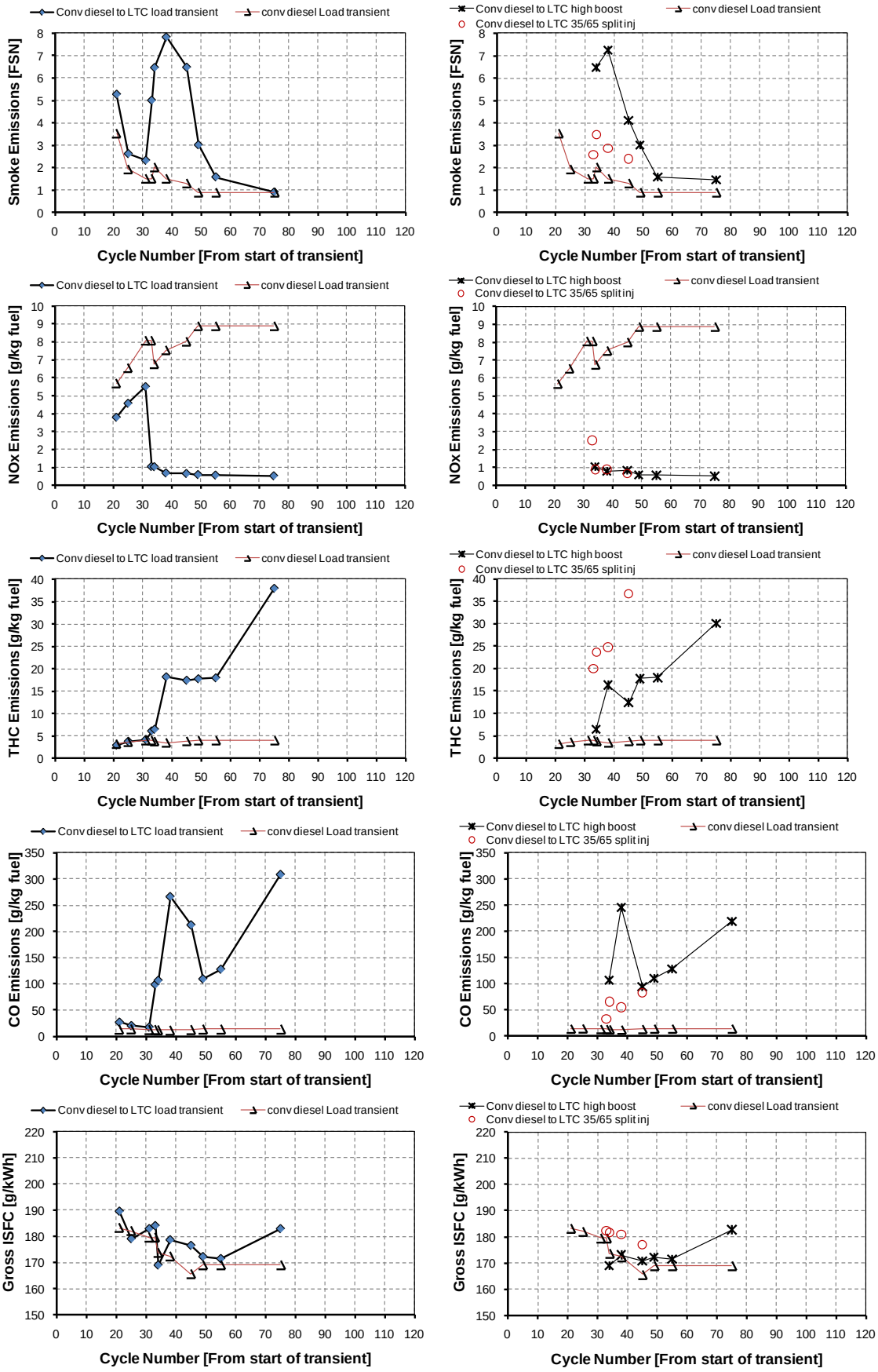

Fig. 7.15: Emissions and GISFC corresponding to the pseudo-transient operating conditions during 'Transient 4' (left hand column: lower intake pressure; right hand column: higher intake pressure)

Emissions of partial combustion by-products at the intermediate cycles were very high during mode transition from conventional diesel to high-EGR LTC operation due to the low in-cylinder oxygen concentration and flame temperature as discussed in the previous section. This leads to low combustion efficiency; however, it did not necessarily deteriorate the GISFC compared to the conventional diesel transient (the exception being at Cycles 38, 45 and 75) as shown in Fig. 7.15. It is expected that the retarded combustion phasing during the load transient in conventional diesel operation increased GISFC. Although the transition from conventional diesel to high-EGR LTC operation was characterized by low combustion efficiency (because of high THC and CO emissions), combustion phasing was maintained close to TDC which maximized the work extracted during the expansion stroke, therefore, recovering a part of the lost combustion efficiency. Also, it is expected that the reduced combustion efficiency in high-EGR LTC operation may partially be offset by the reduced heat transfer losses due to low flame temperatures.

Methods to reduce emissions during combustion mode transition from conventional diesel to high-EGR LTC operation

Although the potential benefit of reducing NO_X emissions during the mode transition from conventional diesel to high-EGR LTC operation was evident, high emissions of smoke and partial combustion by-products were particularly a concern. Therefore, the intermediate cycles were investigated with higher intake pressure to reduce these emissions. Note that the intake pressure was increased only marginally (~5 kPa, refer to the right hand column in Fig. 7.13) to match the corresponding intake pressure during the load transient in conventional diesel operation. Achieving a 5 kPa increase in the intake pressure during the mode transition with just changing the VGT is considered not unreasonable. Increased intake charge pressure reduced the oxygen based equivalence ratio as shown in the right hand column in Fig. 7.13. Increased intake pressure also reduced the emissions of combustion by-products and smoke marginally with insignificant effects on NO_X emissions (refer to the right hand column in Fig. 7.15).

In order to reduce the smoke emissions further at the intermediate cycles with intermediate EGR levels, a split fuel injection strategy was investigated at higher intake charge pressures. In the previous section it was shown that although the 50:50 split fuel injection strategy was effective in reducing the smoke emissions, it also reduced the GIMEP marginally which was undesirable from a driveability point of view. Therefore, an arbitrary fuel split ratio of 35:65 was chosen in this investigation at the intermediate cycles (33, 38, 45 and 55) so that smoke emissions could be reduced without affecting the drive cycle load requirement. Injection timings with the split injection strategy are shown in the right hand column in Fig. 7.13. The effects of this split injection strategy on engine performance and emissions are shown in the right hand column in Figs. 7.14 and 7.15 respectively.

With the split injection strategy, NO_X emissions increased at the 33rd cycle due to the advanced CA50 and higher intake oxygen mass fraction (Y_{O2} >14%), whereas other cycles were unaffected due to the lower intake oxygen mass fractions (Y_{O2} ≤12%) even with advanced combustion phasing. This is consistent with the previous investigation by Tanabe *et al.* [2010]. As discussed in the previous section of this chapter and in Chapter 6, the split fuel injection strategy increased THC emissions. Higher THC emission indicates that there was less conversion of fuel to CO. GISFC marginally increased with the split injection strategy as shown in Fig. 7.15. Note that the THC emissions with the split injection strategy were similar to a low load operating condition (8 mg/cycle fuelling quantity and 1500 rpm engine speed) in conventional diesel operation without any EGR reported earlier by Cong *et al.* [2011a]. Therefore, it is expected that a DOC would be able to handle THC emissions at the intermediate cycles due to high exhaust temperatures at the intermediate cycles. Energy release rates at the intermediate cycles, shown in Fig. 7.16, show a gradual shift from conventional diesel combustion (Cycles 33, 38 and 45) to LTC operation (Cycle 55). Note that LTC operation is indicated by the appearance of the low temperature cool flame reactions at the 55th cycle. The occurrence of cool flame reaction was explained in detail in Chapters 2, 5 and 6.

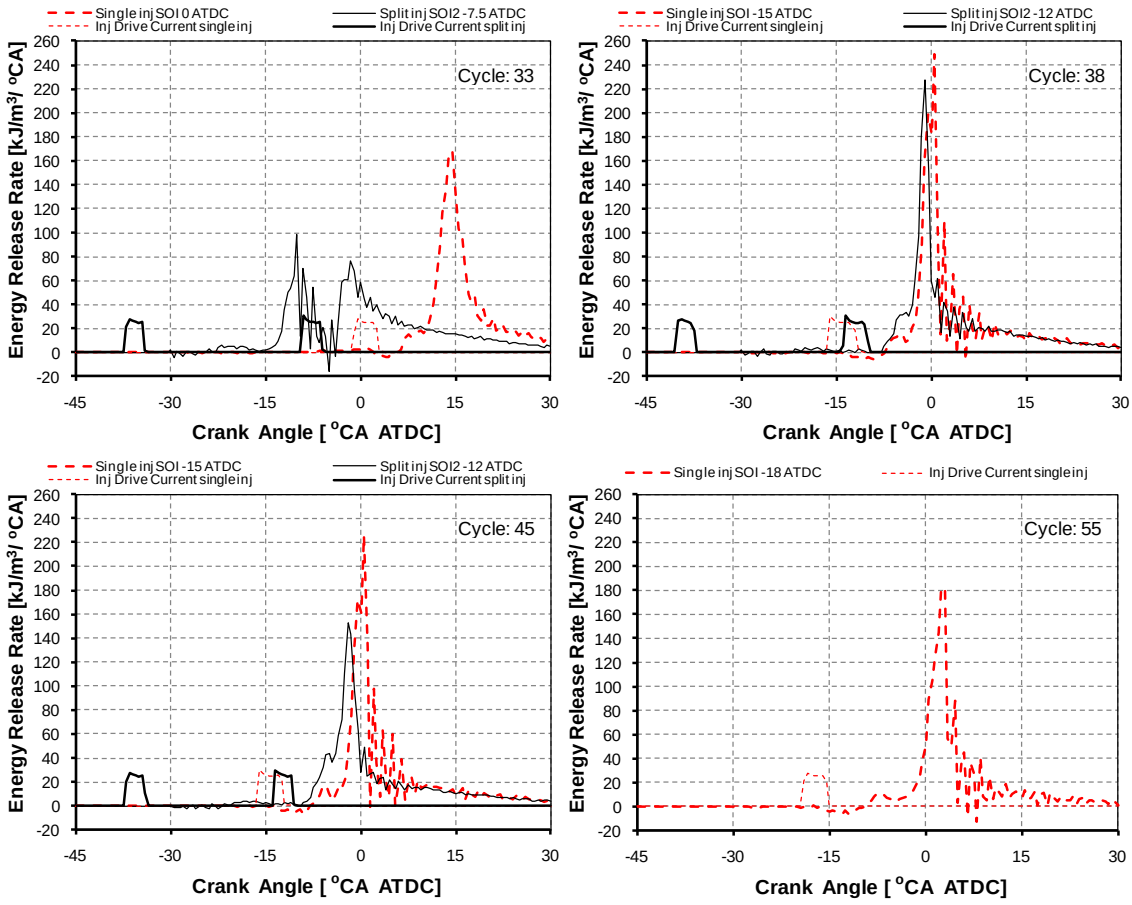

Fig. 7.16: Energy release rate with single and split injection strategies at the intermediate cycles. Injector drive currents are represented in arbitrary units.

In order to show the effects of the fuel injection parameters (i.e., injection pressure, injection timing and fuel split ratio) on emissions and performance of the engine during the combustion mode transition with the split injection strategy, tests were conducted at two intermediate cycles (33 and 38). These cycles were selected as they pose significant difficulties in terms of emissions of THC, CO and smoke during the combustion mode transition as was shown earlier in Fig. 7.15. The fuel injection parameters investigated for the above two cycles are given in Table 7.4. The experimental CA50 values obtained from these investigations are also listed in the table. The in-cylinder performance and emissions of the engine with a slight variation of injection timing, injection pressure and fuel split ratio for both the cycles are shown in Fig. 7.17.

Table 7.4: Split Fuel Injection Parameters at Selected Pseudo-transient Operating Conditions

Cycle	**Fuel quantity (mg/cycle)**	**EGR rate (%)**	**P_{int} (kPa)**	**Injection timing (^oCA ATDC)**		**P_{inj} (MPa)**	**Fuel split ratio (commanded)**	**Case**	**CA50 (^oCA ATDC)**
				SOI1	SOI2				
33	15.4±0.2	41.5	117	-36	-3.75	120	50:50	A	2
				-36	-7.5	100	40:60	B	0
				-37.875	-7.5	100	50:50	C	-1
38	14.6±0.2	50.5	116	-39	-12	90	35:65	D	-0.5
				-42	-12	90	35:65	E	0.5
				-36	-15	70	50:50	F	-3.5

P_{int}: Intake pressure; P_{inj}: Injection pressure

From Fig. 7.17, it can be seen that even a minor change in the operating condition increased GIMEP at the expense of higher smoke emissions. A lower injection pressure (Case F) reduced smoke emissions at high EGR operation (38^{th} cycle). Lower injection pressure allowed a more advanced SOI2 timing without exceeding a rate of pressure rise of 1 MPa/^{o}CA which also avoided injecting a fraction of the fuel mass during the 2^{nd} injection event into the high temperature gases. However, lower injection pressure also increased the injection duration which might offset the above benefit. Although lower injection pressure reduced smoke emissions, THC emissions and combustion variability (COV of GIMEP >4%) increased. This is due to the complex interaction between fuel atomization, vaporization, penetration and mixing with the surrounding air, and the spray-wall interaction; the exact reason, however, could not be resolved from the data collected. As discussed earlier, CA50 influenced NO_X emissions at low EGR levels (Cycle 33), whereas it did not have a significant effect during high EGR operation (Cycle 38) as shown in Fig. 7.17.

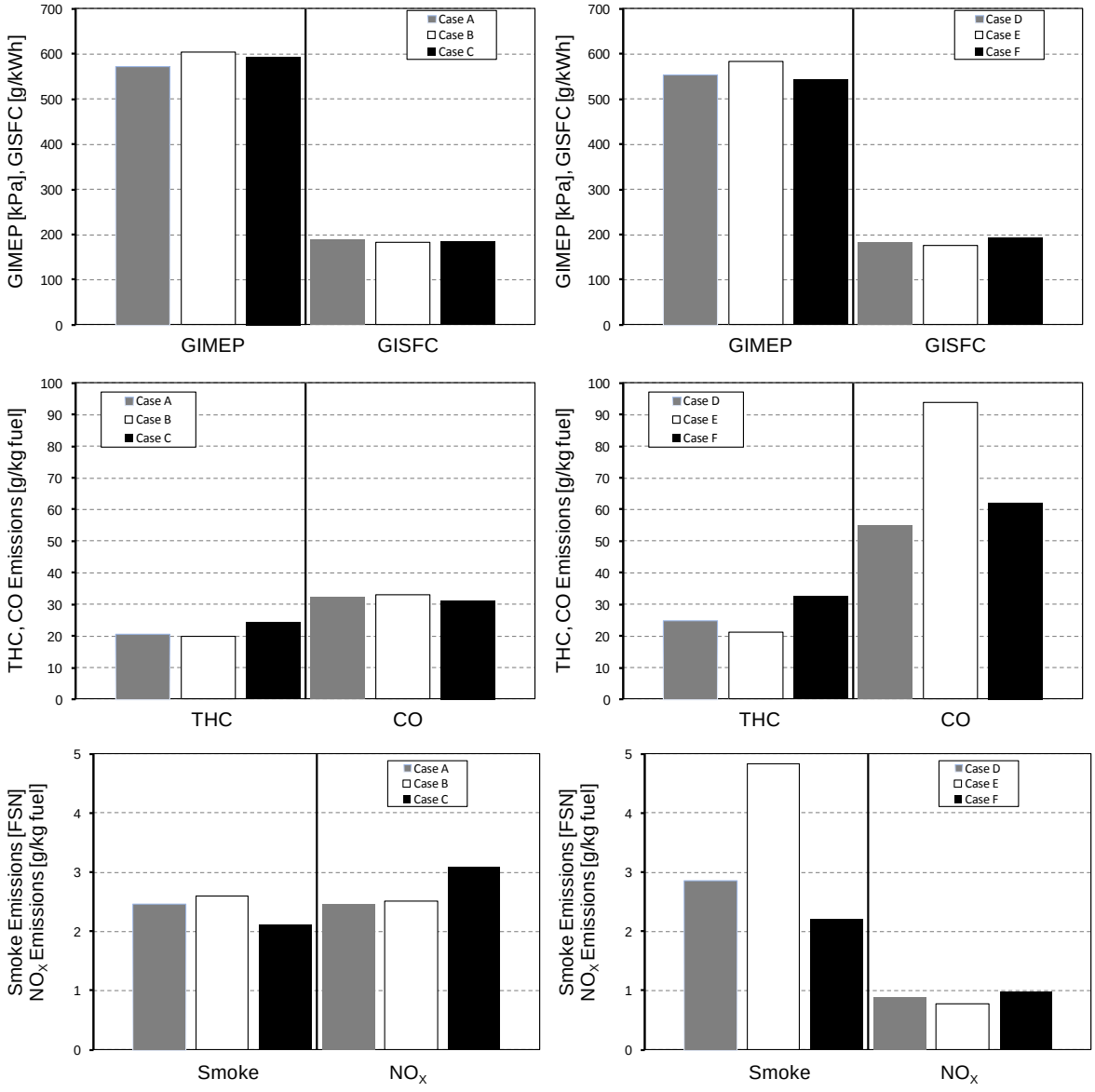

Fig. 7.17: In-cylinder performance and emissions with variable split fuel injection parameters (left hand column: 33rd cycle, right hand column: 38th cycle)

From this sensitivity analysis, it is realized that with carefully selected fuel injection parameters, combustion mode transition from high-EGR LTC to conventional diesel operation or *vice-versa* could meet the drive cycle load requirement with low NO_X emissions. Note that the sensitivity analysis reported in this work did not aim to optimize the performance and emission of the single cylinder research engine during the combustion mode transition. This needs to be done in a multi-cylinder engine which requires engine calibration through, for example, design of experiments (DOE) techniques and is outside the scope of this present work.

7.7 Discussion

In the work reported in this chapter, the transient performance and emission of a 2 litre production diesel engine for a representative vehicle was investigated for dual-mode operation under LTC-conventional diesel combustion during the EUDC phase of the NEDC driving cycle. Operating the engine in the high-EGR LTC mode in the first two replications of the urban drive cycle (ECE15) phase of the NEDC drive cycle seem to be challenging as engine misfiring and unstable operation due to low coolant temperature ($<50^{o}$C) are likely. Therefore, whether the first 272 s of the urban drive cycle can be covered under high-EGR LTC operation is uncertain.

It should be noted that the NEDC driving cycle is not necessarily a true representation of the transient conditions in a real-world driving condition even in Europe, nor is it the regulatory drive cycle in other jurisdictions. The common ARTEMIS driving cycle (CADC) developed under the European ARTEMIS (Assessment and Reliability of Transport Emission Models and Inventory Systems) project, based on statistical analysis of a large database of European real world driving patterns [DieselNet, 2012], is expected to be more representative of a real-world driving cycle in Europe. This cycle includes three real-world driving cycles such as urban, rural road and motorway [Andre, 2004] and the motorway cycle has two variants with maximum vehicle speeds of 130 and 150 km/h [DieselNet, 2012]. In the USA, an FTP-72 cycle is used for emission certification (also known as Urban Dynamometer Driving Schedule, UDDS) which simulates an urban route with frequent stops. In Japan, a JC08 chassis dynamometer test cycle is used for the emission certification of light-duty vehicles which represents driving in congested city traffic, including idling periods and frequently alternating acceleration and deceleration [DieselNet, 2012]. Therefore, the real-world transients and the driving cycles in other jurisdictions are more rapid, aggressive and different than the NEDC driving cycle. Note that the NEDC is a relatively low load and slow acceleration driving cycle which is more conducive to LTC operation, compared to the real-world and other certification driving cycles. The aggressive real-world transients would involve more rapid and frequent acceleration and deceleration events. It is expected that a more aggressive driving cycle will be 'more challenging' for combustion mode transitions in an 'LTC-conventional diesel dual-mode' engine. As a result, to keep performance up while minimizing emissions will require careful tuning of the injection strategy.

It was shown in this chapter that with a marginally higher boost pressure and with a split fuel injection strategy, the emissions of combustion by-products and smoke could be reduced while maintaining the desired engine performance and driveability with minimum NO_X emissions during an aggressive and rapid transient in the NEDC cycle. Therefore, it is expected that these strategies should help LTC cope with more rapid transients and transitions. The reduced EGR requirements of the split injection strategy should also enable a greater frequency of combustion mode transitions.

A production variable geometry turbocharger optimized for conventional diesel operation may not be suitable for an engine employing the dual-mode of combustion. Also, options to resize the

turbocharger would be limited by the engine's need to meet the full load requirement under conventional diesel operation. Therefore, advanced turbocharger technology or an altogether different intake air boosting strategy such as supercharging might be required to handle the combustion mode transitions in order to meet the drive cycle load requirement with acceptable emissions. Given the difficulty of controlling engine performance and emissions during a combustion mode transition, it follows that there is a considerable benefit to be gained from reducing the number of combustion mode transitions. Extension of the present LTC load limit is likely to be critical to the success of this potentially valuable ultra-low NO_X combustion technology. Enhanced boost pressure with the advanced air boosting strategy would lead to the possibility of increasing the LTC load limit.

The knowledge gained through this modelling and experimental study for different combustion mode transitions could be implemented at other transient events as well, as all transient events are expected to have similar EGR valve and turbocharger responses. Details will be different, but the general effects should be similar. With the improved understanding of the combustion process and availability of energy release rate results on a cycle-by-cycle basis, the existing multi-cylinder one-dimensional WAVE model could be refined further to predict the cycle-by-cycle operating conditions with greater accuracy to achieve future improvements to the experimental work. However, it is expected that it will only have a minor effect on the operating parameters (EGR rate and intake pressure) predicted by the WAVE model presented in this chapter. Knowledge of cycle-by-cycle operating conditions would also enable different fuel injection strategies to be investigated to control the combustion process and emissions during the combustion mode transition. With accurate prediction of EGR rate and intake pressure during a transient, model based fuel injection control strategy can be evaluated and used to improve the transient control of an 'LTC-conventional diesel combustion dual-mode' engine.

7.8 Conclusions

The work reported in this chapter has investigated the effects of transient operation of a diesel engine with dual-mode combustion: high-EGR LTC for low and medium loads and conventional diesel operation at high load. Transition from LTC to conventional diesel operation and *vice-versa* to be encountered by a 2 litre multi-cylinder diesel engine used in a passenger vehicle during the EUDC phase of the NEDC driving cycle were simulated with a one-dimensional Ricardo WAVE model. Engine speed, fuelling quantity, intake pressure, transient duration (all derived from the manufacturer's drive cycle test data) and the EGR levels used in conventional diesel and high-EGR LTC operation were input to the model. High-EGR LTC operation was limited to 16 mg/cycle fuel quantity, above which conventional diesel operation was considered. The EGR valve position was set in the model to follow the engine speed and fuel quantity, whereas the VGT vane position was controlled by a PID controller. As discussed in Sec. 7.3, the VGT and EGR position controls were

set up to first reach the target EGR, and then the VGT position was adjusted to increase the intake pressure to match the targeted value, while maintaining EGR rate. Fuel quantity, intake pressure and EGR rate at each cycle during the transient were the output from the simulation. Pseudo-transient operating conditions at the beginning and at the end of the transients and at some intermediate cycles were selected and investigated on the 0.51 litre AVL single cylinder HSDI diesel engine with independently controllable EGR and boost systems to evaluate the performance, combustion and emissions characteristics during combustion mode transitions. Pseudo-transient operating conditions corresponding to a load transient in conventional diesel operation (with low EGR rates) were also investigated at the corresponding cycles. Different fuel injection parameters at the targeted intake pressure (marginally higher than the model predicted intake pressure during the combustion mode transition) with a split fuel injection strategy were investigated as techniques to match the drive cycle load requirement while reducing the smoke and partial combustion by-products emissions during combustion mode transitions. The following are the main conclusions from this investigation.

1. Analysis of the driving cycle test data revealed that majority of the transients in the urban (ECE15) phase of the NEDC driving cycle are achievable within the LTC operating region, whereas frequent combustion mode transitions from LTC to conventional diesel operation or *vice-versa* would be required in the EUDC phase.
2. Due to the high EGR requirement in LTC, exhaust enthalpy and exhaust mass flow rate were reduced and therefore, the production turbocharger operated at its lowest efficiency zone. This led to a slow response of the turbocharger and insufficient intake pressure during the combustion mode transition. Reduced intake pressures along with high EGR levels resulted in unfavourable oxygen based equivalence ratios leading to high emissions of smoke, THC and CO, although NO_X emissions remained low. High THC and CO emissions increased GISFC and reduced GIMEP, which would make it difficult to meet the required drive cycle load at a desired acceleration level without increasing the fuelling quantity. Increased fuel quantity did not increase load; instead smoke, THC and CO emissions increased further due to low oxygen availability.
3. Smoke emissions during a combustion mode transition are largely controlled by the speed of the EGR system response. High smoke emissions were found for cycles with intermediate EGR levels—where intermediate implies EGR levels that are above those required for NO_X control in conventional diesel mode but below the levels required to inhibit soot formation in LTC operation. Reducing the number of cycles that see the intermediate levels of EGR will be essential if the smoke emissions during a combustion mode shift are to be controlled.
4. With a marginal increase in intake pressure during the combustion mode transition, combustion by-products emissions and GISFC were reduced with insignificant effect on NO_X

emissions, although in certain cases smoke emissions increased. Reduced GISFC led to increased GIMEP so that drive cycle load requirement could be maintained.

5. Combustion mode transition (from LTC to conventional diesel or *vice-versa*) needs to be coupled to a similar combustion phasing (CA50) transition (from a near-TDC CA50 to a retarded CA50 or *vice-versa*) strategy so that high combustion efficiency can be achieved with high EGR operation. However, the transition of CA50 should be gradual and accordingly, the injection timings and injection pressures need to be adjusted.
6. Advanced combustion phasing significantly increased NO_X emissions without affecting THC, CO and smoke emissions for intake oxygen mass fractions greater than 14%, whereas it reduced THC, CO and smoke emissions with a marginal effect on NO_X emissions for intake oxygen mass fraction less than 12%.
7. Split fuel injection with equal fraction of fuel during the two injection events at higher intake pressure was effective in reducing smoke emissions from the intermediate cycles during combustion mode transition, although it increased THC emissions and GISFC marginally. On the other hand, reducing the fraction of fuel during the 1^{st} injection event reduced THC emissions, GISFC and increased GIMEP to meet the drive cycle load requirement, although it came at the expense of increased smoke emissions; but smoke emissions were not as high as for the single injection case.
8. Fuel injection parameters (i.e., injection pressure, split or single injection event, fuel split ratio, injection timing) had a significant effect on emission and GISFC during the combustion mode transition. Therefore, these parameters need to be optimized and mapped to the intermediate cycles carefully in order to improve the controllability of the transients to achieve the desired level of emissions and performance.

Chapter 8
CONCLUSIONS AND FUTURE WORK

8.1 Introduction

High-EGR LTC is a promising strategy to simultaneously reduce NO_X and smoke emissions from a diesel engine at low and medium loads. At medium load, due to the reduced availability of in-cylinder oxygen concentration, emissions of partial combustion by-products (i.e. THC and CO) remain excessive and thermal efficiency is reduced. Furthermore, the limitation of reaching only moderate load means that an engine using this strategy needs to transition to more conventional, low-EGR diesel combustion at high load. Managing this transition, while maintaining reasonable efficiency, combustion stability and emissions, remains a significant challenge. In this research project, different techniques were investigated to reduce these emissions and improve thermal efficiency, while maintaining acceptable smoke and NO_X emissions in high-EGR LTC operation. These methodologies were also aimed at making the high-EGR LTC strategy practically viable and to improve combustion robustness.

In this research, specific operating conditions were investigated optically through in-cylinder visualization to assess the spray and combustion phenomena to improve fundamental understanding of high-EGR LTC. At these conditions, the flame temperature was measured by the two-colour pyrometry system developed specifically for this application. This gave reliable measurements at the relatively low temperatures observed in LTC. Specific attention was paid to pseudo-transient operating conditions dealing with combustion mode transitions between LTC and conventional diesel operation. Techniques investigated to enhance LTC operation included increased intake pressure to reduce the emissions of partial combustion by-products and to improve fuel economy while increasing the load boundary; a split fuel injection strategy to reduce the EGR requirements to achieve LTC; and optimized combustion timing to maintain combustion stability and efficiency in LTC. A range of multiple injection strategies were evaluated for controlling the performance and emissions of an ‘LTC-conventional diesel dual-mode’ engine during transient operation.

The conclusions for the individual studies were discussed in the corresponding chapters and therefore are not reproduced here. This present chapter lists the novel contributions and the major conclusions of this research. The implications of these findings to engine system development and recommendations for future research are also discussed in this chapter.

8.2 Novel Contributions and Major Conclusions

This research has studied in detail the use of high levels of EGR to enable diesel engines to operate under low temperature combustion conditions to suppress both in-cylinder NO_X and soot formation, enabling very low engine-out emissions. A substantial reduction (i.e. >10% points) in the EGR level was achieved with the split injection strategy for simultaneous PM and NO_X emissions of

<1 FSN and <1 g/kg of fuel, respectively. Combustion and emissions were studied using cylinder pressure derived energy release analysis, in-cylinder optical imaging, two-colour pyrometry and engine exhaust emissions measurements. The following are the novel contributions and major conclusions from the research presented for each of the different strategies investigated in this work to improve the viability of high-EGR LTC operation.

(a) Effects of boost pressure in single-injection high-EGR LTC

1. Higher flame temperature, longer combustion duration and peak flame temperature occurring close to TDC (shown in Fig. 5.6) at higher intake pressure resulted in reduced bulk quenching in high-EGR LTC operation. Higher in-cylinder oxygen concentration and reduced bulk quenching at higher intake pressure reduced THC emissions and improved fuel economy. Increased intake pressure had no significant effect on NO_X emissions for EGR rates greater than 50%.
2. Increased intake pressure reduced PN emissions both in LTC and conventional diesel combustion. PN emissions were higher with LTC operation compared to conventional diesel combustion. Count median diameters of the emitted particles were smaller in high-EGR LTC operation compared to conventional diesel operation and were independent of injection and intake pressures.

(b) Effects of split injections in LTC

3. A split fuel injection strategy achieved low smoke emissions at EGR levels 10% points below the single injection high-EGR LTC strategy. Smoke emissions were reduced significantly when the fuel from the 2nd injection was injected into the cool flame reactions of the fuel injected during the 1st injection; this is shown by both the exhaust FSN and the soot concentration data shown in Fig. 6.21 obtained from the two-colour pyrometry system.
4. With split injection, the higher intake oxygen mass fraction and higher intake pressure enhanced soot oxidation more than they increased soot formation, as supported by the two-colour pyrometry results shown in Figs. 6.14 and 6.19 respectively, resulting in reduced engine-out smoke emissions. For the high-EGR single injection combustion strategy shown in Fig. 5.2a, optical imaging did not show the broadband soot incandescence observed with the reduced EGR split injection cases shown in Figs. 6.15 and 6.16.
5. EGR rate showed significant influence on THC emissions with the split fuel injection strategy. THC emissions with the split injection strategy were higher than the single injection strategy at a given intake oxygen mass fraction in certain fuel injection timings. It was hypothesized that a large fraction of the fuel residing in the squish region and crevice volume escaped combustion and contributed to high THC emissions. THC and CO emissions as well as GISFC were reduced significantly with the split injection strategy at 12% intake oxygen

mass fraction compared to the single main injection strategy at 8% intake oxygen mass fraction.

6. Higher intake pressure and higher intake oxygen mass fraction with the split injection strategy reduced THC, CO, smoke and GISFC. Higher flame temperatures shown in Fig. 6.19 and Fig. 6.14 corresponding to higher intake pressure and higher intake oxygen mass fraction respectively for the split injection cases compared to the flame temperature with the single-injection high-EGR LTC strategy at 120 kPa intake pressure shown in Fig. 5.6 enhanced THC, CO and smoke oxidation due to higher in-cylinder oxygen concentration. At higher intake pressure, injecting fuel from the 2nd injection event into the high temperature gases reduced the rate of pressure rise, although the retarded SOI2 timing increased smoke emissions marginally (the trade-off between the rate of pressure rise and smoke emissions is shown in Fig. 6.20) without any significant impact on THC and CO emissions and GISFC.
7. Higher injection pressure did not necessarily reduce THC, CO and smoke emissions and GISFC in the split injection strategy at a given intake oxygen mass fraction as shown in Fig. 6.17. However, with the single fuel injection strategy, higher injection pressures in high-EGR LTC operation resulted in lower smoke and THC emissions, thereby marginally reducing GISFC without influencing NO_X emissions.

(c) Combustion mode transition to and from LTC

8. Modelling of the combustion mode transitions (from LTC to conventional diesel operation and *vice-versa*) was used to identify the operating conditions at individual cycles during a transient. It was found that smoke emissions during a combustion mode transition are largely controlled by the EGR system response. High smoke was emitted for cycles with intermediate EGR levels—where 'intermediate' implies EGR levels that are above those required in conventional diesel combustion for NO_X reduction without significantly increasing soot emissions, but below the levels required to inhibit soot formation in LTC operation. Therefore, reducing the number of cycles that see the intermediate levels of EGR will be required to control the smoke emissions during a combustion mode transition.
9. Due to high EGR requirement in LTC, exhaust flow enthalpy and exhaust mass flow rate are reduced and therefore, a production turbocharger would operate in its lowest efficiency zone. This would lead to a slow response of the turbocharger and insufficient intake pressure during combustion mode transition. Reduced intake pressures along with high EGR levels resulted in unfavourable oxygen based equivalence ratios during combustion mode transition leading to high emissions of smoke, THC and CO, although NO_X emissions remained low. Therefore, advanced turbocharger technology (e.g. two-stage turbocharging or an electrically assisted turbocharger) or a different intake air boosting strategy such as a supercharger would be

required to handle combustion mode transition to meet the drive cycle load requirement while keeping the emissions low.

10. Combustion mode transition needs to be coupled with a similar combustion phasing transition strategy (from a near-TDC combustion phasing for high combustion efficiency in high-EGR LTC operation to a retarded combustion phasing for low NO_X emissions in conventional diesel operation) to achieve the desired engine performance and emissions. Accordingly, the fuel injection timing and injection pressure need to be adjusted during the transient.
11. Split fuel injection strategy with optimized fuel injection timing, fuel split ratio and injection pressure with a marginally increased intake pressure was effective in meeting the drive cycle load requirement with acceptable smoke, THC, CO and NO_X emissions in the intermediate cycles during a combustion mode transition. Split fuel injection with equal fraction of fuel during the two injection events was effective in reducing smoke emissions from the intermediate cycles during combustion mode transition, although it increased THC emissions and GISFC. Reducing the fraction of fuel during the 1st injection event increased smoke emissions marginally and increased GIMEP to meet the drive cycle load requirement.

(d) MBT injection timing

12. Partial combustion by-product emissions and gross ISFC reduced at a fixed intake pressure with the MBT injection timing strategy where the start of fuel injection timing was advanced to achieve maximum GIMEP without exceeding the 1 MPa/^{o}CA rate of pressure rise limit. With the MBT injection strategy, increased intake pressure reduced smoke emissions and shifted the peak smoke emissions towards lower intake oxygen mass fractions.
13. Combustion stability was dependent on fuel injection timing and combustion phasing. While constant CA50 combustion phasing led to increasing levels of variability and high THC emissions at low intake oxygen mass fraction, MBT phasing strategy resulted in stabilized combustion and low THC emissions. Boost pressure in high-EGR LTC operation did not significantly influence combustion stability.

8.3 Implications for Engine Systems

The novel contributions outlined in the previous section have significant value for optimizing engines using high levels of EGR. The results provide considerable guidance for LTC specific engine development. Through this understanding of the advanced combustion strategy, an improved combustion model can be developed which can be validated with the majority of experimental combustion data (both thermodynamic and optical) generated in this work. The following are the main implications for the engine systems operating in 'LTC-conventional diesel dual-mode' strategies.

1) Air handling system architecture:

The gas exchange process needs to be controlled to meet the requirement of an LTC-conventional diesel combustion 'dual mode' engine. To maintain driveability, advanced turbocharger technology (e.g. two-stage turbocharging or an electrically assisted turbocharger) or a different intake air boosting strategy such as a supercharger would be required; resizing of the VGT may also be necessary within the scope of maintaining full load performance. Better EGR control will also be a key to improving engine performance and emissions both during steady-state and transient operation. The number cycles that experience the intermediate EGR levels need to be kept to a minimum to reduce smoke emissions during a combustion mode transition.

2) Engine control strategies:

Split injection can help to control emissions during combustion mode transitions especially when used in combination with CA50 phasing control. MBT injection timing and close to TDC combustion phasing control are critical under both steady-state and transient LTC conditions to reduce emissions and improve fuel economy.

3) Exhaust after-treatment implications:

LTC will still require a DPF, both for PN control and to prevent visible smoke emissions during combustion mode transitions and during high load operation. As a result, the focus should be on savings elsewhere—the most obvious place is avoiding or reducing an SCR/LNT requirement. However, reduced soot emissions in LTC may require either a less expensive passive regeneration type DPF or active regeneration is likely to be significantly less frequent. High THC and CO emissions during steady-state LTC operation and during combustion mode transition would require the development of a DOC after-treatment system suitable in the low temperature and low oxygen concentration exhaust gas environment to reduce these emissions further to meet the legislated limits. Note that after-treatment implication has not been investigated in this research and this is an area for future work.

4) Engine thermal management:

High EGR requirement for LTC means that more heat needs to be rejected into the EGR cooler. However, it is expected that reduced exhaust temperatures may partially offset the high EGR rates and the heat rejection to the EGR coolant unit would be similar to the low EGR rates in conventional diesel operation that can be handled relatively easily. Reduced flame temperatures due to high-EGR LTC operation would also reduce the heat transfer losses from the engine that will reduce the load on the engine coolant circuit.

5) Reliability/wear implications:

Getting the correct EGR rate would be the key challenge in the 'LTC-conventional diesel dual-mode' engine. EGR strategy, such as employing a high pressure or low pressure EGR loop would also influence the EGR rates (due to the response time scale of the EGR system) especially during transient operation. With a high pressure EGR loop, very sooty combustion during frequent transient operation is likely to foul the EGR circuit, the turbine, fuel injector, combustion chamber and other engine components and systems. Lubricating oil dilution with fuel due to the advanced injection timings and due to high levels of EGR (containing soot up to varying degree depending on engine operation) may also adversely affect the reliability of the system and would increase engine wear.

6) Transient control:

The number of cycles that experience the intermediate EGR levels need to be kept to a minimum to reduce smoke emissions during a combustion mode transition. An improved air handling system, as discussed above, would also be required to maintain driveability while keeping emissions to a minimum level. High-EGR LTC operation during engine cold start seems to be challenging because of engine misfiring and unstable operation due to low coolant temperature during a driving cycle test (e.g., up to 270 s in an NEDC driving cycle, the coolant temperature was less than 50^{o}C). Therefore, some provision needs to be made to increase the coolant temperature quickly to a desired steady-state value so that the stable LTC strategy can be implemented much earlier in the driving cycle.

7) Noise, vibration and harshness (NVH):

The rate of pressure rise in single injection high-EGR LTC strategy is generally low, which is good from the combustion noise and vehicle NVH point of view. However, combustion noise may be an issue with the split injection strategy at reduced EGR levels unless the injection timings are optimized. It is expected that combustion noise and NVH may increase during combustion mode transitions with the MBT injection timing strategy due to minor variations of EGR rates, injection pressure and boost pressure.

Finally, it should be noted that the base engine architecture needs to be retained as full load operation will still require transition to conventional diesel operation.

8.4 Suggested Future Work

The results from the studies discussed in the previous sections provide insight into some of the aspects of high-EGR LTC operation in a diesel engine. They also provide guidance for what aspects

of future research might be pursued to achieve further reduction in emissions and improvement in efficiency and combustion stability.

The split fuel injection strategy, although it reduced the EGR requirement, generated a high rate of pressure rise during combustion that needs to be controlled to achieve acceptable engine noise level. Also, the advanced combustion phasing (before TDC) with the split injection strategy increased compression work in certain cases and reduced GIMEP despite high combustion efficiency. Therefore, the future work should aim at using more than two fuel injection events per cycle with optimized fuel split fractions during each fuel injection event to reduce combustion noise and to keep the CA50 close to TDC.

The current work suggests that improving the late cycle combustion process may achieve significant reduction in emissions. As mentioned earlier in this work, the high-EGR LTC strategy was investigated in a piston bowl optimized for conventional diesel operation. Given the differences in the fuel injection strategy and the combustion processes, it is likely that the current piston geometry is suboptimal for high-EGR LTC operation. Therefore, substantial performance improvement can be achieved by optimized combustion chamber geometry, although addressing this issue requires careful planning and a substantial modelling approach. In addition, advanced fuel injection strategy (multiple injections and injection rate shaping) and enhanced air motion (with swirl control) need to be investigated with the optimized combustion chamber geometry. Optimization of injector geometry (for example, number of holes, hole size and injection angle) in conjunction with the injection process and combustion chamber geometry are required to provide the best possible combustion system. The interrelatedness of different variables underlines the complexity of the optimization process. However, all these changes need to be considered in the context of not compromising conventional diesel combustion at high loads with the combustion chamber geometry, fuel injection system and swirl ratio optimized for LTC operation.

Cycle resolved or crank angle resolved measurements of THC and CO emissions can help identify the sources and mechanism of these emissions further. Identifying cycle resolved speciated hydrocarbon emissions would assist in quantifying the effects of bulk quenching resulting in partially oxidized combustion products, i.e., volatile lower hydrocarbons (mostly C_1-C_3) and over-mixing resulting in semi-volatile higher hydrocarbons, i.e., unburned fuel (mostly C_{10}-C_{12}) [Han *et al*., 2009; Ogawa and Li, 2010]. Determination of the temporal and spatial distribution of intermediate radicals through optical spectroscopy would improve the understanding of the combustion and emission processes. Understanding the composition and morphology of the emitted particles and the speciated hydrocarbons at different operating conditions would be useful for future after-treatment system development and optimization.

High-EGR LTC operation in this work was investigated with an automotive grade diesel fuel. However, there is a requirement for further research into the effects of alternative fuels (both

oxygenated and non-oxygenated) in high-EGR LTC operation which will then enable the evaluation of the effects of the fuel's ignition quality and composition on combustion and emission processes.

The energy release rate database generated in this work can be used to refine the present engine transient model so that cycle-by-cycle operating conditions can be predicted more accurately. With the accurate prediction of the cycle-by-cycle intake oxygen concentration, cylinder pressure based combustion control strategy (either experimental or model-based) may be evaluated to control the transients.

Frequent combustion mode transitions (to and from LTC) would be required to meet the load demands in real-world driving conditions. Given the difficulty of controlling engine performance and emissions during a combustion mode transition, it follows that extension of the present LTC load limit is likely to be critical to the success of this potentially valuable ultra-low NO_X combustion technology. Extending the LTC load limit can be achieved either by increasing the boost pressure as demonstrated in this work in Chapter 5 or by reducing the EGR requirement to achieve LTC. It is suggested that further research into reducing the EGR requirement for LTC operation can be explored by either reducing the geometric compression ratio of the engine or by varying the effective compression ratio using variable valve timings (VVT). VVT technology would also allow the engine to control in-cylinder conditions such as air motion, pressure and temperature [Tomoda *et al*., 2010]. Early inlet valve closure timing can result in increased effective compression ratio (or in other words retaining the geometric compression ratio), which can be used in the high-EGR LTC strategy at low load to reduce THC emissions and improve fuel economy. Late inlet valve closure (LIVC) timing at medium and high loads can reduce the effective compression ratio to reduce the end-of-compression temperature and correspondingly reduce the EGR requirement for low NO_X (by reducing combustion temperature) and PM (by increasing the ignition delay due to reduced compression temperature) emissions. A VVT system can also increase the work extracted during the expansion stroke selecting a suitable exhaust valve opening time (i.e., increased expansion ratio). Reduced effective compression ratio and enhanced expansion ratio, possible with the VVT technique along with high boost pressure, could lead to the possibility of the engine operating in a Miller cycle. With optimized EGR levels, simultaneous reductions in PM and NO_X emissions can be achieved with high fuel efficiency with acceptable THC and CO emissions. This combination would also enable extending the LTC load limit.

8.5 Closing Comments

To realize a driver-friendly and emissions compliant light-duty automotive diesel engine operating on LTC will require substantial development and calibration work by engine manufacturers. The application of new technologies, as discussed in the preceding paragraphs, will aid to extend the range of LTC operation to higher loads while reducing the loads on engine subsystems, thereby improving performance and reliability. These strategies are underpinned by the

concepts and fundamental understanding presented in this thesis. For example, the importance of ensuring sufficient oxygen is present to oxidize PM formed even in LTC, potentially through increased boost, especially over transient operating conditions, could increase driver satisfaction by reducing fuel-air limits, thereby improving transient response. Controlling the combustion phasing during combustion mode transitions to and from LTC, in conjunction with boost pressure and injection pressure and timing controls, could minimize combustion by-product emissions while also limiting NO_X, potentially resulting in reduced after-treatment requirements and improved fuel economy. Finally, increased use of split injections, carefully tailored to the specific operating condition through the use of adaptive engine controllers, would enable optimized transient response for a given air- and EGR-system condition, maximizing engine performance. Taken together, these concepts can be used to help guide engine developers in applying this low-emission (in terms of NO_X and PM), high-efficiency (similar to conventional diesel operation) combustion strategy to commercially-viable light-duty diesel engines.

REFERENCES

ACEA, The Automobile Industry Pocket Guide, 2011. European Automobile Manufacturers Association.
Available:http://www.acea.be/images/uploads/files/20110921_Pocket_Guide_3rd_edition.pdf
[Accessed: 9th February 2012].

ACEA, Tax Guide 2012. European Automobile Manufacturers Association.
Available: http://www.acea.be/images/uploads/files/20120329_TaxGuide2012Highlights.pdf
[Accessed: 23rd April 2012].

Akihama, K., Takatori, Y., Inagaki, K., Sasaki, S., and Dean, A.M., 2001, "Mechanism of the smokeless rich diesel combustion by reducing temperature", SAE Paper No. 2001-01-0655.

Alam, M., Song, J., and Boehman, A., 2006, "Spray and combustion visualization of a direct-injection diesel engine operated with oxygenated fuel blends", International Journal of Engine Research, vol. 7, pp. 503-521.

Andre, M., 2004, "The ARTEMIS European driving cycles for measuring car pollutant emissions", Science of the Total Environment, 334-335, pp. 73-84.

Anselmi, P., Kashdan, J., Bression, G., Ferrero-Lesur, E., Thirouard, B. and Walter, B., 2010, "Improving Emissions, Noise and Fuel Economy Trade-off by Using Multiple Injection Strategies in Diesel Low Temperature Combustion (LTC) mode", SAE Paper No. 2010-01-2162.

Arcoumanis, C., Bae, C., Nagwaney, A., and Whitelaw, J.H., 1995, "Effect of EGR on combustion development in a 1.9L DI diesel optical engine", SAE Paper No. 950850, pp 169-193.

Arnold, S., 2004, "Turbocharging technologies to meet critical performance demands of ultra-low emissions diesel engines", SAE Paper No. 2004-01-1359.

Asad, U., Zheng, M., Han, X., Reader, G.T., and Wang, M., 2008, "Fuel injection strategies to improve emissions and efficiency of high compression ratio diesel engines", SAE International Journal of Engines, vol. 1, issue 2, pp. 1220-1233.

Asad, U. and Zheng, M., 2009, "Efficacy of EGR and boost in single-injection enabled low temperature combustion", SAE Paper No. 2009-01-1126.

AVL Smoke Value Measurement with the Filter Paper Method, Application Notes, June 2005, AT1007E, Rev. 02.

AVL Report Cylinder Head with Endoscopic Access for Single Cylinder Research Engine No. 5402.055, Revision number 01, September 2009 Edition.

Ayala, A., Brauer, M., Mauderly, J.L., and Samet, J.M., 2011, "Air pollutants and sources associated with health effects", Air Quality, Atmosphere & Health, DOI: 10.1007/s11869-011-0155-2.

Bakenhus, M. and Reitz, R.D., 1999, "Two-colour combustion visualization of single and split injections in a single-cylinder heavy-duty D.I. diesel engine using an endoscope-based imaging system", SAE Paper No. 1999-01-1112.

Barber, C.R., 1946, "Factors affecting the reproducibility of brightness of tungsten strip lamps for pyrometer standardization", J. Sci. Instrum., vol. 23, pp. 238-242.

Benajes, J., Lujan, J.M., Bermudez, V., and Serrano, J.R., 2002, “Modelling of turbocharged diesel engines in transient operation. Part 1: insight into the relevant physical phenomena”, Proceedings of IMechE, Part D: Journal of Automobile Engineering, vol. 216, pp. 431-441.

Benajes, J., Molina, S., and Riesco, J.M., 2004, “The effect of swirl on combustion and exhaust emissions in heavy-duty diesel engines”, Proceedings of IMechE, Part D, Journal of Automobile Engineering, vol. 218, pp. 1141-1148.

Benajes, J., Molina, S., Novella, R., and DeRudder, K., 2008, “Influence of injection conditions and exhaust gas recirculation in a high-speed direct-injection diesel engine operating with a late split injection”, Proceedings of IMechE, Part D, Journal of Automobile Engineering, vol. 222, pp. 629-641.

Benajes, J., Novella, R., Garcia, A., and Artozoul, S., 2009, “Partially premixed combustion in a diesel engine induced by a pilot injection at the low-pressure top dead center”, Energy & Fuels, vol. 23, pp. 2891-2902.

Benajes, J., Molina, S., Novella, R., and Amorim, R., 2010, “Study on low temperature combustion for light-duty diesel engines”, Energy & Fuels, vol. 24, no.1, pp. 355-364.

Bittle, J.A., Knight, B.M., and Jacobs, T.J., 2011, “Two-stage ignition as an indicator of low-temperature diesel combustion”, Combustion Science and Technology, vol. 183, issue 9, pp. 947-966.

Bobba, M., Musculus, M., and Neel, W., 2010, “Effect of post injections on in-cylinder and exhaust soot for low-temperature combustion in a heavy-duty diesel engine”, SAE Paper No. 2010-01-0612.

Bobba, M.K. and Musculus, M.P.B., 2012, “Laser diagnostics of soot precursors in a heavy-duty diesel engine at low-temperature combustion conditions”, Combustion and Flame, vol. 159, pp. 832-843.

Bowman, C.T., 1975, "Kinetics of pollutant formation and destruction in combustion”, Progress in Energy and Combustion Science, vol. 1, no. 1, pp. 33-45.

Brogan, M.S., Clark, A.D., and Brisley, R.J., 1998, "Recent progress in NO_X trap technology”, SAE Paper No. 980933.

Burton, J.L., Williams, D.R., Glewen, W.J., Andrie, M.J., Krieger, R.B., and Foster, D.E., 2009, “Investigation of transient emissions and mixed mode combustion for a light duty diesel engine”, SAE Paper No. 2009-01-1347.

California Air Resources Board, ARB Almanac 2003—Chapter 5: Toxic Air Containment Emissions, Air Quality, and Health Risk. Available: http://www.arb.ca.gov/aqd/almanac/almanac03/pdf/chap503.pdf [Accessed: 4th April 2012].

Cezairliyan, A., and Righini, F., 1996, “Issues in high-speed pyrometry”, Metrologia, vol. 33, pp. 299-306.

Chan, S.H., He, Y., and Sun, J.H., 1999, "Prediction of transient nitric oxide in diesel exhaust”, Proceedings of the Institution of Mechanical Engineers, Part D, Journal of Automobile Engineering, vol. 213, no. 4, pp. 327-339.

Charlton, S.J., 2005, “Developing diesel engines to meet ultra-low emission standards”, SAE Paper No. 2005-01-3628.

Charmley, W.J., 2004, “The federal government’s role in reducing heavy duty diesel emissions”, SAE Paper No. 2004-01-2708.

Chatterjee, S., Walker, A.P., and Blakeman, P.G., 2008, "Emission control option to achieve Euro IV and Euro V on heavy duty diesel engines”, SAE Paper No. 2008-28-0021.

Chen, S.K., 2000, "Simultaneous reduction of NO_X and particulate emissions by using multiple injections in a small diesel engine”, SAE Paper No. 2000-01-3084.

Chiara, F. and Canova, M., 2009, “Mixed-mode homogeneous charge compression ignition-direct injection combustion on common rail diesel engines: an experimental characterization”, International Journal of Engine Research, vol. 10, pp. 81-96.

Christensen, M., Johansson, B., and Einewall, P., 1997, "Homogeneous charge compression ignition (HCCI) using isooctane, ethanol and natural gas- a comparison with spark ignition operation”, SAE Paper No. 972874.

Christensen, M., Johansson, B., Amneus, P., and Mauss, F., 1998, "Supercharged homogeneous charge compression ignition”, SAE Paper No. 980787.

Colban, W.F., Miles, P.C., and Oh, S., 2007, "Effect of intake pressure on performance and emissions in an automotive diesel engine operating in low temperature combustion regimes”, SAE Paper No. 2007-01-4063.

Cong, S., McTaggart-Cowan, G.P., and Garner, C.P., 2009a, "Measurement of residual gas fraction in a single cylinder HSDI diesel engine through skip-firing", SAE Paper No. 2009-01-1961.

Cong, S., McTaggart-Cowan, G.P., and Garner, C.P., 2009b, "The effects of exhaust back pressure on conventional and low temperature diesel combustion", IMechE, Internal Combustion Engines: Performance, Fuel Economy and Emissions Conference, London, December 2009.

Cong, S., McTaggart-Cowan, G.P. and Garner, C.P., 2010, "Effects of fuel injection parameters on low temperature diesel combustion stability", SAE Paper No. 2010-01-0611.

Cong, S., 2011, “An Experimental Study of Low Temperature Combustion in a Diesel Engine”, PhD Thesis, Loughborough University, Loughborough, UK.

Cong, S., Garner, C.P. and McTaggart-Cowan, G.P., 2011a, "The effects of exhaust back pressure on conventional and low temperature diesel combustion", Proceedings of IMechE, Part D, Journal of Automobile Engineering, vol. 225, pp. 222-235.

Cong, S., McTaggart-Cowan, G.P., Garner, C.P., Wahab, E., and Peckham, M., 2011b, “Experimental investigation of low temperature diesel combustion processes”, Combustion Science and Technology, vol. 183, no. 12, pp. 1376-1400.

Dec, J.E., 1997, "A Conceptual model of DI diesel combustion based on laser-sheet imaging”, SAE Paper No. 970873.

Dec, J.E. and Kelly-Zion, P.L., 2000, "The effects of injection timing and diluent addition on late-combustion soot burnout in a DI diesel engine based on simultaneous 2-D imaging of OH and soot”, SAE Paper No. 2000-01-0238.

Dec, J.E., 2009, "Advanced compression-ignition engines—understanding the in-cylinder processes”, Proceedings of the Combustion Institute, vol. 32, no. 2, pp. 2727-2742.

Dent, J.C., 1971, “Basis for the comparison of various experimental methods studying spray penetration”, SAE Paper No. 710571.

Desantes, J.M., Lopez, J.J., Redon, P., and Arregle, J., 2012, “Evaluation of the thermal NO formation mechanism under low temperature diesel combustion conditions”, International Journal of Engine Research”, published online February 2012, DOI: 10.1177/1468087411429638.

Dieselnet: Emission Standards. Available: www.dieselnet.com/standards/ [Accessed: 07th February 2009].

Dieselnet: Emission Test Cycles.
Available: http://www.dieselnet.com/standards/cycles/ece_eudc.php [Accessed: 23rd January 2012].

Diez, A. and Zhao, H., 2010, “Effect of the dwell angle of split injection in a single-cylinder optical diesel engine”, Proceedings of IMechE, Part D: Journal of Automobile Engineering, vol. 224, pp. 815-828.

DMS500 Fast Particulate Spectrometer User Manual, Version 3.1, Cambustion, 2010.

Dockery, D.W., Pope III, C.A., Xu, X., Spengler, J.D., Ware, J.H., Fay, M.E., Ferris Jr, B.G., and Speizer, F.E., 1993, “An association between air pollution and mortality in six US cities”, The New England Journal of Medicine, vol. 329, no. 24, pp. 1753-1759.

Dolak, J. and Reitz, R.D., 2010, “Optimization of the piston geometry of a diesel engine using a two-spray-angle nozzle”, Proceedings of IMechE, Part D, Journal of Automobile Engineering, vol. 225, pp. 406-421.

Easley, W.L. and Mellor, A.M., 1999, "NO decomposition in diesel engines”, SAE Paper No. 1999-01-3546.

Environmental Protection Agency, Control of Emissions of Hazardous Air Pollutants from Mobile Sources, 48058 Federal Register, vol.65, no. 151, August 2000/Proposed Rules.

Environmental Protection Agency, Health Assessment Document for Diesel Engine Exhaust, 56290 Federal Register, vol. 67, no. 170, September 2002/Notices.

Environmental Protection Agency, Air Quality, Health, and Welfare Effects, Chapter 2, Report 420-R-04-007, May 2004.

Environmental Protection Agency, Draft U.S. Greenhouse Gas Inventory Report, 2012. Available from: http://www.epa.gov/climatechange/emissions/usinventoryreport.html [Accessed: 4th April 2012].

European Commission, Brussels, 10.3.2004, COM(2004) 160 final, Report from the Commission to the European Parliament and the Council concerning existing Community measures relating to sources of environmental noise, pursuant to article 10.1 of Directive 2002/49/EC relating to the assessment and management of environmental noise, The Commission of the European Communities.

European Commission, 2008, Commission Regulation (EC) No 692/2008, Implementing and Amending Regulation (EC) No 715/2007 of the European Parliament and of the Council on type-Approval of Motor Vehicles with respect to Emissions from Light Passenger and Commercial Vehicles (Euro 5 and Euro 6) and on Access to Vehicle Repair and Maintenance Information, The Commission of the European Communities.

European Commission 2009, Regulation (EC) No. 443/2009 of the European Parliament and of the Council of 23 April 2009, Official Journal of the European Union.

European Commission, 2011, Commission Regulation (EU) No 582/2011 of 25 May 2011 implementing and amending Regulation (EC) No 595/2009 of the European Parliament and of the Council with respect to emissions from heavy duty vehicles (Euro VI) and amending Annexes I and III to Directive 2007/46/EC of the European Parliament and of the Council, Official Journal of the European Union.

Fang, T., Coverdill, R.E., Lee, C.F., and White, R.A., 2008, "Effects of injection angles on combustion processes using multiple injection strategies in an HSDI diesel engine", Fuel, vol. 87, pp. 3232-3239.

Ferguson, C.R., 1986, "*Internal Combustion Engines, Applied Thermosciences*", John Wiley & Sons, Inc., USA.

Flynn, P.F., Hunter, G.L., Farrell, L., Durrett, R.P., Akinyemi, O., Zur Loye, A.O., Westbrook, C.K., and Pitz, W.J., 2000, "The inevitability of engine-out NO_X emissions from spark-ignited and diesel engines", Proceedings of the Combustion Institute, vol. 28, pp. 1211-1218.

Gaydon, A.G., 1974, "*The Spectroscopy of Flames*", Chapman and Hall Ltd, London.

Glarborg, P., Miller, J.A., and Kee, R.J., 1986, "Kinetic modeling and sensitivity analysis of nitrogen oxide formation in well-stirred reactors", Combustion and Flame, vol. 65, no. 2, pp. 177-202.

Glassman, I., 1989, "Soot formation in combustion processes", Symposium (International) on Combustion, vol. 22, no. 1, pp. 295-311.

Glassman, I., 1996, "*Combustion*", 3rd Edition, Academic Press, USA.

Hagena, J.R., Filipi, Z.S., and Assanis, N., 2006, "Transient diesel emissions: analysis of engine operation during a tip-in", SAE Paper No. 2006-01-1151.

Hagena, J.R., Assanis, D.N., and Filipi, Z.S., 2011, "Cycle-resolved measurements of in-cylinder constituents during diesel engine transients and insight into their impact on emissions", Proceedings of IMechE, Part D, Journal of Automobile Engineering, vol. 225, pp. 1103-1117.

Hamamatsu Photonics, 2006, "*Photomultiplier Tubes, Basics and Applications*", 3rd Edition, Hamamatsu.

Hamamatsu Photosensor Modules H5784 Series Instruction Manual, Hamamatsu, vol. 2E, May 2007.

Han, Y., Kim, K., and Lee, K., 2008, "The investigation of soot and temperature distributions in a visualized direct injection diesel engine using laser diagnostics", Measurement Science and Technology, vol. 19, no. 11, pp. 1-11.

Han, M., Assanis, D.N., and Bohac, S.V., 2009, "Sources of hydrocarbon emissions from low-temperature premixed compression ignition combustion from a common rail direct injection diesel engine", Combustion Science and Technology, vol. 181, pp. 496-517.

He, X., Durrett, R.P., and Sun, Z., 2008, "Late intake valve closing as an emissions control strategy at Tier 2 Bin 5 engine-out NO_X level", SAE Paper No. 2008-01-0637.

Helmantel, A., 2008, "Reduction of NO_X emissions from a light duty DI diesel engine in medium load conditions with high EGR rates", SAE Paper No. 2008-01-0643.

Henein, N.A., Kastury, A., Natti, K., and Bryzik, W., 2008, "Advanced low temperature combustion (ALTC): diesel engine performance, fuel economy and emissions", SAE Paper No. 2008-01-0652.

Heywood, J.B., 1988, "*Internal Combustion Engines Fundamentals"*, McGraw Hill Book Company, Singapore.

Hiroyasu, H., and Arai, M., 1990, "Structures of fuel sprays in diesel engines", SAE Paper No. 900475.

Holman, J.P., 2001, "*Experimental Methods for Engineers"*, 7th edn, McGraw-Hill Book Company, USA.

Horiba Instruction Manual MEXA-7000, 2001.

Horibe, N., Harada, S., Ishiyama, T., and Shioji, M., 2009, "Improvement in premixed charge compression ignition-based combustion by two-stage injection", International Journal of Engine Research, vol. 10, no. 2, pp. 71-80.

Hottel, H.C. and Broughton, F.P., 1932, "Determination of true temperature and total radiation from luminous gas flames", Industrial and Engineering Chemistry Analytical Edition, vol. 4, no. 2, pp. 166-175.

Hwang, W., Dec, J.E., and Sjoberg, M., 2008, "Spectroscopic and chemical-kinetic analysis of the phases of HCCI autoignition and combustion for single-and two-stage ignition fuels", Combustion and Flame, vol. 154, pp. 387-409.

Idicheria, A. and Pickett, L.M., 2005, "Soot formation in diesel combustion under high-EGR conditions", SAE Paper No. 2005-01-3834.

Iwabuchi, Y., Kawai, K., Shoji, T., and Takeda, Y., 1999, "Trial of new concept diesel combustion system-premixed compression-ignited combustion", SAE Paper No. 1999-01-0185.

Jacobs, T.J., Bohac, S.V., Assanis, D.N., and Szymkowicz, P.G., 2005, "Lean and rich premixed compression ignition combustion in a light-duty diesel engine", SAE Paper No. 2005-01-0166.

Johnson, T.V., 2006, "Diesel emission control in review", SAE Paper No. 2006-01-0030.

Johnson, T.V., 2009, "Review of diesel emissions and control", International Journal of Engine Research, vol. 10, pp. 275-285.

Johnson, T.V., 2010, "Review of diesel emissions and control", SAE Paper No. 2010-01-0301.

Johnson, T.V., 2011, "Diesel emissions in review", SAE Paper No. 2011-01-0304.

Johnson, T.V., 2012, "Vehicular emissions in review", SAE Paper No. 2012-01-0368, SAE International Journal of Engines, vol. 5, issue 2, pp. 216-234.

Jones, T.P., 1962, "The suitability of tungsten strip lamps as secondary standard sources in photoelectric pyrometry", Journal of Scientific Instruments, vol. 40, no. 3, pp. 101-104.

Kamimoto, T. and Bae, M., 1988, "High combustion temperature for the reduction of particulate in diesel engines", SAE Paper No. 880423.

Kamimoto, T. and Kosaka, H., 2000, “Laser diagnostics of diesel engines”, Presented in Thermo and Fluid-dynamic Processes in Diesel Engines Conference, Spain, September 2000.

Kamimoto, T. and Murayama, Y., 2011, “Re-examination of the emissivity of diesel flames”, International Journal of Engine Research, vol. 12, pp. 580-600.

Kanda, T., Hakozaki, T., Uchimoto, T., Hatano, J., Kitayama, N., and Sono, H., 2005, “PCCI operation with early injection of conventional diesel fuel”, SAE Paper No. 2005-01-0378.

Kang, H. and Farrell, P.V., 2005, “Experimental investigation of transient emissions (HC and NO_X) in a high speed direct injection (HSDI) diesel engine”, SAE Paper No. 2005-01-3883.

Kashdan, J.T., Anselmi, P., and Walter, B., 2009, “Advanced Injection Strategies for Controlling Low-Temperature Diesel Combustion and Emissions”, SAE Paper No. 2009-01-1962.

Khair, M.K., 2003, “A review of diesel particulate filter technologies”, SAE Paper No. 2003-01-2303.

Khalek, I.A., Kittelson, D.B., and Brear, F., 2000, “Nanoparticle growth during dilution and cooling of diesel exhaust: experimental investigation and theoretical assessment”, SAE Paper No. 2000-01-0515.

Kim, D., Ekoto, I., Colban, W.F., and Miles, P.C., 2008, "In-cylinder CO and UHC imaging in a light-duty diesel engine during PPCI low-temperature combustion”, SAE Paper No. 2008-01-1602.

Kim, K., Han, S., and Bae, C., 2011, “Mode transition between low temperature combustion and conventional combustion with EGR and injection modulation in a diesel engine”, SAE Paper No. 2011-01-1389.

Kimura, S., Aoki, O., Ogawa, H., Muranaka, S., and Enomoto, Y., 1999, "New combustion concept for ultra-clean and high-efficiency small DI diesel engines”, SAE Paper No. 1999-01-3681.

Kimura, S., Aoki, O., Kitahara, Y., and Aiyoshizawa, E., 2001, "Ultra clean combustion technology combining a low temperature and premixed combustion for meeting future emissions standards”, SAE Paper No. 2001-01-0200.

Kimura, S., Ogawa, H., Matsui, Y., and Enomoto, Y., 2002, "An experimental analysis of low-temperature and premixed combustion for simultaneous reduction of NO_X and particulate emissions in direct injection diesel engines”, International Journal of Engine Research, vol. 3, no. 4, pp. 249-259.

Kittelson, D.B., 1998, "Engines and nanoparticles: a review”, Journal of Aerosol Science, vol. 29, no. 5-6, pp. 575-588.

Klimstra, J., 1985, “The optimum combustion phasing angle – a convenient engine tuning criterion”, SAE Paper No. 852090.

Koci, C.P., Ra, Y., Kreiger, R., Andrie, M., Foster, D.E., Siewert, R.M., and Durrett, R.P., 2009, “Multiple-event fuel injection investigations in a highly-dilute diesel low temperature combustion regime”, SAE Paper No. 2009-01-0925.

Kokjohn, S.L., and Reitz, R.D., 2010, “Investigation of charge preparation strategies for controlled premixed charge compression ignition combustion using a variable pressure injection system”, International Journal of Engine Research, vol. 11, no. 4, pp. 257-282.

Kook, S., and Bae, C., 2004, “Combustion control using two-stage diesel fuel injection in a single-cylinder PCCI engine”, SAE Paper No. 2004-01-0938.

Kook, S., Bae, C., Miles, P.C., Choi, D., and Pickett, L.M., 2005, "The influence of charge dilution and injection timing on low-temperature diesel combustion and emissions”, SAE Paper No. 2005-01-3837.

Kook, S., Bae, C., Miles, P. C., Choi, D., Bergin, M., and Reitz, R. D., 2006, “Effect of swirl ratio and fuel injection parameters on CO emission and fuel conversion efficiency for high-dilution, low-temperature combustion in an automotive diesel engine”, SAE Paper No. 2006-01-0197.

Kuhnert, S., Wagner, U., Spicher, U., Haas, S., Gabel, K., and Kutschera, I., 2010, “Influence of injection nozzle hole diameter on highly premixed and low temperature diesel combustion and full load behavior”, SAE Paper No. 2010-01-2109.

Lachaux, T., Musculus, M.P.B., Singh, S., and Reitz, R.D., 2008, "Optical diagnostics of late-injection low-temperature combustion in a heavy-duty diesel engine”, Journal of Engineering for Gas Turbines and Power, vol. 130, no. 3, pp. 032808.

Ladommatos, N., Abdelhalim, S., and Zhao, H., 2000, "The effects of exhaust gas recirculation on diesel combustion and emissions”, International Journal of Engine Research, vol. 1, no. 1, pp. 107-126.

Lancaster, D.R., Krieger, R.B., and Lienesch, J.H., 1975, “Measurement and analysis of engine pressure data”, SAE Paper No. 750026.

Lavoie, G.A., Heywood, J.B., and Keck, J.C., 1970, “Experimental and theoretical investigation of nitric oxide formation in internal combustion engines”, Combustion Science and Technology, vol. 1, pp. 313-326.

Larrabee, R.D., 1959, “Spectral emissivity of tungsten”, Journal of the Optical Society of America, vol. 49, no. 6, pp. 619-625.

Lee, J-H and Lida, N., 2001, “Combustion of diesel spray injected into reacting atmosphere of propane-air homogeneous mixture”, International Journal of Engine Research, vol. 2, no. 1, pp. 69-80.

Leidenberger, U., Muhlbauer, W., Lorenz, S., Lehmann, S., and Bruggemann, D., 2012, “Experimental studies on the influence of diesel engine operating parameters on properties of emitted soot particles”, Combustion Science and Technology, vol. 184, no. 1, pp. 1-15.

Li, T., Suzuki, M., and Ogawa, H., 2009, “Characteristics of smokeless low temperature diesel combustion in various fuel-air mixing and expansion of operating load range”, SAE Paper No. 2009-01-1449.

Li, T., Suzuki, M., and Ogawa, H., 2010, “Effect of two-stage injection on unburned hydrocarbon and carbon monoxide emissions in smokeless low-temperature diesel combustion with ultra-high exhaust gas recirculation”, International Journal of Engine Research, vol. 11, no. 5, pp. 345-354.

Lida, N. and Igarashi, T. 2000, "Auto-ignition and combustion of n-Butane and DME/air mixtures in a homogeneous charge compression ignition engine”, SAE Paper No. 2000-01-1832.

Lu, G. and Yan, Y., 2006, “Temperature profiling of pulverized coal flames using multicolour pyrometric and digital imaging techniques”, IEEE Transactions on Instrumentation and Measurement, vol. 55, no. 4, pp. 1303-1308.

Lu, X., Han, D., and Huang, Z., 2011, “Fuel design and management for the control of advanced compression-ignition combustion modes”, Progress in Energy and Combustion Science, doi: 1016/j.pecs.2011.03.003.

Mancaruso, E., Merola, S.S., and Vaglieco, B.M., 2008, "Study of the multi-injection combustion process in a transparent direct injection common rail diesel engine by means of optical techniques”, International Journal of Engine Research, vol. 9, no. 6, pp. 483-498.

Mase, Y., Kawashima, J., Sato, T., and Eguchi, M., 1998, "Nissan’s new multivalve DI diesel engine series”, SAE Paper No. 981039.

Matsui, Y., Kamimoto, T., and Matsuoka, S., 1979, “A study on the time and space resolved measurement of flame temperature and soot concentration in a D.I. diesel engine by the two-colour method”, SAE Paper No. 790491, SAE Transactions, vol. 88, sec. 2, pp. 1808-1822.

Matsui, Y., Kamimoto, T., and Matsuoka, S., 1980, “A study on the application of the two-colour method to the measurement of flame temperature and soot concentration in diesel engines”, SAE Paper No. 800970, SAE Transactions, vol. 89, sec. 3, pp. 3043-3055.

McTaggart-Cowan, G.P., Bushe, W.K., Rogak, S.N., Hill, P.G., and Munshi, S.R., 2004, "The effects of varying EGR test conditions on a direct injection of natural gas heavy-duty engine with high EGR levels", SAE Paper No. 2004-01-2955.

Mendez, S., Kashdan, J. T., Bruneaux, G., Thirouard, B., and Vangraefschepe, F., 2009, “Formation of unburned hydrocarbons in low temperature diesel combustion”, SAE Paper No. 2009-01-2729.

Michailidis, A.D., Stobart, R.K., and McTaggart-Cowan, G.P., 2010, “Fuel-line stationary waves and variability in CI combustion during complex injection strategies”, Paper No. ICEF 2010-35069, Proceedings of the ASME 2010 Internal Combustion Engine Division Fall Technical Conference, San Antonio, Texas, September 2010.

Miller, J.A. and Bowman, C.T., 1989, "Mechanism and modeling of nitrogen chemistry in combustion”, Progress in Energy and Combustion Science, vol. 15, no. 4, pp. 287-338.

Moreira, A.L.N., Moita, A.S., and Panao, M.R., 2010, “Advances and challenges in explaining fuel spray impingement: how much of single droplet impact research is useful?”, Progress in Energy and Combustion Science, vol. 36, pp. 554-580.

Murata, Y., Kusaka, J., Odaka, M., Daisho, Y. Kawano, D., Suzuki, H., Ishil, H., and Goto, Y., 2007, “Emissions suppression mechanism of premixed diesel combustion with variable valve timing”, International Journal of Engine Research, vol. 8, no. 5, pp. 415-428.

Musculus, M.P.B., 2005, “Measurements of the influence of soot radiation on in-cylinder temperatures and exhaust NO_X in a heavy-duty DI diesel engine”, SAE Paper No. 2005-01-0925.

Musculus, M.P.B., 2006, “Multiple simultaneous optical diagnostic imaging of early-injection low-temperature combustion in a heavy-duty diesel engine”, SAE Paper No. 2006-01-0079.

Musculus, M.P.B., Lachaux, T., Pickett, L.M., and Idicheria, C.A., 2007, "End-of-injection over-mixing and unburned hydrocarbon emissions in low-temperature-combustion diesel engines”, SAE Paper No. 2007-01-0907.

Musculus, M.P.B., Singh, S., and Reitz, R.D., 2008, “Gradient effects on two-color soot optical pyrometry in a heavy-duty DI diesel engine”, Combustion and Flame, vol. 153, pp. 216-227.

Myung, C.L. and Park, S., 2012, “Exhaust nanoparticle emissions from internal combustion engines: a review”, International Journal of Automotive Technology, vol. 13, no. 1, pp. 9-22.

Naber, J.D. and Siebers, D.L., 1996, “Effects of gas density and vaporization on penetration and dispersion of diesel sprays”, SAE Paper No. 960034.

Naidja, A., Krishna, C.R., Butcher, T., and Mahajan, D., 2003, “Cool flame partial oxidation and its role in combustion and reforming of fuels for fuel cell systems”, Progress in Energy and Combustion Science, vol. 29, pp. 155-191.

Neely, G.D., Sasaki, S., Huang, Y., Leet, J.A., and Stewart, D.W., 2005, "New diesel emission control strategy to meet US Tier 2 emissions regulations”, SAE Paper No. 2005-01-1091.

Nishioka, M., Kondoh, Y., and Takeno, T., 1996, “Behavior of key reactions on NO formation in methane-air flames”, Twenty-Sixth Symposium (International) on Combustion, pp. 2139-2145.

Obert, E.F., 1970, “*Internal Combustion Engines and Air Pollution”*, 3rd edn, In Text Educational Publishers, New York.

Ogawa, H., Li, T., Miyamoto, N., Kido, S., and Shimizu, H., 2006, "Dependence of ultra-high EGR and low temperature diesel combustion on fuel injection conditions and compression ratio”, SAE Paper No. 2006-01-3386.

Ogawa, H., Li, T., and Miyamoto, N., 2007, "Characteristics of low temperature and low oxygen diesel combustion with ultra-high exhaust gas recirculation”, International Journal of Engine Research, vol. 8, no. 4, pp. 365-378.

Ogawa, H. and Li, T., 2010, “Volatile organic compounds in exhaust gas from diesel engines under various operating conditions”, International Journal of Engine Research, vol. 12, pp. 30-40.

Okude, K., Mori, K., Shiino, S., Yamada, K., and Matsumoto, Y., 2007, “Effects of multiple injections on diesel emission and combustion characteristics”, SAE Paper No. 2007-01-4178.

Onishi, S., Hong, J.S., Shoda, K., Pan, D.J., and Kato, S., 1979, "Active thermo-atmosphere combustion (ATAC)-a new combustion process for internal combustion engines”, SAE Paper No. 790501.

Pagan, J., 1999, “Study of particle size distributions emitted by a diesel engine”, SAE Paper No. 1999-01-1141.

Park, K., Cao, F., Kittelson, D.B., and McMurry, P.H., 2003, “Relationship between particle mass and mobility for diesel exhaust particles”, Environmental Science and Technology, vol. 37, no. 3, pp. 577-583.

Park, C., Kook, S., and Bae, C., 2004, "Effects of multiple injections in a HSDI diesel engine equipped with common rail injection system”, SAE Paper No. 2004-01-0127.

Pastor, J.V., Garcia, J.M., and Molina, S., 2000, "Analysis methodology of diesel flame by means of in-cylinder endoscopic imaging”, IEEE Xplore.

Payri, F., Pastor, J.V., Garcia, J.M., and Pastor, J.M., 2007, “Contribution to the application of two-colour imaging to diesel combustion”, Measurement Science and Technology, vol. 18, pp. 2579-2598.

Peckham, M.S., Campbell, B.W., and Finch, A., 2011, “Measurement of the effects of the exhaust gas recirculation delay on the nitrogen oxide emissions within a turbocharged passenger car diesel engine”, Proceedings of IMechE, Part D, Journal of Automobile Engineering, vol. 225, pp. 1156-1166.

Pelkmans, L. and Debal, P., 2006, "Comparison of on-road emissions with emissions measured on chassis dynamometer test cycles”, Transportation Research Part D, Transport and Environment, vol. 11, no. 4, pp. 233-241.

Pickett, L.M. and Siebers, D.L., 2004, "Soot in diesel fuel jets: effects of ambient temperature, ambient density, and injection pressure”, Combustion and Flame, vol. 138, pp. 114-135.

Pilling, M.J., 1997, “*Low-temperature combustion and auto-ignition*”, In Compton, R.G., and Hancock, G. (Eds.), *Comprehensive Chemical Kinetics*, Series, vol. 35, Elsevier, The Netherlands.

Plee, S.L., Ahmad, T., Myers, J.P., and Faeth, G.M., 1982, “Diesel NOx emissions-a simple correlation technique for intake air effects”, 19th International Symposium on Combustion, pp. 1495-1502.

Rakopoulos, C.D. and Giakoumis, E.G., 2006, “Review of thermodynamic simulations under transient operating conditions”, SAE Paper No. 2006-01-0884.

Rakopoloulos, C.D., Dimaratos, A.M., Giakoumis, E.G., and Peckham, M.S., 2010, “Experimental assessment of turbocharged diesel engine transient emissions during acceleration, load change and starting”, SAE Paper No. 2010-01-1287.

Reavell, K., Hands, T., and Collings, N., 2002, “A fast response particulate spectrometer for combustion aerosols”, SAE Paper No. 2002-01-2714.

Reitz, R.D., 1998, “Controlling D.I. diesel engine emissions using multiple injections and EGR”, Combustion Science and Technology, vol. 138, no. 1, pp. 257-278.

Rothamer, D.A., and Ghandhi, J.B., 2002, “On the calibration of single-shot planar laser imaging techniques in engines”, SAE Paper No. 2002-01-0748.

Sasaki, S., Ito, T., and Iguchi, S., 2000, “Smoke-less rich combustion by low temperature oxidation in diesel engines”, 9. Aachener Kolloquium Fahrzeug- und Motorentechnik, Aachen.

Sawyer, R.F., 2009, “Science based policy for addressing energy and environmental problems”, Proceedings of the Combustion Institute, vol. 32, pp. 45-56.

Schaberg, P.W., Priede, T., and Dutkiewicz, R.K., 1990, “Effects of a rapid pressure rise on engine vibration and noise”, SAE Paper No. 900013.

Senecal, P.K., Xin, J., and Reitz, R.D., 1996, “Predictions of residual gas fraction in IC engines”, SAE Paper No. 962052.

Shiozaki, T., Nakajima, H., Kudo, Y., Miyashita, A., and Aoyagi, Y., 1996, "The analysis of combustion flame under EGR conditions in a DI diesel engine”, SAE Paper No. 960323.

Siebers, D. and Higgins, B., 2001, "Flame lift-off on direct-injection diesel sprays under quiescent conditions”, SAE Paper No. 2001-01-0530.

Singh, S., Reitz, R.D., and Musculus, M.P.B., 2005, “2-color thermometry experiments and high-speed imaging of multi-mode diesel engine combustion”, SAE Paper No. 2005-01-3842.

Singh, S., Reitz, R.D., Musculus, M.P.B., and Lachaux, T., 2007, “Simultaneous optical diagnostic imaging of low-temperature, double-injection combustion in a heavy-duty DI diesel engine”, Combustion Science and Technology, vol. 179, no. 11, pp. 2381-2414.

Sjoberg, M. and Dec, J.E., 2007, “EGR and intake boost for managing HCCI low-temperature heat release over wide ranges of engine speed”, SAE Paper No. 2007-01-0051.

Smith, O.I., 1981, "Fundamentals of soot formation in flames with application to diesel engine particulate emissions”, Progress in Energy and Combustion Science, vol. 7, no. 4, pp. 275-291.

Stanglmaier, R.H. and Roberts, C.E., 1999, "Homogeneous charge compression ignition (HCCI): benefits, compromises and future engine applications”, SAE Paper No. 1999-01-3682.

Stasio, S., and Massoli, P., 1994, “Influence of the soot property uncertainties in temperature and volume-fraction measurements by two-colour pyrometry”, Measurement Science and Technology, vol. 5, pp. 1453-1465.

Stirling, P. H., and Ho, H., 1961, “Radiative pyrometry”, Industrial and Engineering Chemistry, vol. 53, no. 8, pp. 53A-55A.

Stone, R., 1999, “*Introduction to Internal Combustion Engines”*, 3rd edn, Macmillan, Basingstoke.

Svensson, K.I., Mackrory, A.J., Richards, M.J., and Tree, D.R., 2005, “Calibration of an RGB, CCD camera and interpretation of its two-colour images for KL and temperature”, SAE Paper No. 2005-01-0648.

Tanabe, K., Komatsu, F., and Nakayama, S., 2010, “A study on mode transition control between PCI and conventional combustion in a diesel engine”, International Journal of Engine Research, vol. 12, pp. 69-86.

Tanin, K.V., Wickman, D.D., Montgomery, D.T., Das, S., and Reitz, R.D., 1999, “The influence of boost pressure on emissions and fuel consumption of a heavy-duty single-cylinder D.I. diesel engine”, SAE Paper No. 1999-01-0840.

Taylor, A.M.K.P., 2008, “Science review of internal combustion engines”, Energy Policy, vol. 36, pp. 4657-4667.

Theinnoi, K., Sutshebo, S., Houel, V., Rajaram, R.R., and Tsolakis, A., 2008, “Hydrogen promotion of low-temperature passive hydrocarbon-selective catalytic reduction (SCR) over a silver catalyst”, Energy & Fuels, vol. 22, pp. 4109-4114.

Thring, R.H., 1989, “Homogeneous-charge compression-ignition (HCCI) engines”, SAE Paper No. 892068.

Tomoda, T., Ogawa, T., Ohki, H., Kogo, T., Nakatani, K., and Hashimoto, E., 2010, “Improvement of diesel engine performance by variable valve train system”, International Journal of Engine Research, vol. 11, pp. 331-343.

Total UK Ltd, Marketing Specifications, Issue 44, August 2008.

Tree, D.R. and Svensson, K.I., 2007, "Soot processes in compression ignition engines”, Progress in Energy and Combustion Science, vol. 33, no. 3, pp. 272-309.

Vattulainen, J., Nummela, V., Hernberg, R., and Kytola, J., 2000, "A system for quantitative imaging diagnostics and its application to pyrometric in-cylinder flame-temperature measurements in large diesel engines", Measurement Science and Technology, vol. 11, no. 2, pp. 103-119.

Virtanen, A., Ristimaki, J., Marjamaki, M., Vaaraslahti, Keskinen, J., and Lappi, M., 2002, "Effective density of diesel exhaust particles as a function of size", SAE Paper No. 2002-01-0056.

Warnatz, J., Maas, U., and Dibble, R.W., 2000, *Combustion Physical and Chemical Fundamentals, Modeling and Simulation, Experiments, Pollutant Formation*, 2nd edn, Springer Publication, Germany.

Watson, N. and Janota, M.S., 1982, "*Turbocharging the Internal Combustion Engine*", Chapter 12, The Macmillan Press Ltd, Hong Kong.

Werlberger, P., and Cartellieri, W.P., 1987, "Fuel injection and combustion phenomena in a high speed DI diesel engine observed by means of endoscopic high speed photography", SAE Paper No. 870097.

Westbrook, C.K., 2000, "Chemical kinetics of hydrocarbon ignition in practical combustion systems", Proceedings of the Combustion Institute, vol. 28, pp. 1563-1577.

Williams, A.M., Garner, C.P., Harry, J.E., Hoare, D.W., Mariotti, D., Ladha, K.S., Proctor, J.W., Yang, Y., and Binner, J.G.P., 2009, "Low power autoselective regeneration of monolithic wall flow diesel particulate filters", SAE Paper No. 2009-01-1927.

Winklhofer, E., 2001, "Optical access and diagnostic techniques for internal combustion engine development", Journal of Electronic Imaging, vol. 10 (3), pp. 588-592.

Yamada, H., Suzaki, K., Tezaki, A., and Goto, Y., 2008, "Transition from cool flame to thermal flame in compression ignition process", Combustion and Flame, vol. 154, pp. 248-258.

Yan, J. and Borman, G.L., 1988, "Analysis and in-cylinder measurement of particulate radiant emissions and temperature in a direct injection diesel engine", SAE Paper No. 881315.

Yanagihara, H., 2001, "Ignition timing control at Toyota "UNIBUS" combustion system", Proceedings of the IFP International Congress, pp. 35-42.

Yao, M., Zheng, Z., and Liu, H., 2009, "Progress and recent advances in homogeneous charge compression ignition (HCCI) engines", Progress in Energy and Combustion Science, vol. 35, pp. 398-437.

Yun, H. and Reitz, R.D., 2007, "An experimental investigation on the effect of post-injection strategies on combustion and emissions in the low-temperature diesel combustion regime", Journal of Engineering for Gas Turbines and Power, vol. 129, no. 1, pp. 279-286.

Zhao, H. and Ladommatos, N., 1998, "Optical diagnostics for soot and temperature measurement in diesel engines", Progress in Energy and Combustion Science, vol. 24, no. 3, pp. 221-255.

Zhao, H. and Ladommatos, N., 1999, "*Engine Combustion Instrumentation and Diagnostics"*, Society of Automotive Engineers Inc., USA.

Zheng, M., Reader, G.T., and Hawley, J.G., 2004, "Diesel engine exhaust gas recirculation—a review on advanced and novel concepts", Energy Conversion and Management, vol. 45, no. 6, pp. 883-900.

APPENDICES

Appendix A1

INSTRUMENTATION LIST

Table A1.1: List of Engine Instrumentation

Measuring Parameter	Manufacturer	Measuring Principle	Model	Range	Accuracy/ Sensitivity
Air flow	Elridge Products	Thermal flow	8712MPNH	0-90 kg/h	± 0.5% FS[†]
Fuel flow	AVL	Gravimetric	733	0-150 kg/h	0.12%
Crank angle	AVL	Optical shaft encoder	365C	360-7200 pulse/ rev	± 0.1^{o}CA
Intake and exhaust manifold pressures	Kistler	Piezo-resistive	4045A5	0-500 kPa (absolute)	Linearity: <0.3% FSO[*] Sensitivity: 1 mV/kPa
In-cylinder pressure	AVL	Piezo-electric	QC34C	0-25 MPa (gauge)	195 pC/MPa
Fuel rail pressure	AVL	Strain gauge	SL31D-2000	0-200 MPa (gauge)	4.5 ×10^{-3} mV/V×MPa
Inlet and exhaust pressures	Omega	Strain gauge	PXM219-006GI	0-600 kPa (gauge)	0.25% FS
Intake manifold temperature	Omega	RTD	PR-13	-200 to 500^{o}C	<± 1.3^{o}C
All other temperatures	Omega	K-type thermocouple	-	-200 to 1250^{o}C	± 0.75% of reading

[†] FS – Full scale [*] FSO – Full scale sensor output

Table A1.2: Specifications of the Emission Analysers

Measuring Parameter	Manufacturer	Measuring Principle	Model	Range	Accuracy/ Sensitivity
THC	Horiba Mexa 7100 HEGR	Hydrogen flame ionization detector (HFID)	FIA-725A	0-10~500; 0-1000 ~50000 ppm ['C_1']	10 ppm 'C_1' -
Exh. and Int. CO_2	Horiba Mexa 7100 HEGR	NDIR	AIA-722	0-0.5~20% by volume	0.5% by volume
CO	Horiba Mexa 7100 HEGR	NDIR	AIA-721A	0-50~5000 ppm	50 ppm
NO_X	Horiba Mexa 7100 HEGR	Chemiluminescent	CLA-720A	0-10~500; 1000-10000 ppm	10 ppm -
O_2	Horiba Mexa 7100 HEGR	Paramagnetic	MPA-720	0-1~25% by volume	1% by volume
CO (>5000 ppm)	Horiba Mexa 584L	NDIR	-	0-10% by volume	0.01% by volume
Smoke	AVL	Reflectivity	415	0-10 FSN	±3.5%
Particle size and number	Cambustion	Electrical mobility	DMS500 (M34)	5-1000 nm	-

Appendix A2
ESTIMATION OF UNCERTAINTY

All experimental results regardless of the care taken to obtain them possess errors, either random or systematic, and hence, are subjected to uncertainties. However, systematic errors can be corrected by calibration. The uncertainty in the results due to random errors is obtained statistically. Uncertainty of the measured parameter X is

$$\Delta X = \frac{1.96\sigma}{X_m} \times 100 \tag{A2.1}$$

where X_m is the mean value and σ is standard deviation of the measured quantities.

Total Uncertainty: The total uncertainty, *U*, is the sum of the uncertainties due to systematic error (B) and random error (ΔX).
U is given by:

$$U = \sqrt{(\Delta X)^2 + (B)^2} \tag{A2.2}$$

From the uncertainties of the measured parameters, the uncertainties in the calculated parameters are evaluated by using an expression, which is derived as follows [Holman, 2001].

While calculating the parameter R (x, y), which is a function of measured parameters x and y, and the uncertainties associated with x and y are Δx and Δy respectively, the uncertainty limit for the calculated parameter R will be R±ΔR. ΔR can be calculated using the following equation:

$$\frac{\Delta R}{R} = \sqrt{\left(\frac{\Delta x}{x}\frac{\partial R}{\partial x}\right)^2 + \left(\frac{\Delta y}{y}\frac{\partial R}{\partial y}\right)^2} \tag{A2.3}$$

REFERENCE

Holman, J.P., 2001, "*Experimental Methods for Engineers"*, 7th edn, McGraw-Hill Book Company, USA.

Appendix A3
BORESCOPE WORKING PRINCIPLE AND CONSTRUCTION

In a borescope, light is transmitted along a long tube, whose length is greater than its diameter. A modern rigid borescope consists of an objective lens (towards the object to be imaged in the object plane), a series of Hopkins rod lenses (long glass rods with curved ends called a relay system) separated by short air spaces and an eyepiece (towards the image plane). These image transmission systems are normally constructed of field lenses and image lenses set into the guide tube in alternating sequence as shown in Fig. A3.1. A pair of lenses forms a reversal system. A prism in front of the objective lens dictates the direction of view and field of view as well.

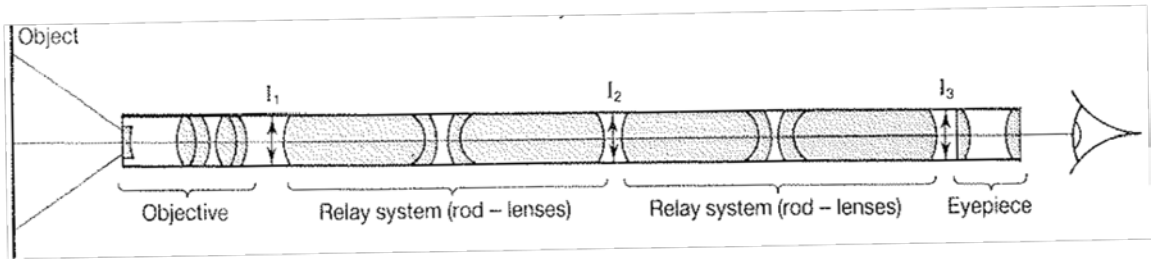

Fig. A3.1: Schematic of a rigid borescope [Heavens and Ditchburn, 1991]. Figure reprinted with permission from *Insight into Optics* © John Wiley & Sons.

The objective lens collects light from the object to be viewed and forms an intermediate image, I1. The light collected by the objective lens passes through the first reversal system on to another plane (I2) inside the borescope. Image I2 is an inverted image of I1. These two rod lenses (relay system) together are termed a reversal system [Dierksheide *et al*., 2002], because they together form an image which is a mirror image of the intermediate image formed by the objective lens. The next reversal system then reverses the image I2 to form another image I3 so that it is in the same orientation as the intermediate image (I1). This image (I3) is then magnified through an eyepiece and is focused on an imaging device (eye or camera). The number of reversal systems in a borescope depends on its length. The objective lens and the rod lenses consisting of two or more glasses each with different refractive indices are bonded together to form a doublet or a multi-element for the light to be refracted towards or away from the optical axis [Miller and Hollingsworth, 1986]. Detailed description regarding the construction and principle of operation of borescopes are given in the literature [Miller and Hollingsworth, 1986; Quint, 1986; Heavens and Ditchburn, 1991; Dierksheide *et al.*, 2002].

The light collecting capability of the objective lens is proportional to the square of its numerical aperture (NA). The NA of a lens depends on its focal length, half of acceptance cone angle (and hence, its field of view) and the refractive index of the medium from where the light

arrives. The field of view (FOV) is the area that an observer can see through the lens system. Generally, the objective lens has a small focal length to have a greater field of view. Although extending the FOV increases image area, the image size is decreased when viewed from an equal distance. Another effect of increasing the FOV is that the entrance pupil formed by the objective lens and the subsequent exit pupil via the relay system and the eyepiece will be reduced in size resulting in a reduction of effective light transmission through the system [Miller and Hollingsworth, 1986]. Large FOV of the borescope also causes image distortion [Dierksheide *et al.*, 2002]. This is due to the fact that borescope lenses project the image of a planar object on to a spherical surface. Since the camera sensor is planar, the image captured by the camera is a projection of the spherical image plane onto its planar sensor surface [Dierksheide *et al.*, 2002].

A modern rigid borescope is regarded as a set of very thick lenses or alternatively, as a set of air lenses in a glass medium. Due to the reduced number of glass/air boundary layers, light is transmitted in the glass medium over a long distance with a lower loss of intensity than air and therefore, the brightness of the image is enhanced. Light transmitted (T_L) in the borescope depends on the radii of the lenses (r), refractive index (n) of the transmitting medium (in this case, glass with a refractive index of ~1.55, rather than air with a refractive index of 1) and the distance between the successive images (d). It is calculated as [Heavens and Ditchburn, 1991]:

$$T_L = K.n^2.r^4/d^2 \qquad \text{(A3.1)}$$

where K is a constant which depends on the luminosity of the object. The brightness, transmissivity, spatial resolution and contrast of the borescope increase with large lens diameter and with the use of fewer lenses. Therefore, for a given application, a short and thick borescope with a small FOV (small FOV will cause less image distortion) is the ideal candidate to obtain the best image quality [Dierksheide *et al.*, 2002]; the optimization of these parameters is, however, application specific. To prevent internal reflections, all the elements in the system have an effective air to glass anti-reflection (AR) coating. Borescopes come with different direction of view (typically 0-120^o) and field of view (typically 5-130^o) [Miller and Hollingsworth, 1986; AVL, 2009; Karl-Storz, 2012].

Bond lines are used to fix the glass elements together and create the doublet forms within a borescope. These bond lines in the relay system can be chipped or separated with excessive load; this would then make the system out of focus with impaired visual quality, although no external dent or bend could be seen on the outside of the instrument. Similarly, repeated high temperature exposure could also cause bond failure and opacity of the adhesives. Most adhesives for engine applications have a temperature ceiling of 120^{o}C [Miller and Hollingsworth, 1986]; therefore, compressed air is used to prevent the borescope from getting damaged by overheating.

REFERENCES

AVL VisioScope 2009, Available: http://www.avl.com/ [Accessed: 25th May 2009].

Dierksheide, U., Meyer, P., Hovestadt, T. and Hentschel, W., 2002, "Endoscopic 2D particle image velocimetry (PIV) flow field measurements in IC engines", Experiments in Fluids, vol. 33, pp. 794-800.

Heavens, O.S. and Ditchburn, R.W., 1991, "*Insight into Optics"*, John Wiley & Sons, England.

Karl Storz-Endoscope, Industrial Group/ Available: www.karlstorzindustrial.com [Accessed: 24th February 2012].

Miller R.A. and Hollingsworth, T.R., 1986, "Rigid endoscopes: optical and design considerations", British Medical Bulletin, vol. 42, no. 3, pp. 226-229.

Quint, R.H., 1986, "Aspects of endoscopic documentation", British Medical Bulletin, vol. 42, no. 3, pp. 230-233.

Appendix A4

PM EMISSIONS AND COMBUSTION STABILITY AT HIGH-EGR LTC

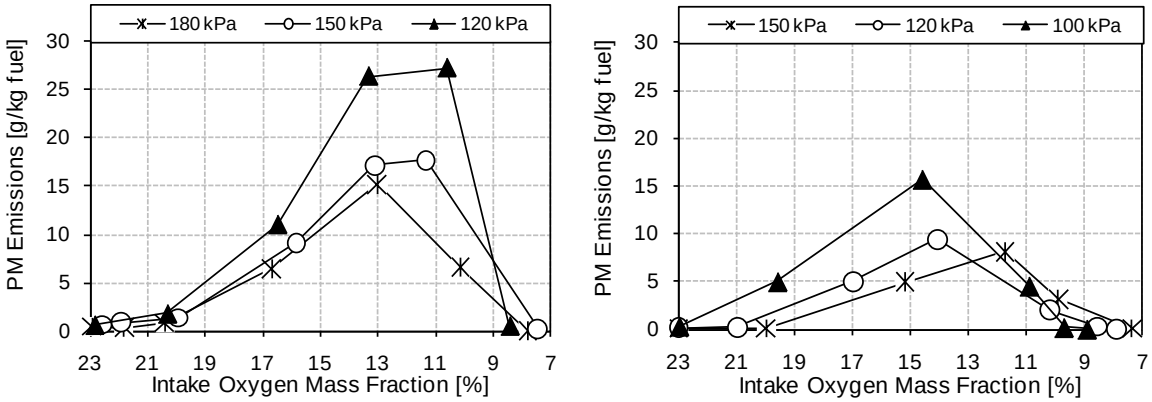

Fig. A4.1: PM emissions at different engine speeds at various intake pressures and intake charge dilution levels. The correlation given in Equation 3.1 in Chapter 3 was used to convert the FSN to PM mass at all intake charge dilution levels. [Left hand figure: 2500 rpm; right hand figure: 1500 rpm]

Table A4.1: Combustion Phasing, Peak Energy Release Rate and Peak Cylinder Pressure Variability

Engine speed [rpm]	Intake pressure (abs) [kPa]	EGR rate [%]	Std. dev. of CA5 [^{o}CA]	Std. dev. of CA50 [^{o}CA]	COV of peak energy release rate [%]	COV of peak cylinder pressure [%]	COV of GIMEP [%]
2500	120	62.0	0.29	0.58	11.90	2.95	2.4
2500	150	65.5	0.15	0.28	5.35	1.42	2.2
2500	180	63.0	0.15	0.24	4.62	1.09	1.8
1500	100	57.0	0.37	0.63	12.46	3.32	1.7
1500	120	61.0	0.22	0.35	6.70	1.47	1.1
1500	150	63.0	0.11	0.19	4.61	0.68	1.1

Appendix A5
SPRAY PENETRATION MODELS

Dent Spray Penetration Model [Dent, 1971]:

Penetration, *S*, of the fuel spray tip across the combustion chamber is given by:

$$S = 3.07 \left(\frac{\Delta p}{\rho_a}\right)^{0.25} (t\ D)^{0.5} \left(\frac{294}{T_a}\right)^{0.25} \quad \text{(A5.1)}$$

where D is the diameter of the orifice, Δp is the differential pressure across the nozzle and *t* is time after SOI timing. ρ_a and T_a are the density and temperature of the in-cylinder gases respectively.

Hiroyasu and Arai Spray Penetration Model [Hiroyasu and Arai, 1990]:

Spray break-up time (t_b) is given by:

$$t_b = 28.65\ \frac{\rho_l\ D}{(\rho_a\ \Delta p)^{0.5}} \quad \text{(A5.2)}$$

where ρ_l is the density of the liquid fuel. Spray penetration is given by:

For $0 < t < t_b$

$$S = 0.39 \left(\frac{2\ \Delta p}{\rho_l}\right)^{0.5}\ t \quad \text{(A5.3)}$$

For $t > t_b$

$$S = 2.95 \left(\frac{\Delta p}{\rho_a}\right)^{0.25}\ (D\ t)^{0.5} \quad \text{(A5.4)}$$

Naber and Siebers Spray Penetration Model [Naber and Siebers, 1996]:

Mean spray dispersion half angle (θ/2) for a non-vaporizing spray is given by:

$$\tan\left(\frac{\theta}{2}\right) = 0.31 \left(\frac{\rho_a}{\rho_l}\right)^{0.19} \quad \text{(A5.5)}$$

The break-up time in the Hiroyasu and Arai model can be compared to the transition time (t_r) of the Naber and Siebers model; the time when the spray transitions from being dominated by injected liquid to being dominated by entrained gas and is given by:

$$t_r = 7.6\ \frac{D.\rho_l}{\sqrt{(p_l - p_a)\rho_a}} \quad \text{(A5.6)}$$

where p_l is the fuel injection pressure and p_a is the gas pressure at SOI timing.

Spray penetration is given by:

$$S = \sqrt{\frac{C_v\sqrt{2\,C_a}}{a.\tan\left(\frac{\theta}{2}\right)}}\sqrt{\sqrt{\left(\frac{p_l - p_a}{\rho_a}\right)}\,D\,t} \qquad \text{(A5.7)}$$

where C_a and C_v are the orifice area contraction coefficient and orifice velocity coefficient respectively. a is a density dependent constant ($a \propto {\rho_a}^{-0.295}$) for a constant wall temperature. For an orifice diameter of 0.185 mm with a length to diameter ratio of 5.1, the values for the orifice discharge coefficients, C_d, C_a and C_v ($C_v = \frac{C_d}{C_a}$) are 0.56, 0.82 and 0.68 respectively.

REFERENCES

Dent, J.C., 1971, "Basis for the comparison of various experimental methods studying spray penetration", SAE Paper No. 710571.

Hiroyasu, H., and Arai, M., 1990, "Structures of fuel sprays in diesel engines", SAE Paper No. 900475.

Naber, J.D., and Siebers, D.L., 1996, "Effects of gas density and vaporization on penetration and dispersion of diesel sprays", SAE Paper No. 960034.

Appendix A6

FUEL VOLUME DISTRIBUTION IN SPLIT FUEL INJECTIONS

The fuel volume distribution between the two injection events was measured with a rate tube. Note that the volume of the fuel injected in the two injection events were measured at an injection pressure of 90 MPa and at various injection timings (same injection pressure and timings used in Chapter 6) at an engine speed of 750 rpm because of the limitation of the rate tube. The pressure history in the fuel line (refer to Fig. A6.1a for SOI1 timing of -39 ^{o}CA ATDC and SOI2 timing of -15 ^{o}CA ATDC) demonstrates the existence of a wave that affects the pressure of the fluid at the injector for the 2nd injection event. The presence of the wave in the fuel line significantly influenced the fuel rail pressure (±8% of the desired value in this case) and hence the injected fuel quantity in the split injection strategy as shown in Fig. A6.1. The three cases shown in Fig. A6.1 represents the variations of fuel quantity between the two injection events. Note that Fig. A6.1b indicates higher fuel quantity in the 1st injection event, Fig. A6.1c indicates equal volume of fuel in the two injection events, whereas Fig. A6.1d indicates lower fuel quantity in the 1st injection event.

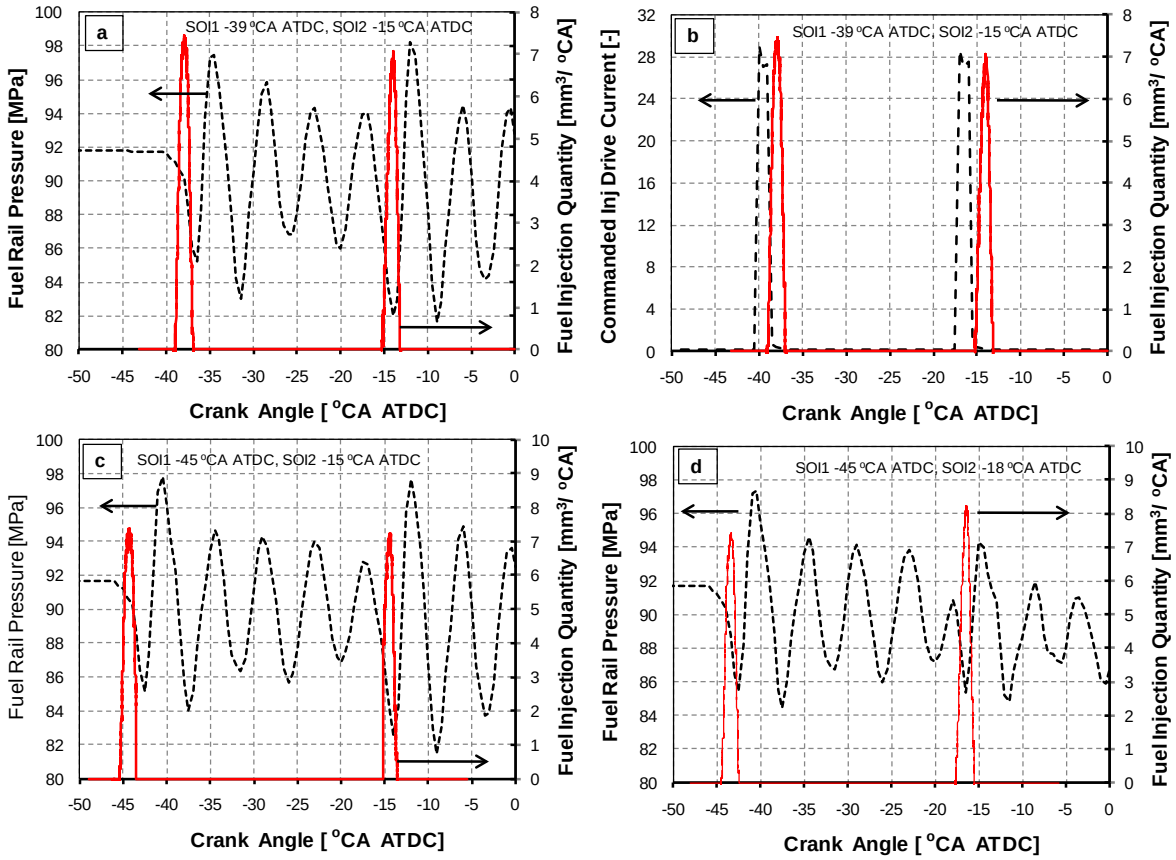

Fig. A6.1: Fuel injection pressure and the effects of SOI2 timings on fuel injection quantity at 90 MPa injection pressure

The commanded injector current signals and the actual start of fuel injection timings are shown in Fig. A6.1b. Note that the injector drive current signal was advanced by 1.5 ^{o}CA compared to the actual start of injection timing at 750 rpm engine speed. Therefore, while analysing the energy release plots, the injector current signal needs to be retarded accordingly (for example, by 3 ^{o}CA at 1500 rpm).